Measurement of Adhesion Using the Island Blister Test

by Scott Anthony Sikorski

B.S., Metallurgy, Columbia University (1987)
M.S., Materials Engineering, M.I.T. (1989)

Submitted to the Department of
Materials Science and Engineering
in Partial Fulfillment of the Requirements
for the Degree of

Doctor of Philosophy
in
Materials Science and Engineering

at the

Massachusetts Institute of Technology

May 1994

Signature of Author .....
Department of Materials Science and Engineering
April 29, 1994

Certified by .....
Frederick J. McGarry
Professor of Polymer Engineering
Thesis Supervisor

Certified by .....
Stephen D. Senturia
Barton L. Weller Professor of Electrical Engineering
Thesis Supervisor

Accepted by .....
Carl V. Thompson II
Professor of Electronic Materials
Chair, Department Committee on Graduate Students

Measurement of Adhesion Using The Island Blister Test

by
Scott Anthony Sikorski

submitted to the Department of Materials Science and Engineering
on April 29, 1994 in partial fulfillment of the requirements for the Degree of
Doctor of Philosophy in Materials Engineering

Abstract

This thesis focuses on the refinement and application of the island blister test (IBT) initially proposed and demonstrated by Allen and Senturia to the measurement of the specific interfacial fracture energy of polyimides (hexafluorodianhydride-aminophenoxybiphenylin (HFDA-APBP), pyromellitic dianhydride-oxydianiline (PMDA-ODA), and biphenyldianhydride-phenyldiamine (BPDA-PDA)) to metals (Cr and Al). A finite element model developed by Margaritis using the modified crack closure technique provides an analysis of the debonding process. The mode I and mode II contributions along with the plastic dissipation are separately calculated through the model. A new sample fabrication process was developed to produce circular blister sites at yields approaching 100%. Refinements in the testing methodology increase testing reproducibility and testing yield. Reproducibility is $\pm$ 13%, in close agreement with the $\pm$ 15% predicted based on an error analysis of the test.

The mode I component of the specific fracture energy is found to provide a criterion for the onset of fracture. This result, found long ago for elastic fracture in homogeneous bodies, is original for the case of interfacial decohesion in the presence of extreme plastic dissipation. The error analysis resulted in a numerically derived relationship that describes the γ_{Ic} in terms of the experimental parameters and elastic constants of the adhered film.

Adhesion to Cr was found in all cases to be superior than to Al. X-ray photoelectron spectroscopy, Auger electron spectroscopy, and scanning electron microscopy were used to explored the nature of the fracture surfaces. The locus of failure of all the polyimides studied on Cr was cohesive in the polymer. When debonded from an Al adherend, the locus of failure was a combination of cohesive in the polyimide and adhesive at the interface between the polyimide and oxidized aluminum. This combination is consistent with the lower measured debond energies. It was found that processing effects can strongly influence γ_{Ic}.

The locus of failure produced by the peel testing the same systems was nearly identical to those described above for the IBT. An attempt was made to evaluate the measured peel energies in terms of the plastic analysis of Kim and Avaras.

An exploratory study of the application of the IBT to metal on polymer systems is reported.

Thesis Supervisors: Dr. Frederick J. McGarry
Professor of Polymer Engineering

Dr. Stephen Senturia
Barton L. Weller Professor of Electrical Engineering

Table of Contents

List of Figures

List of Tables

Acknowledgments

Several people and organizations contributed greatly to the success of this work. First, my advisors Prof. S.D. Senturia and Prof. F.J. McGarry are warmly acknowledged for their support and guidance over the past several years. The encouragement of Prof. McGarry during the difficult early years instilled the confidence in myself necessary to complete this work and is deeply appreciated.

This work was completed through the Resident Work Study program of my employer, the IBM Corp., who provided financial support in the form of tuition and stipend payment. I would like to thank the management team at IBM who supported my application to this program. Especially appreciated are the efforts of Pete Hayunga without whose persistent support none of this would have been possible. Also recognized are Dr. Thomas Redmond, Linda Herman-Spiro, and Dr. John Knickerbocker for their continued support. The financial assistance provided by the Electronics Packaging Program in the form of laboratory and computer usage fees is also greatly appreciated.

George Margaritis has been both a great friend and a tremendous source of information to me who started this work with little understanding of the world of fracture mechanics. George also developed the finite element analysis of the island blister test, without which none of the subsequent understanding would have been possible. Mark Brillhart and Ed Shaffer will be warmly remembered not only for their stimulating comments but also for their friendship which created a amiable work environment.

David Volfson provided much technical assistance in the early days, especially with regard to mask design and the IBT fabrication process. Fred Trusell trained me in the use of much of the laboratory equipment and assisted with modification of the testing apparatus. As a

UROP, Elaine Stafanis quickly grasped the technique and showed great patience in generating much of the IBT data. Pradnya Nagarkar provided me with an understanding of the XPS technique and was always very pleasant to work with. The assistance of the MTL staff, especially Octavio Hurtado and Nestore Polce, is acknowledged.

At IBM, the contributions of Dr. Scott Dwyer for SEM support and Dr. Howard Clearfield for training on the XPS equipment there are kindly acknowledged. Libby Shaw of MIT's Center for Materials Science and Engineering provided technical support for Auger analysis.

All of the support and contributions mentioned above promoted the technical aspects of the thesis and my intellectual development in general. However, equally important, was the support and encouragement of my family throughout the often difficult process of completing a doctorate program. Even beyond this, my brother, Matthew, also provided tremendous assistence with the actual production of the thesis. Without this help, I would surely not have documented this work in a timely fashion. The support and encouragement of my parents in all of my endeavors, but especially this one, is warmly appreciated as I hope they know. Finally, completion of a Ph.D. while working full time allows little time for anything else. The understanding of my wife Nhan in selflessly sacrificing whatever time we might have had together during our first married year is greatly appreciated and this work is dedicated to her.

Chapter 1: Introduction

1.1 Advantages and Challenges of Thin Film Multichip Packaging

The key parameter describing any microelectronic packaging technology is its *packaging density*, the amount of interconnect provided by the package, in units of length per unit area [1]. Higher packaging densities allow positioning of the IC chips closer together, minimizing the length of required interconnects and the associated packaging-related delays. Because the performance of the high speed devices produced today can be limited by delays in the package, increases in the performance of the system as a whole are predicated on advances in packaging density [2].

Thin film multichip-module packaging currently represents the most advanced expression of high density interconnect (Figure 1.1.1) [3]. The low dielectric constant,

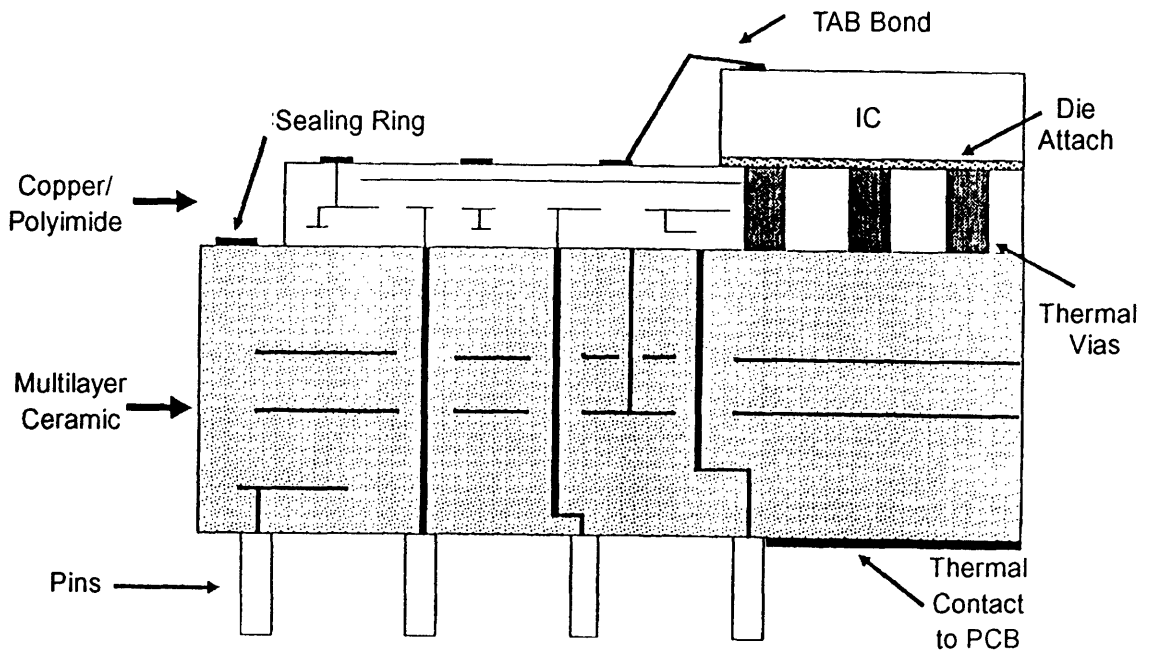

Figure 1.1.1: One possible variation of the thin film multi-chip module [1].

good planarization capabilities, and high temperature stability make polyimide an excellent choice for the insulating material in the thin film structure [4]. Copper and occasionally aluminum metallizations are typically used as the electrical conductor [5]; other metals, such as chromium and titanium, are frequently used as bonding layers or diffusion barriers [6]. The large number of polymers and metals that could be used, coupled with the lack of any standardization in this field, results in a tremendous number of materials and processing combinations available to manufacturers.

While thin film multichip modules present tremendous performance advantages, they also raise many reliability and processing-related concerns [4]. Figure 1.1.2 illustrates the relevant interfaces of concern in thin film structures. The convention followed in this work names the adhered film first followed by the adherend as demonstrated in Figure 1.1.2. Metal on polyimide interfaces are of particular concern because the metal is deposited on fully cured polyimide, limiting the possibilities for chemical reaction. An additional challenge is the cost associated with this technology, both the large capital expense of processing facilities and the higher unit costs resulting

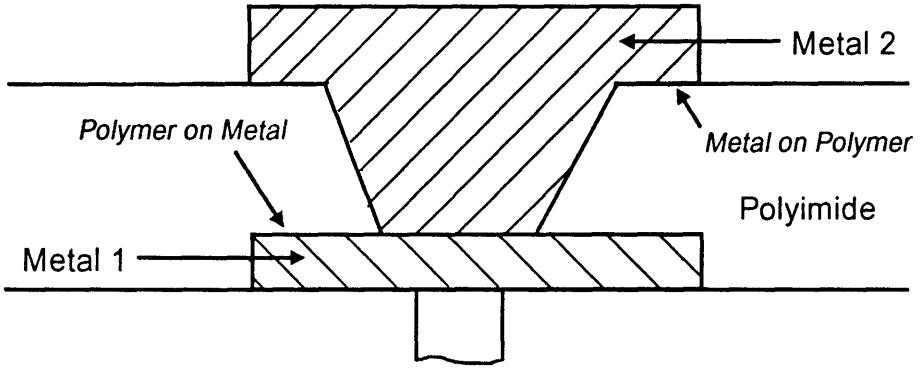

Figure 1.1.2: Interfaces typical in thin film structures.

from yield issues. The reliability uncertainties coupled with high manufacturing costs conspire to restrict widespread usage of this technology.

Adhesion issues are a major component of both the cost and reliability concerns. Adhesion degradation over time is a reliability problem, poor initial adhesion is a manufacturing or yield problem. Therefore, it is critical to ensure that the initial adhesion is satisfactory and that it remains above some minimal level throughout the projected life of the product. The success or failure of any thin film technology is largely a function of how well these adhesion issues are addressed.

The field of microelectronics has two distinct needs for adhesion testing: one related to process and product development, and another related to manufacturing. The development need revolves around materials selection and process optimization. A test must be available to rank different combinations of materials and processing parameters in terms of adhesion behavior before the process routing can be finalized. An ideal test for this application would be able to accurately record the adhesion strength of adhered films with a range of mechanical properties (modulus, residual stress, plasticity). Manufacturing requires an adhesion test that can be used as a quality assurance measure during product fabrication. The test must be quick and easy to perform with results that are operator independent and highly reproducible. It is not obvious that one adhesion test can fill both the development and the manufacturing sets of requirements. Existing comparative tests typically serve the manufacturing function well. The adhesion test that is the subject of this work addresses the development need.

A further need for precise knowledge of the specific fracture energies is in modeling efforts, where the interfacial strengths are compared to strain energy release

rates through a stress analysis. Lacombe *et al.* [7] present a good example of such a methodology. They performed a finite element analysis of a complex multi-layer structure, typical of high density thin film interconnects. The model required inputs of materials properties such as elastic constants and critical fracture energies for key interfaces. The predictions of the model were substantiated through fabrication of the modeled structures and observation of delamination, in this case at the metal-polymer interface of a via sidewall, the area of weakness indicated by the FEA. Clearly, this "testing" of designs without incurring the expense of fabrication represents a very desirable strategy. Success of such modeling efforts is contingent on accurate provision of the materials parameters, a critical one being the specific fracture energy of interfaces (γ_a). This application provides another driving force for the accurate measurement of γ_a; comparative techniques, such as are currently available, are inadequate for this modeling.

The characteristics of an ideal development adhesion test include: accuracy, flexibility, transparency to the operator, and simplicity. *Accuracy* means that the measured quantity is predominantly basic adhesion and not dissipative forces associated with the test; this is the primary requirement. The test must be able to compensate for the effects of residual stress and to separate energy lost to dissipative mechanisms from the true γ_a to fulfill this requirement. *Flexibility* refers to the ability to measure a range of debond energies extending into the realm of very well-adhered films. *Transparency to the operator* means that results are operator insensitive and do not depend on the manner of performing the test. Usually such a requirement dictates the need for some level of automation, or at least the formulation of a standard testing protocol. *Simplicity* means that the test is not too time consuming and is easily adaptable to routine use.

1.2 Methods of Adhesion Testing

Thin film adhesion can be tested in many ways; reviews of adhesion testing techniques have frequently appeared in the literature [8, 9, 10, 11]. This section reviews the advantages and disadvantages of the primary adhesion tests currently practiced in the thin film multichip module industry. The ones most applicable to the needs stated above will be briefly reviewed and the shortcomings of these tests will be highlighted, providing motivation for the development of a superior test.

A very widely practiced adhesion test in the thin films industry is the ***peel test*** (Figure 1.2.1 (a)). Here a blanket film is patterned into strips, either photolithographically or by scribing, a strip is released, and a normal force is applied to the strip. The advantages of this technique are its easy sample fabrication and testing procedure. Recent studies have shown that the peel test is an accurate measure of γ_a only under the condition, $6EP/h\sigma_y^2 < 1$, where E is the elastic modulus, P is the peel force, h is the thickness, and σ_y is the yield stress of the adhered film [12, 13, 14]. For Cu films on polyimide substrates, this condition requires a Cu film thickness of ~1 cm, three orders of magnitude larger than the 10 μm films typically used. For polyimide films on metal, films several hundred microns would be required, still much thicker than the films used in industrial applications. Films which do not satisfy this condition suffer far-field plastic deformation during testing, obscuring measurement of the work of adhesion.

The development of the "Universal Peel Diagram" concept by Kim *et al.* expands the applicability of the peel test down to $t > 1$ μm [12, 13]. By knowing the peel force and the thickness of the coating, the work of adhesion, γ_a, can be read off of this diagram.

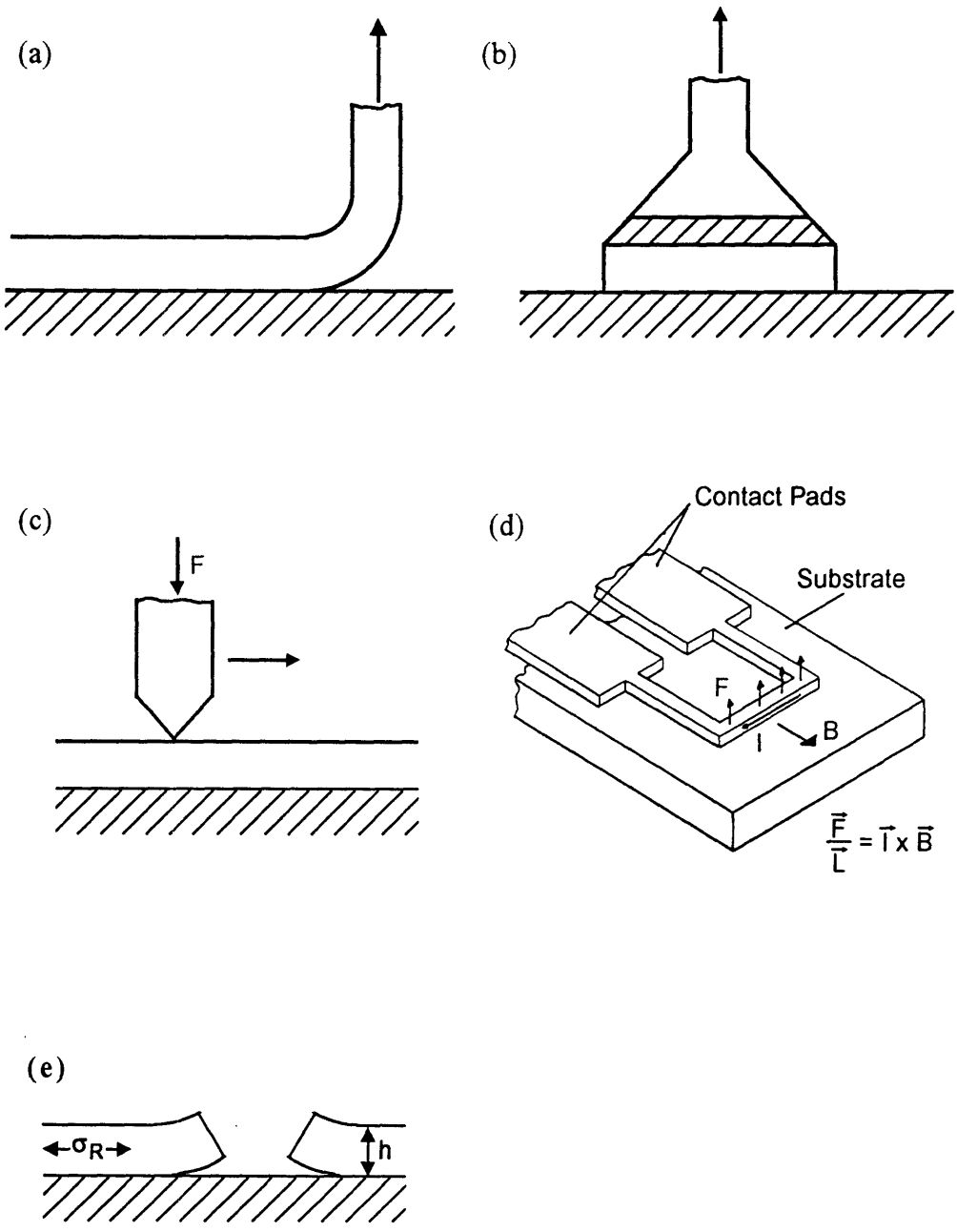

Figure 1.2.1: Illustration of adhesion testing techniques applied to thin film systems: (a) peel test, (b) pin pull test, (c) scratch test, (d) electromagnetic tensile test, and (e) edge delamination test.

Construction of such a diagram can be achieved for any substrate-film system using only peel test equipment, but it requires knowledge of properties of the coating (modulus of elasticity, yield stress, thickness, and a number of parameters that describe film hardening) and the compliant substrate layer (effective modulus of uniaxial strain and thickness). Application of this diagram to the Cu/Si and Cu/polyimide/Si systems has shown that the work of adhesion is typically only 1-2% of the measured peel force. For example, the measured peel force of a 77 μm Cu film off of a Si substrate is 31 g/mm, although the γ_a value extrapolated from the universal peel diagram is a mere 0.54 g/mm [12].

Even with the Universal Peel Diagram, the peel test suffers from the fundamental problem of trying to extract a γ_a value from a measured peel force 100 times large. The accuracy of this procedure is uncertain at best. Avaras *et al.* provide a non-graphical method of subtracting out plastic work, but it is still not applicable to very thin, well-adhered films [15, 16]. This technique is reviewed in detail and applied to data generated in the present work in Chapter 4. In spite of the weaknesses of the peel test, the ease of sample construction and test execution has contributed to its rapid spread.

A popular test for comparative purposes is the ***pull test*** in which a pin is attached to the adherend (usually in the form of a pad) using either epoxy or solder (Figure 1.2.1 (b)). The interface is stressed through application of a force normal to the pin, and the failure strength of the interface is measured. The problems with this test include difficulty in assuring that (1) the applied force is indeed normal with no shear components, (2) the failure occurs at the interface of interest, prompting the need for a

very strong "glue" with which to attach the pin, and (3) no defects are present to act as stress concentrators and precipitate a low strength fracture [17, 18, 19, 20]. The last problem is especially acute and several efforts involving the pull test report a wide scatter in data because of it [21, 22]. More recent evaluations of the pull test incorporate statistical analysis based on a Weibull distribution, initially developed to describe the probability of failure resulting from a population of flaw-induced cracks [21, 22]. In well-adhered systems, compliance effects in the substrate may be important but are typically not accounted for in the analysis. A variation of the pull test is the ***topple test*** where a force parallel to the substrate is applied to an attached rectangular stud. This configuration reduces the need for precise alignment, but the second and third problems discussed above still apply.

The ***scratch test*** involves dragging a stylus across the surface of the metal film and applying increasingly large loads until the interface fails, resulting in a clear channel (Figure 1.2.1 (c)) [23, 24, 25]. A study by Butler *et al.* of vacuum deposited thin metal films on glass has demonstrated that the scratch process is extremely complex and that extraction of work of adhesion values is currently not possible [26]. The scratch test is widely used in the protective coatings industry where the test closely resembles the final application.

The ***electromagnetic tensile test*** measures adhesion by the application of an electrical current through a metal line in the presence of a magnetic field. This produces an **I x B** force normal to the metal/polymer interface (Figure 1.2.1 (d)) [27, 28]. The major limitation is the Joule heating produced by the relatively large currents required to test well adhered films (8 A for a 10 μm Cu film produces a normal force of 1 MPa).

Pulsed currents can help in such cases. Of course, it is essential that the substrate material be dielectric, limiting the applicability of this test strictly to metal on dielectric systems.

The ***edge delamination test*** uses energy stored in the adhered film in the form of residual stresses as a driving force for debonding (Figure 1.2.1 (e)). Recent development work by Shaffer [146-148] has demonstrated that the technique is viable for weakly adhered films under residual tensile stresses. Extension of the test to well adhered, ductile films may require very thick films (> 150 μm), limiting its applicability.

1.3 Blister Tests

The blister test requires no external tractions for debonding, and the peel angle is low relative to other methods. Since the time that the ***standard blister test*** (SBT) (Figure 1.3.1 (a)) was first reported in 1961 by Dannenberg [29], many improvements and refinements have been made. Table 1.1.1 summarizes the critical analytical and experimental aspects of the early work. Initial efforts by Williams *et al.* [30, 31, 32] applied the concepts of continuum mechanics to the blister geometry to relate experimental variables such as critical pressure, p_c, to γ_a. Hinkley [33] assumed that the deformed membranes take the shape of a spherical cap and can be described by membrane theory. His analysis was elasticity-based and the fracture criterion was derived from an energy balance. Gent and Lewendowski [34] used the analysis of Hencky [35] to more accurately describe the shape of the inflated blister. An improved energy balance was also employed to derive a more realistic fracture criterion. Even with these improvements, the form of their solution differed from Hinkley's only in the

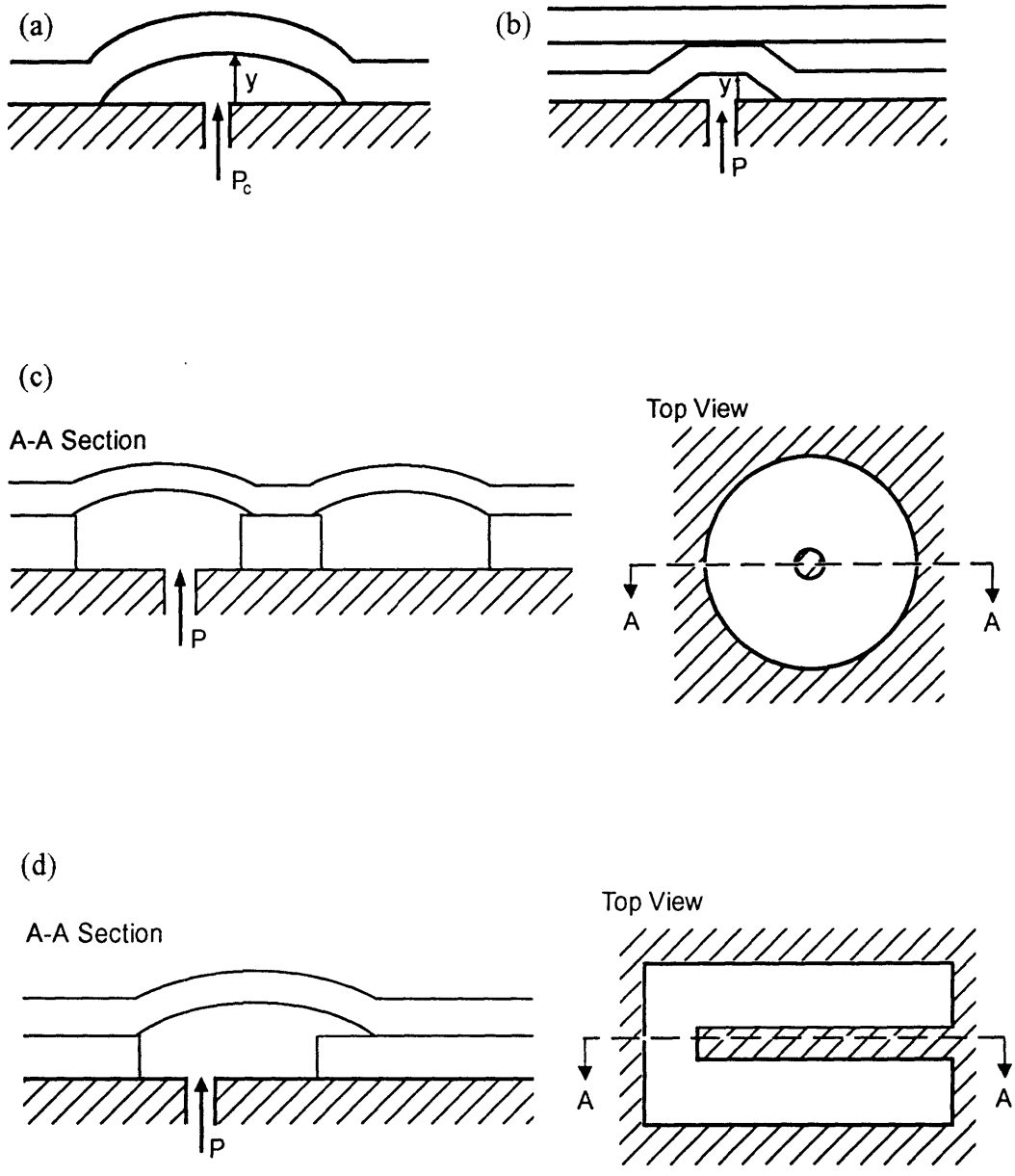

Figure 1.3.1: Illustrations of the geometries of various blister tests: (a) standard blister test, (b) constrained blister test, (c) island blister test, and (d) peninsula blister test.

magnitude of a constant. Chu *et al.* [36, 37, 38] modified Gent and Lewendowski's analysis to account for the rate of pressurization of the blister, resulting in a different fracture criterion and the speculation about variation in viscoelastic effects at the crack tip. All analyses to this point assumed that large scale dissipative mechanisms were absent, did not account for residual stresses, and were incapable of separating the fracture energy into its components.

Using nonlinear von Karman equations for a thin circular plate, Jensen [39, 40] built on Suo and Hutchinson's [41] predictions for an edge crack at an interface between two elastic materials to incorporate a loading mode dependency and the effects of residual stress into the blister analysis.

Table 1.1.1: Summary of relationships used to evaluate standard blister test data.

Workers	**Fracture Criterion γ_a =**	**Expt'l System (film/adherend)**	**γ_a (J/m^2)**
Williams *et al.*[31]	$P_c a/Ec_i$	Solithane/PMMA	
Hinkley [33]	$0.25P_c y$	PS, PMMA/SiO_2	0.1
Gent and Lewendowski [34]	$0.649P_c y$	PSA/teflon, PMMA	20-150
Chu *et al.* [37]	$0.39(R^2/N^2Eh)^{1/5}$	polyisoprene/PMMA	3-4
		PMDA-ODA/SiO_2, Si	0.3-24.8
		BPDA-PDA/SiO_2, Si	0.02-0.26

P_c - critical pressure; a - blister radius; E - Young's modulus; c - geometry dependent constant y - maximum film deflection; R- rate of pressurization; h - film thickness; N - slope of pressure versus time curve.

The geometry of the ***constrained blister test*** (CBT) is similar to the SBT with the addition of a plate positioned parallel to the substrate restricting the vertical deflection of the film (Figure 1.3.1 (b)). Compared to the SBT geometry, where the maximum stress occurs in the center of the blister [42, 43], the CBT geometry reduces these stresses minimizing the risk of film rupture prior to delamination. Napolitano *et al.* [44] incorporate rate effects and viscoelastic behavior in the vicinity of the crack tip through a phenomenological dissipative coefficient. The fracture energy is defined as the minimum value of the product $P_c y$ that results in debonding, where y is the spacer height. Chang *et al.* [45] applied the CBT to the testing of a pressure-sensitive adhesive tape on polycarbonate system and found γ_a to be dependent on the rate of the test. Lai and Dillard [46, 47, 48] evaluated the adhesion of a thick aluminum film analytically using elementary plate theory, and numerically with finite element analysis. The two methods of analysis agreed well, and their results show that the strain energy release rate remains nearly constant as the debond proceeds. Agreement between the two methods deteriorates for testing of thinner, lower modulus films which behave more like membranes than plates. In all of these analyses, γ_a includes viscoelastic and plastic deformations local to the crack tip, and the process zone is assumed to be small relative to critical dimensions of the geometry. No attempts at separating mode I and mode II contributions in the CBT has yet been published.

Allen and Senturia have developed an ***island blister test*** (Figure 1.3.1 (c)) and applied it to the problem of measuring thin polymer films on metal and on polymer [49, 50, 51, 52, 53]. The advantages of the IBT include its ability to account for residual stresses in the film, it can be applied to thin well-adhered films without tearing them, and

it includes less dissipative energy in the measurement than the SBT or the peel test. Although the geometry of the IBT offer certain intrinsic advantages, refinements in sample fabrication, testing methodology and data analysis are required.

Expanding on the IBT concept, Dillard *et al.* developed the ***peninsula blister test*** [PBT] which replaces the axisymmetric island with a peninsula (Figure 1.3.1 (d)) [54, 55, 56, 57]. This test offers many of the advantages of the IBT with the additional advantages of even lower stresses at the crack tip during debonding, and a constant strain energy release rate. Based on a normalized bond dimension and a normalized strain energy release rate (γ/σ^2, where σ is the maximum stress at the crack tip), Lai and Dillard have demonstrated that the PBT is the most "efficient" blister test followed by the IBT and the SBT [57]. This means that for a given materials system, the PBT stresses the film least during debonding, particularly important in ductile, well-adhered systems where stresses beyond the yield point of the adhered film are possible. However, the peninsula geometry renders modeling of the PBT more difficult than its axisymmetric brethren.

Recent work by Liechti *et al.* [58] suggests that even in the PBT, gross plasticity in the adhered film is difficult to avoid in the case of copper films delaminating from polyimide adherends. Their initial effort focused on attempting to define an optimal geometry to minimize dissipative effects, assuming a γ_a of 100 J/m^2. It appears that regardless of the blister geometry chosen, accurate testing of adhesion in the ductile, well-adhered systems of practical interest to the thin films multichip module community will require some way of incorporating far-field dissipative effects such as plasticity.

1.4 Objectives and Scope of Thesis

The goal of this thesis is to provide a test capable of accurately measuring the adhesion of the tough, well-adhered films of interest to the microelectronics community. The previous section has shown that present techniques fall short of meeting these needs. Their major shortcoming is the inability to account for dissipative mechanisms. Accounting for these mechanisms will require numerical modeling based on a realistic constitutive relationship of the adhered film that includes plasticity. In this respect, the much easier to model axisymmetric geometry of the IBT provides a critical advantage over the PBT, justifying its use here.

In pursuit of this goal, work was endeavored upon in two major areas. The first was refinement of the island blister test. Further development in the fabrication, testing, and analysis of the IBT was required to produce circular geometries, to establish a reproducible testing protocol, and to incorporate plasticity. The second was application of the refined IBT to (i) the development of a fracture criteria applicable to the mixed mode loading found at interfaces, (ii) the interrogation of polymer-on-metal systems to demonstrate the important ability to rank specific fracture energy across different materials systems, and (iii) the evaluation of the utility of the widely used peel test.

The thesis is organized in the following manner. Chapter 2 describes the experimental methods used, including refinements of the IBT fabrication process and testing methodology. The techniques used for determination of the mechanical properties required as inputs to the finite element model of the test are also reviewed. The finite element model of the IBT is detailed in Chapter 3 along with a comprehensive error analysis which is extended to provide design guidelines for sample geometry. The

measurement of specific fracture energy with the IBT and the peel test is the subject of Chapter 4. The criterion for fracture is made clear by the IBT data. The peel test data is evaluated in terms of an elastoplastic methodology developed earlier by Kim *et al.* [4-8]. Specific fracture energy numbers generated through the two tests are compared and the implications for usage of the peel test discussed. Chapter 5 covers the locus of failure analysis, focusing mainly on X-ray photoelectron spectroscopy (XPS) results but also including Auger electron spectroscopy (AES) and scanning electron microscopy (SEM) analyses. Finally, a summary of the thesis work and conclusions are offered in Chapter 6.

Chapter 2: Experimental Methods

The adhesion characteristics of three polyimides are explored in this work. The polyimides are: hexafluorodianhydride-aminophenoxybiphenylin (HFDA-APBP) manufactured by Amoco Chemical Company under the trade name Ultradel 4212 or UD4212; pyromellitic dianhydride-oxydianiline (PMDA-ODA) manufactured by Dupont under the trade name Pyralin PI2545; and biphenyldianhydride-phenyldiamine (BPDA-PDA) manufactured by Dupont under the trade name Pyralin PI2611. More information about the chemical structure of these polymers is presented in Chapter 5. This chapter reviews the methods used in fabricating and testing samples for the determination of mechanical properties and adhesion characteristics.

2.1 Mechanical Properties

As will be shown in Chapter 3, accurate determination of the work of adhesion requires knowledge of the mechanical properties of the adhered film under testing. This section presents the techniques used to generate this information. In particular, the elastic modulus, the plastic and viscoplastic behaviors, and the residual film stresses are measured. Since the case of polymer-on-metal adhesion is emphasized in this work, it is the mechanical properties of the polymer films that are important.

2.1.1 Constitutive Behavior

The constitutive behavior of all three polymer films was developed through uniaxial tensile testing. Samples were fabricated by: (1) metallizing a clean silicon wafer with 1 μm of Al, (2) spin casting and curing the polymer of interest, (3) patterning the

polymer by reactive ion etching through a metal hard mask, (4) removing the hard mask in a wet etch, and finally (5) lifting the patterned polymer film off in a dilute solution of HF which undercuts the film by attacking the Al. Alternately, for these polyimide materials which are not sensitive to defects at their edges, the wafer coated with a blanket of Al and the polymer film can be snapped in half and submerged in dilute HF, lifting the film off the wafer. The blanket film can then be cut into strips of the appropriate size using a straight edge and razor. The former technique has the advantage of yielding very precise geometries but at the cost of extra processing and exposure of the polymer to HF. Both processes were used with equal success on all of the polyimide films tested.

Fabricated polymer strips 4-6 mm wide, 5-8 cm long and typically ~20 μm thick were tested on an Instron Model 4505 using Series IX software and a 2000 g load cell at strain rates of 0.01, 0.1, and 1.0/min. The constitutive relationships of Ultradel 4212, PI2545, and PI2611 generated in this fashion are shown in Figure 2.1.1. Knowledge of the ultimate strength of the film, the true stress at fracture, is not required to assess the film adhesion, but there is a correlation between this quantity and the maximum Mises stress generated in the film during debonding, as will be shown in Chapter 4. The modulus (E), static yield (σ_y), yield strain, and ultimate tensile strength of the films of interest tested at a strain rate of 0.01/min are listed in Table 2.1.1.

Table 2.1.1: Mechanical properties of polyimide films generated through uniaxial testing at a strain rate of 0.01/min.. The yield strain is calculated from the modulus and yield stress.

Polymer	Modulus (GPa)	Yield Stress (MPa)	Yield Strain (%)	Ultimate Strength (MPa)
Ultradel 4212	2.7 ± 0.2	48 ± 3	1.78	120 ± 20
PI2545	2.7 ± 0.2	45 ± 3	1.67	160 ± 20
PI2611	8.3 ± 0.6	160 ± 10	1.93	420 ± 50

The viscoelastic properties as well as the elastic ones can play an important role in determining mechanical behavior, especially in polymers. The viscoelasticity of these films has been characterized by others [60, 61] and is not assessed any further in this work. Observation of the plastic behavior of the film as a function of strain rates provides a means of assessing viscoplasticity. The governing equation is:

$$\dot{\varepsilon}_{pl} = D\left(\frac{\sigma_{pl}}{\sigma_y} - 1\right)^b \qquad [2.1.1]$$

where $\dot{\varepsilon}_{pl}$ is the equivalent plastic strain, σ_{pl} is the equivalent plastic stress, σ_y is the static yield stress, and D and b are constants characteristic of the material. Viscoplasticity is negligible in the PI2545 and PI2611 systems, but is significant in Ultradel 4212. The constants b and D for this system are calculated to be 2.20 and 5.63 respectively [61, 62]. The three strain rates provide only three points to be fitted, and so these values of b and D are approximate. As will be shown in Chapter 4, viscoplastic effects are negligible in the calculation of the specific fracture energy, even in Ultradel 4212 systems.

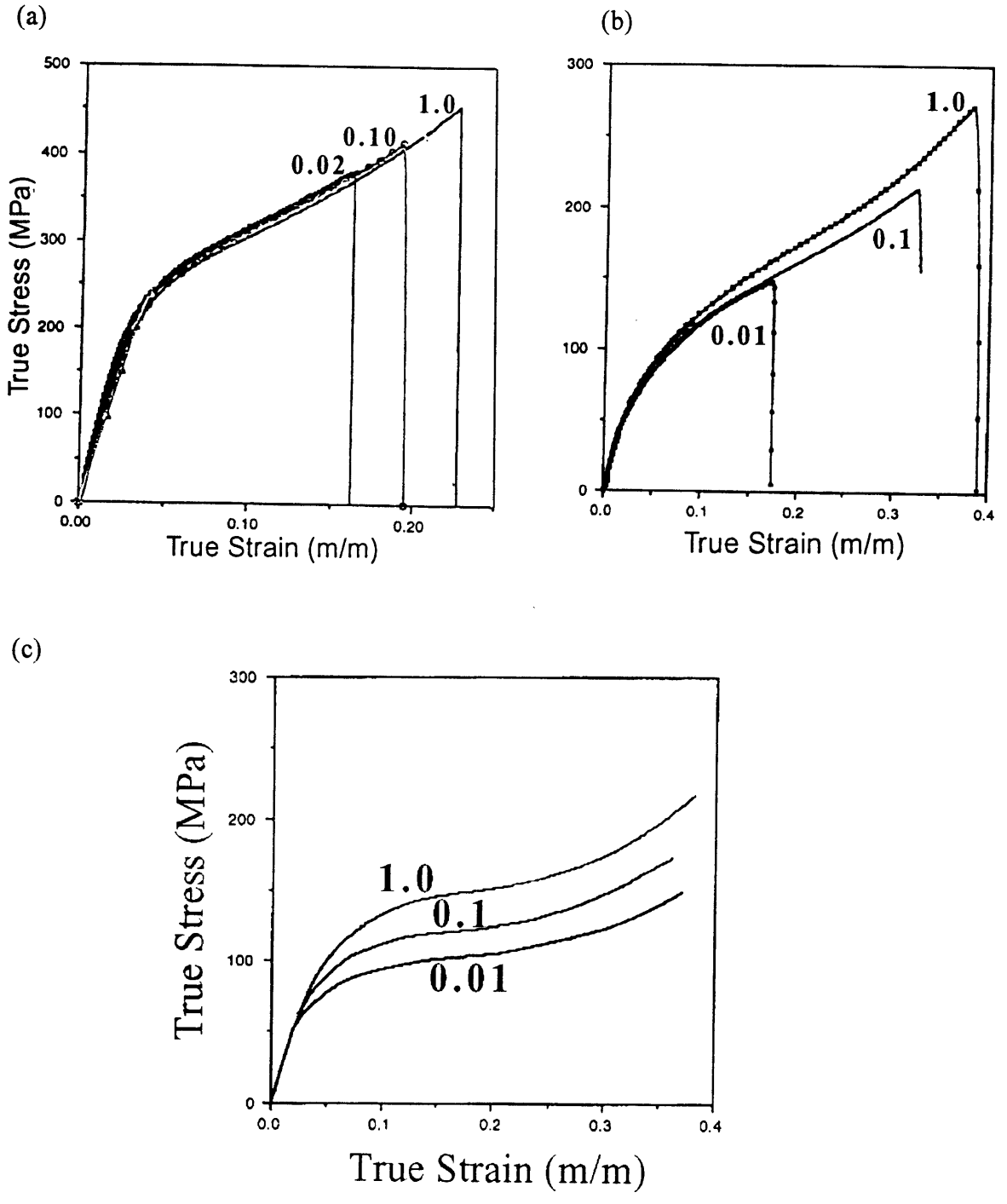

Figure 2.1.1: Stress-strain curves generated at room temperature and different strain rates: (a) BPDA-PDA, (b) HFDA-APBP, (c) PMDA-ODA. [59]

2.1.2 Residual Stress Measurement

The difference in the coefficient of thermal expansion (CTE) between the substrate and the polyimide results in a residual stress in the cured film. For a perfectly elastic system, this effect is quantified through the well known expression:

$$\sigma_o = \int_{T_o}^{T_1} \frac{E}{1-\nu} (\alpha_{film} - \alpha_{substrate})\, dT \qquad [2.1.2]$$

where E and ν are the modulus and Poisson's ratio of the substrate, α represents the coefficient of thermal expansion, and the limits T_o and T_1 are usually taken as room temperature and the maximum temperature achieved during cure respectively.

Residual film stress measurement was done on samples fabricated with no central island using the load-deflection technique. The technique as practiced in this work is well described by earlier researchers [63, 49, 64, 65, 66]. Using the standard blister geometry (Figure 2.1.2), the blister is pressurized, and film deflection is measured as a function of pressure. Film deflection is measured by focusing the microscope on the unpressurized film in the center of the blister and measuring the net deflection of the film with a digital micrometer as the film is incrementally pressurized. Pressure is monitored

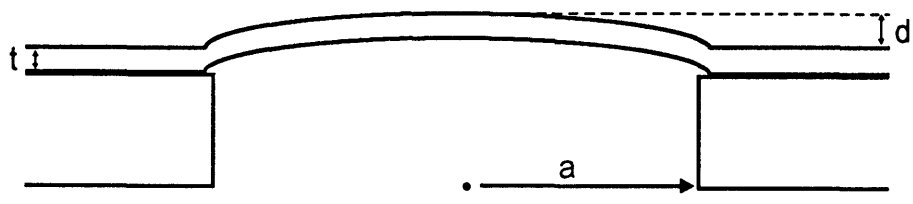

Figure 2.1.2: Geometry of load deflection samples.

using a Kulite pressure sensor calibrated for the working range 0.1-1.0 MPa. An attached computer system monitors the pressure and deflection data, does the required calculations, and provides the final values of stress and biaxial modulus.

The first analysis of this technique was based on plate theory and was provided by Beams [67]. The equation which expresses pressure (P) as a function of vertical film deflection (*d*) is:

$$P = \frac{C_1 h}{a^2}\sigma_o d + \frac{C_2 f(\nu)}{a^4}\frac{E}{1-\nu}d^3 + p_o \qquad [2.1.3]$$

where *a* is the radius of the blister, *h* is the film thickness, E is the Young's modulus of the film, σ_o is the residual stress in the film, and ν is the Poisson's ratio of the film. C_1 and C_2 are constants and $f(\nu)$ is a slowly varying function of the Poisson's ratio. The exact values vary depending on the nature of the analysis. Finite element modeling provides the values of $C_1 = 4.0$, $C_2 = 2.67$, $f(\nu) = (1.026 + 0.233\nu)^{-1}$ [64, 65]. The Poisson's ratio is assumed to be 0.4 for all films investigated. The p_o term compensates for offset error and is required for accurate measurements.

Since Equation 2.1.3 applies only when the film remains in the elastic regime, the validity of the analysis depends on satisfaction of this assumption. Assuming the deformed film takes the shape of a spherical cap, the maximum strain in the film is related to the film geometry and pressure through:

$$\varepsilon = 1.5\left(\frac{d}{a}\right)^2 \qquad [2.1.4]$$

where ε is the maximum strain in the blister [49]. The blister sites had a consistent geometry with a maximum d of 1.0 mm and an a of 12.7 mm resulting in a maximum strain of 0.93%, well below the yield strains for these materials (Table 2.1.2).

Typical residual stress data gathered using the load-deflection test are presented as a function of film thickness in Table 2.1.2. Theoretical values calculated by Margaritis using a finite element analysis that accounts for the viscoelastic behavior of the film are shown for comparison [60, 61].

For all thicknesses of Ultradel 4212 tested on Cr and for thin films of PI2611, the measured load-deflection data agrees with the FEA to within 2 MPa . Both PI2545 and especially PI2611 show a significant thickness effect: thicker films are more highly stressed in tension than thinner ones. This effect has been seen by previous researchers [67] and is explained on the basis of molecular ordering. Thicker films are thought to be less ordered resulting in a higher in-plane CTE [69] which translates into a higher residual stress according to Equation 2.1.1.

Table 2.1.2: Residual stresses in polyimide films as a function of film thickness and substrate metallization. The measured stress is from load-deflection measurements and has an error bar of ± 2 MPa. The calculated stress is from finite element analysis [60, 61].

Film	Substrate Coating	Film Thickness (μm)	Measured Stress (MPa)	FEA Calculated Stress (MPa)
Ultradel 4212	Cr	10.7	32	34
		18.1	31	
		26.7	34	
	Al	12.0	28	34
PI2545	Cr	8.2	18	-
		16.7	22	
		17.9	26	
		22.8	27	
	Al	23.3	19	-
	Ti	22.4	28	-
PI2611	Cr	6.6	5	4.2
		10.7	11	
		35.5	39	
	Al	30.7	31	4.2
		43.1	37	

An additional effect is the difference between films spun on Cr and Al metallized wafers. For the three polyimide types explored, higher film stresses were generated on Cr coated wafers. Machell *et al.* found that lower surface energy substrates produce lower film birefringence [70]. The effect was not sensitive to polymer type. Since the birefringence (Δn) is related to film stress ($\Delta\sigma$) through the stress-optic law:

$$\Delta n = C\Delta\sigma \qquad [2.1.5]$$

where C is the operative stress-optical coefficient, lower surface energy substrates are expected to generate lower residual film stresses. The surface energy of Cr is higher than

that of Al, consistent with the difference in residual film stress on these two metallizations according to Machell's observations.

The important point is that the residual stress is a function of both film thickness and substrate metallization. Since the exact form of these dependencies was not known, film stresses had to be quantified in order to provide accurate input to the finite element analysis of the debonding process, as explained further in Chapter 3. However, the stress data are reproducible and in agreement with both FEA calculations and the results of Noe for the PI2545 and PI2611 systems [68]. Future researchers working with these polyimides on Cr or Al can use Table 2.1.2 as a guideline to what film stress to expect.

2.2 The Island Blister Test

The process originally practiced for fabricating island-blister samples was time-consuming and had a low yield. The square perimeter geometry was also awkward for modeling. Lack of standardization of the rate of pressurization and of the criterion for determining when crack propagation actually occurred created a large operator dependency which hindered reproducibility. This section describes refinements made to the IBT in the areas of sample fabrication and testing procedures. The goals of these refinements are improvement of test reproducibility and creation of circular geometries which are more amenable to modeling.

2.2.1 Sample Fabrication Process

In the sample fabrication technology previously reported by Allen and Senturia [49, 52], the back of a silicon wafer was patterned with silicon dioxide, the front was doped with boron forming a p^+ layer etch stop, and KOH was used as the silicon etchant.

To shorten fabrication time, improve yield and produce circular blister sites, this fabrication process was substantially modified. These modifications also eliminate the need for high temperature oxidation and doping of the silicon, two processes not typically available in thin film packaging facilities. The 25.4 mm diameter round sites with 2.54 mm diameter island used in this work are substantially larger than the geometries used by Allen [49] and later by Volfson and Trusell [71]. The larger features enhance processing and testing yield and near 100% process and test yields are obtainable under conditions of disciplined processing. The newly developed fabrication process is broken into four sequences of operations. These are described below and correspond to Figures 2.2.1 and 2.2.2. Complete processing details are provided in Appendix A.

Back Side Patterning

Single crystal silicon wafers of (100) orientation approximately 500 μm thick, 100 mm in diameter, and polished on one side, are used as substrates. The wafers are ground down to a final thickness of 400 +/- 25 μm and each side is polished to a mirror finish by a vendor[1]. Even with depositing of the 300 A Cr layer before polyimide apply, adhesion of the polyimide used as the silicon etchant mask is compromised if the backside of the wafer is not polished. Limited experimentation suggested that increasing the Cr layer thickness to ~2500 A may allow the use of single side polished wafers. The wafer is cleaned and given a dehydration bake. At this point, samples for testing the

[1] Backside polishing was done by RIOTECH in Pheonix, AZ. The specification was "to mirror finish."

1. Pattern back with photosensitive polyimide (PD2721)

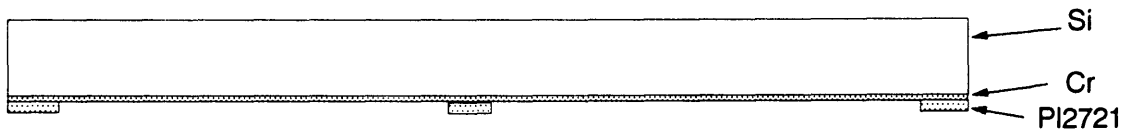

2. Metallize and apply polymer on front

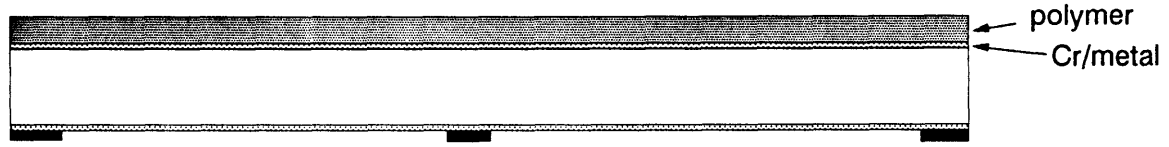

3. Etch silicon and adherend metal from back

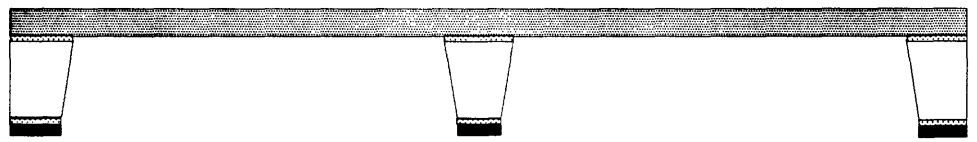

4. Mount on PMMA backing plate

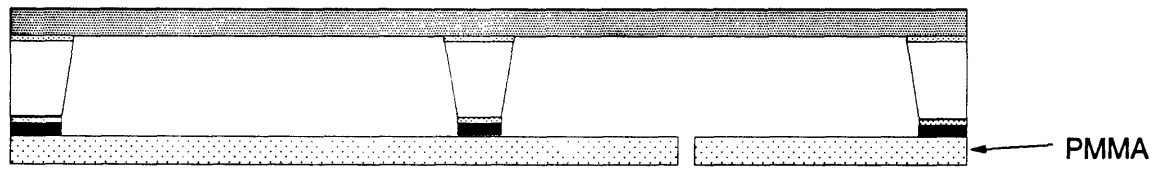

NOT TO SCALE

Figure 2.2.1: Fabrication process for polymer-on-metal IBT samples.

1. Pattern back with photosensitive polyimide (PD2721)

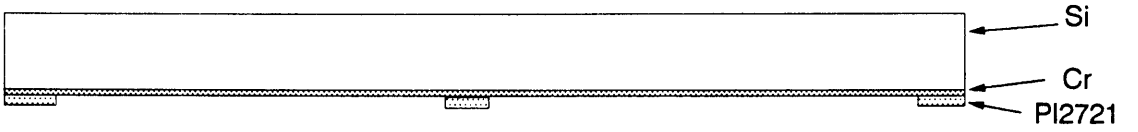

2. Metallize and apply polymer on front

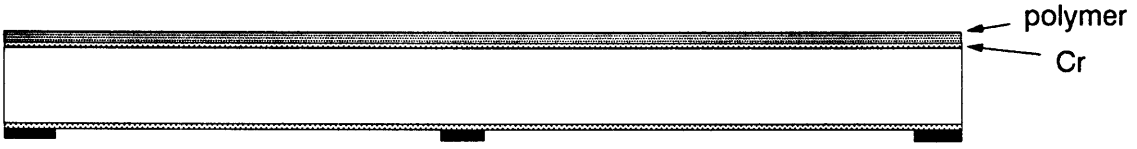

Metallize and apply polymer backing layer on front

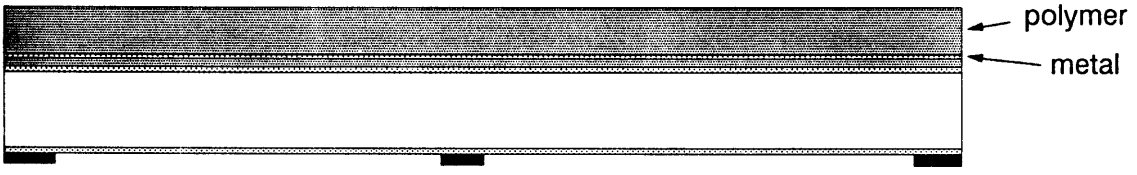

3. Etch silicon, Cr, polymer layer, and adherend metal from back

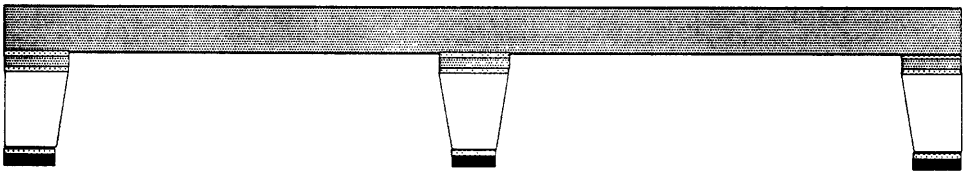

4. Mount on PMMA backing plate

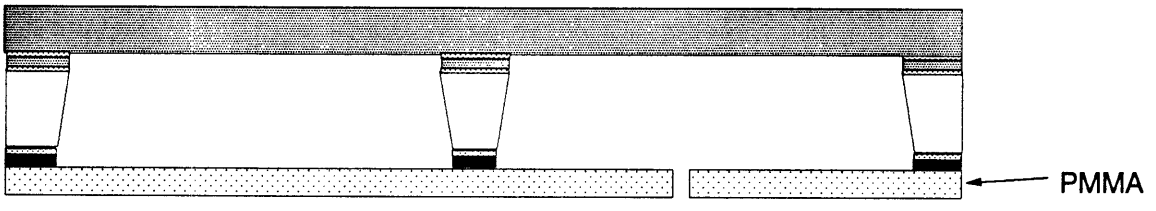

NOT TO SCALE

Figure 2.2.2: Fabrication process for metal-on-polymer IBT samples.

adhesion of polymer to all metals except chromium have a silicon-rich silicon nitride layer (~160 nm) deposited on both sides of the wafer by chemical vapor deposition.

The back side of the wafer is now patterned with the blister geometry (step 1 in Figure 2.2.1). Excellent resistance to the strong acids used to etch the silicon makes polyimide a good choice for this application. A photosensitive material is most efficient, and so Dupont's PD2721 is used. Following final cure, the chemistry and properties of PD2721 are essentially the same as Pyralin PI2555. Samples were also made using a non-photosensitive material, PI2611, patterned with an oxygen plasma through a metal hard mask, although this processing is more laborious. These samples were even more resistant to the HF-based etchant. It is expected that the photosensitive version of PI2611, when available, may be the best choice. Both masking polymers are more robust if a thin (~30 nm) chromium (Cr) layer is first electron-beam evaporated on the silicon wafer serving as an adhesion promoter. Figure 2.2.3 shows a photograph of the wafer after completion of the PD2721 back side process.

Front Side Metallization and Polymer Apply

The front side of the wafer is exposed to an oxygen plasma to clean residual polyimide from the back side processing. The wafer is then immersed in buffered oxide etch (BOE) to remove the native oxide on the silicon[1]. Processing up to this point is the same whether the sample is for polymer-on-metal (Figure 2.2.1) or metal-on-polymer (Figure 2.2.2) adhesion testing. Subsequent processing is dependent on which type of test is to be run.

[1] The native oxide can be left on but its thickness and properties are sensitive to process history. Its removal guarantees a repeatable starting point. In addition, there is evidence to suggest that materials adhere better to the hydrophobic clean Si surface than to the hydrophillic oxide [38, 33].

For polymer-on-Cr samples, a chromium layer is now e-beam evaporated (~50 nm) to serve as both an etch-stop for the silicon etchant and as the adherend. For polymer on other metals, a Cr etch-stop layer is evaporated followed by *in-situ* evaporation of the adherend metal. Although e-beam evaporation was used in these studies due to equipment availability, the technique allows for usage of any type of physical vapor deposition, chemical vapor deposition, or plating method of depositing thin metal films. The polymer film is then spin applied, softbaked, and cured[1] within one hour after metal deposition to minimize oxidation and contamination of the adherend (step 2 in Figure 2.2.1).

For metal-on-polymer samples, a chromium etch stop layer is evaporated, and a thin layer of the polyimide of interest is spin applied, softbaked, and cured; the polyimide surface may then be treated with an oxygen plasma exposure; the adherend metal layer is evaporated; and a polyimide backing layer is spin applied, softbaked, and cured (step 2 in Figure 2.2.2).

Membrane Formation

The wafer is placed in a Teflon fixture for back side etching (Figure 2.2.4). First, the back side chromium layer is etched using a solution of perchloric acid and ceric ammonium nitrate. If a silicon nitride etch-stop layer was deposited, it is now removed from the back side using an O_2/SF_6 plasma. For silicon, an HF-based etchant (6:1:1 solution of $HF:HNO_3:CH_3OOCH$) replaced the previously used KOH solution. The KOH process is highly anisotropic, preferentially etching the (110) planes leading to rectangular blister sites. The HF-based solution works by first oxidizing the silicon with

[1] Refer to Appendix B for polyimide cure schedules.

the nitric acid, then dissolving this oxide with the hydrofluoric acid [72]. This process is not sensitive to the crystallographic orientation of the single crystal silicon and is, therefore, an isotropic etching process allowing for the production of circular blister sites. The advantages of this etchant composition has been recognized by others [63, 68]. Again, if a silicon nitride layer was deposited earlier, it is now removed from the front side through the blister pattern using an O_2/SF_6 plasma. The chromium adhesion layer on the front side is then etched with a dilute solution of hydrochloric acid (step 3 in both Figure 2.2.1 and Figure 2.2.2).

For metal-on-polymer samples, the bottom polymer layer is now removed with an oxygen plasma and the metal layer above this is removed, using hydrochloric acid in the case of chromium and a phosphoric:nitric:acetic acid mixture (PAN) in the case of aluminum. The sample is thoroughly rinsed and dried.

Dicing and Mounting

The wafer is diced into four quarters. A 2" x 2" piece of PMMA with an 1/8" hole drilled in the center serves as the mounting plate for the sample. For each sample, the island is adhered to a separate piece of PMMA with a small drop of cyanoacrylate adhesive (step 4 in both Figure 2.2.1 and Figure 2.2.2) . It is important to ensure that the hole in the PMMA is aligned under the membrane portion of the sample to allow admission of gas for pressurization during testing. A fast drying two-part epoxy is used to form an edge seal around the periphery of the die. A photograph of a completed sample ready for testing is shown in Figure 2.2.5.

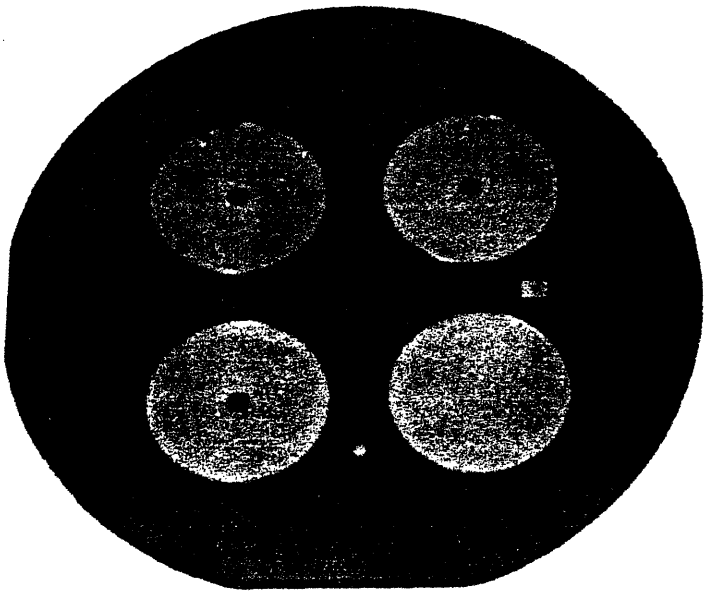

Figure 2.2.3: Photograph of IBT wafer after completion of the PD2721 backside processing.

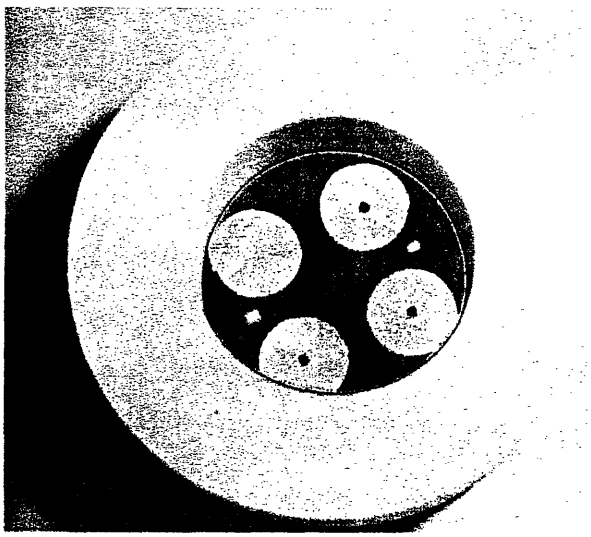

Figure 2.2.4: Photograph of Teflon fixture for HF-based backside etching process.

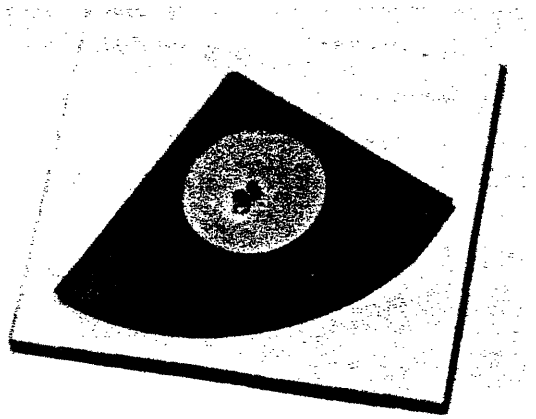

Figure 2.2.5: Photograph of a completed polymer-on-metal IBT sample ready for testing.

2.2.2 Testing Methodology

The sample is mounted into the testing apparatus which consists of a Nikon microscope with a pressurized stage and a calibrated X-Y stage, as shown in Figure 2.2.6. Photographs of the experimental setup are presented in Figure 2.2.7. The test involves pressurizing the blister with dry N_2 at a controlled ramp rate and observing the crack front for motion through an optical microscope. The pressure at which the crack propagates is the critical pressure (p_c). Crack propagation is defined as a movement of the crack front of 2 μm. The radius of the bonded region on the island (r_i) is determined by measurement of the image as projected by a camera fed through a microscope at 400X using the calibrated X-Y stage. As the debonding proceeds, the inner radius decreases and several pairs of p_c, r_i data can be collected, each constituting a separate measurement of work of adhesion. Appendix C describes the testing methodology in full detail.

The Retaining Pin Concept

After fabrication of the sample, the island is not a perfect circle; often it takes a hexagonal shape with rounded corners. Before data collection begins, it is necessary to develop a circular crack front. A retaining pin was used to clamp the center of the island in place while the pressure was increased above p_c causing debonding to occur (Figure 2.2.8). The film peels off the island until it reaches the edge of the retaining pin, at which point it must stop. The retaining pin allows for a constant increase in the pressure without worrying about the crack front "running away". Thus, the retaining pin improves overall yield by arresting crack propagation and allows for consistency in testing from sample to sample.

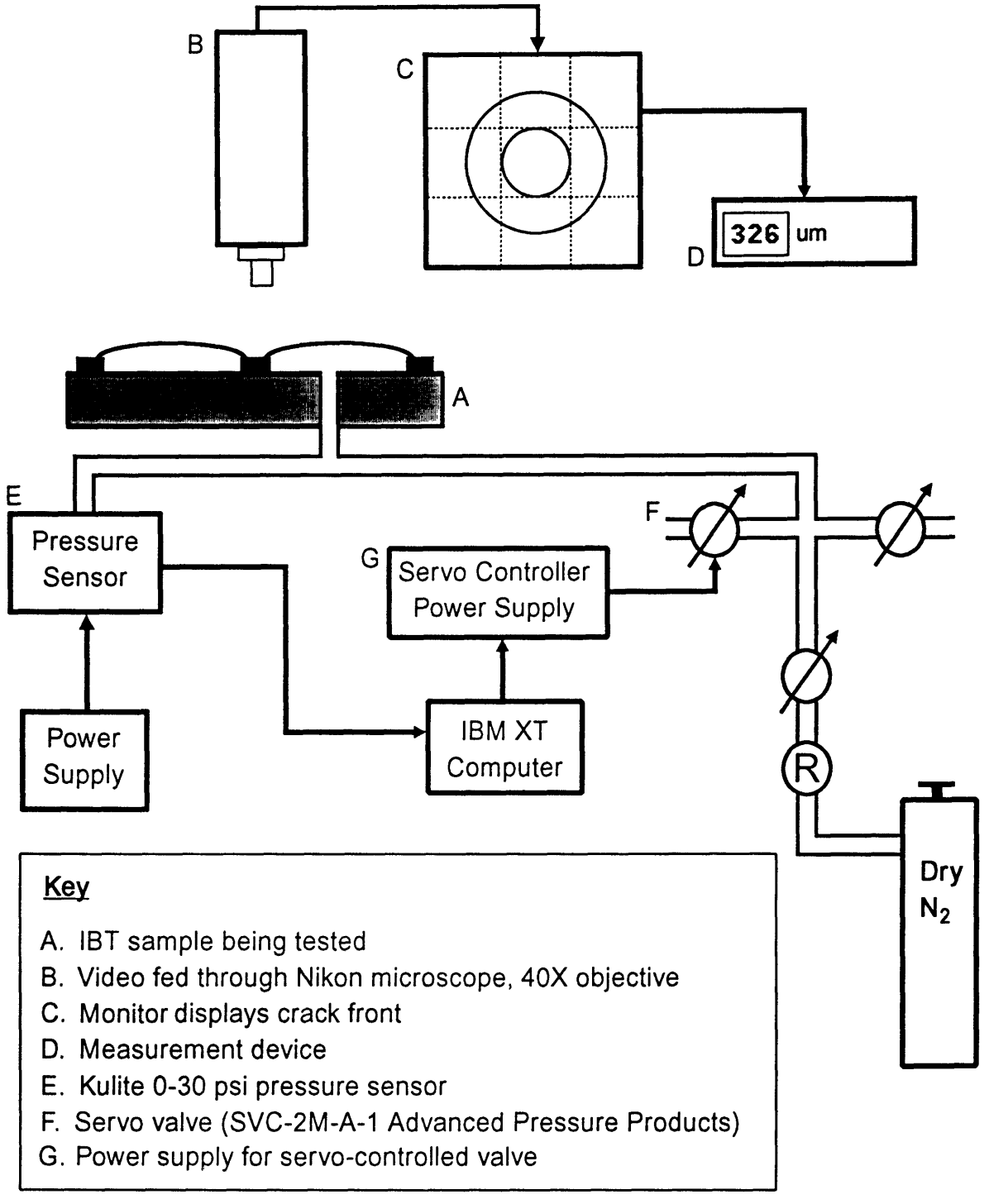

Figure 2.2.6: Schematic of IBT testing apparatus.

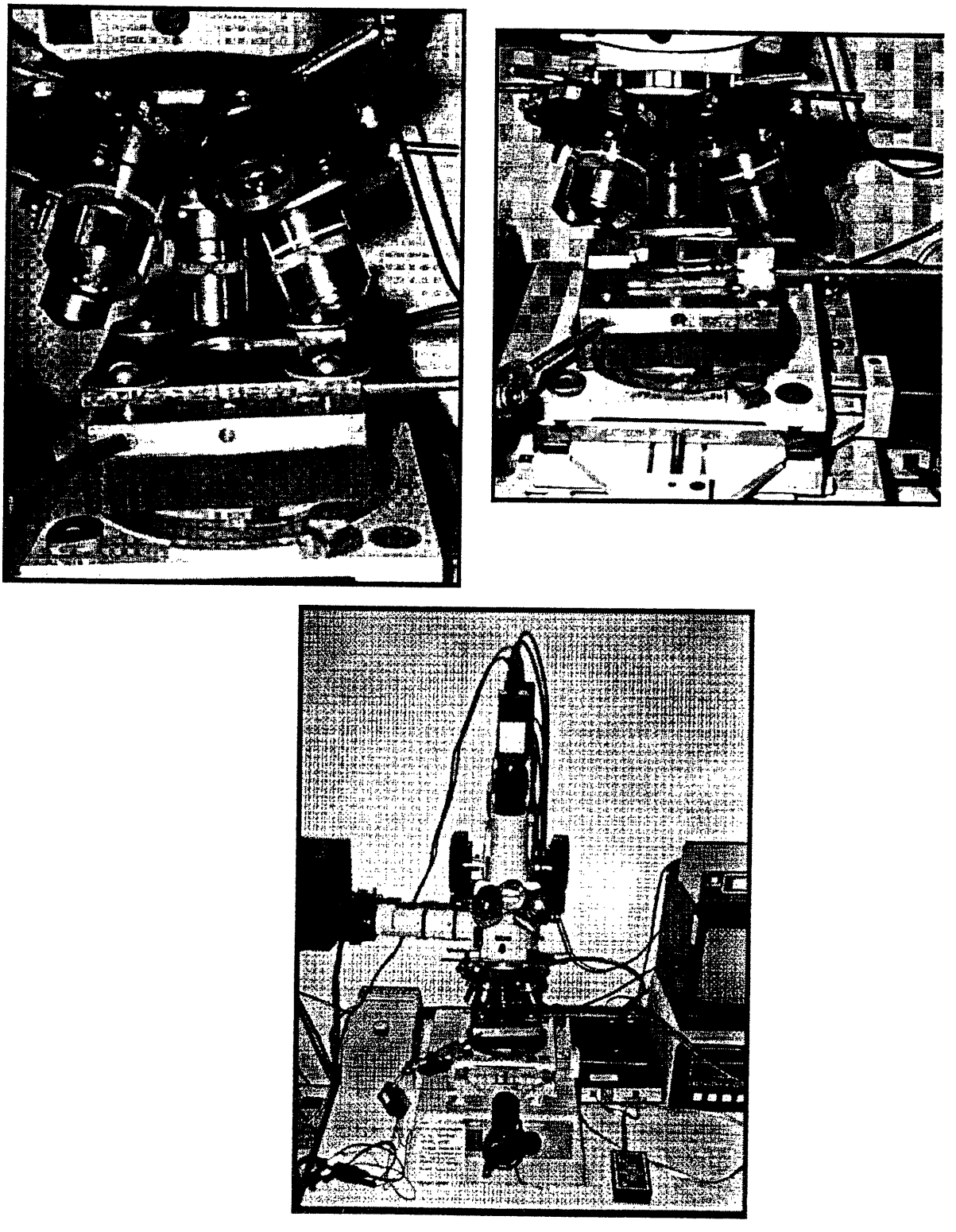

Figure 2.2.7: Photographs of IBT testing apparatus.

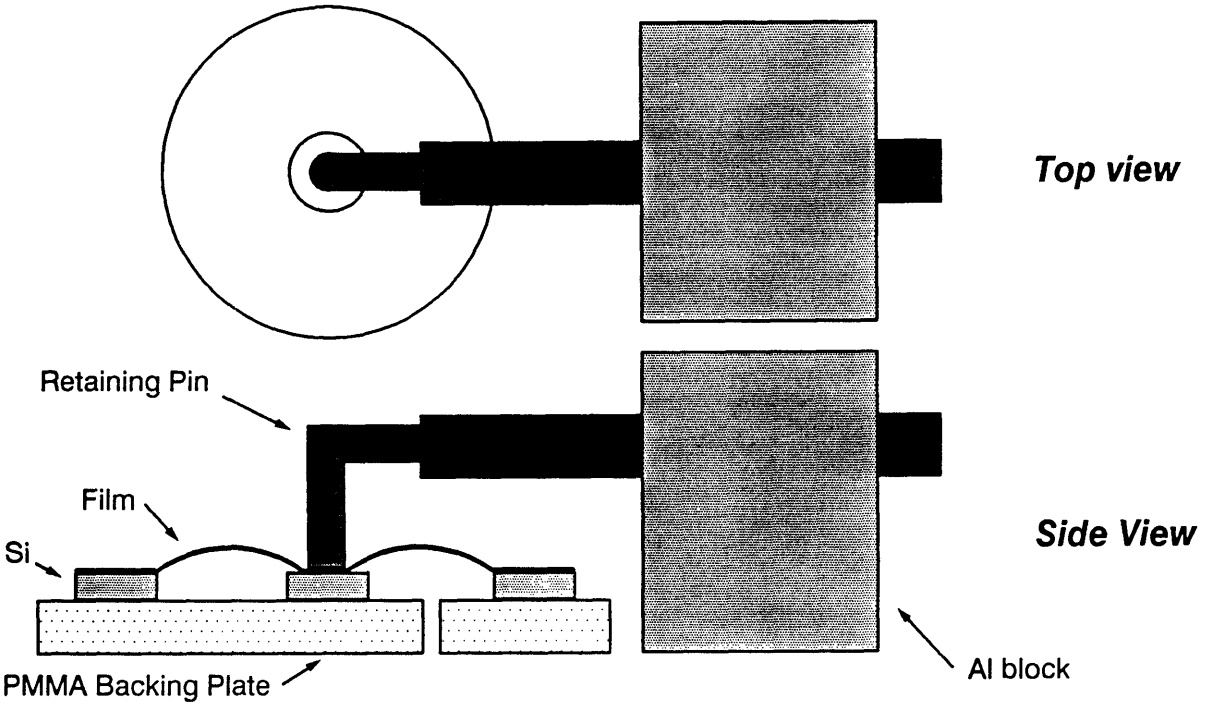

Figure 2.2.8: Schematic of retaining pin concept.

In very well adhered systems, the seal between the test wafer and the PMMA would rupture at higher testing pressures. This was overcome by designing and building a plate (retaining plate) with appropriate cut-outs to accommodate the expanding blister and the retaining pin. The plate, secured by four bolts, tightly clamped the wafer to the PMMA eliminating the edge seal rupture problem.

Automated Pressure Control

The rate at which the pressure is ramped and the criterion which defines crack propagation must be rigorously controlled to insure consistent data collection. In the past, the pressure in the blister had been increased by manual operation of a sensitive needle valve. This procedure is difficult to reproduce across samples and operators. A servo-controlled valve was installed to automatically control this critical process. Manual control over pressure is still possible, so flexibility has not been compromised.

Characterization of the valve consisted of entering a specific starting pressure, ending pressure, and ramp rates into the control program and comparing actual pressure to target pressure. For example, Figure 2.2.9 demonstrates valve control in the 12 to 15 psi range, relevant to the testing of the PI2611-Cr system. As desired, the valve increases pressure to slightly less than the target pressure, but at a constant ramp rate. This level of control is much superior to what can be achieved manually.

A rate of pressure increase of 0.00069 MPa/min (0.10 psi/min) was implemented. Faster rates gave artificially high values of the critical pressure because the pressure would be raised above p_c before significant crack propagation could be observed. Lower rates gave the same value of p_c but extended the testing time inconveniently.

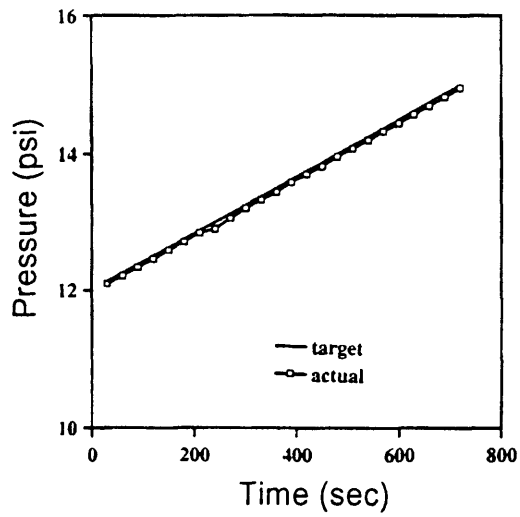

Figure 2.2.9: Example of servo-valve control functionality.

2.3 The Peel Test

Sample Fabrication

The fabrication process for peel samples is very similar to the one used to fabricated strips for uniaxial Instron testing. Since the films are not lifted off the substrate at the end of the process, the wafer does not have to be metallized with Al. To initiate the peel, part of the film must release from the wafer. This was accomplished by depositing a release layer over approximately one-quarter of the wafer. Metal release layers such as Al and Cu were used in the initial work with Ultradel 4212 systems. If Al is used, release is accomplished by a short exposure to HF. When Cu was used, a stainless steel razor blade was used to initiate the release. The easiest release, however, was provided by simply coloring in a portion of the wafer with a permanent marker[1] prior to adherend metallization.

The patterning of the strips can be done either photolithographically or by cutting the film with a straight edge and razor blade. Strips tested in this work were 4-7 mm in width. Because it avoids exposure to any potential corrosive acid, the recommended technique is using the permanent marker as a release layer and forming the strips by cutting with a razor blade. This method was used for all PI2545 and PI2611 testing.

Testing Methodology

Once formed, the peel strips are loaded into an Instron. The wafer is secured to the stage and the free end of the film is held at a 90° angle to the wafer. Loading is achieved by moving the stage down at a constant rate while the gripped end of the film is

[1] The particular marker used was a *Sharpie* by Sanford, color black thick tip.

maintained at a constant position. As the crack front propagates and the free end of the film grows it becomes difficult to maintain the 90° angle without the use of a special fixture. Such a fixture, designed and built at IBM Corp.[1], is shown in Figure 2.3.1. The near frictionless x-y motion of the stage guarantees that the perpendicular geometry is

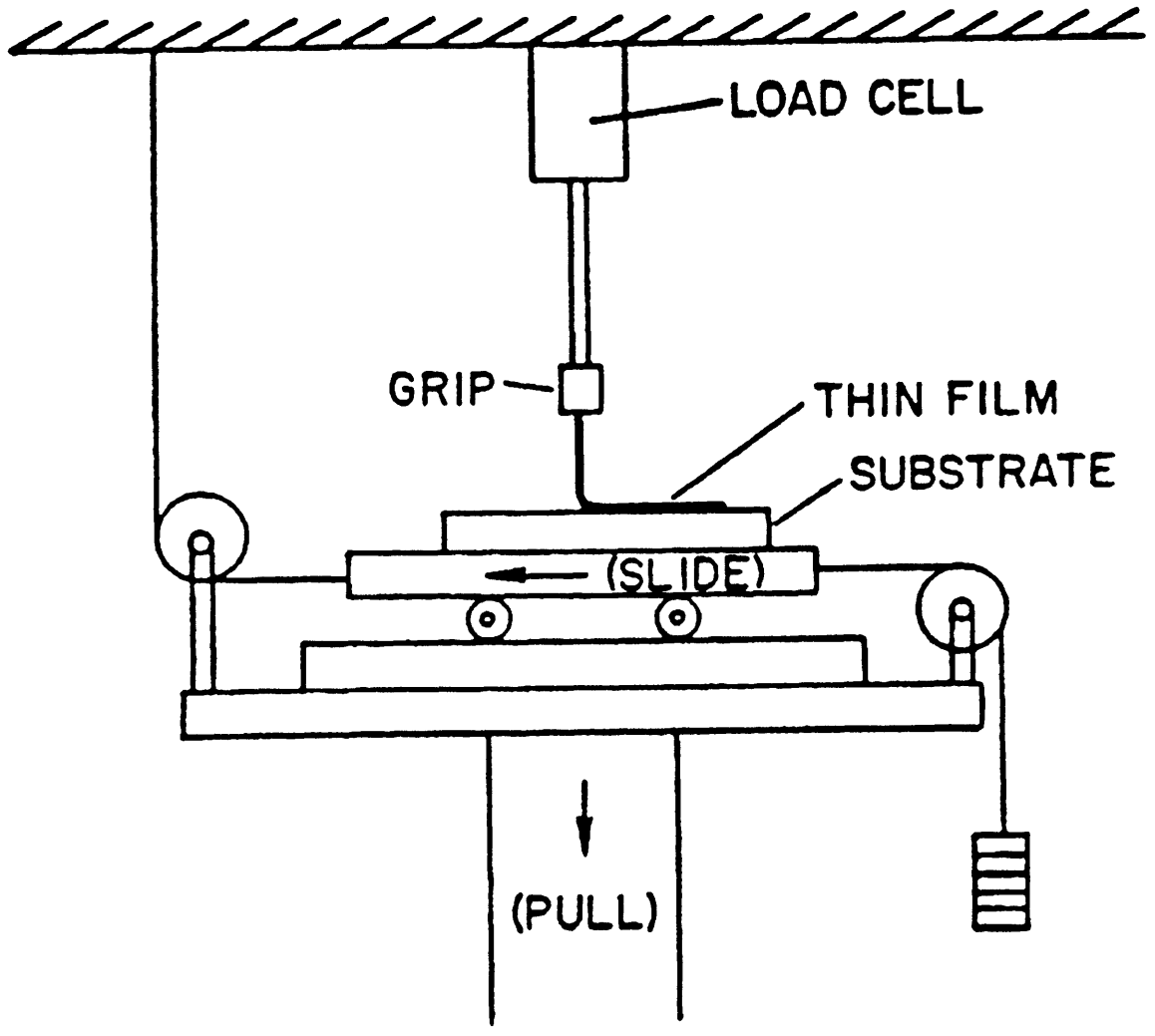

Figure 2.3.1: Schematic of pull test apparatus.

[1] C. Kim at IBM Microelectronics Division's East Fishkill, NY facility is gratefully acknowledged for his assistance with this fixture and training on the Instron at IBM.

maintained. The Ultradel peel testing was done using the Instron at MIT described in the last section at a peel rate of 2.0-2.5 mm/min. The PI2545 and PI2611 peel testing was done at IBM using an Instron Model 1122 with a 500 g load cell and at a rate of 2.0 mm/min. For each system studied, at least three strips on two wafers were tested.

Data Analysis

As the film is loaded, a critical load is achieved where steady state occurs. The load then plateaus as the peel continues. It is this value, in Newtons, that is collected. The fracture energy is a function of the peel angle according to:

$$\gamma_a = \frac{F(1 - \cos\beta)}{w} \qquad [2.3.1]$$

where w is the width of the strip. For the present situation of $\beta = \pi/2$, the fracture energy (J/m^2) is then simply the peel force (N) divided by the strip width expressed in meters.

The simple analysis presented above is typically employed by the majority of practitioners of this test [73]. The analysis is valid only if film plasticity is experienced only in the vicinity of the crack tip. As mentioned in Section 1.2, this criterion is not satisfied for the systems of interest to our work. The peel data generated in this work are analyzed using both Equation 2.3.1 and the alternate procedure for subtracting out the plastic contribution recommended by Kim and Avaras [16]. The details of this method are presented with the peel data in Section 4.2.

Chapter 3: Analysis of the Island Blister Test

This chapter presents details of the finite element model (FEM) used to analyze data generated by the island blister test. Before proceeding into the details of the FEM, the mechanics of interfacial fracture are reviewed in section one of this chapter to provide motivation for the approach adopted in this work. The second section reviews the finite element model itself. The third section presents an incremental error analysis of the technique based on the precision and accuracy of the measurements that serve as inputs to the model. This numerical analysis results in the derivation of an equation that relates the specific fracture energy to the geometry of the test specimen, the elastic properties of the film, and the critical pressure. The final section applies this equation to define limits on the geometry as a function of the strength of the interface.

3.1 Introduction

Two complementary techniques are provided by the field of fracture mechanics for assessing the possibility of fracture in any structure, whether it be homogeneous or composite. The first is based on the stress intensity factor, K, a parameter that quantifies the magnification of a far-field applied stress in the area of a crack tip. In general, three modes of loading are possible. Mode I (normal mode) loading is from stresses normal to the face of the crack. Shear stresses parallel to the interface and parallel to the direction of crack propagation produce Mode II or shear loading. Finally, stresses parallel to the interface but perpendicular to the direction of crack propagation give rise to Mode III loading. We are interested in only mode I and mode II loading in the present work. The magnitude of K is calculated through:

$$\sigma_{ij} = \frac{K_I}{\sqrt{2\pi r}} f_{ij}^{I}(\theta) + \frac{K_{II}}{\sqrt{2\pi r}} f_{ij}^{II}(\theta) \qquad [3.1.1]$$

as expressed in polar coordinates, where σ_{ij} is the local stress at a point in the vicinity of the crack tip, r is the radial distance of that point from the crack tip, θ is the angle of that point off the center line of the crack, and the geometrical functions $f^{I}_{ij}(\theta)$ and $f^{II}_{ij}(\theta)$, available in handbooks [74]. Therefore, K uniquely defines the stress field around the crack. The fracture criterion is then satisfied when K achieves some critical level denoted by K_c, which is a property of the material. Westergaard [75] demonstrated that the localized stress expressed in Equation 3.1.1 is related to the homogeneous, far-field stress, σ_o, through the relationship:

$$\sigma_{ij} = \sigma_o \sqrt{\frac{a}{2r}}\, f_{ij}(\theta) \qquad [3.1.2]$$

Equations 3.1.1 and 3.1.2 can be combined to express K as a function of the macroscopic parameters defining the system:

$$K = \sqrt{K_I^2 + K_{II}^2} = \beta\sigma_o \sqrt{\pi a} \qquad [3.1.3]$$

where β is a function of the geometry of the test piece. At failure, K equals K_c and σ_o is replaced by the fracture stress, σ_f. It is customary to describe the relative amount of mode I and mode II loadings present through the relationship:

$$\psi = \tan^{-1}\left(\frac{\sigma_{12}}{\sigma_{22}}\right)_{r\to 0} = \tan^{-1}\left(\frac{K_{II}}{K_I}\right) \qquad [3.1.4]$$

Equation 3.1.1 indicates that at the crack tip, the stress is singular; σ_{ij} tends to infinity as r approaches zero. This is physically unrealistic since the stresses exceed yield

point of the material, and there is localized plastic flow before such levels are reached. The methodology based on the stress intensity factor is valid as long as this plastic flow occurs only in the vicinity of the crack tip. For bimaterial systems, a first order estimate of the size of this plastic zone is [76]:

$$r_p \cong \Lambda\left(\frac{K}{\sigma_y}\right)^2 \qquad [3.1.5]$$

where Λ is a dimensionless factor ranging from 0.1-0.6 depending on material properties and the loading mode mixity. As will be shown in the next chapter, for the well-adhered ductile films investigated in this work, the size of the plastic zone is on the order of mm whereas typical film thicknesses are on the order of μm. Consequently, the methodology of defining β for the specific geometry in question and determining the K_{Ic} by measuring the fracture stress for a given crack size is not applicable to the systems investigated in this work.

In summary, the stress intensity methodology can account for multiple modes of loading, but is limited to elastic (i.e. brittle) systems. Even with this restriction, a great amount of research has been published over the last four years detailing investigations of mixed mode loading and its relationship to interfacial fracture [77-84]. Much of the research is theoretical, and the experimental parts typically involve pieces of aluminum or glass bond together with an adhesive, often an epoxy. The assumption then is that stresses are concentrated in the brittle epoxy and the plastic zone is small. The ductile films used in this work do not even approximately satisfy these assumptions, and so the approach is not appropriate here.

The second method is based on energy balance considerations. The energy required to propagate a crack a distance δa is equivalent to the energy required to create the additional surface area (γ). This energy must be balanced by the external work applied to the system (W_{ex}) minus the energy elastically stored in the system (U) and the energy dissipated (W_d) through plasticity or viscoelasticity:

$$\gamma = \frac{dW_{ex}}{da} - \frac{dU}{da} - \frac{dW_d}{da} \qquad [3.1.6)]$$

Griffith [85] substituted the stress field calculations for an elliptical flaw generated by Inglis [86] into Equation 3.1.6 for elastic systems ($W_d = 0$):

$$\frac{dU}{da} = \frac{\pi a^2 \sigma^2 B}{E} \qquad [3.1.7]$$

where σ is the applied stress, B is the thickness of the test specimen, and E is the modulus. At fracture, this reduces to the well known equation:

$$\sigma_f = \sqrt{\frac{2E\gamma}{\pi a}} \qquad [3.1.8]$$

where σ_f is the stress that would result in crack propagation. In the case of brittle materials where dissipative mechanisms are restricted to the vicinity near the crack tip, the term γ corresponds to the surface energy. Irwin [87] and Orowan [88] extended Griffith's elastic-brittle fracture concept to ductile materials through the addition of γ_p, the plastic energy per unit crack extension:

$$\sigma_f = \sqrt{\frac{2E(\gamma+\gamma_p)}{\pi a}} \qquad [3.1.9]$$

For metals, Orowon estimated γ_p to be as much as three orders of magnitude greater than γ. The sum $\gamma+\gamma_p$ is often replaced by G and termed the strain energy release rate. In the present work, which deals with interfacial or adhesive fracture, the symbol γ_a is retained to express this quantity. Note that γ_a is meant to include the plasticity local to the crack tip and will be referred to in the remainder of this work as *the specific fracture energy*. Under mixed mode loading conditions:

$$\gamma_a = \gamma_I + \gamma_{II} \qquad [3.1.10]$$

Another way the energy method is applied is through measurements of the compliance. The governing equation is:

$$\gamma = \frac{F_b^2}{2H}\left(\frac{\partial C}{\partial a}\right) \qquad [3.1.11]$$

where F_b is the generalized body force, H is the specimen thickness, C is the compliance, a is the increment of crack advance. Application of Equation 3.1.11 again requires that the system behave elastically; the compliance may be difficult to measure, depending on the geometry of the test piece.

Another way of finding the strain energy release rate is through the crack closure method. This technique is based on Irwin's [89] observation that in the extension of a crack by Δa, the work required to close the crack to its original length is equal to the energy absorbed in the process. Symbolically, this statement translates to:

$$\gamma_a = \frac{1}{\Delta A}\int_0^{\Delta A}\int_0^{u_i} \tau_i \, du_i \, ds \qquad \text{when } \Delta A \to 0, \quad i = 1,2,3 \qquad [3.1.12]$$

where A is the crack surface area, τ_i's are the tractions on the prospective crack surface, and u_i's are the displacements of the crack surface. For cases where stresses and crack openings are released linearly, the relationship can be expressed as:

$$\gamma = \lim_{\Delta a \to 0} \frac{1}{2\Delta a} \int_0^{\Delta a} \sigma_y(\Delta a - r,0)\, \tilde{v}(r,\pi)\, dr + \lim_{\Delta a \to 0} \frac{1}{2\Delta a} \int_0^{\Delta a} \tau_{xy}(\Delta a - r,0)\, u(r,\pi)\, dr \qquad [3.1.13]$$

where polar coordinates are used, σ_y and τ_{xy} are the stresses near the crack tip, v and u are the sliding and opening displacements between points on the crack face, and Δa is again the amount of crack propagation. The two integrals in Equation 3.1.13 express the strain energy release rate in the sliding (II) and normal modes (I) respectively. Westergaard's [90] elastic functions expressing displacements of the crack faces as a function of stresses can be substituted, and the familiar relationships between the strain energy release rates and the stress intensity factors are derived:

$$G_I = \frac{K_I^2}{E}\beta,\ G_{II} = \frac{K_{II}^2}{E}\beta \qquad [3.1.14]$$

where $\beta = 1$ for plane stress, and $\beta = 1/(1-\upsilon^2)$ for plane strain. Equation 3.1.12 is the general relationship, always applicable while Equation 3.1.13 is restricted to linear systems, and Equation 3.1.14 is valid only for systems exhibiting elastic behavior. This basic methodology is used in this work for separately calculating the mode I and mode II contributions of the specific fracture energy..

3.2 The Finite Element Model[1]

In the original crack closure method [91], the specific fracture energy associated with the propagation of a crack in a linear elastic system, given by Equation 3.1.13, was calculated from the nodal forces and displacements of four noded quadrilaterals. In the case of eight noded quadrilaterals under plane strain or plane stress conditions (Figure 3.2.1), the mode I and mode II components of the specific fracture energy of an interfacial crack between a linear elastic material and a rigid substrate are given by the following formulae:

$$\gamma_I = \frac{1}{2\Delta et}(F_{z,i}u_{z,i+2} + F_{z,i+1}u_{z,i+3}) \qquad [3.2.1]$$

and

$$\gamma_{II} = \frac{1}{2\Delta et}(F_{x,i}u_{x,i+2} + F_{x,i+1}u_{x,i+3}) \qquad [3.2.2]$$

In the above formulae, γ_I and γ_{II} are the mode I and mode II components of the specific fracture energy; $F_{z,i}$ and $F_{z,i+1}$ are the nodal forces at nodes i and i+1 along the z axis; $u_{z,i+2}$ and $u_{z,i+3}$ are the displacements of nodes i+2 and i+3 along the z axis; $F_{x,i}$ and $F_{x,i+1}$ are the nodal forces of nodes i and i+1 along the x axis; $u_{x,i+2}$ and $u_{x,i+3}$ are the displacements of nodes i+2 and i+3 along the x axis; Δe is the length of each element; and t is their thickness, which is usually taken as one. The finite element code calculates nodal forces and nodal displacements directly. Stresses and strains are derived from these forces and displacements. Because it is based on the nodal forces and displacements, the modified

[1] The methodology set forth in this section was developed by G. Margaritis. Some parts of this section appeared previously in [60, 61]. It is provided here for continutity and as a convenience to the reader.

crack closure method is reported to be more accurate than stress-based methods and can be applied to relatively coarse meshes [92].

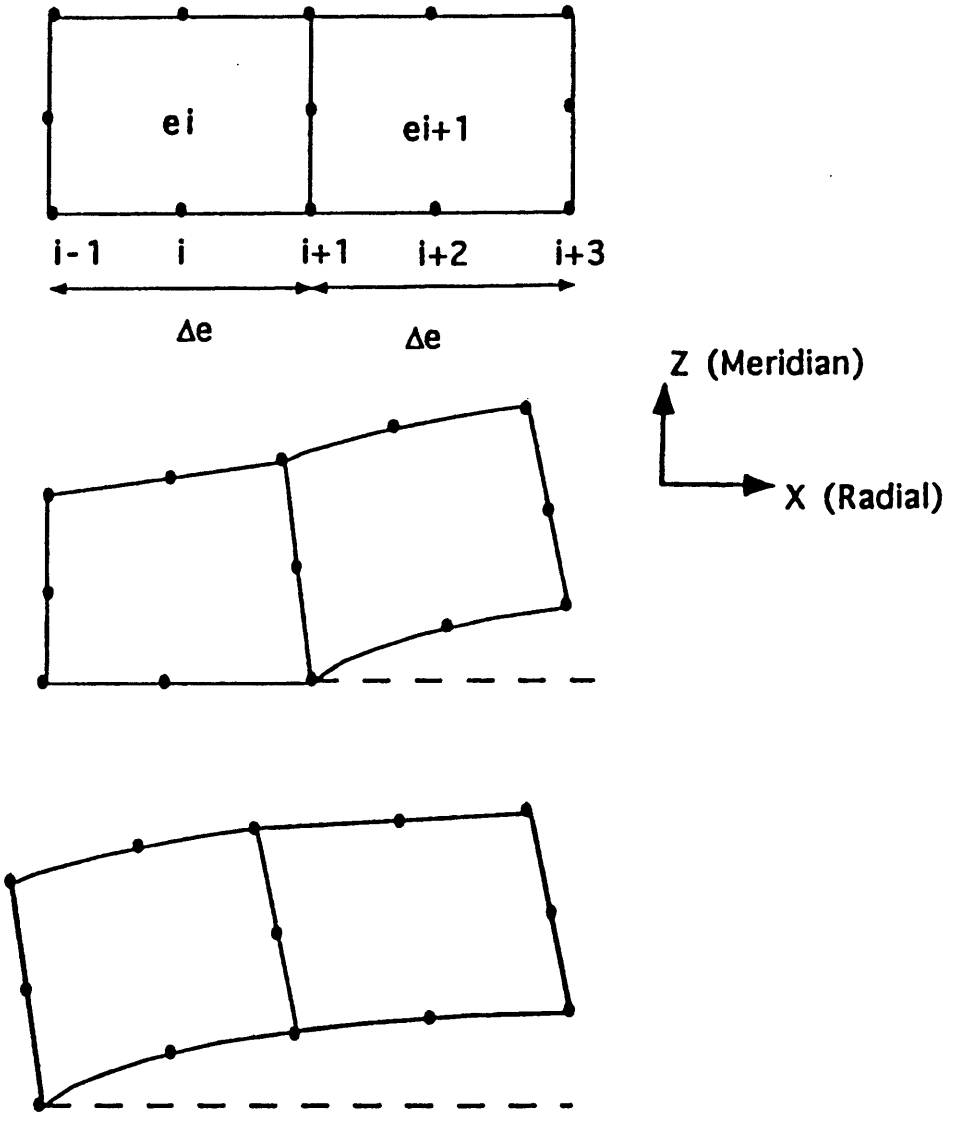

Figure 3.2.1: Schematic diagram of two crack tip elements in their undeformed state (a), and their deformed state before (b) and after (c) crack propagation [60, 61].

Analysis of the axisymmetric geometry requires modification of Equations 3.2.1 and 3.2.2. The nodal forces of an axisymmetric geometry are the total forces on a complete circle, with the center as the axis of symmetry, and the radius as the distance of the node from the axis. The nonlinearity of the film behavior, and therefore the relationship between nodal displacements and forces also must be included. Consequently, the correct forms Equation 3.1.12 become:

$$\gamma_I = \frac{1}{\pi((r_i + \Delta e)^2 - r_i^2)} \sum_{j=1}^{10} \left(F^j_{z,i} \Delta u^j_{z,i} + F^j_{z,i+1} \Delta u^j_{z,i+1} \right) \qquad [3.2.3]$$

and

$$\gamma_{II} = \frac{1}{\pi((r_i + \Delta e)^2 - r_i^2)} \sum_{j=1}^{10} \left(F^j_{r,i} \Delta u^j_{r,i} + F^j_{r,i+1} \Delta u^j_{r,i+1} \right) \qquad [3.2.4]$$

where the superscript j refers to the increment number, and r_i is the distance of the crack tip from the center of the island.

The large deflection elastic-plastic analysis was performed in ABAQUS [93], a commercially available FEM code. A *C* program was developed to automatically create the input deck for the finite element model based on the specific geometry of each individual case (Appendix D). For example, the size of the island, the membrane area, and the thickness of the film vary for each sample. The input deck for ABAQUS and hence the *C* program that creates this input deck are composed of three major parts. In the first part, the geometry of the test is defined based on user inputs. These inputs include the total number of elements (k), the radius of the island (r_i), the radius of the site or outer radius (r_o), the film thickness (h), the elastic modulus (E), and the residual film stress (σ_r). Key nodes are calculated based on these inputs. The intermediate nodes and

elements are then fully defined and generated automatically. The substrate was assumed to be perfectly rigid, and all nodes over the island were rigidly pinned to it. These assumptions are justified by the large difference between moduli of polymer films and metals or silicon. The nodes along the axis of symmetry in the middle and the nodes on the right edge of the film were pinned in the radial direction. The bottom node of the right edge was also pinned in the meridian direction to prevent separation of the film from the substrate after the application of pressure. Axisymmetric eight-noded quadrilaterals (CAX8) were used as elements. This fully defines the geometry of the specimen.

The second part of the program provides the both elastic and plastic material inputs. As a first-order attempt to account for viscoelasticity, the 10 minute relaxation modulus is substituted for the elastic modulus. This is the modulus that would be measured if the polymer were strained an equivalent amount and allowed to relax for 10 minutes. The Poisson's ratio is then input. A piecewise linear representation of the film plasticity is then input. These representations are based on uniaxial tensile testing of thin strips of the films. The tensile data along with the piecewise linear models are shown together in Figure 3.2.2 for the three materials studied. The viscoplastic rate dependency is then input. All that is required here are the two constants, b and D from Equation 2.3.2. The viscoplastic model was used only for Ultradel since the plastic behavior of the other materials showed relative little dependency on strain rate (Figure 2.1.2).

The third part of the program instituted the loadings on the system over a series of four steps. In the first step, the film was loaded with the biaxial residual stress in the film. In the second step, the film was loaded with 75% of the total pressure over a series

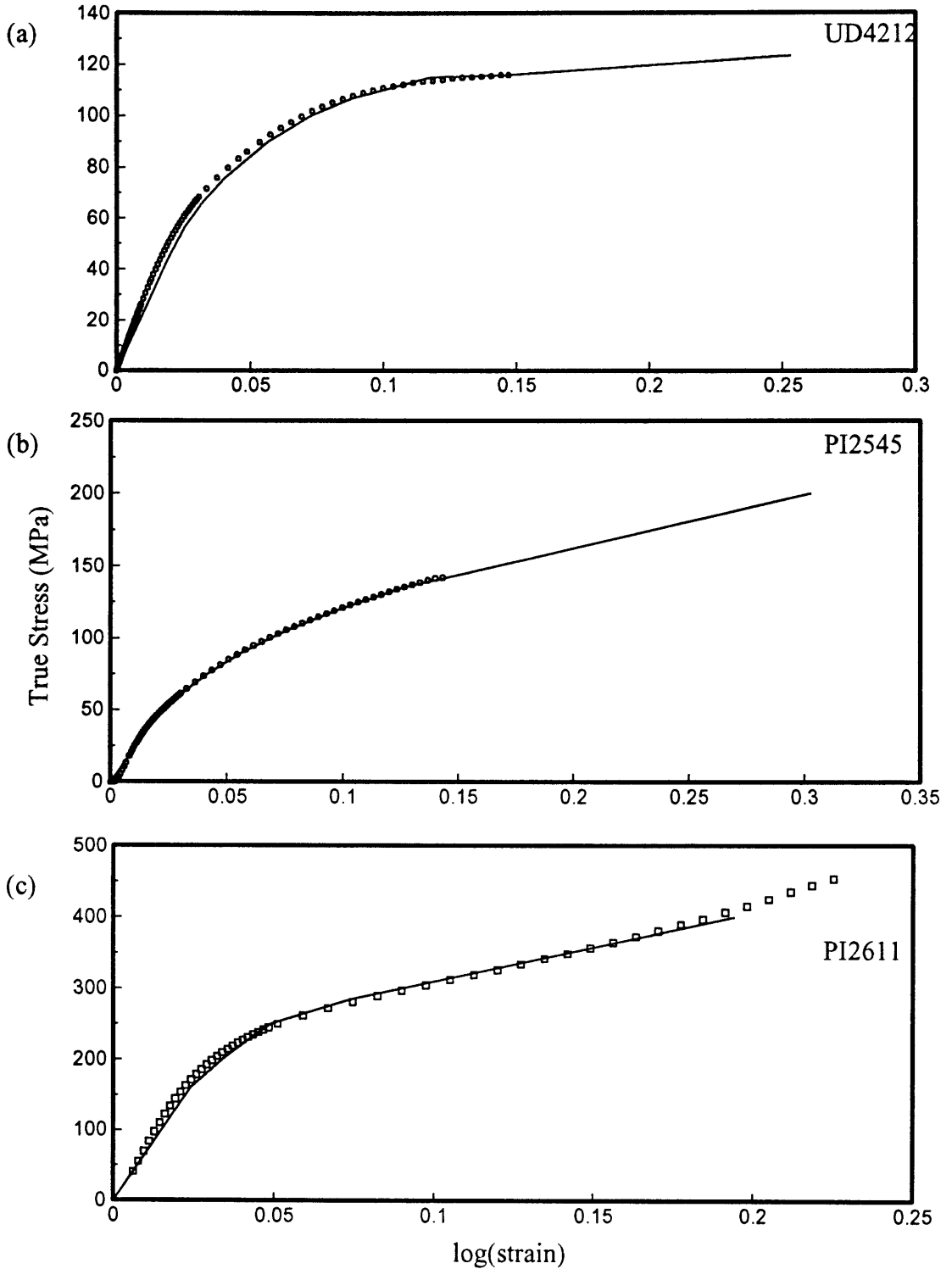

Figure 3.2.2: Stress-strain behavior for polyimides tested at 0.01/mm. Uniaxial tensile data shown by symbols, piecewise linear representation used in FEA shown as solid lines. (a) UD4212, (b) PI2545, (c) PI2611.

of ten increments. The third step loaded the film with the final 25% of the pressure over a series of 6 increments. In the final step, the element at the crack tip is released over a series of ten increments subjecting two of its nodes to deflection (refer to Figure 3.2.1). Two steps are used to provide the full loading on the film, insuring a convergent solution, especially necessary for systems experiencing large film deflections. The use of multiple step with a fixed number of increments did not significantly affect the results of the analysis.

The important outputs from the analysis are the reaction forces at the two nodes released at the start of the fourth step ($F_{z,i}^{j}$, $F_{z,i+1}^{j}$, $F_{r,i}^{j}$, $F_{r,i+1}^{j}$ from Equations 3.2.3 and 3.2.4) and the film deflections ($\Delta u_{z,i}^{j}$, $\Delta u_{z,i+1}^{j}$, $\Delta u_{r,i}^{j}$, $\Delta u_{r,i+1}^{j}$) over the ten increments, j, that these nodes experience during this step.

Xess, a spreadsheet application found in the Athena environment at MIT, was used for post-processing the data according to Equations 3.2.3 and 3.2.4. Appendix E shows one such spreadsheet. The reaction forces are equally divided over the ten increments. The displacements are taken from the finite element model for both nodes released during the final step. Previously it was stated that the simpler forms of Equation 3.1.12 were only valid for linear systems. Figure 3.2.3 shows typical curves of nodal force as a function of the film displacement for two cases. Figure 3.2.3(a) shows Ultradel on chromium, a case of relatively poor adhesion; the relationship is seen to be approximately linear. However, for well-adhered systems, as demonstrated by the case of PI2545 on chromium shown in Figure 3.2.3(b), the curves are non-linear. In each figure, the mode I and mode II contributions are shown separately for the two nodes.

(a)

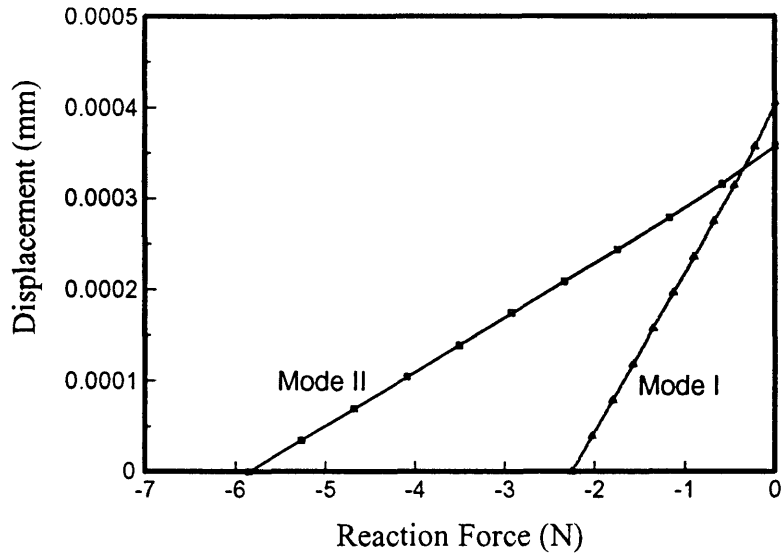

(B)

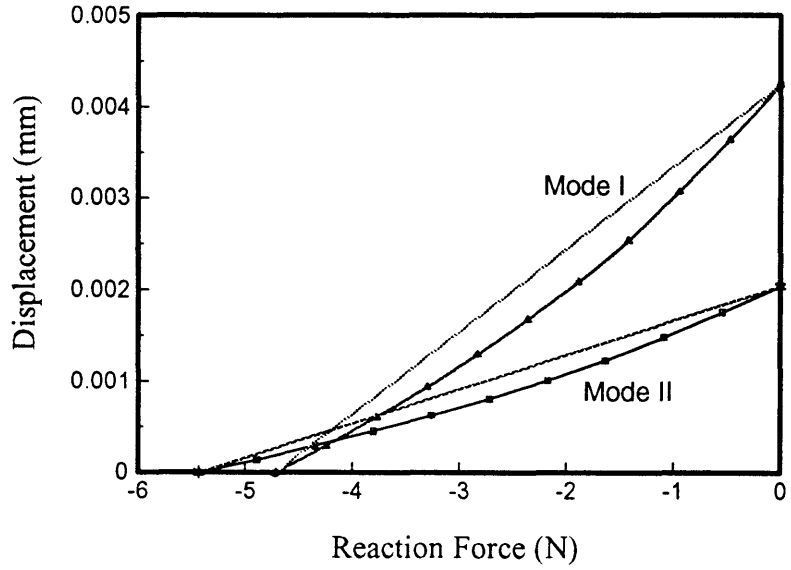

Figure 3.2.3: Displacement versus reaction force at the first node released during debond for (a) PI2545 on AlCr, and (b) PI2545 on Cr. For case (b), the relations are non-linear; the dotted lines are for comparison to the linear case.

A convergence study with three meshes, with 500, 1000, and 1500 elements, showed that the mesh with 1000 elements was sufficient [62, 63]. In another attempt to check the FEM results, measurements of the vertical deflections of the three films were compared with the defections calculated by the FEM (Figure 3.2.4). These data were collected with the same apparatus as used for the load-deflection measurement described in Section 2.1.2. For each material, two cases are explored, a low pressure one corresponding to debonding from an Al-coated adherend and a high pressure one corresponding to debonding from a Cr-coated adherend. In all cases, the low pressure curves correspond well with the FEM. At the higher pressure, the agreement between experimental and FEA results is reasonable for PI2545 and PI2611. In the higher pressure Ultradel case, the FEA predicts larger film deflection than is measured experimentally. One explanation is that at this pressure Mises stresses in the film are beyond the yield stress, and viscoelastic properties, largely neglected in the analysis, are becoming important. Film relaxation is expected to increase film deflection, consistent with the direction of the discrepancy. In comparing the experimental and finite element results, consider that difficulty in focusing on the surface of the featureless polyimide films contributes some unknown but possibly significant amount of error in the deflection measurement data.

The methodology presented in this section was used to analyze all of the IBT data in the next chapter, providing both the mode I and mode II components of the specific fracture energy (γ_I and γ_{II}).

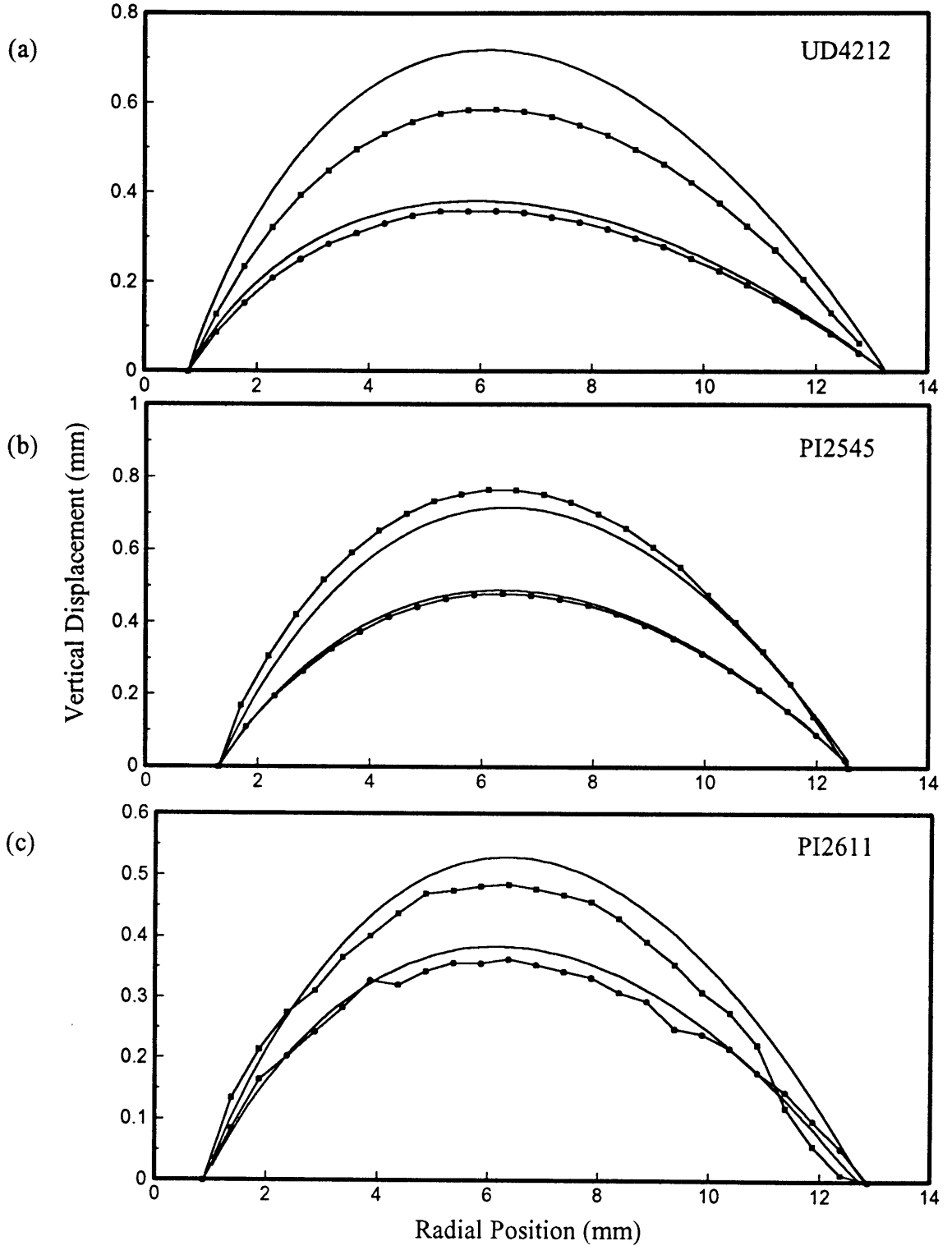

Figure 3.2.4: Vertical deflection as a function of radial position for (a) Ultradel 4212, (b) PI2545, and (c) PI2611. Two cases are shown for each material. The case with larger deflection is appropriate for pressures experienced in testing on Cr, the other for testing on Al.

3.3 Error Analysis

An analysis of the error in the γ_I calculation provided by the FEA proceeded in the following manner. The γ_{Ic} of a specific data set, calculated using the elastic FEA, was used as a baseline (Ultradel-Cr; inner radius, r_i = 0.63 mm; outer radius, r_o = 13.2 mm; polymer thickness, h = 0.0104 mm; critical pressure, p_c = 0.01538 MPa; Young's modulus, E = 2300 MPa; residual film stress, σ_o = 32 MPa). Each of the parameters was changed by +/-12% and +/- 25% from their nominal values, and γ_{Ic} was recalculated using the elastic FEA, giving a total of five data points for each parameter. A one-dimensional polynomial equation was least-squares fit to this data. All fits had an R^2 value of greater than 0.995. All of the one-dimensional parameters were then combined to form an overall expression for γ_{Ic}:

$$\gamma_{Ic} = \frac{r_o^{3.5}}{h\, r_i^{1.5}} \left[C_1 \frac{p_c^{3/2}}{E^{1/2}} - C_2 \sigma_r \right] \qquad [3.3.1]$$

where C_1 is 0.86 and C_2 is 9.5×10^{-8}. If the units of the radii and the film thickness are expressed in mm, and p_c, E, and σ_r are in MPa, then γ_{Ic} is in J/m^2.

Now that a numerical equation which expresses γ_{Ic} as a function of experimental parameters exists, a standard differential error analysis can be applied [94][1]. The relationship which determines how error in each parameter, x, propagates into γ_{Ic} is:

$$\delta\gamma_{Ic} = \left| \frac{d\gamma_{Ic}}{dx} \right| \delta x \qquad [3.3.2]$$

For a polynomial of the form: $\gamma_{Ic} = x^n$, Equation 3.3.2 can be expressed as:

[1] The methodology governing the error analysis presented in this section is based on [94] and all general equations can be found there.

$$\frac{\delta\gamma_{Ic}}{|\gamma_{Ic}|} = |n|\frac{\delta x}{|x|} \qquad [3.3.3]$$

where $\frac{\delta x}{|x|}$ is the percent error in parameter x and $\frac{\delta\gamma_{Ic}}{|\gamma_{Ic}|}$ is the percentage error of γ_{Ic}. For a complex function of many variables, the errors of each parameter are combined in quadrature to calculate the total error in γ_{Ic}:

$$\delta\gamma_{Ic} = \sqrt{(\frac{\partial\gamma_{Ic}}{\partial x}\delta x)^2 + \ldots . + (\frac{\partial\gamma_{Ic}}{\partial z}\delta z)^2} \qquad [3.3.4]$$

We proceed by evaluating the error in the term outside the brackets in Equation 3.3.1, then the term inside the brackets, and combining the results according to Equation 3.4.1. All calculations use the typical errors in each parameter listed in Table 3.3.1 and shown as a percent of their nominal value.

Table 3.3.1: Estimated errors in experimental parameters.

Parameter		Typical Value	Typical Error	% Error
r_o	outer radius	13.0 mm	0.05 mm	0.4%
r_i	inner radius	0.70 mm	0.005 mm	0.7%
h	film thickness	0.020 mm	0.001 mm	5.0%
p_c	pressure	0.015 MPa	0.0003 MPa	2.3%
E	modulus	2300 MPa	200 MPa	8.7%
σ_r	residual stress	30 MPa	2 MPa	6.7%

The error (e_1) in the term outside the brackets in Equation 3.3.1 is then calculated as:

$$e_1 = \sqrt{(3.5\times 0.4\%)^2 + (1.5\times 0.3\%)^2 + (1.0\times 5.0\%)^2} = 5.3\%$$

The error (e_2) in the term multiplied by C_1 is:

$$e_2 = \sqrt{(1.5\times 2.3\%)^2 + (0.5\times 8.7\%)^2} = 5.6\%$$

The error (e_3) in the term multiplied by C_2 is equivalent to the error in the residual stress, 6.7% since it is raised to the first power. These errors combine to give a total error (e_T) in γ_{Ic} as follows:

$$e_T = \sqrt{e_1^2 + (e_2 + e_3)^2} = 13.3\%$$

Under these assumptions, the total error in the calculation of γ_{Ic} is 13.3%.

Note that this entire exercise has been carried out under the assumption of elastic film behavior. Although reasonable in the baseline case investigated above, this is not always a good assumption as will be demonstrated in the following section. When film plasticity is present, the error in accounting for this phenomenon must also be considered. As a first order estimate, the baseline condition was considered with different representations of the plasticity, the extremes being the perfectly elastic case and the perfectly plastic case. Figure 3.3.1 illustrates the range of behavior considered. Based on this analysis, the contribution to the error in γ_{Ic} from plasticity is estimated to be approximately 5% beyond the e_T calculated previously, for total error of approximately +/- 18%.

3.4 Test Limitations

Proceeding in a manner similar to that described in the previous section, the Mises stress at the centroid of the element released in the fourth step of the FEM can be expressed:

$$\sigma_{Mises} = 0.044 \frac{p_c}{h} \left(\frac{r_o^{5/2} E}{r_i \sigma_r} \right)^{2/3} \qquad [3.4.1]$$

The units of σ_{Mises} are MPa. This stress level is closely associated with the maximum Mises stress in the film. Note that this analysis also does not account for plasticity. As will be demonstrated in Chapter 4, agreement between Equation 3.4.1 and FEM calculations is very good for all three polymers, with a typical difference in values of less than 5%.

Before sample fabrication begins, it is important to ensure that the film thickness is sufficient to withstand stresses incurred during testing. As will be demonstrated in Chapter 4, thinner films develop higher stresses during debonding, stresses that can exceed the ultimate strength of the film, resulting in film rupture. Equations 3.3.1 and 3.4.1 can be manipulated in a way that enables prediction of the critical film thickness

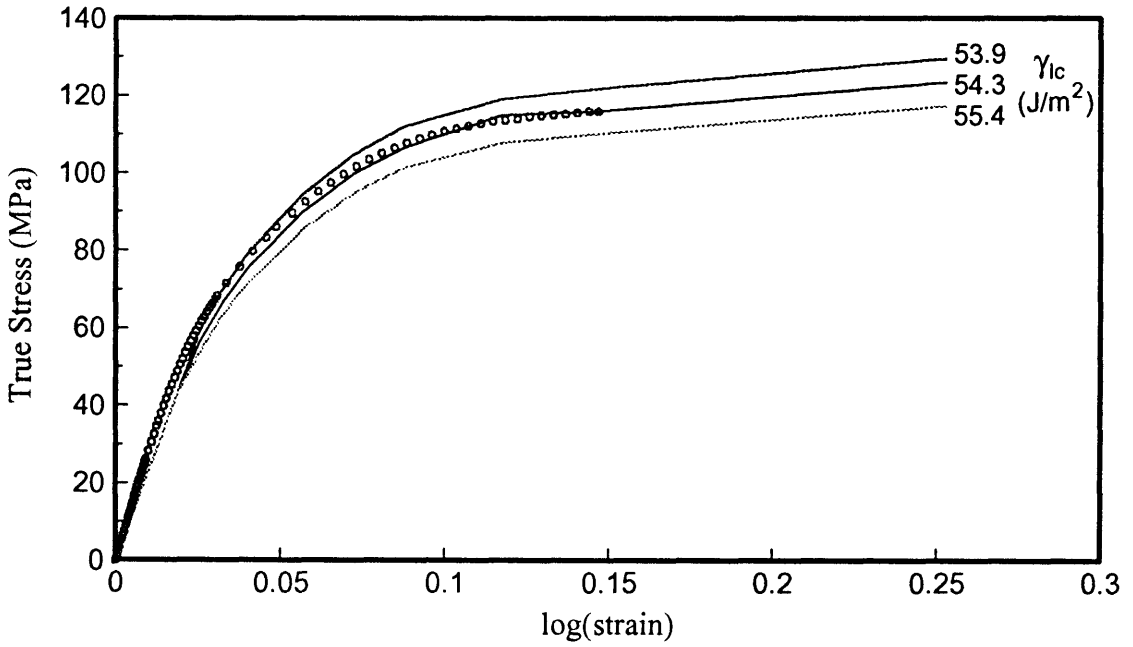

Figure 3.3.1: Behavior of 20μm Ultradel 4212 film under uniaxial tension. Three models of the film behavior are shown; the middle one was used in specific fracture energy calculations. Experimental data denoted with symbols (o).

required for a given blister site geometry (r_i and r_o) and mechanical properties of the film ($E_{membrane}$, σ_r, G_{Ic}). Equation 3.3.1 can be rearranged to express p_c as a function of the rest of the parameters.

$$p_c = 22.73h\sigma_{Mises}\left(\frac{r_i\sigma_r}{r_o^{5/3}E}\right)^{2/3} \qquad [3.4.2]$$

This expression of p_c can then be substituted into Equation 3.4.2 providing:

$$\gamma_{Ic} = \frac{r_o^{3.5}}{r_i^{1.5}h}\left[\frac{C_3h^{1.5}\sigma_r\sigma_{Mises}^{1.5}r_i}{E^{1.5}r_o^{2.5}} - C_2\sigma_r\right] \qquad [3.4.3]$$

where C_3=93.2. For a specific system (e.g. Ultradel 4212 - Cr), the σ_r, and E are known. If the maximum σ_{Mises} exceeds the ultimate strength of the film, the film will rupture prior to debonding. To determine the geometry at which this occurs, the ultimate strength of the film is substituted for σ_{Mises} and all that remains are the parameters that describe the geometry, r_o, r_i, and h. All samples built have r_o equal to approximately 13.0 mm. Therefore, if γ_{Ic} is known or can be estimated for a specific system, then we are left with an equation with r_i and h only:

$$\gamma_{Ic} = C_1\sqrt{\frac{h}{r_i}} - \frac{C_2}{r_i^{1.5}h} \qquad [3.4.4]$$

where C_1 and C_2 are constants that depend only on E, σ_r, and r_o. The values of these constants for the three polyimides of interest are shown in Table 3.4.1.

Table 3.4.1: Constants for Equation 3.4.4 for materials under investigation.

Material	C_1	C_2
UD4212	490.8	0.0256
PI2545	621.3	0.0151
PI2611	353.5	0.0226

Figure 3.4.1 illustrates the case of Ultradel 4212 on both (a) Cr (G_{Ic} = 55 J/m^2) and (b) Al (G_{Ic} = 27 J/m^2). The area above each curve represents the acceptable design space. Samples built with geometries falling below the curve rupture prior to debonding. Based on uniaxial tensile testing, the ultimate tensile strength of Ultradel was assumed to be 120 MPa (Table 2.1.1). The data in Figure 3.4.1 suggest that the methodology described effectively predicts which geometries will be successful for these Ultradel-on-metal systems.

As will be seen in the next chapter, PI2545 adheres so well to chromium that at practical thicknesses the film experiences much plasticity invalidating Equations 3.3.1 and 3.4.1. The application of this methodology to the PI2545 system is therefore limited to the case of adhesion to aluminum. The cases of PI2545 and PI2611 on aluminum are shown in Figure 3.4.2. The case of PI2611 on chromium is somewhat anomalous and will be explored in more detail in Chapter 4.

(a)

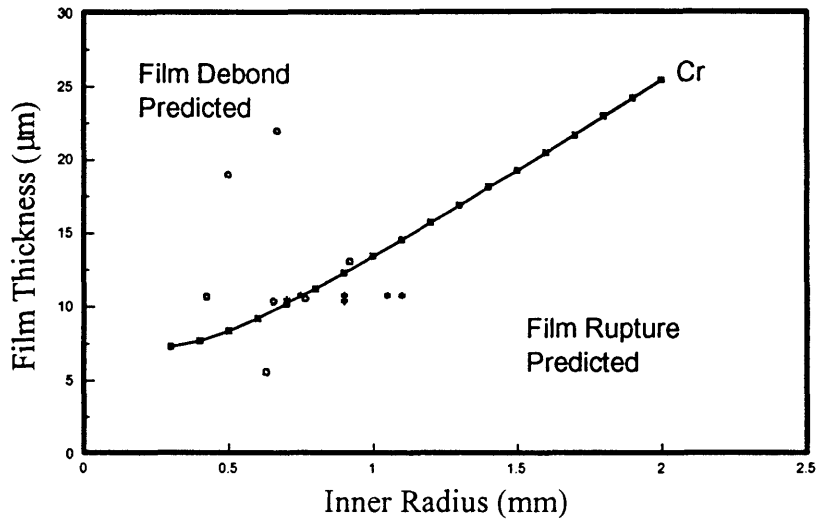

(b)

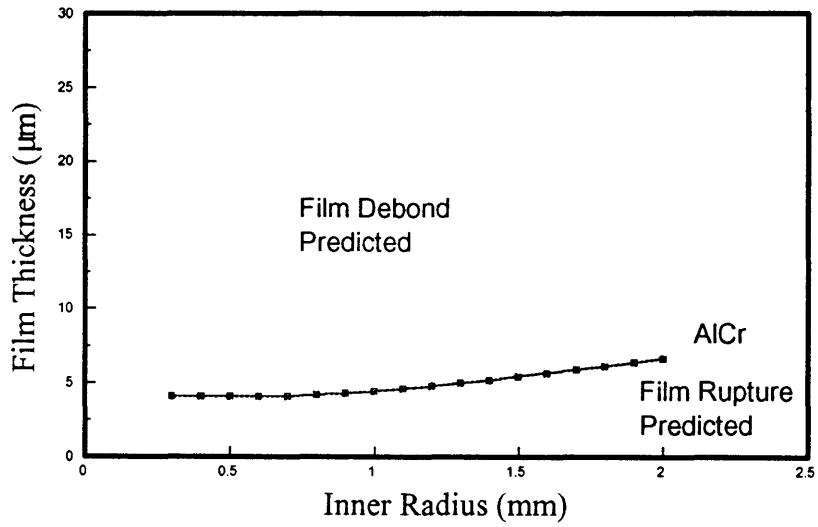

Figure 3.4.1: Design space for Ultradel 4212 on (a) Cr and on (b) AlCr. Film debonding is predicted in regions above the curves. Samples denoted by o debonded; samples denoted by * ruptured.

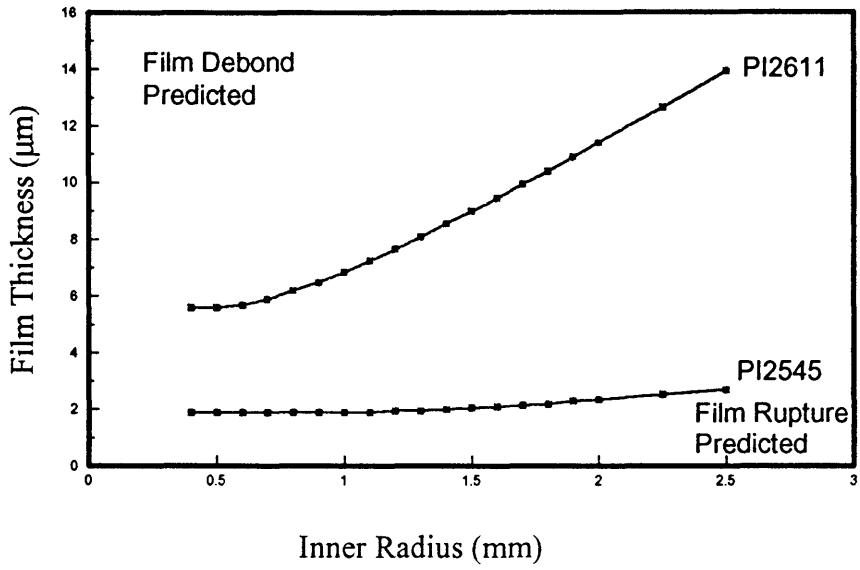

Figure 3.4.2: Design space for PI2611 and PI2545 on AlCr. Film debonding is predicted in regions above the curves.

Chapter 4: Measurement of Specific Fracture Energy

In the first section of this chapter, the specific fracture energy measurements generated by the island blister test are presented, broken down into mode I and mode II components along with the plastic work contribution. It is shown that the mode I component, γ_{Ic}, provides an indication of the onset of crack propagation. In the second section, fracture energy data from peel testing of the same systems are presented and evaluated in terms of the elastoplastic analysis developed by Kim *et al.* [15, 16]. Trends in specific fracture energy as measured by the IBT and peel test are compared. The literature regarding predictors of interfacial fracture is reviewed in the final section. As alluded to in Chapter 3, the majority of the recent research that investigates mixed mode interfacial fracture is elasticity based. For systems with large scale plasticity, it is shown that no consensus exists as to what single indicator predicts the onset of fracture, although some authors postulate that the mode I component of the interfacial strain energy release rate may provide this function. The most important result distilled form the data of this section is the experimental finding that γ_{Ic} is constant and independent of the value of γ_{II}. This appears to be the first experimental demonstration of this criterion for plasticity dominated interfacial failure, long accepted to be the indicator of failure in homogeneous, elastic systems.

4.1 Island Blister Test Results

This section is broken down into three subtopics. The first proposes a criterion for fracture based on the decoupling of the specific fracture energy by loading mode.

The second discuss the state of stress in the film during debonding. The third investigates the rise in fracture energy as the test proceeds and the inner radius decreases.

4.1.1 Criterion for Fracture

Table 4.1.1 presents the mode I and II components of the specific fracture energy as a function of the film thickness for all of the systems studied. Also shown are the total specific fracture energy, γ_a, and the total plastic dissipation, W_p. The difference between Cr^{poor} and Cr^{good} in Table 4.1.1 for the UD4212-Cr samples is processing related with origins described in more detail in Chapter 5. Several key points are to be drawn from the data in Table 4.1.1. First, the value of γ_I at fracture is independent of film thickness, not true for the mode II component and γ_a. For each system shown, the γ_I value at fracture is approximately constant while the γ_{II} as well as the plastic work values tend to increase with thickness. Second, the γ_{Ic} values are not only constant, but they are independent of the values of γ_{II}. These observations lead to the important conclusion that it is the mode I component of the specific fracture energy that indicates the onset of crack propagation; the fracture criterion for these systems is that $\gamma_I = \gamma_{Ic}$ at fracture, and the value of γ_{Ic} is constant with respect to γ_{II}.

Third, comparison of the relative magnitudes of the specific fracture energies and the W_p term proves the significance of plasticity in these polyimides, especially when debonded from Cr. The FEM generated results are compared with calculations of γ_{Ic} using the numerically derived solution, Equation 3.3.1. Agreement is typically within 20% for all systems except the most well adhered systems, PI2545 on Cr and PI2611 on

Cr. For the case of PI2611 on Cr, if the modulus used in Equation 3.3.1 is 2300 MPa, the value used for UD4212 and PI2545, as opposed to the physically realistic value of 6700 MPa, the agreement is almost perfect. The results of this calculation are shown in parenthesis in Table 4.1.1. The discrepancy in the PI2545 on Cr system is investigated in Section 4.2.

Table 4.1.1: Summary of IBT data as a function of film thickness for the different systems tested. Data in columns 4-7 were generated through the FEM. The γ_I shown in column 3 was calculated through the numerically derived solution represented by Equation 3.3.1.

System	Thickness (μm)	γ_I (J/m^2) Eq. 3.3.1	γ_I (J/m^2) FEM	γ_{II} (J/m^2) FEM	γ_a (J/m^2) FEM	W_p (J/m^2) FEM
UD4212-Cr^{poor}	5.6	**54**	**56**	23	79	57
	10.6	**49**	**54**	33	87	110
	11.1	**48**	**57**	38	95	144
	18.1	**54**	**64**	50	114	191
	19.0	**57**	**57**	38	95	132
	22.0	**58**	**65**	50	114	184
UD4212-Cr^{good}	19.1	**89**	**102**	48	150	367
	20.2	**103**	**112**	43	155	540
	27.9	**70**	**86**	39	125	305
UD4212-AlCr	10.2	**30**	**30**	28	58	34
	12.0	**31**	**34**	33	67	64
PI2545-Cr	7.9	**113**	**172**	43	215	329
	22.8	**103**	**169**	89	258	428
	26.8	**125**	**208**	99	307	498
PI2545-Al	20.5	**39**	**28**	38	66	62
PI2545-AlCr	19.7	**17**	**19**	28	47	35
	23.3	**12**	**15**	25	40	23
PI2611-Cr	28.3	**83** (142)	**97**	163	260	344
	42.0	**99** (171)	**172**	206	379	332
	42.0	**82** (141)	**135**	179	314	514
PI2611-AlCr	37.1	**30**	**27**	41	68	22

Now that the significance of the mode I component of the specific fracture energy has been demonstrated, it is important to explore the reproducibility of this result. The analysis of Section 3.2 predicts a total error of +/-15%. A series of Ultradel on Cr samples were fabricated and tested over the course of a year. Table 4.1.2 summarizes these results. The adhered film thickness on all samples was in the range of 10.4-11.1 μm. Samples with the same thickness originated from the same wafer.

Table 4.1.2: Demonstration of the reproducibility of the IBT. All samples are Ultradel 4212 on Cr. Specific fracture energies were calculated by the FEA. The inner radius (r_i) is also noted for each sample. Samples with the same film thickness came from the same test wafer.

Thickness (μm)	Sample	r_i (mm)	γ_{Ic} (J/m^2)	γ_{II} (J/m^2)
10.4	A	0.654	48	33
	B	0.735	51	34
	C	0.710	46	32
10.6	D	0.765	54	33
	E	0.770	50	34
10.7	F	0.423	47	33
11.0	G	0.520	56	36
11.05	H	0.785	58	38
	I	0.621	66	41
	J	0.650	49	35
11.1	K	0.920	57	39
	L	0.805	66	40
AVERAGE		-	**54**	**36**
standard deviation			**7**	**3**

The average γ_{Ic} of the 12 samples is 54 J/m^2 with a standard deviation of 7 J/m^2, or 13%, in good agreement with the predicted error. The mode II component is also quite constant with a standard deviation of 8%. The γ_{Ic} values are also seen to be independent of the starting inner radii (r_i). These data inspire confidence in the testing methodology. The fact that the testing of these samples was done by two different operators at different times suggests that the new testing methodology (Appendix C) reduces the operator dependency and enhances reproducibility.

4.1.2 Film Stress During Testing

The meridian (S_{11}), axial (S_{22}), and circumferential (S_{33}) stresses for a sample case, UD4212-Cr, are shown in Figure 4.1.1(a) as a function of radial position across the blister site. The axial stresses are essentially negligible. Over a large portion of the membrane, S_{11} and S_{33} are approximately equal, indicating a state of near equal biaxial stress. All components experience a maximum in the vicinity of the crack tip. The meridian stress is especially high, a result of the low peel angle formed by the debonding film and the substrate (Figure 4.1.2).

The Mises stresses are of particular interest because of their importance in the determination of the onset of plasticity. The Mises stress is defined in terms of the equivalent tensile stress, $\bar{\sigma}$:

$$\sigma_{Mises} = \bar{\sigma} = \sqrt{\tfrac{3}{2} S_{ij} S_{ij}} \qquad [4.1.1]$$

where the conventions of repeated indices have been applied. The deviatoric stress tensor, S_{ij} is defined as:

$$S_{ij} = \sigma_{ij} - \tfrac{1}{3}\sigma_{kk}\delta_{ij} \qquad [4.1.2]$$

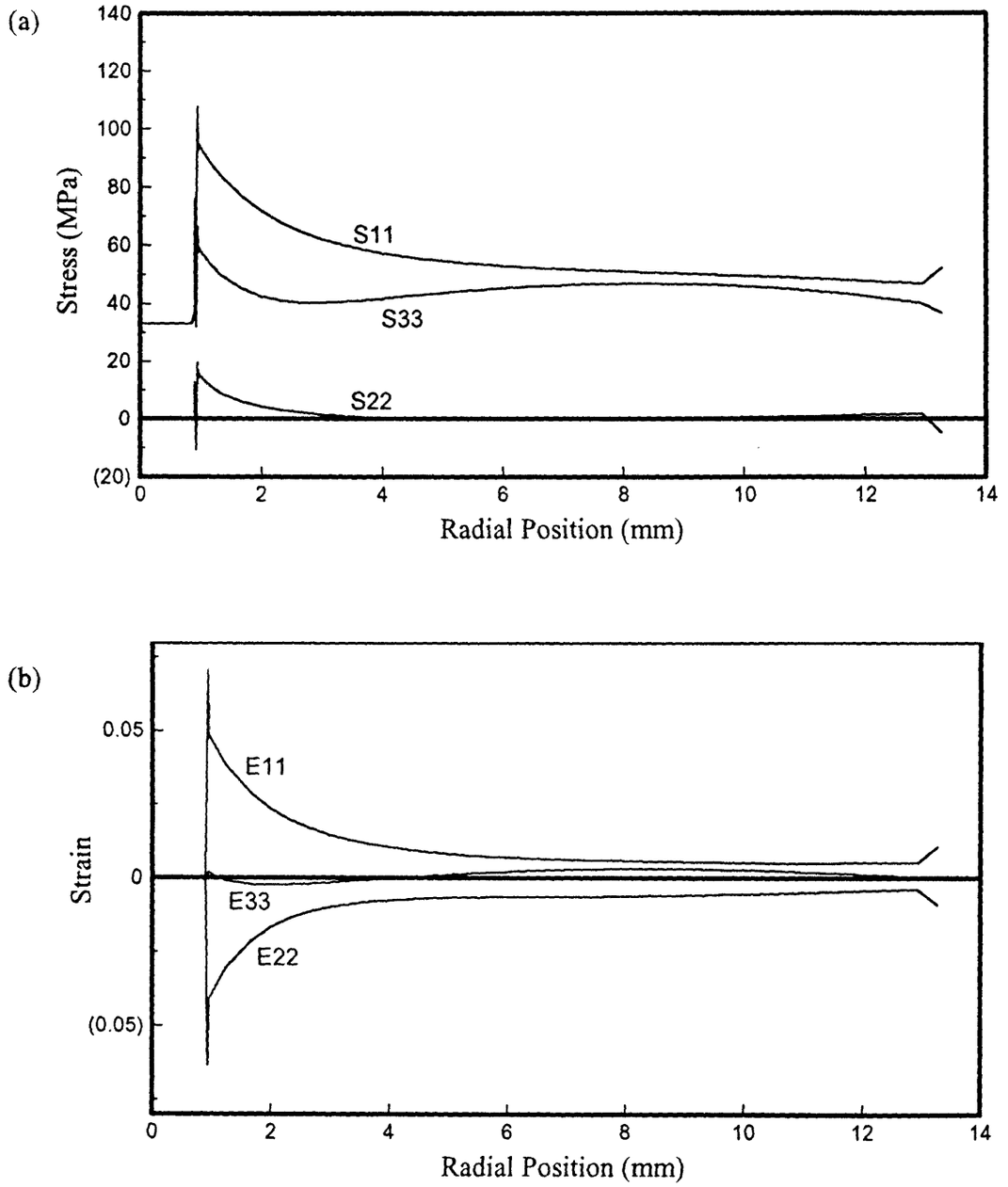

Figure 4.1.1: (a) Stresses and (b) strains as a function of radial position in an UD4212-Cr IBT sample.

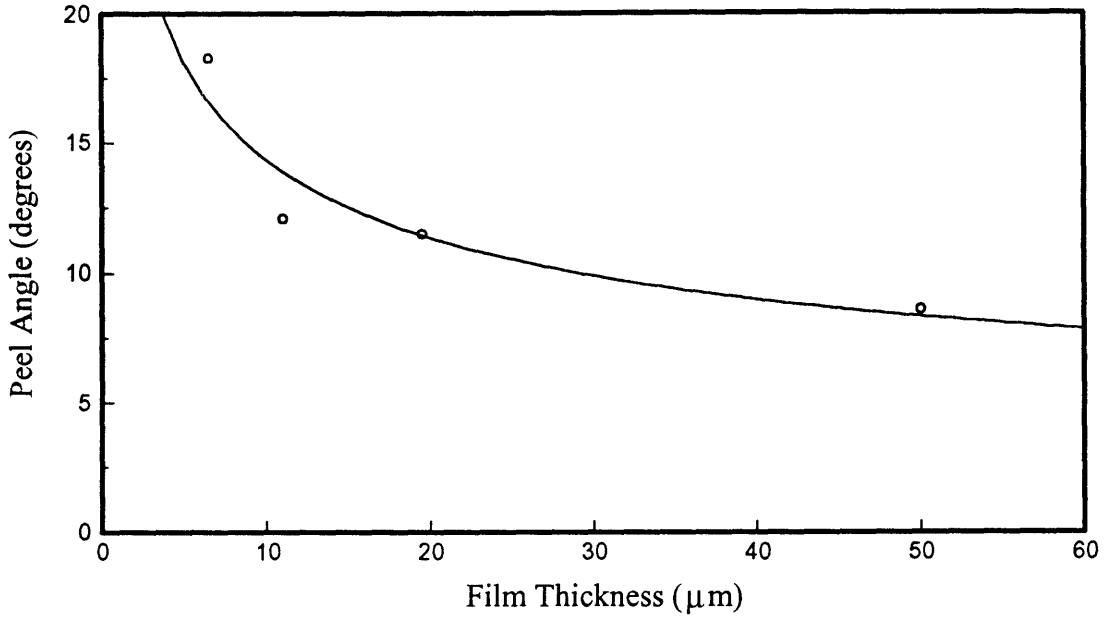

Figure 4.1.2: Peel angle as a function of film thickness. Note that the 50μm point in not experimental, but was generated, for comparison, by assuming that γ_I = 60 J/m^2 and determining the associated pc from FEM analysis, by trial and error.

where δ_{ij} is Kronecker's delta. The Mises criterion states that the material will yield where σ_{Mises} exceeds the static yield stress, σ_y, as determined through uniaxial tensile testing. Contour plots of the Mises stresses in the film at debond are shown in Figure 4.1.3 for the representative case of PI2545 debonding from (a) Cr and (b) AlCr. The stress state shown is at the moment just prior to crack propagation, although the film is shown immediately following release of the two nodes of the element at the crack tip so that this element is deflecting also. Note the very high stress levels, especially in the cases of the Cr adherend.

Table 4.1.3 shows that the maximum Mises stress measured at the centroid of the debonding element decreases slightly with increasing film thickness for a given

(a)

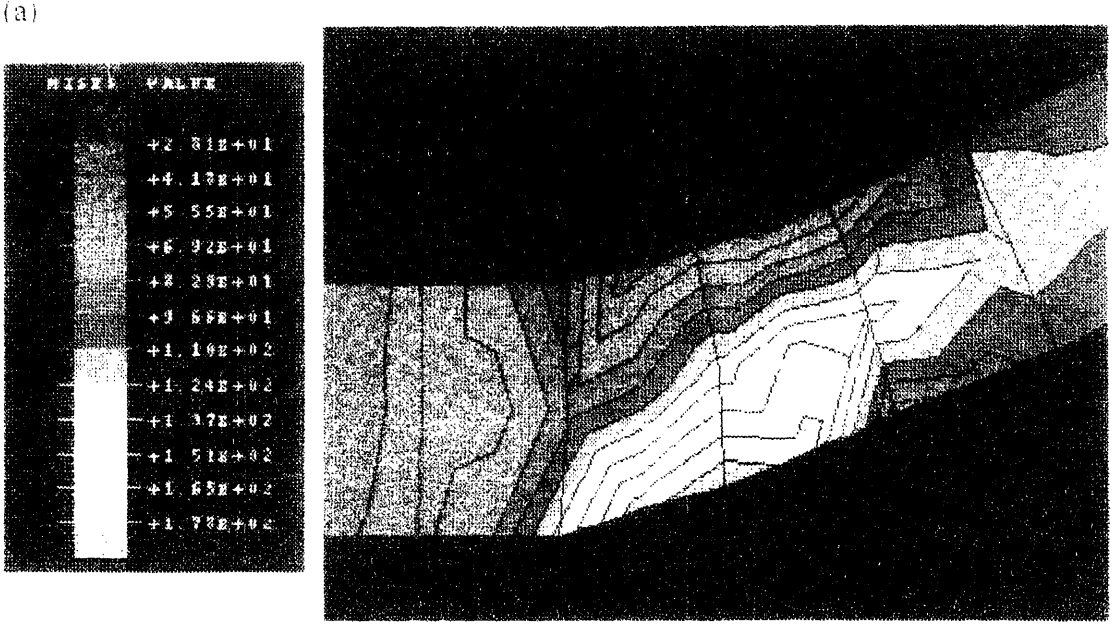

(b)

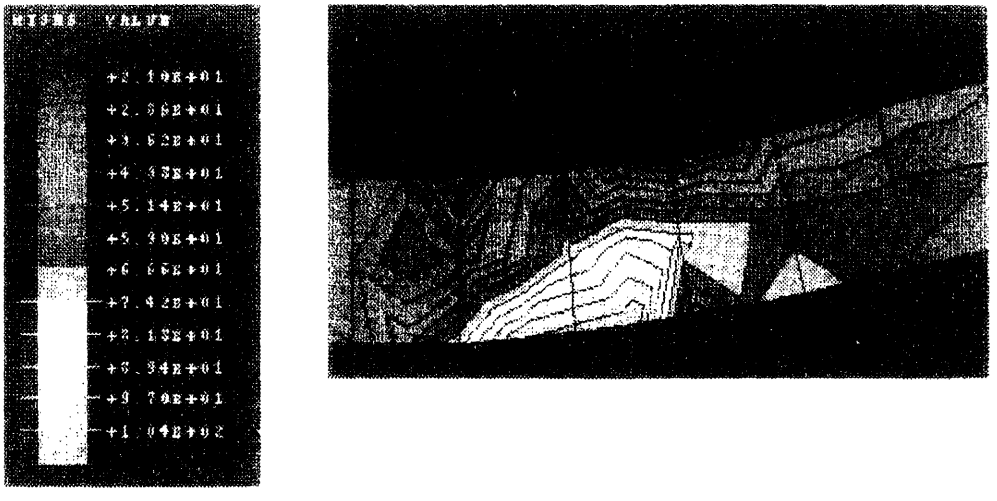

Figure 4.1.3: Mises stress contours at crack tip just prior to debond for (a) PI2545-Cr, and (b) PI2545-AlCr. The film is shown after release of the crack tip nodes.

film-adherend combination. For Ultradel on Cr system, the value at intermediate thicknesses is around 115 MPa, very nearly the ultimate tensile stress for this material at low strain rates (Figure 2.1.1). From Section 2.4, films in this thickness range were right on the boundary between debonding and rupturing, consistent with these high calculated stresses. Of course, it is the value of the maximum principal stress relative to the ultimate tensile strength of the material that will determine if through-thickness failure (rupture) occurs. The Mises stresses are expected to be close to the value of this maximum principal stress, justifying their use as a first order criterion here.

The maximum σ_{Mises} is slightly lower for Ultradel on Al. The origins of this difference could be either a reaction product that forms a lower strength interphase, or the presence of a low strength adhesive component to the failure. The fourth column in Table 4.1.3 shows the maximum σ_{Mises} as calculated by the FEM where it is compared with the estimate from the numerically derived Equation 3.3.2 found in column 5. The value provided by Equation 3.3.2 is seen to compare well with the FEM result in all cases. This level of agreement is surprising considering that the equation was developed assuming an elasticity based relationship and we are clearly beyond the elastic regime here. However, the largest discrepancies are found in the cases of the highest stress - the thinnest UD4212 film on Cr and the thinner PI2611 film on Cr.

The size of the plastic zone, r_p, is defined as the area over which the Mises stress at the centroid of the element exceeds the yield stress of the polymer. For the case of UD4212 on Cr^{poor}, r_p generally decreases with increasing thickness. The large scatter in r_p for UD4212 on Cr^{poor} stems from the closeness of σ_{Mises} to σ_y across the entire

membrane section of the film, as illustrated in Figure 4.1.4. As for UD4212-Cr and PI2545-Cr, r_p is on the order of millimeters, several hundred times the film thickness, again emphasizing the pervasiveness of plasticity in these systems. The PI2611 systems showed markedly smaller plastic zones, a consequence of the thicker films tested and the material's high yield point (160 MPa).

Table 4.1.3: Maximum von Mises stress at element centroids in adhered films for polymer-on-metal systems. The size of the plastic zone, r_p, is defined in Figure 4.1.6. The finite element result is shown in column 4. The calculation based on the numerically derived equation presented in Chapter 3 is given in column 5.

System	Polyimide Thickness (μm)	r_p (mm)	Max. σ_{Mises} FEA (MPa)	Max. σ_{Mises} Eq. 3.1.4 (MPa)	W_p (J/m^2)
UD4212-Cr^{poor}	5.6	-	138	159	-
	10.6	4.5	115	114	110
	11.1	9.7	115	116	-
	18.1	4.8	115	112	-
	19.0	1.4	110	90	-
	22.0	2.0	115	94	184
UD4212-Cr^{good}	19.1	9.8	132	127	367
UD4212-AlCr	12.0	1.9	101	94	45
PI2545-Cr	22.8	12.6	173	173	428
PI2545-AlCr	19.7	0.7	75	65	35
PI2611-Cr	28.3	0.4	279	363	344
	42.0	-	270	279	514
PI2611-AlCr	43.1	0	93	85	22

The importance of incorporating the adhered film's relaxation modulus and plastic behavior in the FEM is demonstrated in Table 4.1.4. The specific fracture energies were computed for a representative case (UD4212-Cr^{poor}) for three situations: the elastic case using the glassy modulus (2700 MPa), the elastic case using the 10

minute relaxation modulus (2300 MPa)[1], and the elastoplastic case using the plastic model from Figure 3.2.2(a) including the relaxation modulus. This system was chosen because it experiences a level of plastic yielding intermediate of all the systems explored. Systems with heavy plasticity like PI2545-Cr are expected to be more sensitive, while those with little plasticity, like any polyimide on AlCr, should be less sensitive. The lower relaxation modulus increases the calculated value of γ_{Ic}. This is sensible in view of Equation 3.3.1 where γ_{Ic} is shown to be proportional to $(E)^{-1/2}$; a decrease in E should result in a higher γ_{Ic} all else being equal. The addition of plasticity to the model reduces the calculated γ_{Ic}, a physically realistic result since, given a constant critical pressure, plasticity dissipates energy, leaving less energy to be applied to the actual debonding. As

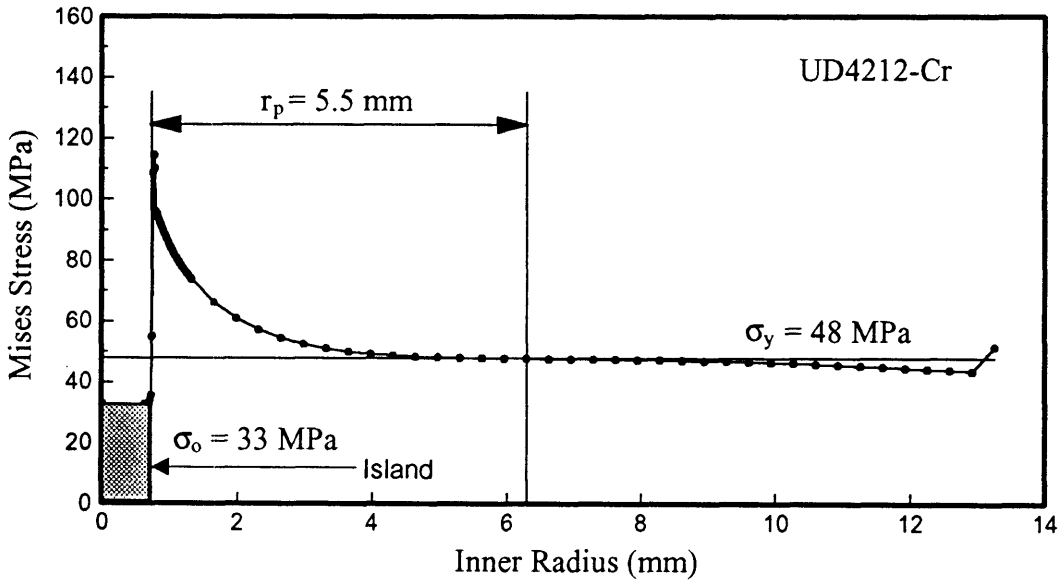

Figure 4.1.4: Mises stress in UD4212 film debonding from a Cr adherend. The plastic zone, rp, is defined as the region over which $\sigma_{Mises} > \sigma_y$.

[1] Values of the relaxation modulus were calculated according to the methology presented in [60, 61].

anticipated, the incorporation of plasticity into the analysis changes the results, presumably improving their accuracy. The addition of viscoplastic effects results in only a modest change in the specific fracture energies.

Table 4.1.4: The effect of mechanical properties assumptions on the FEA calculated specific fracture energies for a representative system (UD4212-Cr).

Mechanical Properties	γ_{Ic} (J/m^2)	γ_{II} (J/m^2)	W_p (J/m^2)
Elastic with glassy modulus	52.9	52.3	0
Elastic with relaxation modulus	57.1	51.9	0
Elastic-Plastic with relaxation modulus	48.5	33.2	109.5
Elastic-Viscoplastic with relaxation modulus	50.5	34.8	103.3

4.1.3 The Dependency of γ_{Ic} on the Inner Radius

The γ_{Ic} values presented in Tables 4.1.1 and 4.1.2 have all been reduced from the first pair of (critical pressure, inner radius) data taken during the test. As stated in Section 2.3, it is possible to collect several pairs of these points and calculate independent values for the specific fracture energy from each. Figure 4.1.5 indicates that for these polyimides tested on Cr, γ_{Ic} values steadily increase as the radius decreases. On the Al adherend, the γ_{Ic} values are much more invariant of the radius. There are several possible explanations for this phenomenon.

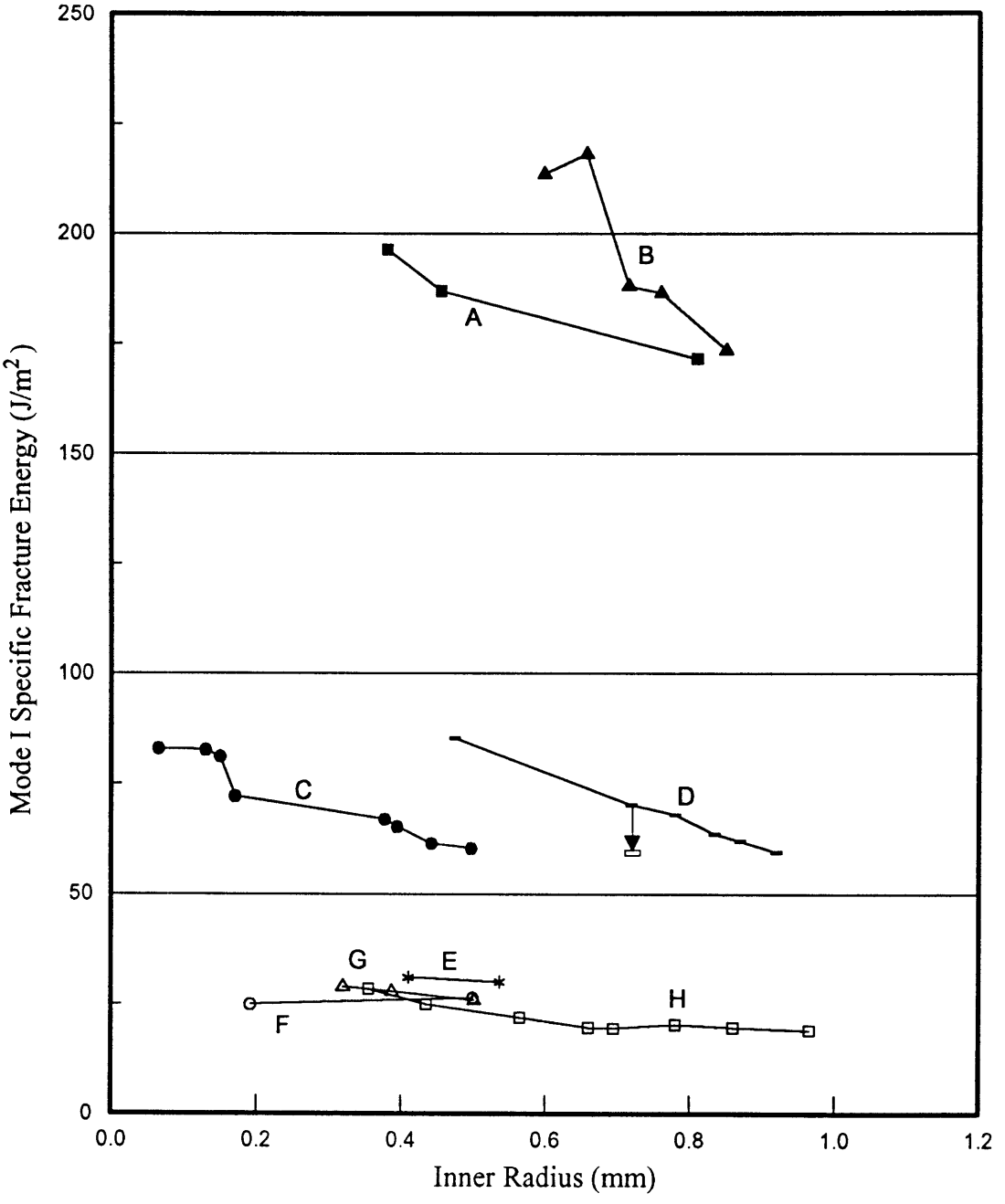

Figure 4.1.5: Calculated Mode I specific fracture energy as a function of inner radius for several systems. Samples are: (A) 42.0 μm PI2611-Cr, (B) 22.8 μm PI2545-Cr, (C) 19.0 μm UD4212-Cr, (D) 11.0 μm UD4212-Cr, (E) 10.2μm UD4212-AlCr, (F) 43.0 μm PI2611-AlCr, (G) 20.5μm PI2545-Al, (H) 19.7μm PI2545-AlCr.

As amply demonstrated in the previous section, all the polymers tested experience extremely high stresses both in the region of the crack tip due to the stress singularity created by the crack tip and simultaneously from far-field stresses satisfying the Mises yield criterion. During testing, after the first point is taken, the stresses are relaxed by reducing the load down to 75% of the critical pressure, p_c. The pressure is then slowly increased again until the new p_c is achieved, and the cycle is repeated as described in Appendix C. This cycling introduces a plastic history that is not accounted for in the finite element model. The material near the crack tip is stressed beyond its yield point. On reloading its properties differ from those of virgin material; the effective yield point is now the highest stress seen in previous loading. Considering that for PI2545 and UD4212 the yield stress is around 45-48 MPa and Mises stresses of over 80 MPa are experienced 1 mm away form the crack tip, this effect may be very significant.

To investigate this phenomenon further, tensile strips of UD4212 were fabricated and uniaxially tensile tested in the following manner. The strip was loaded at a rate 0.01 mm/mm to ~110 MPa and then partially unloaded to ~ 70 MPa. Finally, the strip was loaded at the same rate to the same stress. Figure 4.1.6 illustrates this cyclic loading and unloading. It is seen that the stress-strain relation on reloading is linear and elastic; subsequent loading and unloading follows the same path with only a marginal permanent strain.

A first order attempt at incorporating this effect into the model involved attributing elements near the crack tip with a different yield point. Figure 4.1.7 indicates the progression in yield point assumed as the crack tip is approached. Those few elements right at the crack tip were given a yield stress of 114 MPa, those slightly further

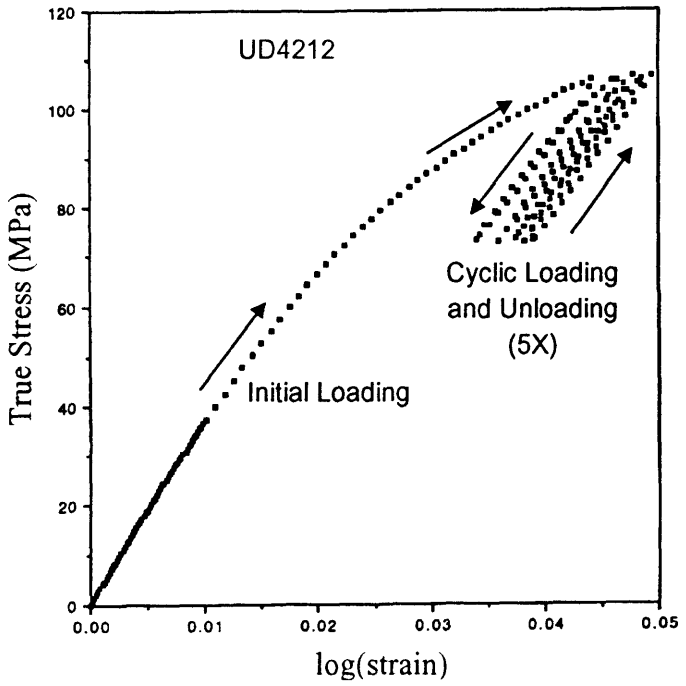

Figure 4.1.6: Stress-strain behavior of UD4212 in cyclic loading and unloading beyond its initial yield point.

away a yield stress of 97 MPa, and these even further a yield stress of 85 MPa. This step-wise representation is a primitive attempt to model the yield stress as the maximum Mises stress previously experienced. This methodology was applied to the case of UD4212-Cr as a cursory exploration. The results, shown by the arrow in Figure 4.1.7, indicate that the agreement in γ_{Ic} between the first data point analyzed in the traditional way and the fifth data point analyzed according to this modification is very good. Using the usual plastic model, the first data point yielded a γ_{Ic} of 58 J/m^2 and the fifth point, a γ_{Ic} of 70 J/m^2. Reevaluation of the fifth point with the modified model resulted in a reduced γ_{Ic} value of 59 J/m^2, extremely close to the first value. While this technique may provide constant values of γ_{Ic} as a function of r_i, its implementation is tedious as the

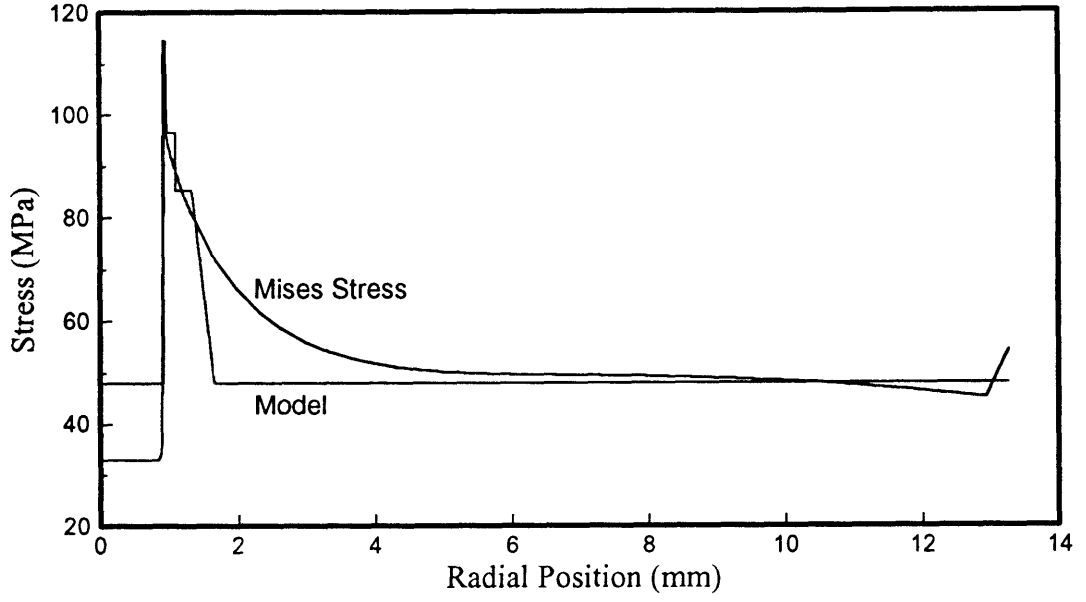

Figure 4.1.7: Modified model of constitutive relationship for UD4212.

Mises stress profile must be known *a priori*. A better solution may be to rely on only the first point taken, evaluating it according to the standard protocol mentioned in Chapter 3.

Although this plastic history effect provides one possible explanation, viscoelasticity, largely unaccounted for in the analysis, offers an another. Maseeh [42, 43] has noted the viscoelastic tendencies of thin polyimide films and has proposed a first order model of their behavior. Viscoelasticity may contribute additional strain in the film through creep phenomenon. Stresses achieved in the film are sufficient for such effects but the time scale of the experiment (5-10 minutes per data point) is expected to be too short for serious creep strains to develop.

Another viscoelastic effect found by Maseeh in polyimide is a reduction in residual film stress after the film is loaded beyond its viscoelastic limit. The effect is attributed to energy dissipated by the reorientation of polymer molecules during the stress cycling. Such an effect would reduce the critical pressure required for debond

because less energy would be required to overcome the tensile stress of the film. This works in the direction opposite to that observed. Also the pressure is unloaded to about 75% of the p_c, and not completely unloaded. For the well-adhered systems, the residual stress plays a small role in determination of the fracture energies, so this effect is not expected to contribute significantly to the outcome of the FEM.

The final, and perhaps most pertinent, viscoelastic effect is stress recovery after loading beyond the viscoelastic limit of the material. Qualitatively, stress recovery refers to the gradual reversion of a polymeric body deformed beyond its yield point to its original shape. Maseeh experimented with blister samples of the type used for residual stress measurements in the present work [42, 43]. After deforming the samples beyond their viscoelastic limit, the samples were allowed to sit and recover. After ~130 hours, the original shape was regained. The physical explanation lies in the entropy change resulting from molecular orientations that occur during large scale inelastic deformation of polymers. Upon relief of the stress that caused the orientation, the polymer seeks to increase its entropy by reverting to its initial, more disordered state. This creates back stresses which drive the polymer towards its original shape [95, 96, 97].

The opportunity for stress recovery occurs after a data point is taken and the membrane stresses are partially relieved as mentioned earlier. The pressure force would have to overcome any back stresses present, diminishing the amount of energy available for crack propagation. Experimentally, this situation would result in higher pressures required for crack propagation. If this effect were not accounted for, calculated values of γ_{Ic} would be larger than the actual specific fracture energy. The occurrence of stress recovery is then consistent with the high values γ_{Ic} resulting from high critical pressures.

The argument against this effect, like the creep strain effect, is the relatively small time scale of the experiment and the fact that the blister is unload only to 75% of the critical pressure. The stress recovery reported by Maseeh occurred over a period of 130 hours and occurred in films completely relieved of their external loads.

None of the above comments regarding the occurrence of viscoelasticity in the IBT constitute proof that viscoelastic effects are completely absent. They only provide some physical reasoning against their significance. The fact that the viscoelasticity in polyimides is non-linear makes it especially difficult to incorporate into any model. The ABAQUS environment used for the modeling allows the incorporation of linear viscoelasticity but not simultaneously with the plasticity model. An entirely new constitutive relation that includes both the non-linear viscoelasticity and plasticity would have to be developed and substituted into the model. Such a constitutive relation was not available for this work. Since the film plasticity has already been shown to be important, the trade-off was made to account for it in lieu of applying the linear viscoelasticity model. Further investigation into the importance of viscoelastic effects, and how to incorporate them into the analysis is an important area for future research.

In summary, well adhered films showed an increase in γ_{Ic} as the test proceeded and the inner radius decreased. The possible influences of viscoelasticity were reviewed but thought to be second order because of the relatively short time frame of the experiment. An explanation based on plastic history effects derived from the cyclic nature of the test was offered. A primitive method of accounting for these effects was implemented and shown to provide a more constant value of γ_{Ic}.

4.2 Peel Test Results

The results of the peel test, practiced as described in section 2.3, are summarized in Table 4.2.1. The same systems tested with the IBT were evaluated with the peel test. The IBT results are presented again for comparison. Note that the γ_a value from the IBT is simply the sum of the mode I and mode II components. The important trends are that, (i) the peel energy is a function film thickness, and (ii) the peel energies are always larger than the IBT energies. It is expected that plasticity is largely responsible for both of these discrepancies. The significance of plasticity has long been recognized and several attempts have been made to account for it [15, 98, 99]. Two such attempts will be reviewed here, and the second will be used to evaluate the data produced in this work.

The amount of plastic dissipation in the film can be estimated through the dimensionless peel force parameter, η:

$$\eta = \frac{6EP}{\sigma_y^2 h} \qquad [4.2.1]$$

where P is the peel energy directly measured in the test. For values of η less than one, the peel energy accurately represents the fracture energy ($P = \gamma_a$). The well-adhered systems tested in this work produce values of η ranging from 25 to 135, indicating that plasticity contributes significantly to γ_a. In such cases, the work of adhesion (γ_a) can be separated according to:

$$\gamma_a = P - P_y \qquad [4.2.2]$$

where P_y is the energy dissipated through plasticity. Gent and Hamad [99] propose a simple model of P_y for an elastic-perfectly plastic system based on elementary bending theory:

$$P_y = \sigma_y h^2/4R \qquad [4.2.3]$$

where R is the radius of curvature formed by the film at the point of debonding (Figure 4.2.1). Evaluation of P_y is straightforward except for the determination of R. Gent and Hamad used photography to take this measurement.

Kim and Aravas [15, 16] treat the debonding film as an elastoplastic beam under plane strain and apply slender beam theory to the moment-curvature relation for pure bending. They assume elastic-perfectly plastic behavior in both tension and compression. Finite element analysis was used to study stress fields at the crack tip. Their analysis describes the plastic expenditure as:

$$P_y = \frac{\sigma_y^2 h}{2E} f(k_B) \qquad [4.2.4]$$

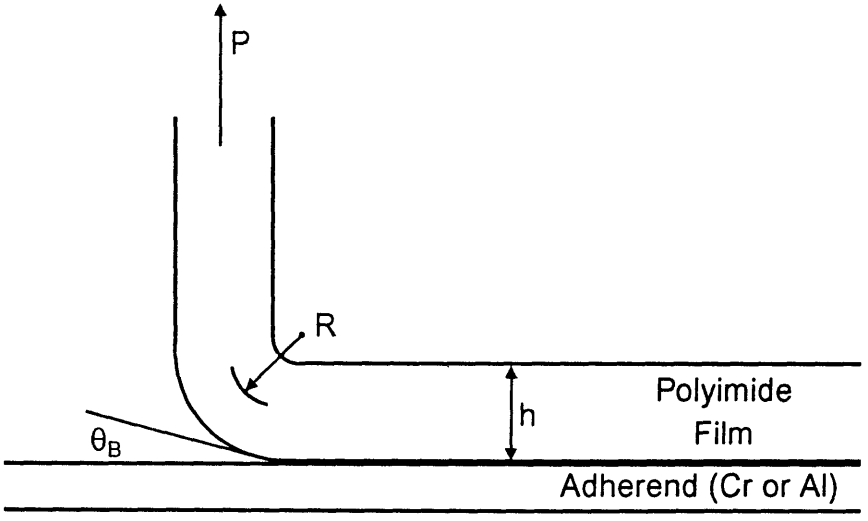

Figure 4.2.1: Schematic of peel test geometry showing the peel angle θ_B.

where k_B is the maximum curvature experienced in the film. This curvature is a function of the peel angle, θ_B, as defined in Figure 4.2.1, and the dimensionless peel force, η:

$$k_B = 1 + \tfrac{1}{12}\eta(1 - \sin\theta_B) + [[1 + \tfrac{1}{12}\eta(1 - \sin\theta_B)]^2 - \tfrac{4}{3}]^{1/2} \qquad [4.2.5]$$

The exact form of $f(k_B)$ depends on whether reverse plasticity is present, which is the case for $k_B > 2$. For these cases, this function is defined as:

$$f(k_B) = k_B + \frac{7}{4} + \frac{1}{3k_B} + \frac{1}{2k_B^2} - \frac{1}{12k_B^4} \qquad [4.2.6]$$

Table 4.2.1 Compilation of peel test adhesion data. All Ultradel testing was done at a rate of 2.5 mm/min. PI2545 and PI2611 systems were peeled at 2.0 mm/min. The total specific fracture energy for the IBT test is taken from Table 4.1.1 for reference. The last column shows the peel angle required for the peel results to be equivalent to the IBT ones.

System	Thickness (μm)	IBT γ_a (J/m^2)	Peel Test γ_a (J/m^2)	angle (θ_B) for peel=IBT
UD4212-Cr	18.4		419	12.7
	19.2	108	423	12.5
	32.4		548	8.4
UD4212-AlCr	12.0	67		
	19.1		100	32.5
	19.1		105	30.5
PI2545-Cr	15.0		180	see text
	22.8	258		
PI2545-AlCr	15.0		89	24.3
	15.0		96	22.5
	19.7	47		
PI2611-Cr	26.7		420	22.0
	28.3	260		
	31.4		528	19.1
PI2611-AlCr	36.7		387	see text
	37.1	68		

As in the model by Gent and Hamed, a key variable in the definition of k_B is the peel angle, a quantity not easily determined. Kim *et al.* suggest finite element analysis of the deflections at the crack tip [15]. Since such analysis was not employed in the present work, the data are simply presented as a function of θ_B. Kim *et al.* do state that the value of θ_B is "very small" for the case of copper peeled from a polyimide substrate, but this may be due to the assumption of elastic behavior of the substrate. They note that if the substrate is allowed to deform plastically, much larger peel angles are expected.

Equations 4.1.3 - 4.1.5 were used to evaluate the peel data generated for UD4212, PI2545, and PI2611, each on Cr and AlCr metallized silicon wafers. In the absence of θ_B measurements, the γ_a is shown through figures which plot the specific fracture energy as a function of θ_B. The UD4212-Cr system is used as an example of this calculation in Figure 4.2.2 which shows the peel energy (P) as a function of its components, the specific fracture energy (γ_a), and the plastic dissipation (P_Y). The data for all three polyimides on a Cr adherend is shown in Figure 4.2.3 (a); the data for the Al adherend case is shown in (b). The angle required to obtain equivalency between the calculated peel energy and the IBT result is indicated with asterisks in Figure 4.2.3. For example, in the case of PI2611-Cr, the peel angle at the crack tip would have to be around 19° for the peel result to match the IBT value of $\gamma_a = 260$ J/m^2.

Since the peel angles were not actually measured, all that can be done is to determine if peel angles required for test equivalence are sensible. For constant γ_a, thicker films produce smaller peel angles, as demonstrated by the UD4212-Cr and PI2611-Cr peel data. This is physically reasonable since a thicker film will have a larger

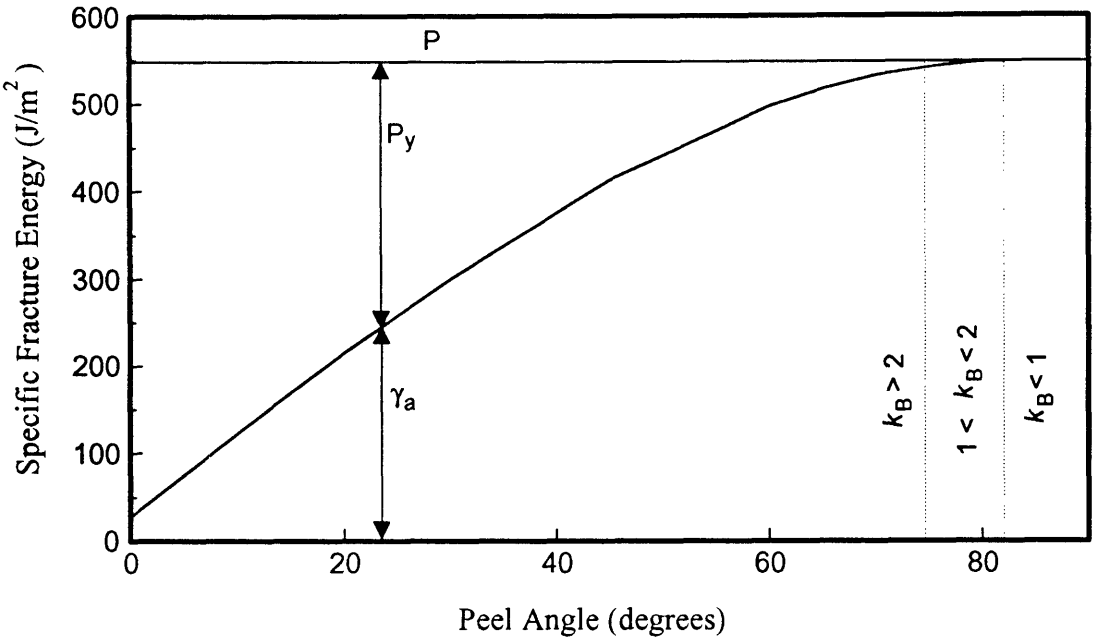

Figure 4.2.2: Breakdown of measured peel energy into plastic and specific fracture energy contributions for UD4212-Cr. Regimes of reverse plasticity (k_B>2), no reverse plasticity (1<k_B<2), and elasticity (k_B<1) are shown.

radius of curvature, which is inversely proportional to the peel angle. Comparison of the Ultradel on Cr and AlCr data shows that for lower values of γ_a the required peel angle increases. This result is counterintuitive since weaker adhesion should produce a smaller θ_B; less force is required to propagate the peel, meaning that less stress builds up in the film, producing less film bending. The specific fracture energy for UD4212-AlCr is a very weak function of the peel angle (Figure 4.2.3 (b)), implying that a large change in θ_B results only a small differential in γ_a. Thus, the calculation is very sensitive to error in the assumed γ_a value.

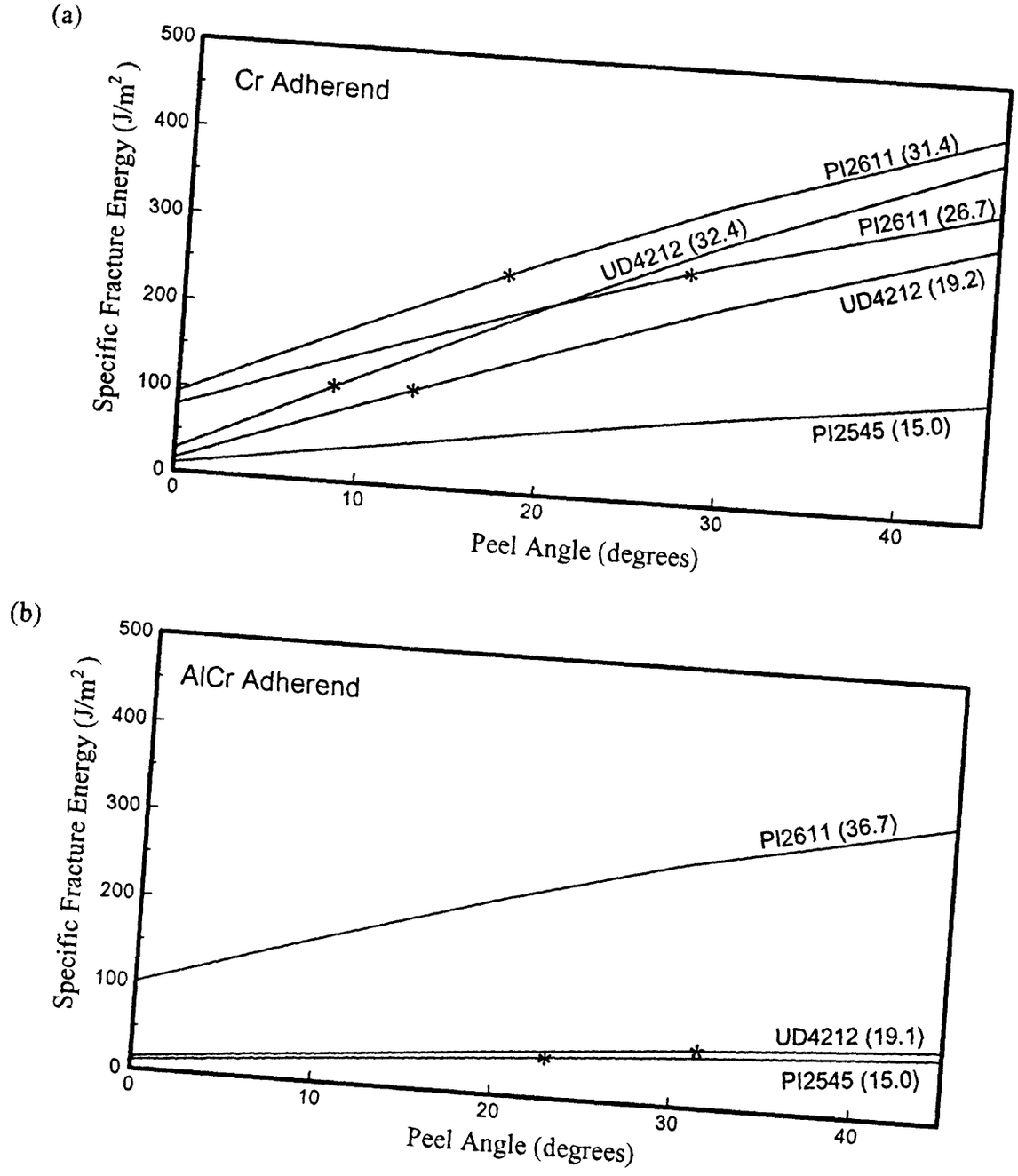

Figure 4.2.3: Specific fracture energies from peel test data evaluated using the methodology for accounting for film plasticity developed by Kim *et al.* [15] for polyimide on (a) a Cr adherend, and (b) an AlCr adherend. The thickness of the polyimide film, expressed in μm, is shown in parenthesis.

The case of PI2545-Cr is anomalous. The γ_a value derived from the IBT analysis is much higher than even the measured peel force (P), which doesn't account for film plasticity. This system was seen to be susceptible to extensive plasticity in the IBT analysis and the same trend in γ_a values is expected here. No peel angle adjustment can compensate for the mismatch. One possible explanation is that a real difference in quality of the interfaces exists among the particular samples tested. A second possibility is that for the relatively thin film tested (15 μm), the peel analysis is not valid. Kim and Avaras caution that the analysis pursued above is not applicable for thin, very well adhered films [15]. The PI2545 on Cr is the thinnest, best adhered film tested, possibly invalidating the analysis. The first explanation is investigated more fully in Chapter 5, where this discussion is rejoined after presentation of the locus of failure information.

The other anomalous system is PI2611 on AlCr. Here, the peel test results in a much greater peel energy (P = 387 J/m^2) than measured in the IBT (γ_a = 68 J/m^2). Even at $\theta_B = 0°$, the γ_a from the peel test reaches a minimum of only ~100 J/m^2. The same two explanations are offered, only here, the first is more likely. The PI2611 films tested were relatively thick (37 μm) and not expected to be that well adhered. The possibility of a true difference in interfacial fracture energy between the peel and the IBT samples appears strong and is also investigated fully in the next chapter.

One of the requirements of a good, practical adhesion test is the ability to rank the relative values of specific fracture energy for a variety of systems. This will now be done using the measured peel energies (P) and the energies modified by deduction of the plastic work expenditure, γ_a. Based on values of P, PI2611 and UD4212 on Cr appear to

have the strongest adhesion, and PI2545 and UD4212 on AlCr the weakest. The complete peel energy ranking is:

UD4212/Cr ~ PI2611/Cr > PI2611/AlCr > PI2545/Cr > PI2545-AlCr ~ UD4212/AlCr

Referring to the plots in Figure 4.2.3, we can similarly rank γ_a:

PI2611/Cr ~ UD4212/Cr > PI2611/AlCr > PI2545/Cr > UD4212/AlCr ~ PI2545-AlCr

essentially the same ranking.

In summary, the systems explored in this work experience significant film plasticity during peel testing. The framework developed by Kim *et al.* for incorporating the effects of film plasticity was applied. The importance of the peel angle was shown. Values of this angle required to produce peel values of γ_a equivalent to those generated by the IBT are in the physically reasonable range of 12-32°. Explanations for cases which deviate from these peel angles are proposed and will be explored in more detail after the locus of failure is analyzed.

It is interesting to note that the IBT geometries studied created peel angles in the range of 8-18°. If the peel angles from the peel test (θ_B) could be shown to be in the predicted range, we would have a very interesting correlation: both tests would have approximately the same peel angle and both would produce approximately the same values of γ_a. Margaritis has initiated an effort to model the peel test using a FEA which applies the same modified crack closure method described in Section 3.2. Future work will involve analyzing the peel data presented in this work with this FEM. Both the peel angle and the direct calculation of the specific fracture energies should be possible. The

level of agreement between these future FEM calculations and the analysis pursued above will provide one way of evaluating the appropriateness of the methodology of Kim *et al.* for the materials systems of interest here.

4.3 Metal on Polymer Systems

An exploratory study of metal on polymer systems is presented in this section. The case of a 25 μm copper film adhered to a polymide-coated substrate is used as an example. Assuming that the γ_{Ic} of such a system is 50 J/m^2 and that the modulus of the copper film is close to that of the bulk metal (124 GPa), equation 3.3.1 predicts that a critical pressure (p_c) of approximately 23 psi will be required for crack propagation. Such pressures are obtainable and are typically experienced in testing PI2611 on Cr. However, equation 3.4.1 estimates the Mises stress near the crack tip for this case to be in excess of 10,000 MPa. Physically, this value is unrealistically large, but it does indicate that very substantial stresses are created and the likelihood of extensive film plasticity and film rupture is high.

The FEM was applied to this scenario but convergence was impossible to achieve without using more than 1 hour of CPU time on the CRAY supercomputer. The high crack tip stresses result in large deflections hindering convergence. The highest γ_{Ic} achievable in less than 30 minutes CPU time was ~3 J/m^2.

A physical explanation of the situation is offered next. The large modulus of the metal film allows only small *vertical* film deflections and a low peel angle resulting in low calculated values of γ_{Ic}. As in the polymer on metal case, it is expected that very significant stresses in the radial direction are developed leading to satisfaction of the

Mises yield criterion over large portions of the film. This creates large deflections in the radial direction, producing high values of γ_{II} and difficulty for the FEM in finding convergent solutions.

Two potential solutions are offered. Both involve using a polymeric backing layer to form a composite membrane structure. The first, illustrated in Figure 4.3.1, involves first depositing a thin stack of metal (50 nm Cr/100 nm Cu/50 nm Cr in this example) on a polyimide-coated substrate, followed by application of a 25 μm polyimide backing layer. The modulus of the composite membrane is calculated using the rule of mixtures assuming compatibility of strain in each material of the membrane. A

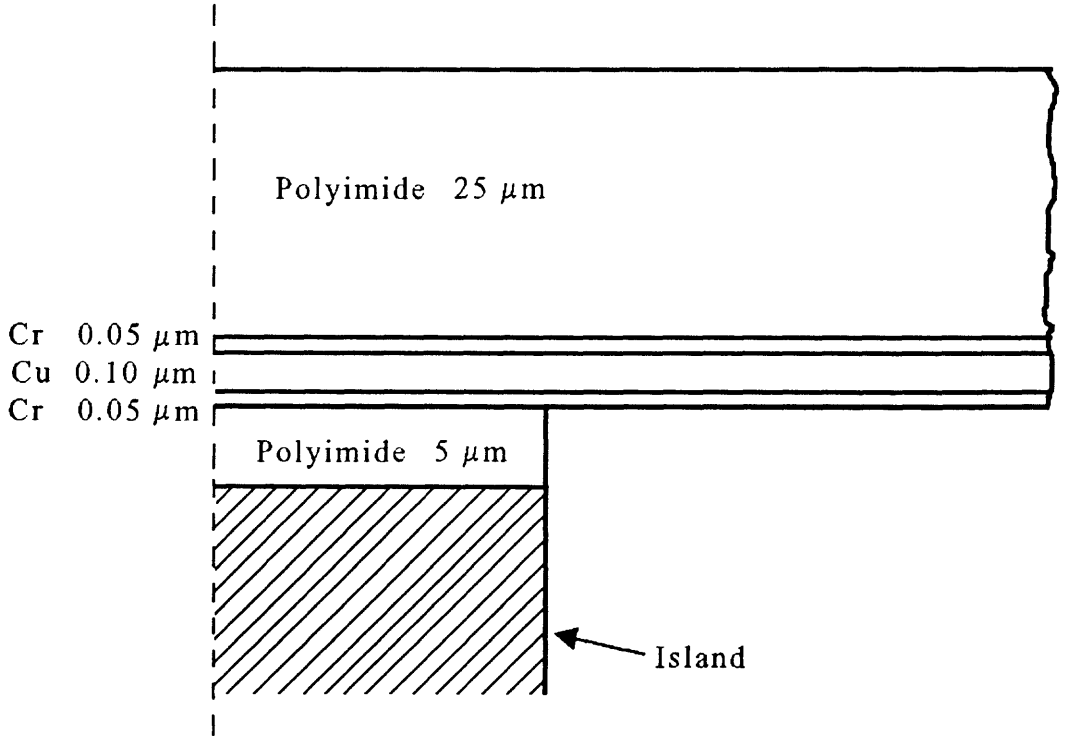

Figure 4.3.1: Schematic of metal-on-polymer IBT with polyimide backing layer.

composite modulus of ~4.5 GPa is found assuming moduli of 124 GPa, 239 GPa, and 3 GPa for Cu, Cr, and polyimide respectively. This modulus allows enough deflection at reasonable stresses to generate significant γ_i; the problem is the strain in the film. Figure 4.2.3 demonstrates that the strains near the crack tip are ~5%. The ultimate strain in these metal films is ~0.5% indicating that the metal film will crack during the test, confusing interpretation of the results.

The alternate solution involves etching the metal structure off the bottom of the polyimide backing layer as shown in Figure 4.3.2. In this case, the *initial* membrane behavior duplicates that of the polymer on metal case discussed earlier. However, once debond is initiated, the metal film peels off the polyimide adherend and remains attached

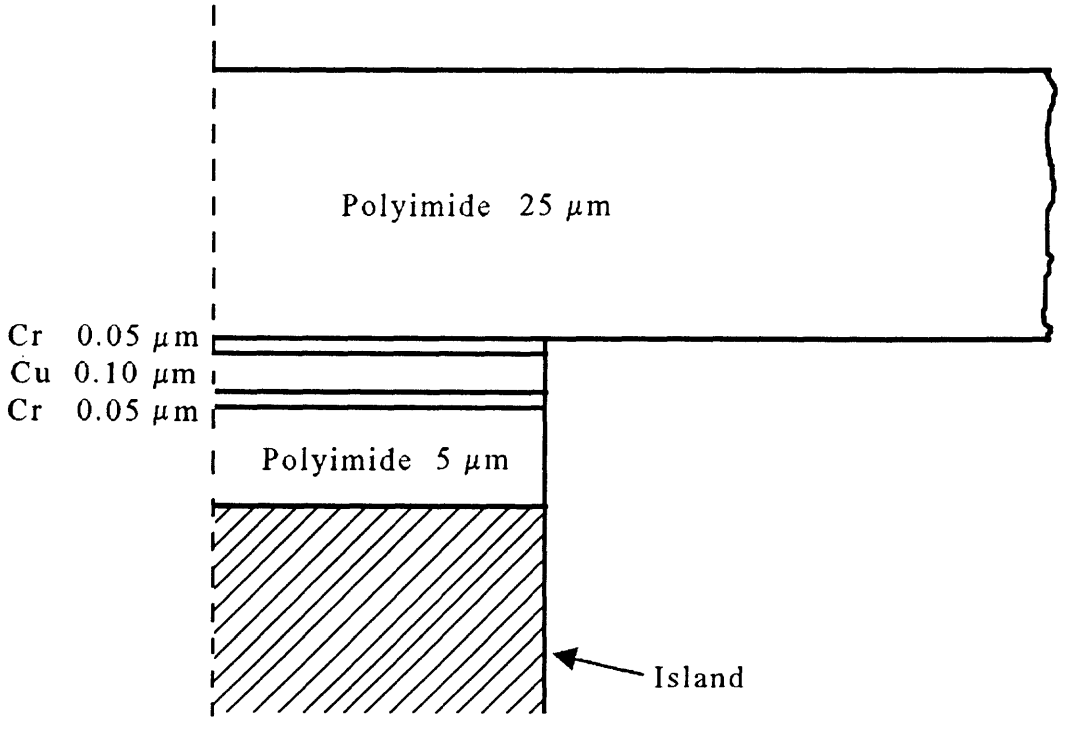

Figure 4.3.2: Alternate structure for metal-on-polymer IBT with polyimide backing layer.

to the backing layer polyimide. At this point, the same problem as found in the first potential solution is encountered - the excessive strains should crack the metal film.

To test the second solution, CrCuCr on PI2545 and CrCuCr on PI2611 samples were built according to Figure 4.3.2. The exact structure shown was used where the adherend polyimide was ~5 μm thick and the backing layer polyimide was the same type as the adherend and was ~25 μm thick. The critical pressure increased as the test proceeded and the inner radius decreased. This behavior is expected to be related to the cracking of the metal film adhered to the bottom of the backing layer, a phenomenon visually observed during testing. One way to minimize the effect of the cracking metal is to use only the first (p_c, r_i) pair measured. The values of γ_{Ic} measured based on this first pair were 3-40 J/m^2 for CrCuCr on PI2611 and 40-100 J/m^2 for CrCuCr on PI2545. The wide scatter of the data is expected to be related to the variable effect of the metal on the back side of the delaminating film. As anticipated, these values are less than those measured for the polyimide on metal structure, where γ_{Ic} was found to be ~175 J/m^2. Better adhesion in the polymer on metal case presumably stems from the fact that the polyimide is applied in the form of a polyamic acid and cured at 350-400°C, allowing it to react chemically with the metal adherend and produce a good bond [132]. In the metal on polymer case, the metal is deposited on the previously cured polyimide which is now relatively inert making chemical bonding less likely.

4.4 Discussion

The most interesting result presented in this chapter is the independence of γ_{Ic} of geometry and shear loading. To provide a context for this finding, the literature whose subject matter is interfacial fracture is reviewed in more detail below. For the simple case of an isotropic body, loaded in one mode only and behaving elastically, the critical stress intensity factor and the associated critical strain energy density serve equally well to predict failure. For such systems, Irwin [100] predicted, "that a crack moves along a path normal to the direction of greatest tension, so that the component of shear stress resolved on the line of expected extension is zero." Irwin is postulating that cohesive, elastic (brittle) fracture is controlled by the level of mode I loading. Erdogen and Sih have demonstrated that mode II and mode III crack extension does not occur in ideally brittle materials [101] substantiating Irwin's prediction. However, our situation is complicated in three ways: (1) the loading mode is mixed, a situation difficult to deal with even for isotropic elastic bodies, (2) the failure is at or near an interfacial failure which may constrain the trajectory of the crack, and (3) the stress in the film may exceed its yield stress over large parts of the film and so the criterion of plastic deformation only local to the crack terminus is not obeyed. This section presents a brief chronological review of the relevant work of previous researchers who addressed the issue of mode mixity in interfacial fracture.

Previous work can be roughly grouped into two categories: (i) work done in the 1970's by Tratina, Williams, Anderson, Chang, *et al.* [102-105] focused on aluminum blocks bonded together with adhesive., (ii) ongoing work by Hutchinson, Thouless, Sou,

Evans, Jensen *et al.* [77-81, 106-109] focused on describing the stress state at the interfacial crack tip using extensive elasticity-based mathematical formulations and decoupling the mode I and mode II components of the specific fracture energy. Comprehensive summaries of these two bodies of work can be found in [30] for the former work and in [106] for the later.

Using finite element displacement and compliance methods to calculate both γ_I and γ_{II} at fracture, Chang [104] used single lap shear joint specimens which allows for varying the ratio of mode I to mode II loading at the interface to show that the adhesive fracture energy for mode II loading is greater than that for a mode I loading. For the case of two pieces of aluminum bonded together using epoxy, a Griffith analysis agreed well under the condition that:

$$\gamma_a = f_I \gamma_{Ic} + f_{II} \gamma_{IIc}$$

where f_I and f_{II} are the fractions of total strain energy attributed to tensile and shear loading respectively.

Trantina used slanted aluminum pieces bonded together with epoxies or other adhesives and created a crack in the adhesive to form a single edge notch (SEN) specimen [103]. The degree of slanting determined the loading mode mix when a tensile stress was applied to the sample. Trantina developed a finite element analysis of such a system that provided the nodal displacements at the crack tip. The mode I and mode II stress intensity factors were calculated directly from the transverse and normal displacements, respectively. The interrelationship between K_I and K_{II} was investigated as a function of varying crack orientation. The critical strain energy density was calculated

independently based on a compliance method. The analysis depends upon satisfaction of the pivotal assumption that this bimaterial composite behaves the same as a homogeneous system. With this analysis, Trantina showed that, (i) the mode I strain energy rate for crack extension increases significantly as the mode II strain energy rate for crack extension increases, (ii) γ_{IIc} is larger than γ_{Ic}, and (iii) that the $\gamma_I + \gamma_{II} = \gamma_c$ failure criteria is not appropriate for the adhesive system.

Bascom [105] looked at same system as Trantina (aluminum-epoxy) at 45° loading and so assumed an equal mix of mode I and mode II loading. Used Trantina's FEM, he investigated the effect of various surface preparations. Failure was found to be primarily interfacial but radio tracing and AES experiments show that it was actually a thin cohesive failure in the adhesive (residual adhesive thickness of 500-8900 A). Using values of the total stress intensity parameter (K) from Trantina's FEM for an angle of 45° and related to it G through $K^2 = GE$, Bascom found a mixed mode fracture energy of 140 J/m^2 compared with 136 J/m^2 for simple opening mode G_{Ic} for the same polymer. The surface roughness of the adherend was found to influence these results in a complex way.

Excessive plasticity and other dissipative mechanisms has been addressed by Chang *et al.* [102] for the case of delamination of a cantilever beam bonded to a rigid substrate. Their analytical solution accounts for plastic bending of the beam by assuming elastic-perfectly plastic behavior but does not include plasticity in the adhesive. Experimental results based on an aluminum beam and structural adhesive provided a

constant value of γ_a even with varying length of cantilever beam. No attempt was made to decouple mode I and mode II contributions.

The work cited thus far was based on adhesives and epoxy bonding structural materials together. More germane to our interests in thin film debonding, Anderson *et al.* [30, 110-111] used the standard blister test to explore the effects of mixed mode loading using a polyurethane elastomer bonded to polymethylmethacrylate (PMMA). Films sufficiently thin could be accurately analyzed using plate theory. Much thicker adherends could be treated as a semi-infinite medium. Analytical solution are available for both cases. The interesting intermediate case required numerical analysis for solutions. The change in strain energy density per increment in surface area (γ_a) in the film is calculated as a function of pressure and geometry. Further work by the same group [30, 110] used finite element modeling to calculate the mode I and mode II components. Applying this model to the experimental system of polyurethane on PMMA, they found that γ_a increased as the mode II contributed increased. Although dissipative mechanisms were assumed negligible, the authors suggest that this trend may be caused by more extensive crack tip plasticity or viscoelasticity in the presence of a larger mode II component. Another explanation was based on differences in fracture surface area as loading mode is changed. Rougher fracture surface topographies were found using SEM analysis for cases of increased shear mode contributions. The definition of γ_a is based on the *projected* area of the created crack surface and therefore does not account for surface roughness.

Cao and Evans [108] worked with a variety of test geometries to effect a range of phase angles using glass plates and rods bonded to aluminum with a brittle adhesive. Invoking an elasticity based analysis, they found the critical strain energy release rate to increase with increasing phase angle. More mode II loading translated into higher measured values of γ_c. They note that this trend is in agreement with a simple contact zone model proposed by Evans and Hutchinson [77] but could also be due to crack tip blunting and plasticity.

Analyzing a cut in an adhered film under equal biaxial stress, Jensen *et al.* [107] specify a phenomenological interfacial fracture criteria as:

$$\gamma_C = \frac{1}{2}\left(\frac{1-\upsilon^2}{E} + \frac{1-\upsilon_s^2}{E_s}\right)\left(K_I^2 + \lambda_2 K_{II}^2\right) + \frac{\lambda_3}{4}\left(\frac{1}{\mu} + \frac{1}{\mu_s}\right)K_{III}^2 \qquad [4.4.2]$$

where K is the stress intensity factor, E is the elastic modulus, ν is Poisson's ratio, μ is the shear modulus, λ_2 and λ_3 range from 0 to 1 and scale the effect of the shearing modes on delamination. The subscript *s* refers to the substrate material. The analysis does not account for dissipative mechanisms, assumed to be minimal in the absence of any externally applied tractions. Preliminary investigation by the authors with polyimide on glass and by Cao and Evans [108] with epoxy on glass substantiate the results of the analysis if $\lambda_2 = \lambda_3 = 0.15$. The λ parameters are used to fit the data and are not able to be predicted *a priori*. The data of both groups of workers show an increase in γ_C for larger phase angles ψ. The magnitude of the γ_C values ranged from 5-20 J/m^2 for the epoxy on glass case.

The studies by Jensen *et al.* [107] and Cao and Evans [108] are representative of the type of work that has been done by the second group of researchers mentioned at the beginning of this section. Other examples can be found in [78-82]. Universal among them all is the assumption of dissipative mechanisms limited to the terminus of the debond.

In summary, the previous work reviewed above can be categorized in different ways. The first grouping is by application: work that involved epoxies and adhesives bonding structural pieces together and work with thin film systems. The second grouping is by assumptions made in the analyses: work that separated the individual mode I and mode II contributions but did not account for dissipative mechanisms and work that did not decouple the different modes of loading but did incorporate dissipative mechanisms. Overall, the surveyed literature has not demonstrated that the mode I dependency of cohesive, elastic fracture in homogeneous systems is directly translatable to thin adhered films under residual stress and experiencing significant dissipative work expenditures. To the contrary, the work reviewed found that the addition of the shear modes generated higher values of γ_a than in the presence of pure mode I loading conditions. Therefore, the result from the present work that the criterion for fracture is the obtainment of a critical value of the mode I component of the specific fracture energy (γ_{Ic}) appears to be an original result for well-adhered thin film systems. The original hypothesis of Irwin shown to be true for cohesive fracture in homogeneous elastic bodies has been regained for interfacial fracture in the presence of extremely plastic dissipation and residual film stresses.

A cursory study of a representative metal on polymer system was presented. Cracking of the adhered metal film during testing due to the high strains generated in the vicinity of the crack tip was both anticipated and experienced. The only viable solution suggested was to use a thick (25 μm) polymer backing layer and to etch the metal off the bottom of this layer prior to testing. In this case, the first set of critical pressure, inner radius measurements taken provides the best estimate of γ_{Ic}. The lower modulus of the polymer adherend is expected to result in significant deformation of the adherend during testing. Accurate analysis of this behavior may require modification of the FEM. An initial attempt could involve modeling the adherend as a single row of elements in the same way the adhered film is represented.

Chapter 5: Locus of Failure Analysis

This chapter reports on the application of surface analysis techniques to the investigation of the locus of failure in IBT and peel samples. The ultimate goal is to correlate these results with the adhesion data in an attempt to explain variations in specific fracture energy. Accurate determination of the location of fracture in the system is an important part of developing this understanding. The fracture surfaces of IBT and peel test samples were analyzed using X-ray photoelectron spectroscopy (XPS) and Auger electron spectroscopy to determine the identities and bonding states of species present, and scanning electron microscopy (SEM) to examine the topography of the fracture surfaces.

Polymer-on-metal systems, including HFDA-APBP, PMDA-ODA, and BPDA-PDA each on Cr and Al, are explored. Both the film side and the substrate side of the failure are analyzed. Specific fracture energy data generated from IBT and peel testing of Ultradel 4212, PI2545, and PI2611 to both Cr and Al are summarized in

Table 5.1.1: Summary of polyimide to metal adhesion data. The thickness of the adhered film is given in parenthesis for peel test samples.

Polyimide	Substrate Coating	IBT (FEA) γ_{Ic} (J/m^2)	Peel Test γ_a (J/m^2)
HFDA-APBP (Ultradel 4212)	Cr (good)	100	425 (19 μm)
	Cr (poor)	54	-
	AlCr	32	105 (19 μm)
PMDA-ODA (PI2545)	Cr	175	180 (15 μm)
	Al	28	-
	AlCr	17	90 (15 μm)
BPDA-PDA (PI2611)	Cr	145	530 (32 μm)
	AlCr	27	380 (37 μm)

Table 5.1.1. As shown in Chapter 4, IBT results are independent of film thickness. Peel test data is given for film thicknesses similar to those used for the IBT. In all cases, adhesion to Cr is superior to adhesion to Al.

5.1 Introduction

X-ray photoelectron spectroscopy (XPS) was applied extensively in this work to investigate the chemical environment of fracture surfaces created by the IBT and the peel test. This brief introductory section serves to explain the basic principles of the technique, to examine the advantages and disadvantages of the technique relative to the problem at hand, and to describe the details of the experimental set-up used in this work.

XPS involves irradiating the sample with monochromatic x-rays and analyzing the energies of the electrons expelled from the surface. This activity is governed by the relationship:

$$KE = h\nu - BE - \varphi$$

were KE is the kinetic energy of the released electron, BE is the initial binding energy of the electron, h is Planck's constant, ν is the energy of the monochromatic incident x-rays, and φ is the "work function", a correction factor dependent on the specific spectrometer and sample [112]. The $h\nu$ and φ terms are accounted for by an automated program and can be treated as constants. The electron binding energy, and therefore the kinetic energy measured at the spectrometer, is solely a function of the bonding environment of the parent atom.

Electrons traveling through solids experience much inelastic scattering which reduces their KE. Consequently, only electrons originating from the outermost layers

reach the spectrometer with their characteristic energy (BE). Electrons which suffer inelastic losses contribute to the background. This scattering of electrons makes the technique very surface sensitive, typically providing information about only the top several monolayers of the surface. The information sampling depth is a function of the take-off-angle (TOA), the angle formed by the incident beam and the plane of the sample.

Different bonding configurations (e.g. C-O vs. C=O bonds) involve distinct energy levels, allowing them to be distinguished based on their positions in the XPS spectrum. The technique's sensitivity to bonding environments enables the detection of reactions. Reaction of metal atoms with a polymer to create a new metal-polymer primary bond will be evidenced by the formation of a new peak in the XPS spectra. The limitation here is that in a complex polymer that has carbon or other atoms in several types of bonding arrangements, the separation of peaks representing those different configurations may be so small as to challenge the technique's ability to definitively resolve them. This is especially true with polyimides, which have carbon atoms in a variety of bonding arrangements.

It is the ability of XPS to identify chemical compositions and stoichiometries, to distinguish among bonding configurations for any given element, and thereby to perceive the formation of new binding arrangements possibly due to reactions, that makes XPS an excellent forensic technique in investigating fracture surfaces. For these reasons it is applied here to analyze both the film and adherend sides of the fracture. Figure 5.1.1 illustrates the terminology applied to the various fracture surfaces explored in this section.

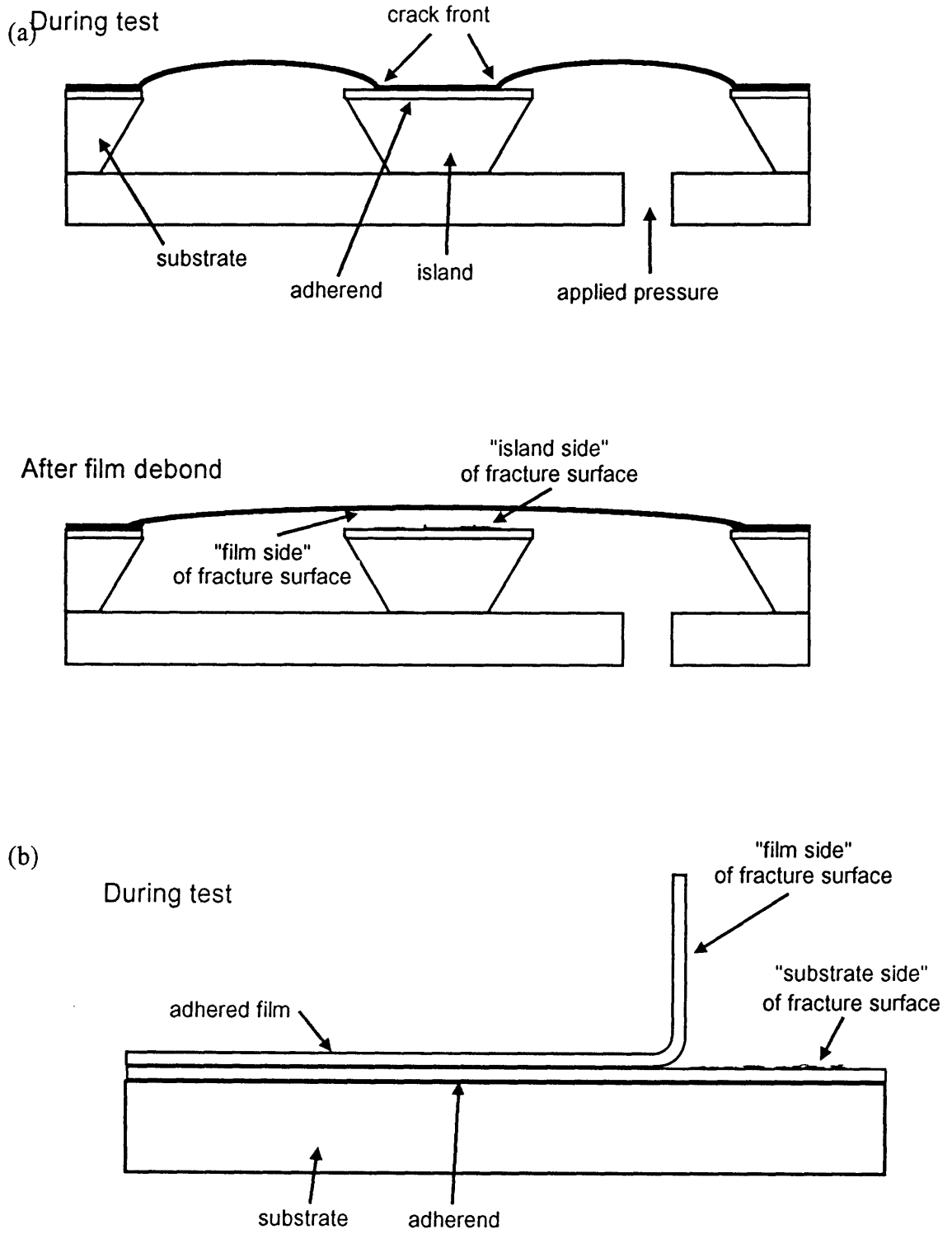

Figure 5.1.1: Schematic of fracture surface terminology: (a) island blister test, and (b) peel test.

The XPS spectra presented in the remainder of the chapter were generated mostly using a Surface Science Instruments SSX-100 ESCA spectrometer located at the East Fishkill, NY facility of the IBM Microelectronics Division[1]. Some of the spectra were generated with Dr. Pradnya Nagarkar using the same model tool at the joint MIT-Harvard surface science facility (XPS located at Harvard University). In both cases, monochromatic Al Kα x-rays ($h\nu$ = 1486.6 eV) at a TOA of 60° were used. The gun energy was calibrated using the C (1s) level of carbon bonded to itself or hydrogen (285.0 eV) [112]. For each sample, the film and the substrate sides of the failure were analyzed. Non-conducting samples were flooded with 3-5 eV electrons to provide charge compensation. Unfortunately, most samples were exposed to ambient laboratory conditions for several weeks prior to XPS analysis, allowing for contamination. Table 5.1.2 summarizes the parameters used for the various scans.

Table 5.1.2: XPS scan parameter set.

Element	Range (eV)	# Scans	Resolution	Spot Size (μm)
survey	0-1000	1	4	1,000
C (1s)	275-295	5	2	600
N (1s)	390-410	5	2	600
O (1s)	525-545	5	2	600
F (1s)	675-695	5	2	600
Cr (2p)	560-580	5	2	600
Al (2p)	63-83	5	2	600

Spectral envelopes are deconvolved into constituent peaks using computerized routines. All peaks were constrained to be 100% Gaussian; Chi-squared values were

[1] The assistence of Dr. Howard Clearfield in training on the XPS tool at IBM is gratefully acknowledged.

typically 1.5-2.5 (1.0 represents a perfect fit). The outcome of these fitting routines is somewhat sensitive to the number of peaks selected and to the initial positioning of these peaks, both of which are set by the operator. Allen is correct in noting that confidence in results is obtained only through self-consistency across a broad spectrum of data [49].

5.2 HFDA-APBP on Metals

This section presents data from XPS analyses of fracture surfaces created by debonding Ultradel 4212 films from Cr and Al metallized wafers. The loci of failure on IBT samples are compared to peel samples and the effects of processing history on γ_{Ic} for Ultradel-on-Cr samples are investigated.

5.2.1 HFDA-APBP Reference Spectra

The repeat unit of HFDA-APBP is shown in Figure 5.2.1 (a) with all of the carbon bonds numbered for easy reference. Table 5.2.1 summarizes peak assignments by Nagarkar [113] (column 3) and the reference spectra generated in this work (column 4). The final column presents molecular modeling results for the carbon (1s) spectrum and experimental results for the oxygen (1s), nitrogen (1s), and fluorine (1s) spectra from Buchwalter *et al.* [114]. In this table, as well as similar ones that follow, carbon (1s) positions are referenced relative to the phenyl carbon at 285.0 eV with the relative intensity given in parenthesis. For example, the peak representing the carbonyl carbon in the reference spectrum is positioned at +4.0 (= 289.0 eV) and accounts for 6% of the total *carbon (1s)* intensity. The reference spectrum shown in column 3 of Table 5.2.1 was generated from a thick spin-cast coating, cleaned by abrasion with a stainless steel razor blade just prior to introduction into the XPS chamber to remove any surface

(a)

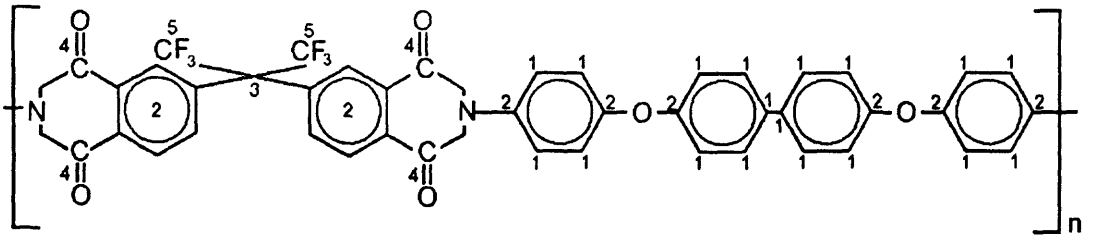

Amoco Ultradel™ UD4212 (HFDA-APBP)

(b)

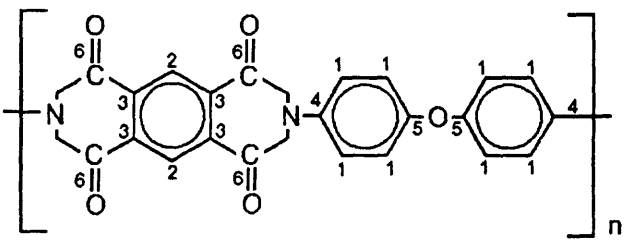

DuPont Pyralin™ PI2545 (PMDA-ODA)

(c)

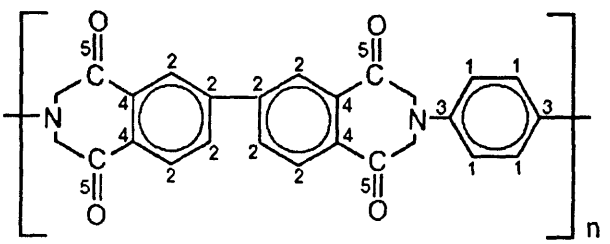

Dupont Pyralin™ PI2611 (BPDA-PDA)

Figure 5.2.1: Chemical repeat units of the polyimides investigated: (a) HFDA-APBP, (b) PMDA-ODA, (c) BPDA-PDA.

contamination. This technique has been found to provide a very clean surface for XPS [115] and was used to create all reference surfaces analyzed. The actual envelopes for the reference spectra are shown in Figure 5.2.2 (a-d). Film stoichiometry is very close to theoretical (Table 5.2.3) and, overall, the reference spectra generated in the present work agree well with the results of the previous researchers [113, 114].

Table 5.2.1: Peak assignments and energies for HFDA-APBP reference spectra.

Atom	Association	Nagarkar[113]	Reference	Theoretical
C	1. **C**-H^{APBP}	285.0 (37)	285.0 (46)	285.0 (41.9)
	2. **C**-O, **C**-N, **C**-H^{HFDA}	+1.0 (42)	+1.0 (32)	+0.9 (41.9)
	3. alpha **C**	+2.2 (2)	+2.0 (10)	+2.4 (2.4)
	4. **C**=O	+4.0 (8)	+4.0 (6)	+3.7 (9.5)
	π-π^*	+6.7 (4)	+6.9 (2)	-
	5. **C**-F	+8.6 (7)	+8.7 (4)	+7.4 (4.8)
N	C-**N**	400.9	401.1	400.8 (100)
O	C=**O**	532.3 (58)	532.5 (80)	532.2 (66.7)
	C-**O**	+1.4 (42)	+1.4 (20)	+ 1.4 (33.3)
F	C-**F**	688.6	689.2	688.8 (100)

5.2.2 HFDA-APBP on Chromium

The primary goal of the work presented in this section is to determine the locus of failure in Ultradel 4212-on-Cr IBT and peel samples. Table 5.1.1 indicates a difference in γ_{lc} between Cr films labeled "poor" and "good". Subtle changes in the sample fabrication process can result in significant changes in the mechanical functionality of the system. In general, it is best to strive to maintain the purity of any interface during fabrication [116-118]. Evaporation using source material that is not highly oxidized,

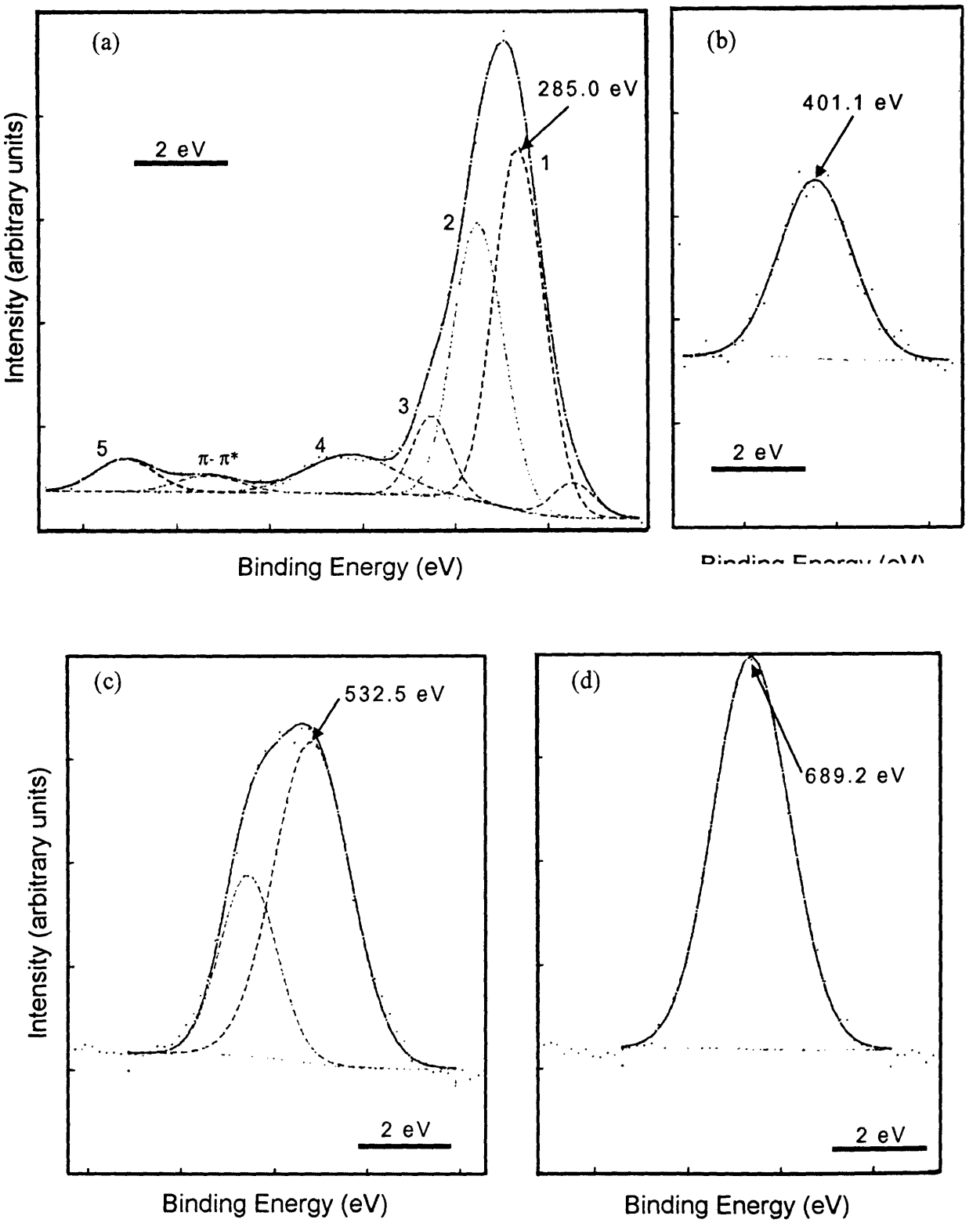

Figure 5.2.2: HFDA-APBP reference spectra: (a) carbon 1s, (b) nitrogen 1s, (c) oxygen 1s, (d) flourine 1s.

preheating the substrate *in vacuo* (better than $3x10^{-6}$ torr) and, applying the polyimide within one hour of removal of the wafer from the evaporation chamber are all expected to promote a high quality polymer-on-metal interface and to provide the optimum in adhesion. A low quality Cr film can be the product of any of the following processing conditions: high pressure during evaporation (e.g. > $3x10^{-6}$ torr), no *in situ* substrate preheat prior metal deposition, a long time period between Cr evaporation and polyimide application, or the use of highly oxidized or insufficiently replenished source material for the Cr evaporation. Such conditions are expected to result in excessive oxidation or contamination of the Cr surface prior to application of the polymer coating, causing poorer film adhesion. It is a further goal of this section to determine whether the condition of the polyimide at the locus of failure provides any explanation for the degradation in adhesion as a function of these processing conditions.

Ultradel on "High Quality" Chromium

Columns 5 and 6 of Table 5.2.2 summarize the peak assignments and intensities for the case of HFDA-APBP cure on "high quality" Cr. The reference data (column 7) are taken from Table 5.2.1. The carbon (1s) spectrum of the island is very similar to that of the film (Figure 5.2.3) and both are similar to the reference spectrum. Several weeks elapsed between testing of the samples and the XPS analysis allowing for contamination with adventitious carbon. These hydrocarbons have a binding energy of 284.6 eV [119] and, hence, are indistinguishable from the phenyl carbon peak at 285.0 eV. This may explain why the peak at 285.0 eV is more intense than theory predicts.

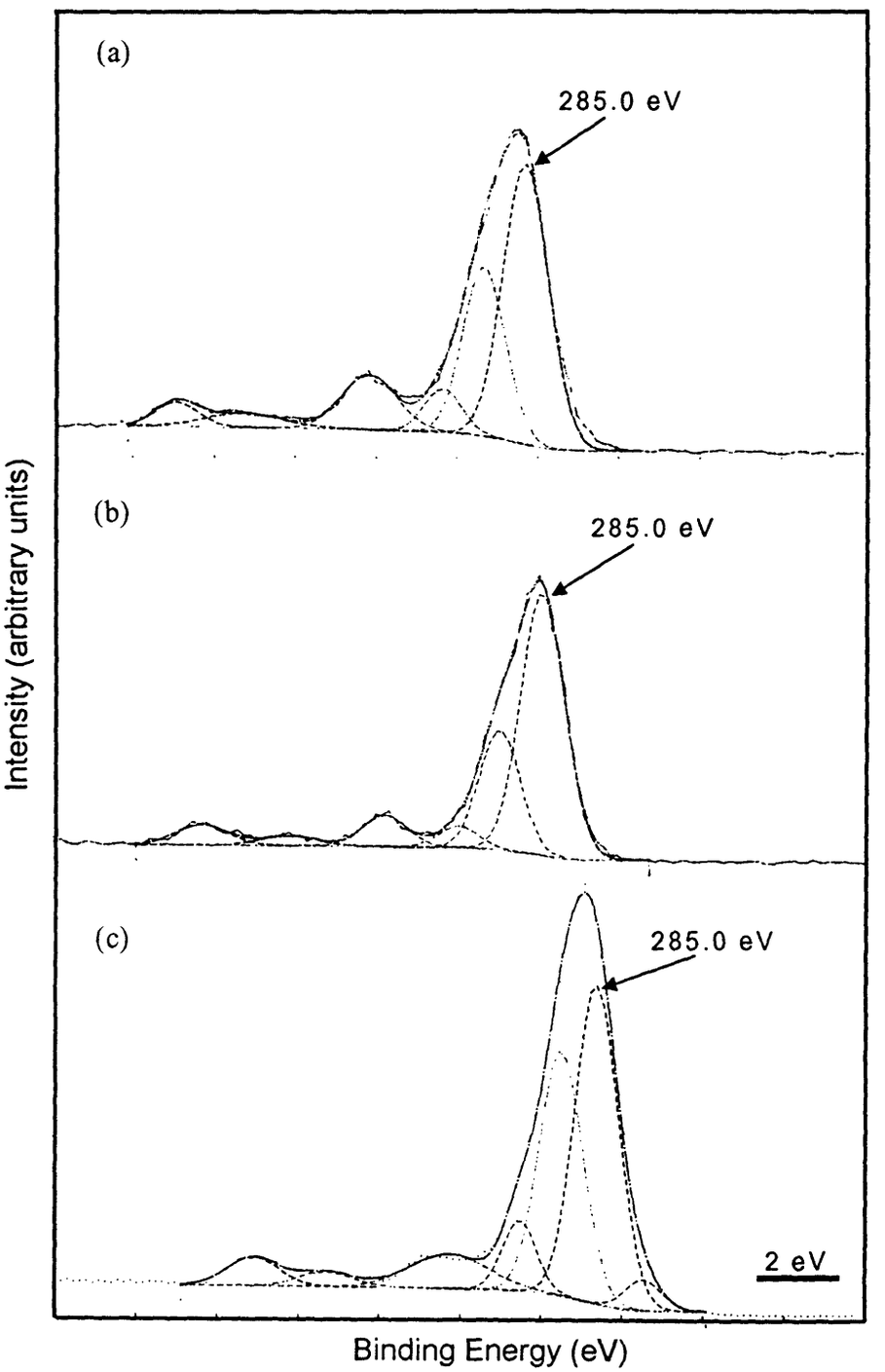

Figure 5.2.3: Carbon (1s) spectra of HFDA-APBP on "high quality" Cr: (a) film side of IBT fracture, (b) island side of IBT fracture, (c) reference spectrum.

The oxygen (1s) envelope is deconvolved into three peaks for both the island and the film sides of the fracture surface. Both show the carbonyl and ester oxygen peaks. The film side has an additional high energy peak at too high a bonding energy to be related to oxygen, but corresponding exactly to the Auger peak for sodium, a very typical contaminant. Another possibility is that this broad peak (FWHM=2.3 eV) represents the π-π^* shake-up, a phenomenon found by others to occur in the oxygen spectrum of polyimides [120]. The island side contains a peak centered around 530.6 eV

Table 5.2.2: Peak assignments and energy levels for HFDA-APBP on Cr. Peak positions with relative intensity in parenthesis are listed. The Cr reference data shown in brackets is taken from [121].

Atom	Association	Film (poor Cr)	Island (poor Cr)	Film (good Cr)	Island (good Cr)	Reference
C	?	-1.1 (2)	-	-	-	-1.1 (3)
	1. **C**-H ^{APBP}	285.0 (18)	285.0 (21)	285.0 (48)	285.0 (57)	285.0 (42)
	2. **C**-O, **C**-N, **C**-H^{HFDA}	+1.2 (18)	+1.3 (20)	+1.0 (27)	+1.1 (24)	+0.9 (33)
	3. alpha **C**	+2.2 (36)	+2.4 (40)	+2.1 (6)	+2.1 (4)	+1.9 (7)
	4. **C**=O	+3.1 (15)	+3.5 (5)	+3.9 (11)	+3.9 (7)	+3.5 (8)
	5. π-π^*	+4.9 (11)	+5.0 (14)	+7.0 (4)	+6.3 (3)	+6.7 (3)
	6. **C**-F	-	-	+8.6 (4)	+8.4 (5)	+8.5 (4)
N	C-**N**	400.2	400.3	400.9	400.4	400.8
O	Cr_2O_3	-	531.1 (18)	-	530.6 (14)	[530.3-530.8]
	C=**O**	532.8 (49)	533.0 (39)	532.4 (51)	532.2 (53)	532.6 (71)
	C-**O**	+1.6 (51)	+1.5 (43)	+1.4 (35)	+1.4 (33)	+1.4 (29)
	π-π^* (?)	-	-	+3.8 (14)	-	-
F	C-**F**	688.8	687.6	689.1	689.1	689.0
Cr	**Cr**$_2$O$_3$ ($2p_{3/2}$)	-	576.6 (69)	-	576.6 (66)	[576.6 (67)]
	Cr$_2$O$_3$ ($2p_{1/2}$)	-	+9.9 (31)	-	+9.9 (34)	[+9.7 (33)]

corresponding to the Cr_2O_3 oxygen peak, found by other researchers to be located in the range of 530.3-530.8 eV [121]. The nitrogen (1s) and fluorine (1s) spectra for film and

island exhibit one peak each, corresponding to the imide nitrogen and the CF_3 fluorine respectively. Only the island side demonstrates the presence of chromium. The location and separation of the two peaks in the doublet of the Cr (2p) envelope indicates that the chromium is present as an oxide and not the pure metal. Doublets of the p-orbital are expected to have an intensity ratio of 2:1 ($2p_{3/2}$:$2p_{1/2}$) [112], exactly as found experimentally.

The overall film stoichiometry is shown in row 3 of Table 5.2.3. The film and island both exhibit nearly stoichiometric amounts of the polyimide constituents, and a small amount of Cr (0.2 at %) is found on the island side. The data presented above suggest that in this system, the fracture occurs almost exclusively by cohesive failure in the polymer. The small amount of Cr_2O_3 on the island may be evidence of some minute percentage of adhesive fracture, perhaps due to very localized contamination or excessive oxidation Observation of the island side of the fracture surface under high magnification scanning electron microscopy (SEM) reveals a featureless planar surface; there is no indication of the topography expected to be associated with a mixed mode fracture. Alternatively, the residual polyimide on the island could be thin enough to allow some very weak Cr signal through. However, for this latter possibility, the residual layer would have to be less than ~30 A in thickness.

Table 5.2.3: Stoichiometry of HFDA-APBP systems. The columns labeled C, O, N, and F show the relative percentages of these elements detected based on a total amount of 100. The Cr and Al give the atomic percentages of these elements present.

Sample	Test	C	N	O	F	Cr	Al
Theoretical	-	75.4	3.5	10.5	10.5	0	0
Reference	-	76	4	13	8	0	0
UD4212-Cr (film)	IBT	76	3	11	10	0	0
UD4212-Cr (island)	(good Cr)	76	4	12	8	0.2	0
UD4212-Cr (film)	IBT	79	6	14	1	0	0
UD4212-Cr (island)	(poor Cr)	64	10	24	2	6	0
UD4212-Cr (film)	Peel	75	2	16	7	0	0
UD4212-Cr (substrate)		71	3	17	9	7	0
UD4212-AlCr (film)	IBT	78	4	10	9	0	0
UD4212-AlCr (island)		55	2	28	15	0	40
UD4212-AlCr (film)	Peel	80	3	11	7	0	0
UD4212-AlCr (substrate)		53	2	36	10	0	41

Ultradel on "Low Quality" Chromium

The chemistry of the fracture surface from HFDA-APBP on poor quality Cr is quite different from the polymer on high quality Cr case. Table 5.2.2 summarizes the peak intensities for the low quality case in columns 3 and 4, based on which the following observations are drawn. The positioning of the imide N peak at 400.8 eV in the nitrogen (1s) spectrum, the CF_3 peak at 688.8 eV in the fluorine (1s) spectrum, along with the carbonyl and ester peaks in the oxygen (1s) spectrum, suggest of the presence of polyimide. Figure 5.2.4 shows the carbon (1s) envelope from the low quality sample for both the film (a) and the island (b) sides of the fracture. In both cases, the high BE fluorine-related peak is completely missing and the distribution of peak intensities under the main envelope is very different than the reference spectrum. Even in the fluorine (1s) spectrum the signal is very weak, accounting for only 1-2% of the total stoichiometry

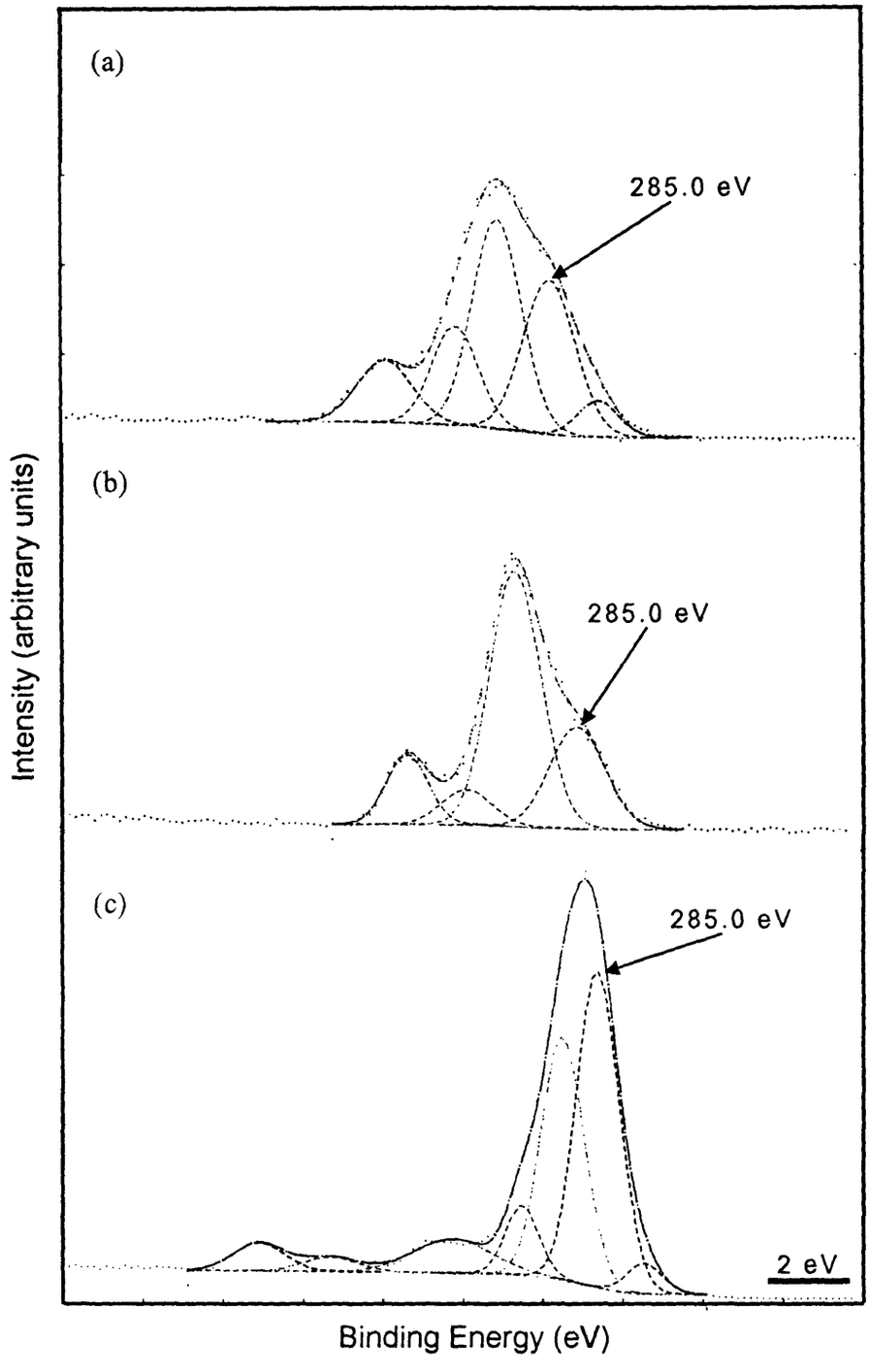

Figure 5.2.4: Carbon (1s) spectra of HFDA-APBP on "low quality" Cr: (a) film side of fracture, (b) island side of fracture, (c) reference spectrum.

(Table 5.2.3). The fluorine deficiency is consistent with the observations of Nagarkar who has noted a depletion of fluorine at Ultradel-metal interfaces, presumably due to a reaction that forms metal fluorides [122]. No Cr is found on the film side.

A more significant amount of Cr (~6 at %) is present on the island side, but it matches the spectrum for the oxide Cr_2O_3 (at 576.6 eV) rather than the fluoride (at 581.0 eV). The island side oxygen (1s) spectrum has an additional peak accounting for ~15% of total oxygen intensity, located approximately where the Cr_2O_3 peak is expected. In summary, it appears that the fracture primarily occurs cohesively in an interphase which may be either polyimide modified by the reaction with metal, or contaminated polyimide, with some adhesive fracture accounting for the small amount of Cr present. The major differences between this and the high quality Cr case are, (1) the broader main carbon 1s envelope with the different distribution of peak intensities, (2) the absence of the F peak in this spectrum, and (3) the presence of a higher percentage of Cr and, therefore, presumably more of an adhesive failure component. The XPS results are repeatably achieved on samples processed at different times but under similar "low quality" conditions. Under SEM examination, fracture surfaces appear featureless and indistinct, whether from high or low quality samples

These observations provide an explanation of the lower γ_{Ic} measured in the low quality Cr case. "Low quality" processing conditions which promote excessive oxide growth or contamination of the interface would hinder reaction of the fluorine functionality with the chromium metal and degrade adhesion. Working with glass-fiber-filled Teflon, Park [123] found that the formation of CrF_3 was critical to achieving good adhesion of the polymer to Cr coated copper foil, supporting this

possibility. Applying this hypothesis to the case of "high quality" Cr, the fluorine-chromium reaction is expected to take place creating a solid interface. Failure is then pushed up into the polyimide, which is now the weakest point in the system, consistent with the near pristine polyimide signal found on each side of the fracture. Consumption of the fluorine through creation of a metal fluoride might be expected to result in a fluorine deficiency on the island side which is not experienced. It could be that the fracture occurs far enough removed into the polyimide to mask this modified interphase.

Fracture Surfaces from the Peel Test

The fracture surfaces of peel test samples were also analyzed, and these results are shown in Table 5.2.4. The samples were fabricated under "high quality" conditions except for the lack of substrate preheat *in situ* to the metal evaporation. On the substrate side of the fracture, the phenyl peaks of the carbon (1s) envelope, shown in Figure 5.2.5 (b), are broader than the reference and the spectrum exhibits no fluorine related peak similar to the "low quality" Cr IBT case, although there is fluorine present (refer to Table 5.2.3). An additional low energy peak is also present in the C (1s) spectrum. Such peaks have been frequently seen by previous researchers and are suspected to be manifestations of residual solvent in the film. Others use peaks that are only partially Gaussian for deconvolution, often obviating the need to fit an additional low energy peak [135]. No consensus on its origin currently exists. This pervasive peak occurs not only in the carbon (1s), but also occasionally the nitrogen (1s) and the oxygen (1s) spectra of all the polyimides investigated. It does not appear to be related to the locus of failure and so

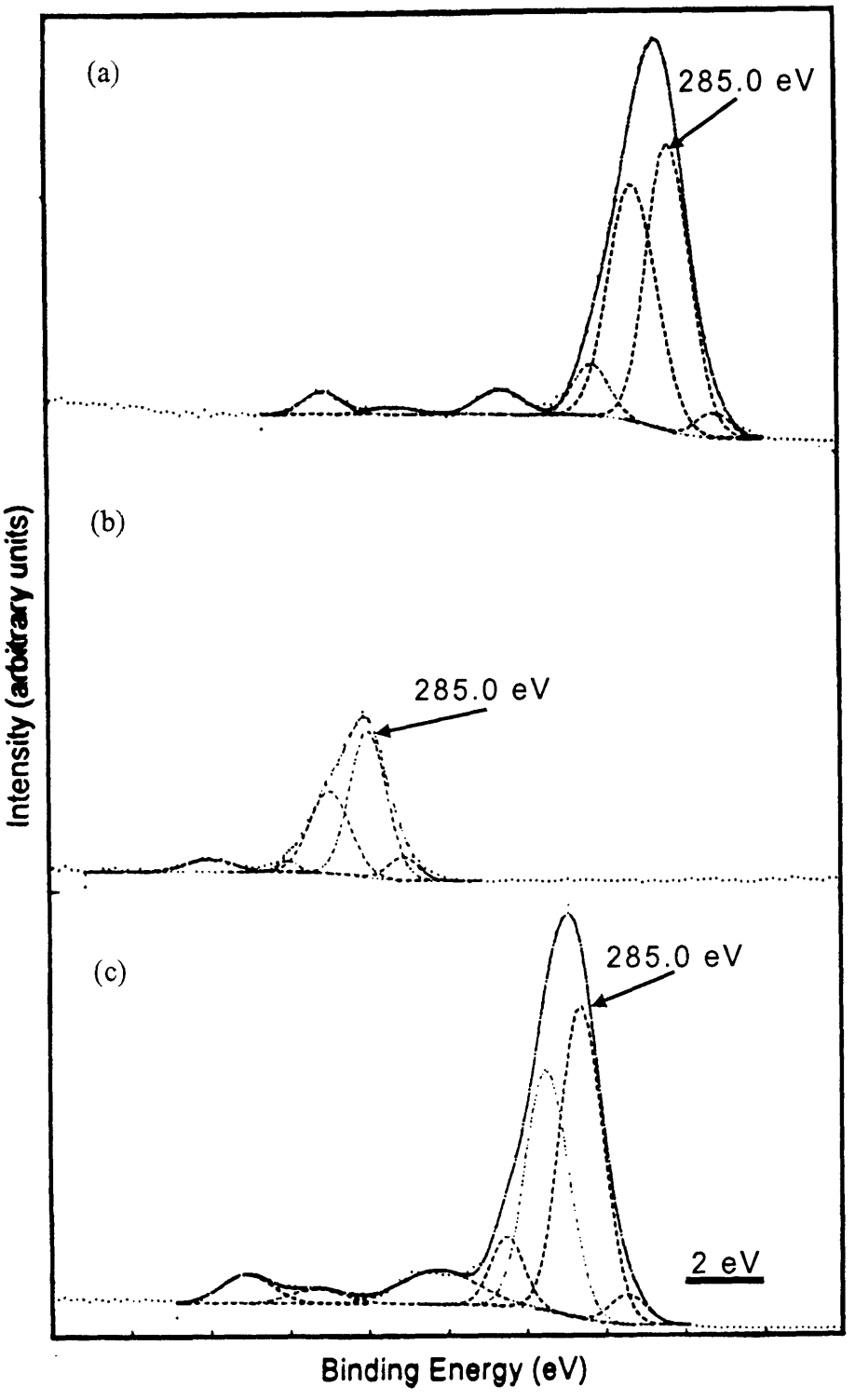

Figure 5.2.5: Carbon (1s) spectra of HFDA-APBP on Cr: (a) film side of peel fracture, (b) substrate side of peel fracture, (c) reference spectrum.

will not be mentioned hereafter. The positions of the peaks in the Cr (2p) spectrum are close to those of Cr_2O_3, but are too low in energy for the possibility of CrF_3 being present. For this compound, the Cr ($2p_{3/2}$) peak is around 580.1 eV.

The film side of the peel fracture is very similar to the pristine polyimide as represented by the reference spectra. No metal species are present. The XPS spectra are also very similar to the analogous ones taken from the film side of the "high quality" Cr IBT sample. The film and the substrate data together suggest that failure is primarily cohesive in the slightly degraded polymer with about the same amount of adhesive failure as seen in the "low quality" IBT sample.

Table 5.2.4: Peak assignments and energy levels for HFDA-APBP on Cr from peel test fracture surfaces. Peak positions are listed with relative intensity in parenthesis. The Cr reference data shown in brackets are taken from [121].

Atom	Association	Film	Island	Reference
C	?	-1.1 (3)	-0.9 (7)	-1.1 (3)
	C-H^{APBP}	285.0 (43)	285.0 (53)	285.0 (42)
	C-H^{HFDA}, **C**-O, **C**-N	+0.9 (40)	+1.0 (33)	+0.9 (33)
	alpha **C**	+2.0 (6)	+2.1 (2)	+1.9 (7)
	C=O	+4.3 (4)	+4.0 (6)	+3.5 (8)
	π-π^*	+7.0 (1)	-	+6.7 (3)
	C-F	+8.8(3)	-	+8.5(4)
N	C-**N**	401.2	400.9	400.8
O	Cr_2O_3	-	530.5 (7)	[530.3-530.8]
	C=**O**	532.5 (76)	532.0 (58)	532.6 (71)
	C-**O**	+1.2 (24)	+1.5 (35)	+1.4 (29)
F	C-**F**	688.2	689.1	689.0
Cr	Cr_2O_3 ($2p_{3/2}$)	-	577.5 (67)	[576.6 (67)]
	Cr_2O_3 ($2p_{1/2}$)	-	+9.5 (33)	[+9.7 (33)]

The XPS data from the peel sample seem to fall in between the extremes represented by the "low" and "high" quality IBT samples. The lack of the fluorine related peak and the broader low BE peaks in the C (1s) spectrum of the substrate side of the fracture, along with the matching amount of Cr present is similar to the "low quality" sample. The generally good quality of the carbon (1s) spectrum and the more accurate location of the N, F, and O peaks, especially on the film side, indicate less degradation or contamination, reminiscent of the "high quality" sample. These observations are consistent with the processing history of the peel sample, which satisfies most but not all of the criteria for a high quality interface.

5.2.3 HFDA-APBP on Aluminum

Fracture surfaces from the IBT and peel tests of Ultradel 4212 on an AlCr bilayer (1000/50 nm) were analyzed using XPS. Peak position and intensity data are summarized in Table 5.2.5. All Ultradel-on-AlCr samples were processed under "high quality" conditions, except for the lack of substrate preheat prior to metallization. The presence of ~40 atomic % aluminum on the island side (Table 5.2.3) indicates a mixed mode fracture with nearly equal amounts of adhesive and cohesive failure.

On the island side of the IBT, the carbon (1s) spectrum is missing the fluorine-related peak, the carbonyl peak is more deficient than usual, and the peaks in general are somewhat broader than the reference ones (Figure 5.2.6 (a)). The absence of the fluorine peak may be related to the failure's proximity to the metal interface, again in accordance with Nagarkar's previous observations [122]. If this were the case, the aluminum (2p) envelope would show the presence of a fluoride at ~76.1 eV. Figure 5.2.7 (a) shows a peak 75.9 eV accounting for one third of the total intensity, illustrating

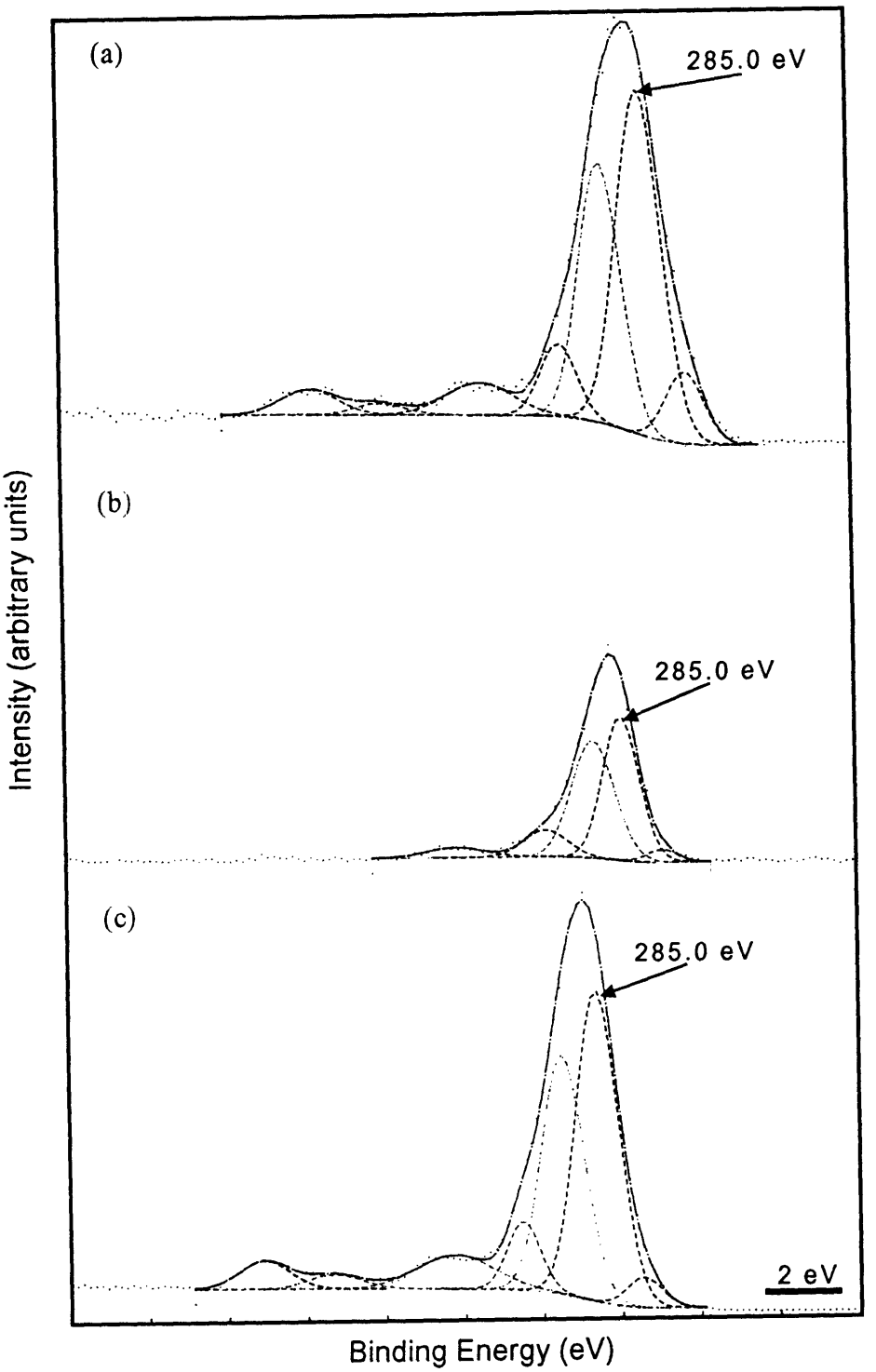

Figure 5.2.6: Carbon (1s) spectra of HFDA-APBP on AlCr: (a) film side of IBT fracture, (b) island side of IBT fracture, (c) reference spectrum.

that this is indeed the case. The two other peaks correspond to an oxide (74.8 eV) and the pure metal (72.5 eV). The oxygen (1s) envelope is deconvolved into three peaks, the additional one at low BE related to the aluminum oxide. The fluorine spectrum shows two additional peaks, whose positions are approximately correct for a metal fluoride and oxyfluoride.

Table 5.2.5: Peak assignments are energy levels for HFDA-APBP on AlCr. Peak positions with relative intensities in parenthesis are listed. The reference data for Al shown in brackets are taken from [119].

Atom	Association	IBT (film)	IBT (island)	Peel (film)	Peel (substrate)	Reference
C	?	-1.1 (8)	-1.0 (3)	-	-1.2 (17)	
	C-H^{APBP}	285.0 (43)	285.0 (42)	285.0 (65)	285.0 (50)	285.0 (41.9)
	C-H^{HFDA},**C**-O **C**-N	+1.1 (31)	+0.7 (41)	+1.0 (17)	+0.8 (19)	+0.9 (41.9)
	alpha **C**	+2.1 (7)	+1.9 (10)	+1.9 (5)	+1.9 (7)	+2.4 (2.4)
	C=O	+4.1 (6)	+4.2 (5)	+3.8 (6)	+3.9 (7)	+3.9 (9.5)
	π-π^*	+6.7 (2)	-	+6.3 (3)	-	-
	C-F	+8.4 (4)	-	+8.3 (4)	-	+8.6 (4.8)
N	C-**N**	400.8	400.9	400.6	400.7	400.9
O	Al-**O**	531.6 (20)	531.5 (51)	530.9 (5)	530.9 (17)	[531.6]
	C=**O**	532.8 (53)	532.8 (40)	532.4 (63)	532.1 (44)	532.2 (66.7)
	C-**O**	+1.2 (27)	+1.3 (9)	+1.4 (32)	+1.1 (34)	+1.4 (33.3)
F	Al-**F**	-	-2.8 (82)	-	-2.5 (52)	-
	C-**F**	689.2	689.2 (18)	688.8	688.8 (48)	688.8
Al	**Al**	-	72.6 (21)	-	-	[72.3-72.8]
	Al-O	-	75.3 (47)	-	74.8 (87)	[74.0-74.7]
	Al-F	-	75.9 (32)	-	76.2 (13)	[~76.1]

The film side carbon (1s) envelope shows all of the polyimide peaks, including the fluorine-related one (Figure 5.2.6 (a)). The oxygen (1s) spectrum exhibits a small peak corresponding to aluminum oxide, although no aluminum peaks were found.

Overall, the film side is very nearly stoichiometric (Table 5.2.3). It appears that part of the failure occurred at the boundary of the bulk polyimide and an interphase composed of a modified polyimide, and part of the failure occurred between this interphase and the aluminum film.

The peel samples had only 0.5 μm of Al on 50 nm of Cr. In all essential respects, the XPS data from the fracture surfaces of the peel sample are the same as those from the IBT sample. Table 5.2.5 shows that the peak positions and intensities are similar, with the one difference being the lack of any pure metal signal on the substrate side (Figure 5.2.7 (b)). The stoichiometry of the peel and IBT fracture surfaces are very similar (Table 5.2.3). The carbon (1s) spectra of the film and substrate sides are presented in Figure 5.2.8 (a) and (b) respectively. The absence of the fluorine-related peak on the substrate side is again noted. These strong similarities between peel and IBT fracture surfaces indicate that locus of failure for these two adhesion tests is the same for this system.

SEM examination of the substrate side of both IBT and peel fracture surfaces, shown in Figure 5.2.9, reveals features 5-10 μm in diameter on a homogeneous background. Features on the peel sample are larger and more numerous. The ability of Auger electron spectroscopy to analyze a small area is used to determine the chemical composition of the feature; it is mostly Al and O with some C. This is interpreted as being oxidized aluminum with some adventitious carbon. The matrix area shows stronger C and O signals along with F and N, representing the constituents of the polyimide. The polyimide in the matrix area and the aluminum oxide in the features is consistent with a mixed mode failure; areas over the features fail adhesively between the

(a)

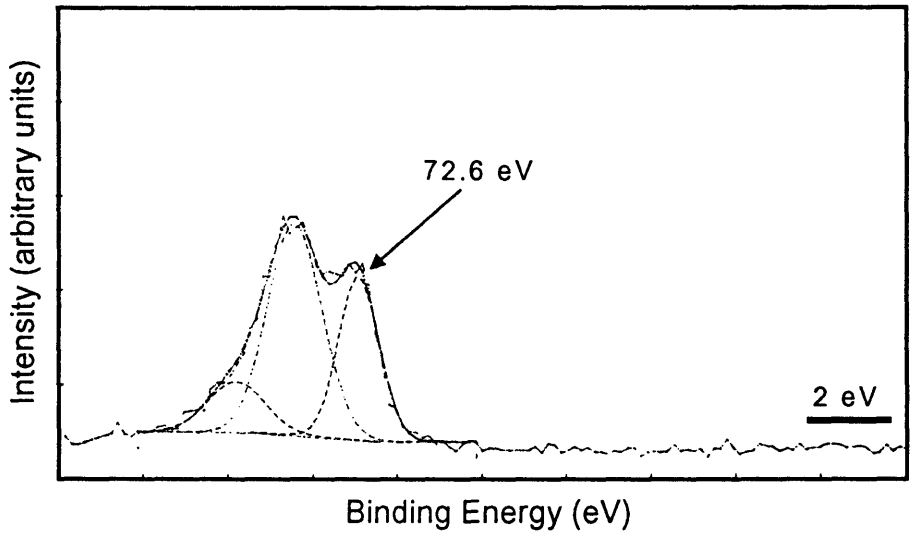

(b)

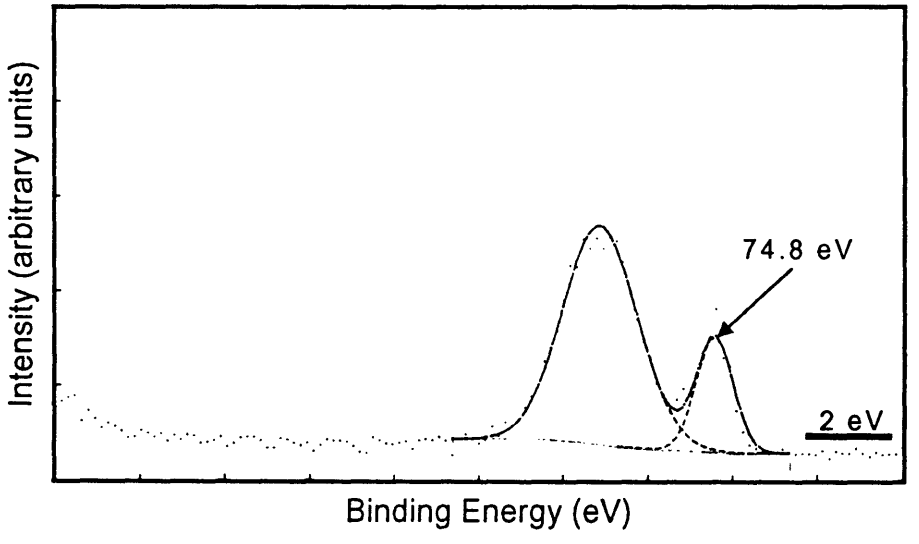

Figure 5.2.7: Aluminum (2p) spectra from HFDA-APBP on AlCr: (a) island side of IBT fracture, (b) substrate side of peel fracture.

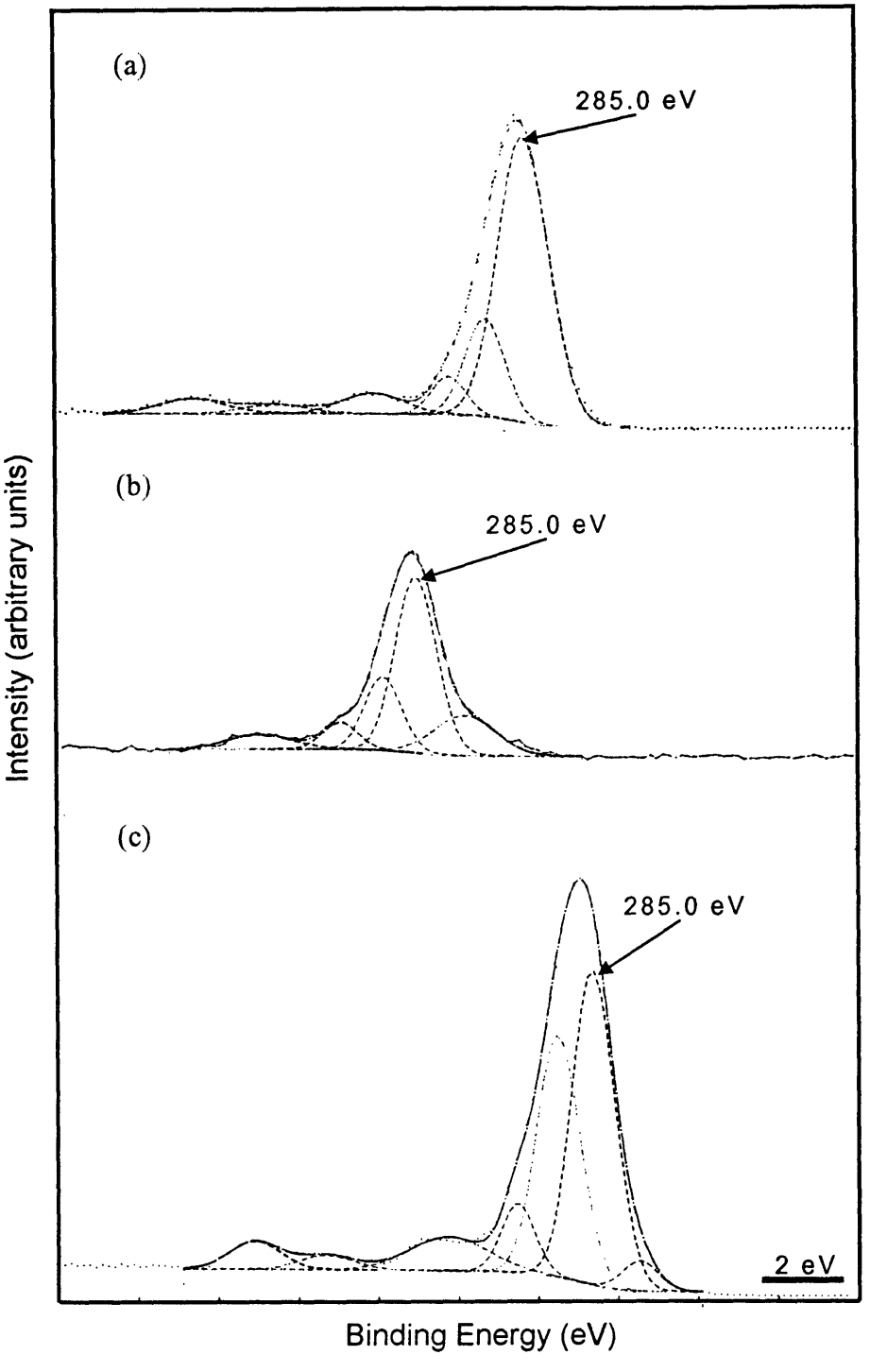

Figure 5.2.8: Carbon (1s) spectra of HFDA-APBP on AlCr: (a) film side of peel fracture, (b) substrate side of peel fracture, (c) reference spectrum.

(a)

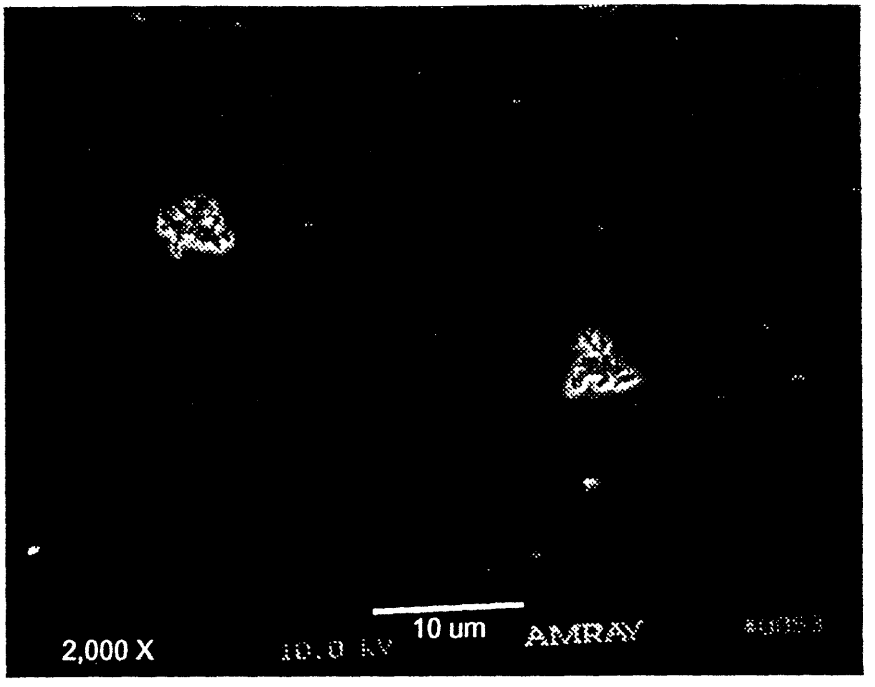

(b)

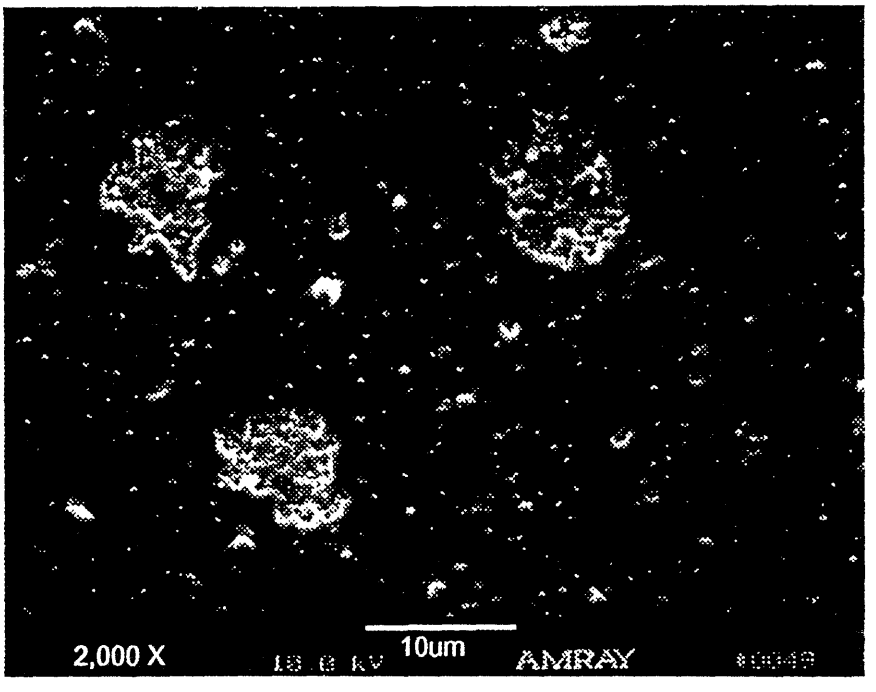

Figure 5.2.9: SEM micrographs of adherend side of HFDA-APBP on AlCr fractures: (a) island side of IBT fracture, (b) substrate side of peel fracture.

polyimide and the oxidized Al, and areas over the matrix fail cohesively in the polyimide. This scenario is also consistent with the XPS data.

Summary of HFDA-APBP on Metal

In Ultradel on "high quality" Cr systems, failure occurs almost entirely in the polyimide in a cohesive fashion. The 0.2 at. % present on the island side is indicative of either a small amount of adhesive failure or a cohesive failure in the polymer shallow enough to receive signal from the interface (<30 A). For Ultradel on "low quality" Cr, the failure is predominantly cohesive in an interphase that appears to be either degraded or contaminated polyimide. The 6% Cr present on the island suggests either a higher percentage of adhesive failure or an even thinner residual polymer layer. These results are consistent with differences in the processing histories and γ_{Ic} between these two types of samples. XPS data of fracture surfaces created by the peel test were congruous with their fabrication, having met most but not all of the criteria for a "high quality" sample. The much larger γ_a of peel samples (425 J/m^2 for h = 19 μm) relative to the γ_{Ic} of even the "high quality" IBT samples (110 J/m^2) is thus not explained on the basis of a difference in locus of failure, but rather, may be related to a mechanical effect such as the unaccounted for plasticity present in the peel test.

Fracture in the Ultradel on AlCr IBT samples is mixed mode. Residual polyimide on the substrate side indicates some degree of cohesive failure in the polyimide while the strong presence of aluminum oxide in the "feature" areas suggests a significant amount of adhesive failure along the interface. In comparison with the same polymer on Cr, the much greater presence of metal on the substrate side in the Ultradel-AlCr system (0.2%

or 6% vs. 40%) suggests that there is a higher degree of adhesive failure in the Al containing system. SEM results support this conclusion. This enhanced adhesive component of the failure provides one possible explanation for the lower γ_{Ic} of Ultradel on AlCr relative to that of Ultradel on Cr (regardless of the quality of the Cr).

5.3 PMDA-ODA on Metal

5.3.1 PMDA-ODA Reference Spectra

The repeat unit of PMDA-ODA is shown in Figure 5.2.1 (b); the carbons are numbered according to bond type for convenience in the ensuing discussion. The carbon (1s) envelope of this polymer shows two major peaks. The peak at the higher binding energy, the one further to the left by convention, is unambiguously due to carbons associated with the carbonyl bond (labeled "6" in Figure 5.2.1 (b)). Deconvolution of the major envelope is less obvious and was originally separated into two peaks of approximately equivalent magnitude [124-127]. The lower energy one, positioned around 285 eV, was thought to be associated with the hydrogen bonded carbons of both the PMDA (labeled "2") and the ODA (labeled "1") portions of the repeat unit. The higher energy one, positioned around 286 eV, was attributed to a combination of the carbons bonded to the carbonyl carbons (labeled "3"), the carbons bonded to nitrogen (labeled "4"), and those bonded to the ester oxygen (labeled "5"). This scheme leaves ten carbons in the lower energy peak and eight in the higher one, a configuration consistent with the approximately equivalent magnitudes of the two peaks.

Later, Buchwalter and Baise [128] assigned only the carbons in the phenyl rings of ODA ("1") to the lower binding energy peak, again at 285.0 eV, leaving the peak at

286.1 eV to be comprised of signals from the aromatic carbons in the PMDA ring ("2" and "3") along with carbons attached to nitrogen ("4") and ester oxygen ("5"). Many subsequent researchers relied on these assignments [49, 128-131]. Under this scheme, peaks 1 and 2 account for 36.3% of total intensity each, also in agreement with experimental data.

Most recently, Silverman, Haight, and Ho [120, 132, 133] have applied molecular orbital calculations to determine that this major peak should actually be deconvolved into three peaks instead of only two. Haight *et al.* [134] assigned the phenyl carbons of ODA ("1") to the lowest peak (285.0 eV), the phenyl carbons of the PMDA ("2" and "3") along with the carbons bonded to nitrogen ("4") to the middle peak (~286 eV), and the carbons bonded to the ester oxygen ("5") to the third peak (~287 eV). These assignments results in a carbon ratio of 8:8:2:4 going from lowest to highest energy, in very good agreement with experimental data. This final set of assignments is still currently accepted as being the most accurate [133]. This chronology of peak assignments is summarized in Table 5.2.1. The historical perspective of C (1s) assignments for this polymer is given (1) to illustrate the difficulty that can be had in deconvolving complex spectra and, (2) to demonstrate that the literature must be referred to carefully in such cases.

The assignment of the third peak to the ester carbons is important because earlier investigators [49, 128] suggested that the occasional appearance of this third peak initiates from a reaction between the polyimide and a metal, leading to an Al-O-C bonding configuration [129] for example. While this cannot be ruled out, the most recent work described above provides an alternative. The major envelope of the carbon (1s)

spectra generated in the course of the present work is fitted with three peaks in accordance with current standard practice.

The reference carbon (1s) spectrum generated in this work is shown in Figure 5.3.1 (a) with the data summarized in column 6 of Table 5.3.1.

Table 5.3.1: Theoretical bond assignments and energy levels (in eV) for PMDA-ODA by different researchers. Peak positions are listed with relative intensities in parenthesis. Reference spectra generated in this work are summarized in column 6.

Atom	Association	Leary[124]	Buchwalter[128]	Haight[134]	Reference	Num. (%
C	?	-	-	-	-1.1 (8)	-
	1. **C**-H^{ODA}	285.0 (44)	285.0 (39)	285 (32)	285.0 (36)	8 (36.3
	2. **C**-H^{PMDA}	285.0	+1.1 (46)	+1 (41)	+0.7 (44)	2 (9.1
	3. **C**-C=O	+1.1 (44)	+1.1	+1		4 (18.2
	4. **C**-N	+1.1	+1.1	+1	-	2 (9.1
	5. **C**-O-**C**	+1.1	+1.1	+2 (9)	+1.8 (6)	2 (9.1
	6. **C**=O	+3.9 (12)	+3.8 (15)	+4 (18)	+4.1 (6)	4 (18.2
O		-	-	-	-1.2 (12)	
	C=**O**	532.2 (75)	532.4 (76)	(77)	532.6 (65)	4 (80)
	C-**O**-C	+1.3 (25)	+1.3 (24)	(23)	+0.7 (23)	1 (20)
N	isoimide	-1.5 (4)	-1.5 (8)	-	-	-
	C-**N**	400.8 (96)	400.8 (92)		401.0 (100)	2 (100)

The broad band centered around 291 eV represents the π-π^* shake-up, a process through which an electron inelastically loses energy by scattering as it travels through a solid. This phenomenon results in the appearance of small broad peaks, typically accounting for 10-15% of the total intensity, at the high binding energy side of the spectrum [112]. For polyimides, UV data indicate that the shake-up peak should occur ~4 eV removed from the π valence levels [129, 134, 136], approximately where it is

found for all of the polyimides studied as will be seen. A shake-up peak is also occasionally seen in the oxygen (1s) and nitrogen (1s) spectra of polyimides [134].

Table 5.3.2: Summary of XPS results for PMDA-ODA systems. The columns labeled C, N, and O show the relative percentages of these elements detected based on a total amount of 100. The Al, Cr, and F columns give the atomic percentage of these elements present.

Sample	Test	C	N	O	Al	Cr	F
Theoretical		75.9	6.9	17.2	0	0	0
Reference		76.1	2.3	21.6	0	0	0
PI2545-Cr (film)	IBT	78	7	15	0	0	0
PI2545-Cr (island)		76	6	17	0	1	0
PI2545-Cr (film)	Peel	75	5	19	0	0	0
PI2545-Cr (island)		74	4	22	0	2	0
PI2545-Al (film)	IBT	82	6	12	0	0	0
PI2545-Al (island)		67	5	28	27.6	0	6.1
PI2545-AlCr (film)	IBT	83	6	11	0	0	0
PI2545-AlCr (island)		68	5	27	28.3	0	3.8
PI2545-AlCr (film)	Peel	78	4	18	0	0	0
PI2545-AlCr (island)		79	4	16	28.6	0	0

The oxygen reference spectrum (Figure 5.3.1 (b)) has a major peak at 532.6 eV, due to the carbonyl oxygens of PMDA, and a minor peak at a binding energy 1.3 eV less than the ester oxygens of PMDA. Polyimides are almost universally found to contain a low carbonyl:ester oxygen ratio, not only for PMDA-ODA [49, 124, 128, 134, 137] but also HFDA-APBP [113, 122] and BPDA-PDA [138, 139]. For the case of PMDA-ODA, Leary and Campbell [124] suggest that the carbonyl deficiency may stem from low molecular weight species at the surface; Haight *et al.* [134] propose the possibility of cross-linking between and within polyimide strands, or three-dimensional order and

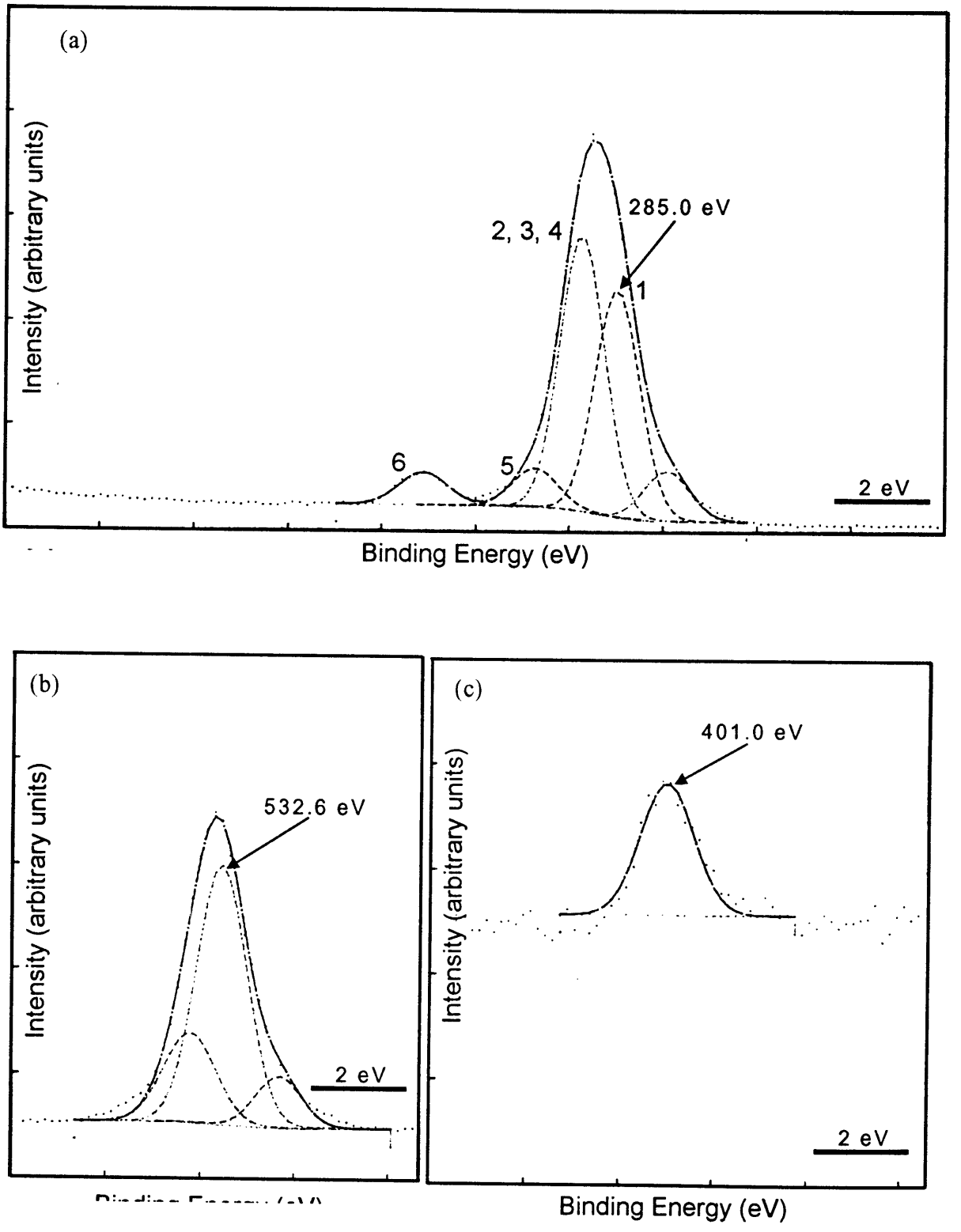

Figure 5.3.1: PMDA-ODA reference spectra (a) carbon 1s; (b) oxygen 1s; (c) nitrogen 1s.

packing effects. There is an additional low energy peak centered at 531.4 eV, found by previous researchers and attributed to residual solvent in the film as mentioned in Section 5.2.

Figure 5.3.1 (c) shows the nitrogen (1s) reference spectra. Here there is only one peak, located at 401.0 eV and attributed to the imide nitrogens. Other researchers [124, 128] have found an extra low BE peak that typically accounts for 5-10% of total nitrogen intensity. Buchwalter and Baise [128] contend that this weak signal initiates from isoimide moeities. Table 5.3.2 presents the film stoichiometries for all of the PMDA-ODA systems including the reference and theoretical compostions. The reference film is abundant in oxygen at the expense of nitrogen.

5.3.2 PMDA-ODA on Chromium

The PMDA-ODA on Cr samples fill all of the "high quality" criteria described in Section 5.2.2. The peak assignment and intensity data are summarized in Table 5.3.3 for both IBT and peel test samples. For the IBT sample, both the film and the island side look very similar to the reference spectra. The carbon (1s) spectra of the film side, the island side, and the reference are compared in Figures 5.3.2 (a-c). The increased size of the peak associated with the ODA phenyl carbon is again explained as carbon contamination. All of these samples were exposed to uncontrolled laboratory ambient for several months prior to XPS analysis. Regardless, the major features associated with the polyimide spectrum are present.

Both sides exhibit a weak oxygen peak on the low binding energy side (Figure 5.3.3). On the island side, this peak at 530.7 eV is associated with Cr_2O_3, as is borne out by the strong presence of a Cr signal which is consistent with its oxide. Like the

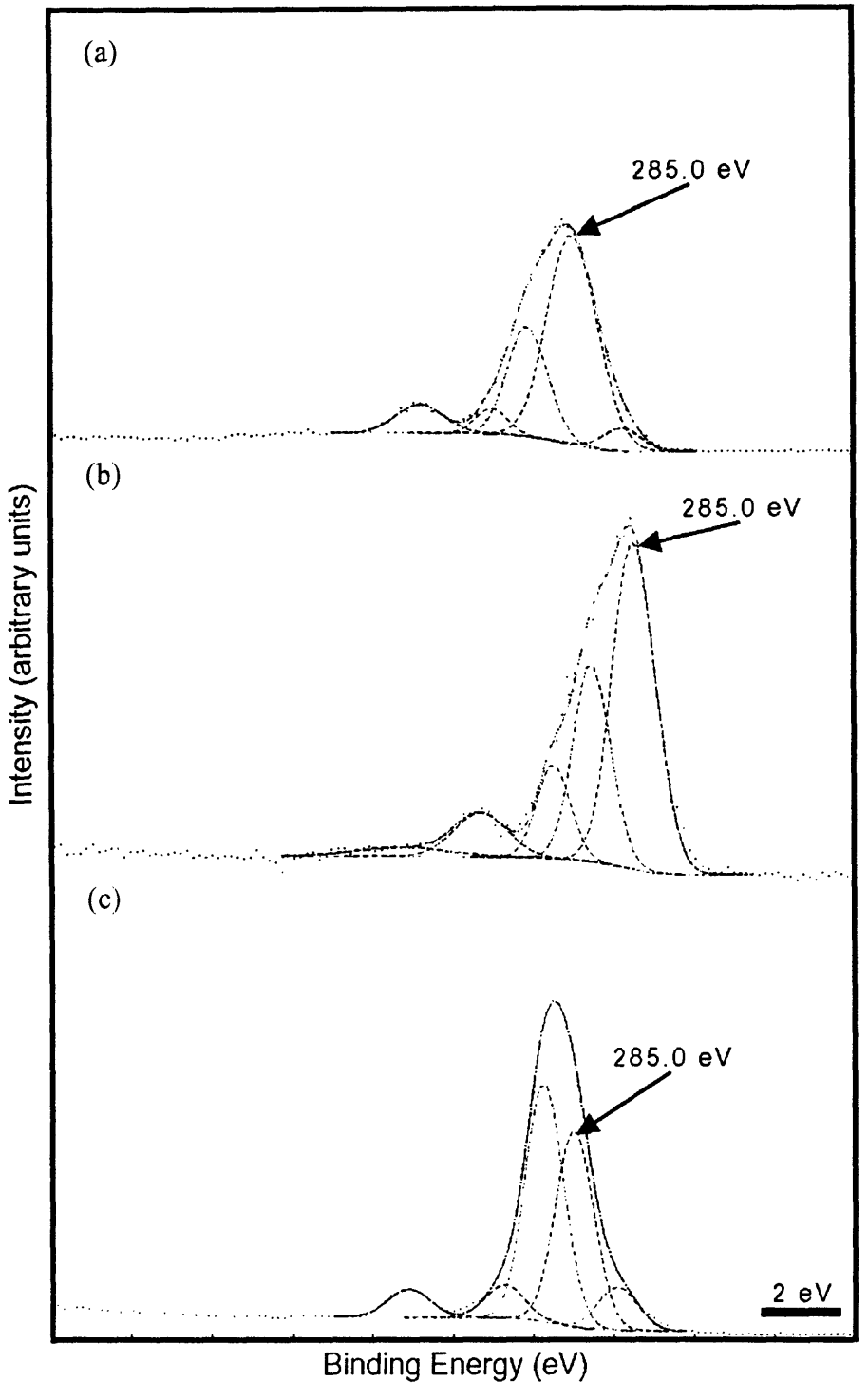

Figure 5.3.2: Carbon (1s) spectra of PMDA-ODA on Cr: (a) film side of IBT fracture, (b) island side of IBT fracture, (c) reference spectrum.

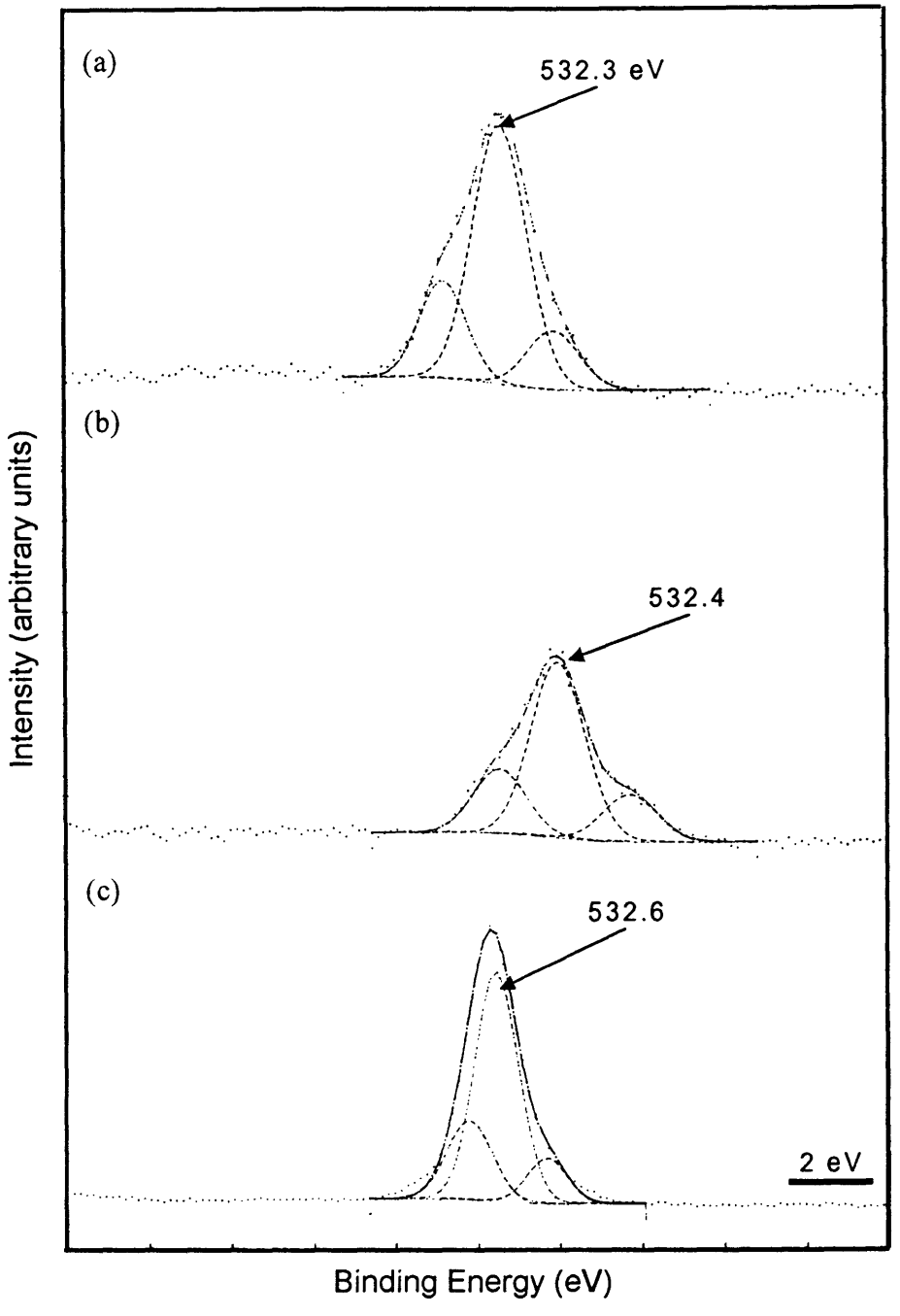

Figure 5.3.3: Oxygen (1s) spectra of PMDA-ODA on Cr: (a) film side of IBT fracture, (b) island side of IBT fracture, (c) reference spectra.

additional low BE oxygen peak in the reference film, the one in the film side of the fracture is at a slightly higher energy than expected for Cr_2O_3, and there is no trace of Cr on the film side. This suggests that the origin of this peak, possibly residual solvent, is the same for both the reference and the film side of the IBT sample.

Table 5.3.3: Peak assignments and energy levels (in eV) for PMDA-ODA on Cr. Peak positions are listed with relative intensities in parenthesis. Cr_2O_3 reference data shown in brackets are taken from [121].

Atom	Association	IBT (film)	IBT (island)	Peel (film)	Peel (substrate)	Reference
C	?	-1.2 (5)	-	-1.1 (4)	-0.8 (6)	-1.1 (8)
	C-H^{ODA}	285.0 (58)	285.0 (51)	285.0 (42)	285.0 (36)	285.0 (36)
	C-H^{PMDA}, C-N	+1.1 (25)	+1.1 (27)	+1.0 (36)	+1.1 (33)	+0.7 (44)
	C-O-C	+2.0 (4)	+2.0 (11)	+2.0 (7)	-	+1.8 (6)
	C=O	+3.9 (8)	+3.9 (8)	+4.0 (9)	+4.1 (8)	+4.1 (6)
	π-π^*	-	+5.5 (3)	+5.3 (2)	-	-
N	isoimide?	-1.4 (34)	-	-1.4 (14)	-	-
	C-N	400.8 (66)	400.5 (85)	401.1 (86)	400.9	401.1 (100)
	????		+1.25 (15)		-	-
O	Cr_2O_3	-	530.7 (17)	-	530.8 (6)	[530.3-530.8]
	?	531.0 (14)	-	531.3 (6)	-	531.4 (12)
	C=O	532.3 (65)	532.4 (62)	532.4 (56)	532.4 (83)	532.6 (65)
	C-O	+1.4 (21)	+1.4 (22)	+1.1 (38)	+1.5 (11)	+0.7 (23)
Cr	Cr_2O_3 ($2p_{3/2}$)	-	576.6 (58)	-	576.6 (63)	[576.6 (67)]
	Cr_2O_3 ($2p_{1/2}$)	-	+9.8 (42)	-	+9.7 (37)	[+9.7 (33)]

The nitrogen (1s) spectra of both the island and film exhibit an extra peak. In the case of the film, the additional low energy peak is not unusual for PMDA-ODA films [128, 140]. Its presence has been attributed to isoimide moities [128], to residual solvent in the film [49], and to amine radicals [141]; this may also explain the extra low energy oxygen peak. The origin of the weak high energy peak in addition to the main, imide

peak on the island side is unknown. Table 5.3.2 indicates that both sides of the fracture surface are nearly stoichiometric. All of the above evidence supports the conclusion that the fracture is entirely cohesive in the polyimide.

The carbon (1s) spectra of the film side and the substrate side of the peel fracture are compared with the reference spectrum in Figure 5.3.4. Again both sides exhibit all of the features typical of polyimide with no real degradation. The oxygen (1s) spectra show the same trends as with the IBT: the substrate side has the peak at an energy consistent with Cr_2O_3 (530.8 eV) while the peak on the film side at 531.3 eV matches that of the reference spectrum. The substrate side shows ~2 atomic % Cr, similar to the ~1 atomic % on the island side of the IBT fracture. Table 5.3.2 shows the similarities in stoichiometry. The failure for both IBT and peel samples is cohesive in the polyimide.

5.3.3 PMDA-ODA on Aluminum

Two structures were investigated using the IBT. The first involved spin casting the PMDA-ODA on a silicon wafer previously coated with 160 nm of silicon nitride followed by 50 nm of Al (PMDA-ODA on Al). The second imposed a thin layer of Cr between the silicon nitride etch stop and the aluminum adherend (PMDA-ODA on AlCr). The purpose of the Cr layer is to provide additional protection against attack by the tenacious HF-based silicon etchant. Only the latter structure was investigated using the peel test, where the Cr is essential for good adhesion to the Si wafer.

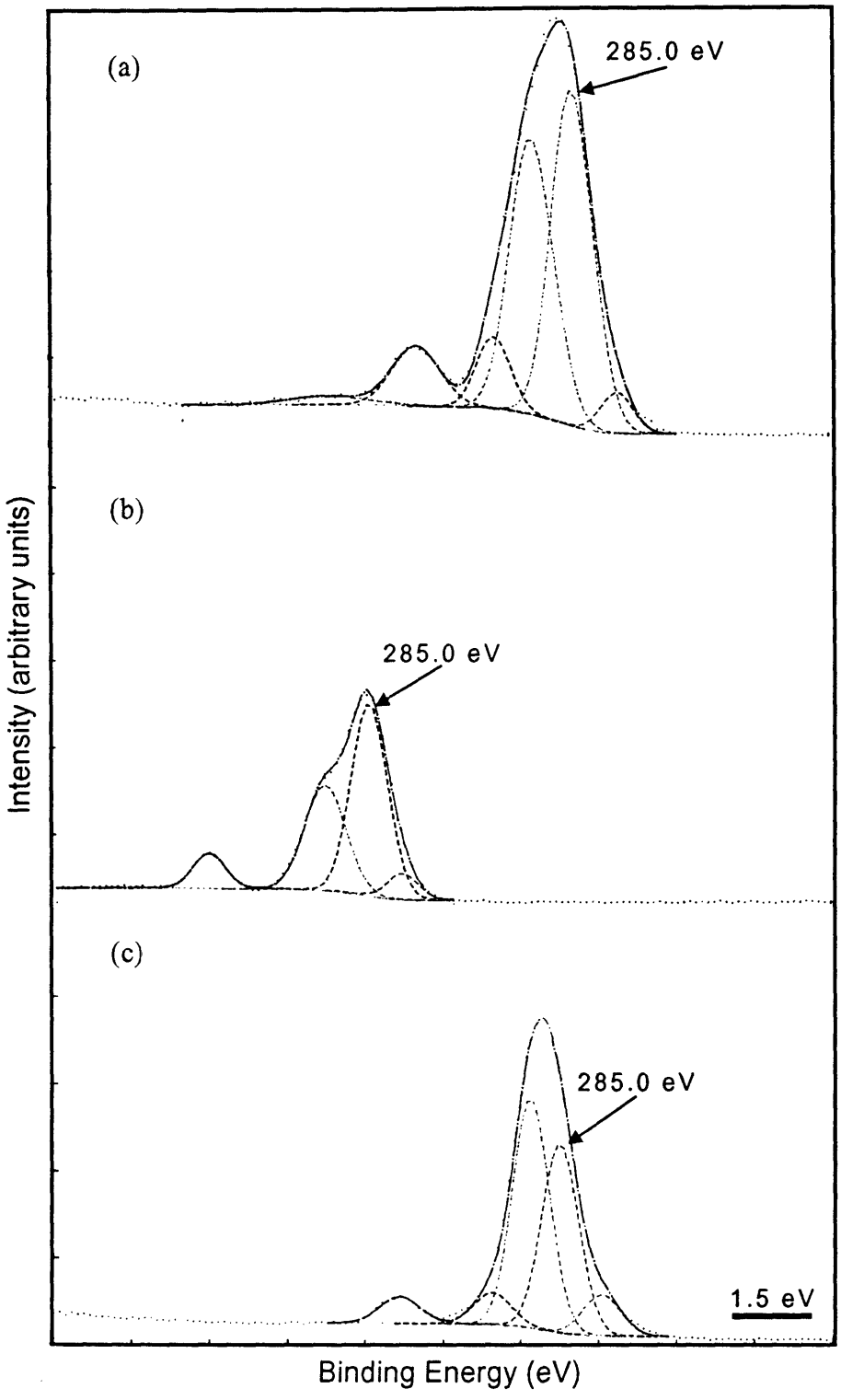

Figure 5.3.4: Carbon (1s) spectra of PMDA-ODA on Cr: (a) film side of peel fracture, (b) substrate side of peel fracture, (c) reference spectrum.

PMDA-ODA on Al

Table 5.3.4 presents the peak assignments and relative intensities for PMDA-ODA on Al IBT samples. The film side looks very much like virgin polyimide with no traces of metal. The stoichiometry is very close to theoretical (Table 5.3.2). The only difference is the addition of a small, very broad, high BE peak in the oxygen (1s) spectrum, a manifestation of the carbonyl and ester shake-ups as found by [134]. The island side shows not only the components of the polyimide (C, N, O), but also a large amount (27.6 at.%) of aluminum and significant fluorine (6.1 at.%). Presumably, the fluorine comes from the HF-based silicon etchant, indicating that the 160 nm silicon nitride layer alone is not sufficient to retard the 6:1:1 solution. Deconvolution of the fluorine (1s) envelope results in two peaks (Figure 5.3.5 (a)). The higher energy one accounts for 67% of the total intensity and is near the energy (686.5 eV) proposed earlier for AlF_3 in the HFDA-APBP on Al system. Much too low in energy to be associated with carbon, the small low energy peak is assumed to represent ionic fluorine (F^-) known to exist ~4 eV lower in energy than the carbon bonded halide [112]. It could also be the fluoride of a contaminant such as sodium or silicon, but since the survey scan lacked these elements, the former assignment is adopted. The island side oxygen (1s) spectrum exhibits an additional peak on the low BE side positioned at 531.3 eV, the correct location for the Al_2O_3 peak [119]. Here the presence of the Al justifies the assignment of this peak to the metal oxide, whereas in the reference film which had no metal species present, this assignment cannot be made. It is possible that the peak at 531.3 eV on the island side oxygen (1s) spectrum is a composite of these two effects, although this peak

(a)

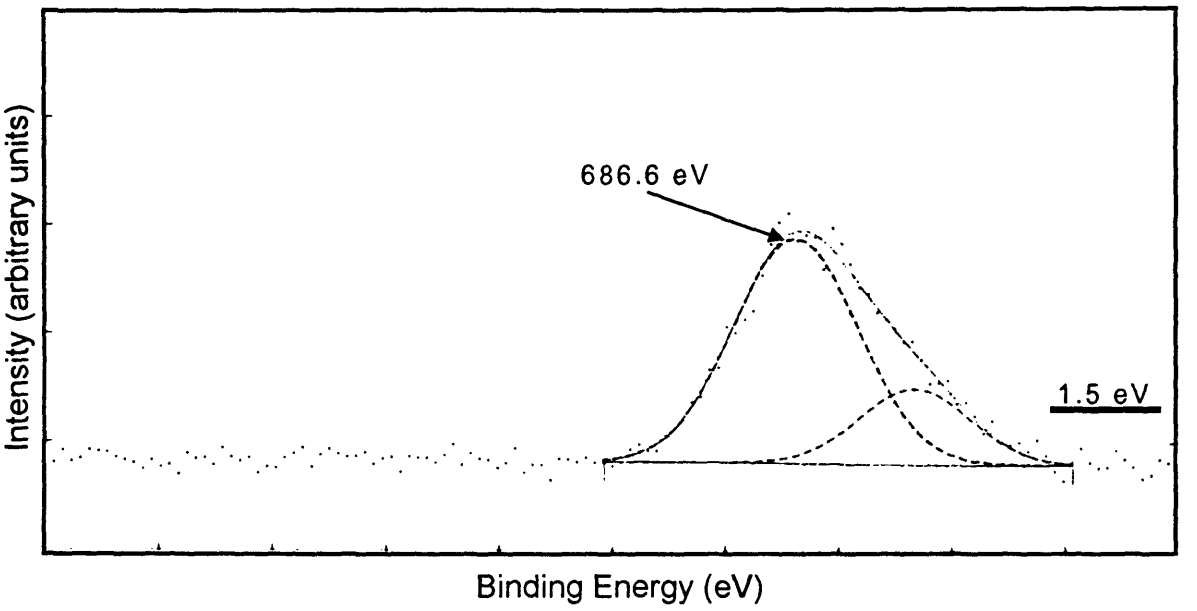

(b)

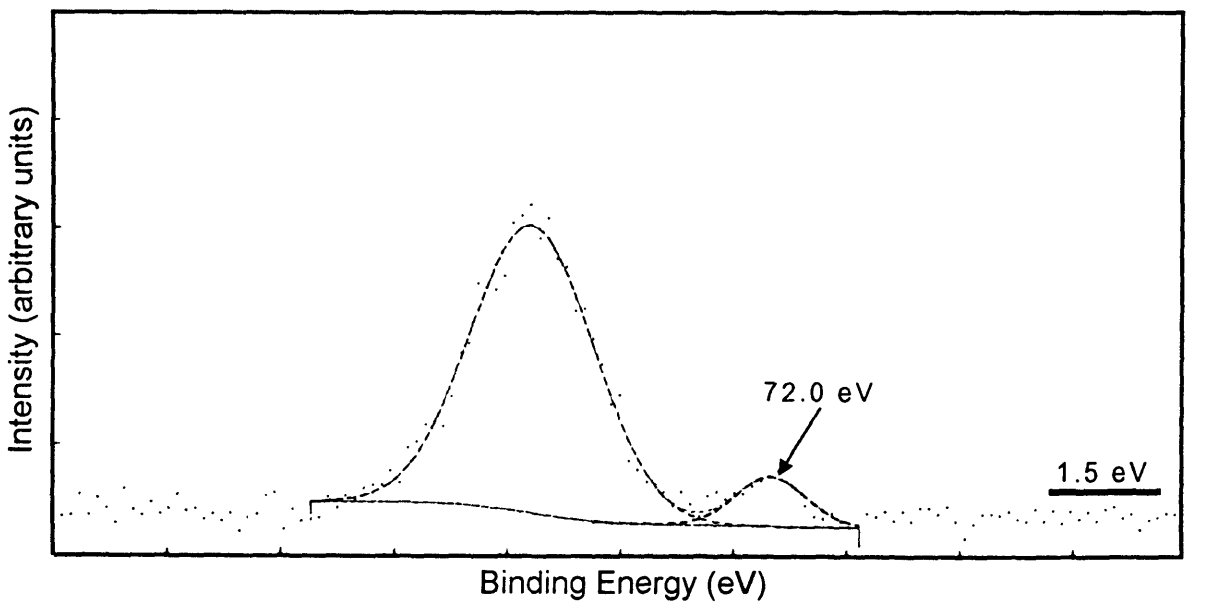

Figure 5.3.5: XPS spectra from island side of PMDA-ODA on Al: (a) fluorine 1s, (b) aluminum 2p. For (a), lower energy peak assigned to F^-, and higher energy peak assigned to floride. In (b), the lower energy peak is associated with pure metal, and the higher energy peak is associated with oxide or possibly a combination of oxide and fluoride.

was not seen on the adherend side of the PMDA-ODA on Cr samples, only on the film side.

The Al (2p) spectrum demonstrates a low energy peak corresponding to the pure metal, and a broad peak centered at 75.1 eV which could conceivably be deconvolved into two peaks, one at 74.7 eV (Al_2O_3) and one at 76.1 eV (AlF_3) (Figure 5.3.5 (b)). This assignment would be consistent with the presence of the Al_2O_3 peak in the oxygen (1s) spectrum and the AlF_3 peak in the fluorine (1s) spectrum.

Table 5.3.4: Peak assignments and energy levels for PMDA-ODA on Al. Peak positions are listed with relative intensities in parenthesis. Al reference data shown in brackets are taken from [119].

Atom	Association	Film	Island	Reference
C	?	-	-	-1.1 (8)
	C-H^{ODA}	285.0 (37)	285.0 (55)	285.0 (36)
	C-H^{PMDA}, **C**-N	+0.9 (36)	+1.1 (26)	+0.7 (44)
	C-O-**C**	+1.9 (9)	+2.1 (8)	+1.8 (6)
	C=O	+3.9 (12)	+4.0 (12)	+4.1 (6)
	π-π^*	+6.5 (5)	-	-
O	?	-	-	531.4 (12)
	Al_2O_3	-	531.3 (43)	-
	C=**O**	532.3 (60)	532.4 (36)	532.6 (65)
	C-**O**	+1.4 (36)	+1.3 (21)	+0.7 (23)
	π-π^*	+6.1 (4)	-	-
N	C-**N**	400.7	400.5	401.0
F	**F**$^-$	-	685.0 (23)	~684.6[5-1]
	AlF_3	-	686.6 (77)	~686[5-5]
Al	**Al**	-	72.0 (9)	[72.3-72.8]
	Al_2O_3	-	75.1 (91)	[74.0-74.7]
	AlF_3	-	-	[76.1]

The presence of polyimide on both fracture surfaces combined with the presence of aluminum on the island side suggest that the locus of failure was either a very shallow

(~3 nm) cohesive failure in the polyimide, such that the metal film can still be detected beneath the residual polyimide, or a mixed mode failure involving both cohesive failure in the polyimide and adhesive failure and the polyimide-Al interface.

PMDA-ODA on AlCr

The difference between these samples and those from the previous section is the imposition of a 50 nm Cr layer between the silicon nitride and the aluminum adherend metal. Table 5.3.5 summarizes the XPS peak intensity and position data for both film and island sides. The only differences found between these data and the PMDA-ODA on Al data are in the intensity distribution under the main envelope of the island side carbon (1s) spectra, and in the amount of fluorine present. Figure 5.3.6 shows the carbon (1s) spectra of (a) the island side of the IBT Al sample, (b) the island side of the IBT AlCr sample, and (c) the substrate side of the AlCr peel sample. For the AlCr IBT sample, the low energy peak from the phenyl carbons of ODA is reduced, the peak from the amine nitrogen linkage at 286.9 eV is exaggerated, and the carbonyl peak is much broader than for the Al IBT sample. This is the sort of carbon (1s) distribution previously experienced with Ultradel on "low quality" Cr samples. This difference in carbon (1s) spectra, the source of which is unclear, provides one possible explanation for the lower γ_{Ic} in the AlCr system (30 J/m^2 as opposed to 19 J/m^2). As mentioned previously, all aluminum containing samples were deposited at room temperature but otherwise fit the "high quality" description. The reduced presence of fluorine in the AlCr sample suggests that the addition of the Cr layer does help retard the etchant but is not completely successful.

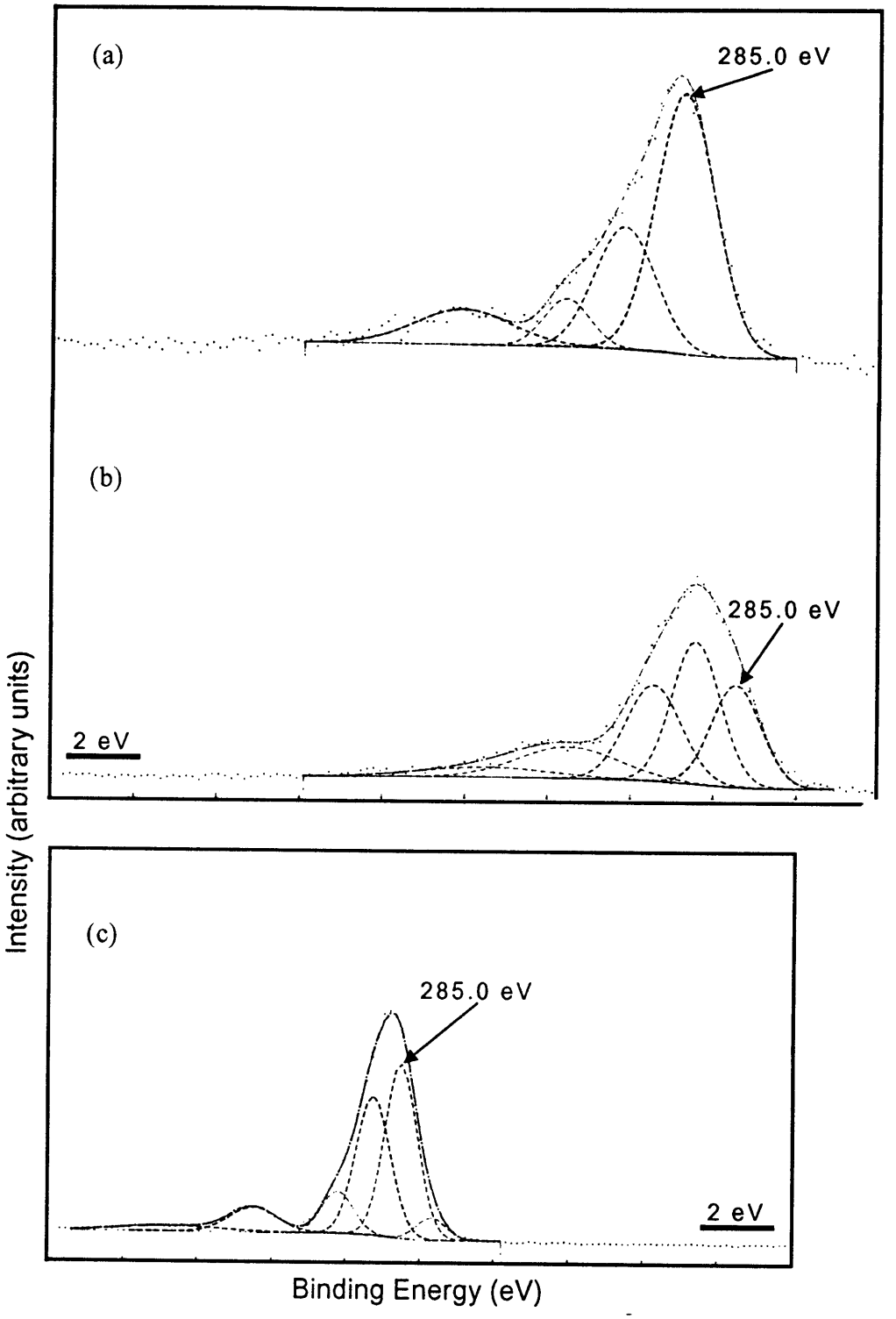

Figure 5.3.6: XPS spectra of PMDA-ODA on Al-containing metallurgies: (a) island side of IBT fracture from -Al system, (b) island side of IBT fracture from -AlCr system, (c) substrate side of peel fracture from -AlCr system. Refer to Figure 5.3.1(a) for comparison with PMDA-ODA carbon (1s) reference spectrum.

Complete elimination of fluorine will require either a thicker Cr layer or a thicker silicon nitride layer or perhaps both.

Other than these differences, the AlCr IBT sample shows the same chemistry at the locus of failure as the Al IBT sample, indicating that here too the locus of failure is either a combination of cohesive fracture in the polyimide and adhesive failure at the interface or such a shallow cohesive failure in the polyimide that the signal from the

Table 5.3.5: Summary of peak positions and relative intensities for PMDA-ODA on AlCr. Peak positions are listed with relative intensities in parenthesis. Al reference data shown in brackets is from [119].

Atom	Association	IBT (film)	IBT (island)	Peel (film)	Peel (substrate)	Reference
C	?	-	-	-1.0 (6)	-0.8 (5)	-1.1 (8)
	C-H^{ODA}	285.0 (40)	285.0 (23)	285.0 (28)	285.0 (36)	285.0 (36)
	C-H^{PMDA}, **C-N**	+0.9 (39)	+0.9 (32)	+0.8 (39)	+0.8 (39)	+0.7 (44)
	C-O-C	+2.0 (5)	+1.9 (25)	+1.9 (11)	+1.7 (10)	+1.8 (6)
	C=O	+3.9 (12)	+3.8 (14)	+4.1 (13)	+4.0 (8)	+4.1 (6)
	π-π^*	+6.6 (4)	+5.7 (6)	+6.6 (3)	+5.4 (1)	-
O	?	-	-	531.2 (10)	-	531.4 (12)
	Al_2O_3	-	531.4 (52)	-	532.0 (15)	[531.6]
	C=O	532.1 (54)	532.6 (39)	532.4 (51)	533.4 (78)	532.6 (65)
	C-O	+1.4 (36)	+1.3 (9)	+1.3 (37)	535.2 (6)	+0.7 (23)
	π-π^*	+6.4 (10)	-	+5.2 (3)	-	-
N	isoimide?	-	-	-1.2 (12)	-	-
	C-N	400.6	400.6	401.0 (88)	400.8	401.0
Al	**Al**	-	72.0 (10)	-	-	[72.3-74.8]
	Al_2O_3	-	75.0 (90)	-	74.6 (28)	[74.0-74.8]
	AlF_3	-	-	-	76.1 (72)	[76.1]

underlying metal is detectable. SEM analysis of the AlCr case, shown in Figure 5.3.7, demonstrates two distinct regions at the locus of failure, a pattern of dendritic features superimposed on a background matrix.

Auger electron spectroscopy[2] (AES) was used to compare the chemical composition of the features to the matrix. By sputtering with argon ions while collecting data, a depth profile is achieved. Figure 5.3.8 (a) shows that the feature is a heavily oxidized Al-rich region that quickly gives way to a stronger Cr signal. The leftmost part of Figure 5.3.8 (b) indicates that Al starts out with two peaks assumed to represent the pure and oxidized forms of the metal. One peak is prevalent at the surface but quickly diminishes as the second grows. Note that the abscissa in each part of this figure is normalized to the maximum intensity of each element. The strength of the oxygen peak tracks this first Al peak suggesting that it is an oxide. Cr appears as a single peak. The carbon signal is very weak as evidenced by the noisy background, and is typical of adventitious carbon.

Figure 5.3.9 (a) shows that the matrix is a heavily oxidized mix of Al and Cr that gives way to a much stronger Al signal. The carbon signal Figure 5.3.9 (b) starts out very strong but quickly abates, indicative of a thin organic compound. The XPS analysis confirms that this is polyimide.

The explanation is the same as applied to the case of HFDA-APBP on AlCr: the features represent areas of extensive oxidation of the Al and the polyimide does not adhere well to this oxide. The oxygen signal in Figure 5.3.8 (b) is proposed to be connected with the Al as an oxide. The oxygen signal in the matrix scan is then expected

[2] The assistence of Dr. Libby Shaw of MIT's Surface Science Facility in operating the AES equipment is gratefully acknowledged.

(a)

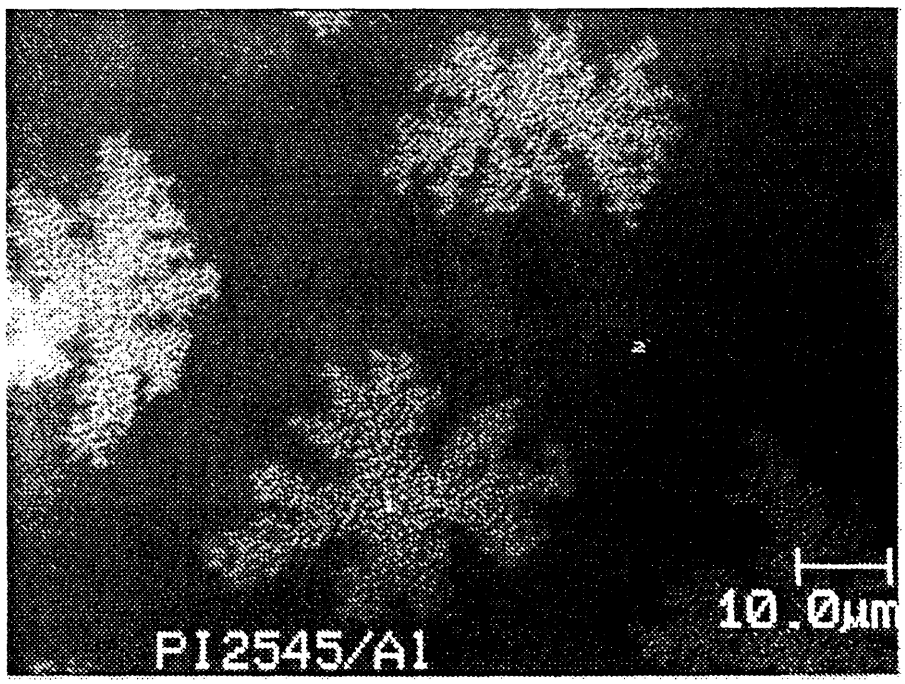

(b)

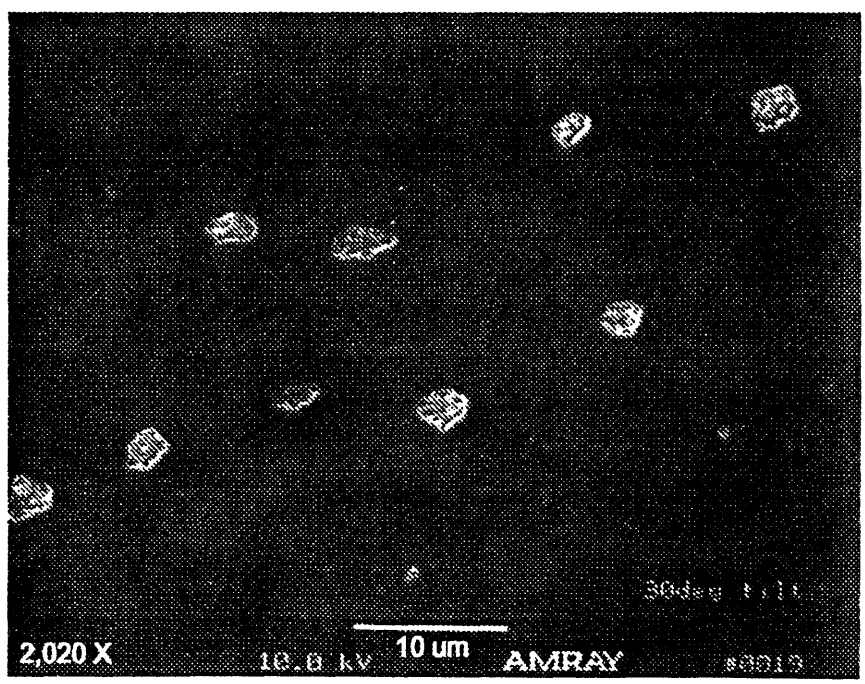

Figure 5.3.7: SEM micrographs of the adherend side of PMDA-ODA on AlCr fracture surfaces: (a) island side of IBT fracture surface, (b) substrate side of peel fracture surface.

(a)

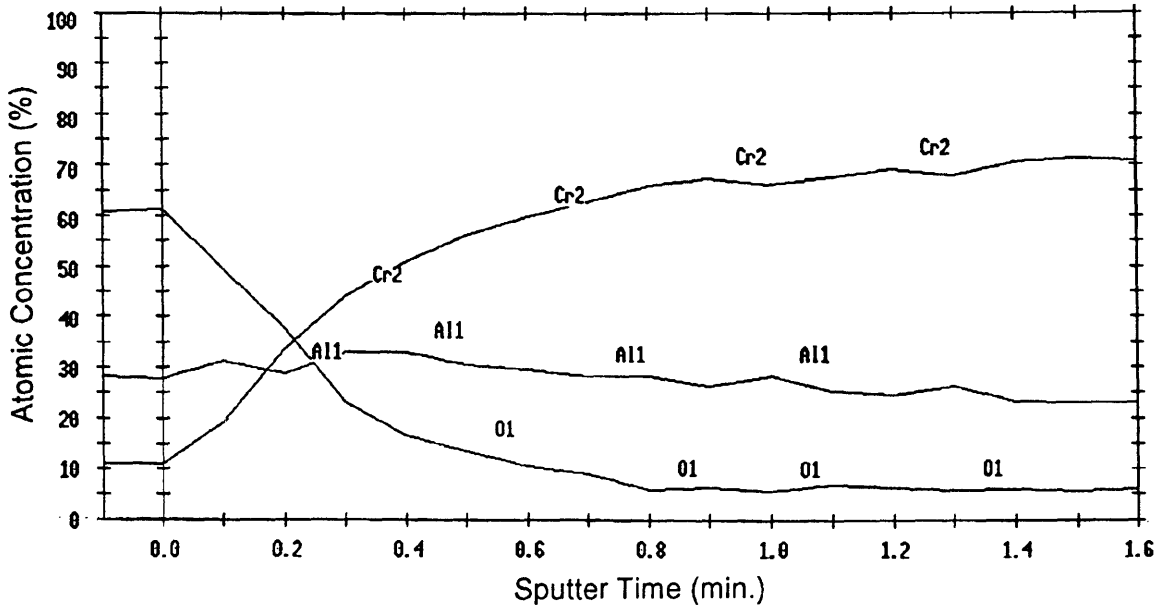

(b)

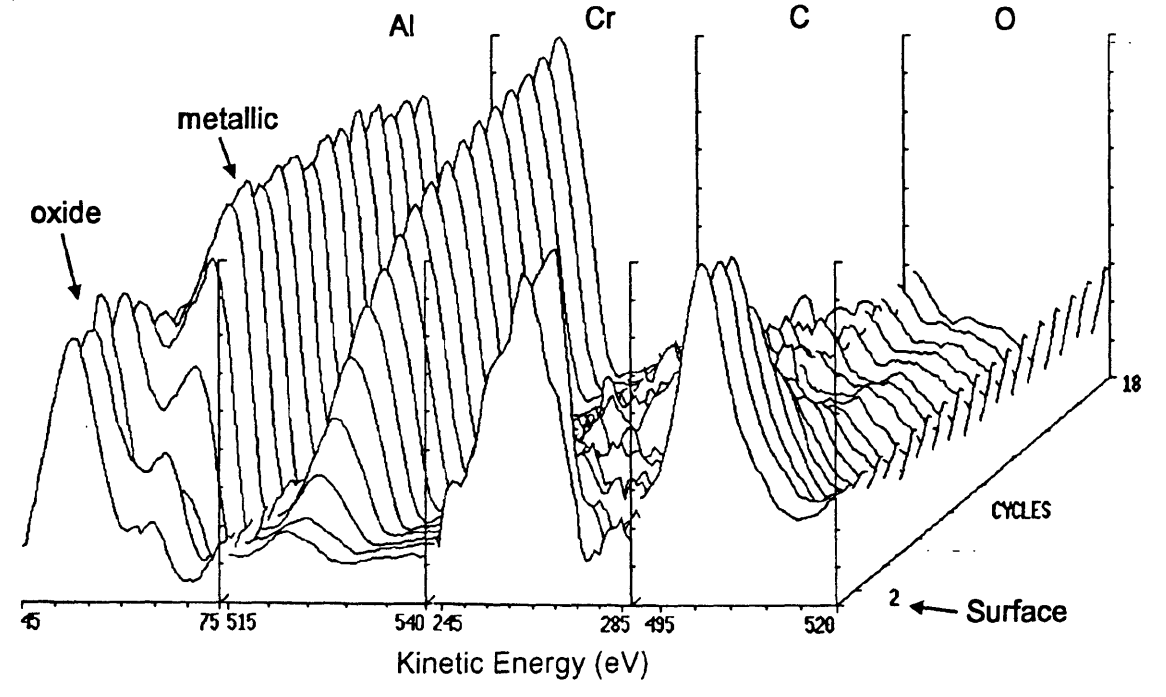

Figure 5.3.8: AES depth profile of "feature" in Figure 5.3.6: (a) atomic concentration (%) as a function of sputter time for Cr, Al, O; (b) intensity of Al, Cr, C, O normalized to the maximum for each element as a function of sputter time.

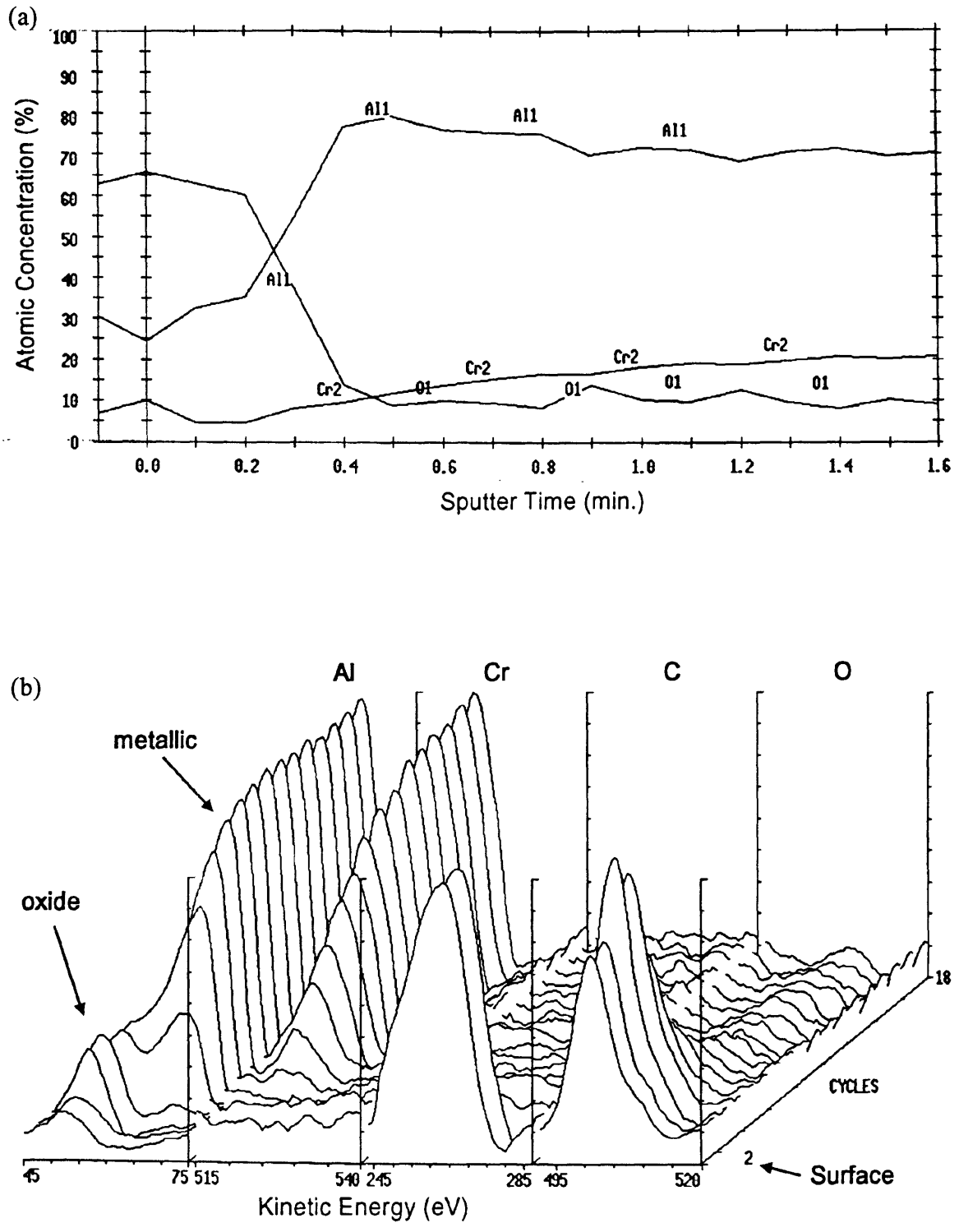

Figure 5.3.9: AES depth profile of matrix in Figure 5.3.6: (a) atomic concentration (%) as a function of sputter time for Cr, Al, and O; (b) intensity of Al, Cr, C, and O normalized to the maximum for each element as a function of sputter time.

to be connected with the residual polyimide, which is quickly sputtered through, giving way to the underlying Al present mostly as the pure metal. The percentage of area covered by the features corresponds roughly with the ~28 atomic % Al found using XPS (Table 5.3.2). Fluorine was also detected with the AES although its role, if any, is not clear.

PMDA-ODA on AlCr Peel Test Sample

Table 5.3.5 summarizes the XPS data generated from the PMDA-ODA on AlCr peel sample. The difference in fabrication between the peel and the IBT samples is in the thickness of the Al layer. The IBT samples had a 50 nm Al layer while the peel samples have a 1 μm layer, both on 50 nm Cr. The film side is nearly stoichiometric (Table 5.3.2) and looks very much like the reference. No Al was found on the film side. The island side carbon (1s) envelope, compared with those of the IBT samples in Figure 5.3.6 (c), is deconvolved into a series of peak whose positions and intensities compare well with the reference spectrum (Figure 5.3.1 (a)) indicating the presence of near pristine polyimide. It does not have the degraded appearance of the Al-containing IBT samples (refer to Figure 5.3.6).

The Al (2p) spectrum is deconvolved into two peaks, one at 74.6 eV corresponding to the oxide, and the stronger one at 76.1 eV, the location of the fluoride. While a trace of fluorine was detected (~0.7 atomic %), it is not enough to account for the significant amount of fluoride the peak in the Al (2p) spectrum represents. Another possibility is that charging occurred, shifting the entire spectrum to higher energies. Since the Al scan was done last, this is possible. If charging did occur, the lower peak

would correspond to the pure metal with the oxide creating the higher energy, stronger peak. These more sensible assignments would then be in agreement with those of the PMDA-ODA on AlCr IBT sample (Table 5.3.5).

Figure 5.3.7 shows an SEM micrograph of the substrate side of the fracture surface created by (a) island blister testing and (b) peel testing of PMDA-ODA on the AlCr adherend. The larger size of the features in the IBT sample (~40 μm in major dimension compared with ~10 μm on the peel sample) may be a consequence of its thinner Al layer (5 nm versus 1,000 nm). The topographies of the fracture surfaces are both suggestive of mixed mode fracture. It is clear that number density of the features attributed to oxidized aluminum is much higher on the IBT sample. Since the film adheres less well to these features, their greater number in this case may contribute to the lower γ_{Ic} measured with the IBT relative to the peel test (19 J/m^2 versus 90 J/m^2). It is also possible that the sample fabrication process of the IBT, in using a thinner Al layer and allowing for the ingress of fluorine, modifies the polymer-metal interface in a way that degrades its mechanical integrity. The slightly degraded appearance of the carbon (1s) spectrum of the AlCr sample supports this conclusion. A further possibility is that this difference is a manifestation of the different quantities measured by the two tests, resulting in overestimation of the adhesion on AlCr by the peel test.

Summary

The PI2545 data presented above lead to the following conclusions. The peak at 286.6 eV in the carbon (1s) spectrum is attribute to the amine in the PMDA, as opposed to earlier assignments of it being a new peak related to a reaction between the

PMDA-ODA and the metal. The PI2545-Cr fails cohesively in the polyimide as demonstrated on both IBT and peel samples. The γ_{Ic} measured by the IBT (175 J/m^2) compares well with the γ_a measured by the peel test (180 J/m^2) but perhaps only by coincidence. The carbon (1s) spectra from the IBT samples looks like pristine polyimide while those of the peel samples look somewhat degraded. The adherend side of each sample type exhibits ~1-2 atomic percent of oxidized Cr. PMDA-ODA on Al behaves in essentially the same way as on AlCr, although the carbon (1s) spectrum of the AlCr system looks more degraded than that of the Al sample; this may explain the somewhat lower γ_{Ic} in the AlCr system (19 J/m^2 compared to 30 J/m^2). The sample fabrication process allows some fluorine to penetrate to the interface. The majority of the fluorine appears to be tied up with the aluminum, the balance existing as an ion (F^-). It only appears on the island side and its effect on adhesion is unclear, although the residual polyimide does not appear degraded. A combination of XPS, AES, and SEM analyses suggests that, for both Al and AlCr IBT samples, the fracture is mixed mode occurring cohesively in the polyimide and adhesively at the polyimide-aluminum oxide interface.

Possible explanations for the much higher adhesion values measured by the peel test include the larger population of the second phase oxide in the IBT sample, degradation resulting from fluorine contamination, and potential inaccuracies of the peel measurement stemming from the overly simplified data analysis. The issue could be clarified by doing a side-by-side comparison of the two tests using the same adherend thickness (1 μm Al/5 nm Cr recommended) and a thicker silicon nitride layer (~1μm)

with the IBT to retard the fluorine from the HF-based silicon etchant. This work is left to future researchers.

5.4 BPDA-PDA on Metal

Results of XPS analysis of failure surfaces generated by IBT and peel testing of BPDA-PDA on AlCr and Cr are reported in this section. The BPDA-PDA on AlCr samples were fabricated by spin casting the polyamic acid on wafers metallized first with 50 nm Cr followed by 1 μm of Al. Adhesion data from both tests for these systems are presented in Table 5.2.1. The reference spectra for virgin BPDA-PDA are first reviewed, followed by an evaluation of spectra taken from IBT and peel fracture surfaces.

5.4.1 BPDA-PDA Reference Spectra

The monomer of BPDA-PDA is shown in Figure 5.2.1 (c). The carbon bonds are numbered for clarity in the following discussion. Peak positions and assignments for thick films of BPDA-PDA are shown in Table 5.4.1. It is universally agreed that the smaller envelope in the spectrum corresponds to the carbonyl (labeled "5"). However, there is a lack of agreement regarding assignments under the main envelope. The close proximity of the two lowest energy peaks complicates deconvolution of the main carbon (1s) envelope. By constraining the fitting program, Anderson [142] was able to experimentally verify molecular orbital calculations according to the assignments presented in column 3 of Table 5.4.1. The peak at 284.6 eV is attributed to the phenyl carbons of PDA (labeled "1"). Shifted only 0.5 eV towards the higher BE side, the phenyl of BPDA (labeled "2" and "3") accounts for the peak at 285.1 eV. The nitrogen

linkage (labeled "4") is assigned to the peak removed by +1.3 eV from the PDA phenyl peak.

Chenite [138] assigned the carbons bonded to the carbonyl carbons ("3") along with the carbons bonded to nitrogen to the higher energy peak at 286.7 eV. Buchwalter [139] fits the main envelope with only two peaks, attributing the lower energy one to all phenyl carbons ("1", "2", "3") and the higher energy one to only the nitrogen linkages ("4"). Lu *et al.* follow these conventions also [143].

Table 5.4.1: Theoretical bond assignments and energy levels (in eV) for BPDA-PDA by different researchers. Peak positions are listed with relative intensities in parenthesis.

Atom	Association	Anderson[142]	Chenite[138]	Buchwalter[139]	Reference	Num. (%
C	?	-	-	-	-1.0 (5)	-
	1. C-H^{PDA}	284.6	285.4	285.0 (77)	285.0 (71)	4 (18.2
	2. C-H^{BPDA}	+0.5	+0.5	285.0	-	8 (36.4
	3. C-C=O	+0.5	+1.3	285.0	-	4 (18.2
	4. C-N	+1.3	+1.3	+0.9 (8)	+0.9 (13)	2 (9.1
	5. C=O	+3.6	+3.8	+3.5 (15)	+3.6 (10)	4 (18.2
	π-π^*	-	-	-	+5.9 (1)	-
N	C-N	400.9	400.9	400.9	400.6	2 (100
O	C=O	532.3	532.3	531.8 (93)	532.2 (91)	4 (100
	C-O	-	-	533.6 (7)	533.9 (13)	-

The carbon (1s) reference spectrum generated in this work is fit according to the assignments of Buchwalter since they provide the most natural fit. Fitting according to the assignments of Anderson was attempted but was never successful. The automated fitting program always separated the peaks by more that the 0.5 eV required for this scheme. Interpretation of the nitrogen (1s) and the oxygen (1s) envelopes is straightforward since they are each expected to contain only one peak, the amine nitrogen

at 400.9 eV and the carbonyl oxygen at 532.3 eV. Buchwalter [139] and Nagarkar [119] both find an additional higher BE oxygen peak and attribute it to the presence of ester linkages in the material.

Reference spectra, found in Figures 5.4.1 (a-c), are similar to those generated by Nagarkar [119]. The main peak in the oxygen (1s) spectrum represents the carbonyl contribution. The minor peak is attributed to ester linkages as seen by previous researchers. Film stoichiometries are summarized in Table 5.4.2. Similar to PMDA-ODA, the reference film is slightly sub-stoichiometric in nitrogen as also found by Nagarkar [119].

Table 5.4.2: Summary of film stoichiometries for BPDA-PDA systems. Each column gives the atomic percentage of that specific element. Theoretical is based on formula: $C_{22}N_2O_4$.

Sample	Test	C	N	O	Al	Cr	F
Theoretical		78.6	7.1	14.3	0	0	0
Reference		81	4	15	0	0	0
PI2611-Cr (film)	IBT	80	7	13	0	0	0
PI2611-Cr (island)		80	6	14	0	2	0
PI2611-Cr (film)	Peel	79	7	14	0	0	0
PI2611-Cr (substrate)		80	5	15	0	2	0
PI2611-AlCr (film)	IBT	76	8	16	0	0	0
PI2611-AlCr (island)		71	4	25	23	0	1
PI2611-AlCr (film)	Peel	81	5	14	0	0	0
PI2611-AlCr (substrate)		71	4	25	24	0	0

5.4.2 BPDA-PDA on Cr

Figure 5.4.2 compares the carbon (1s) spectra from (a) the island side of the IBT fracture with (b) the substrate side of the peel fracture and (c) the reference spectrum.

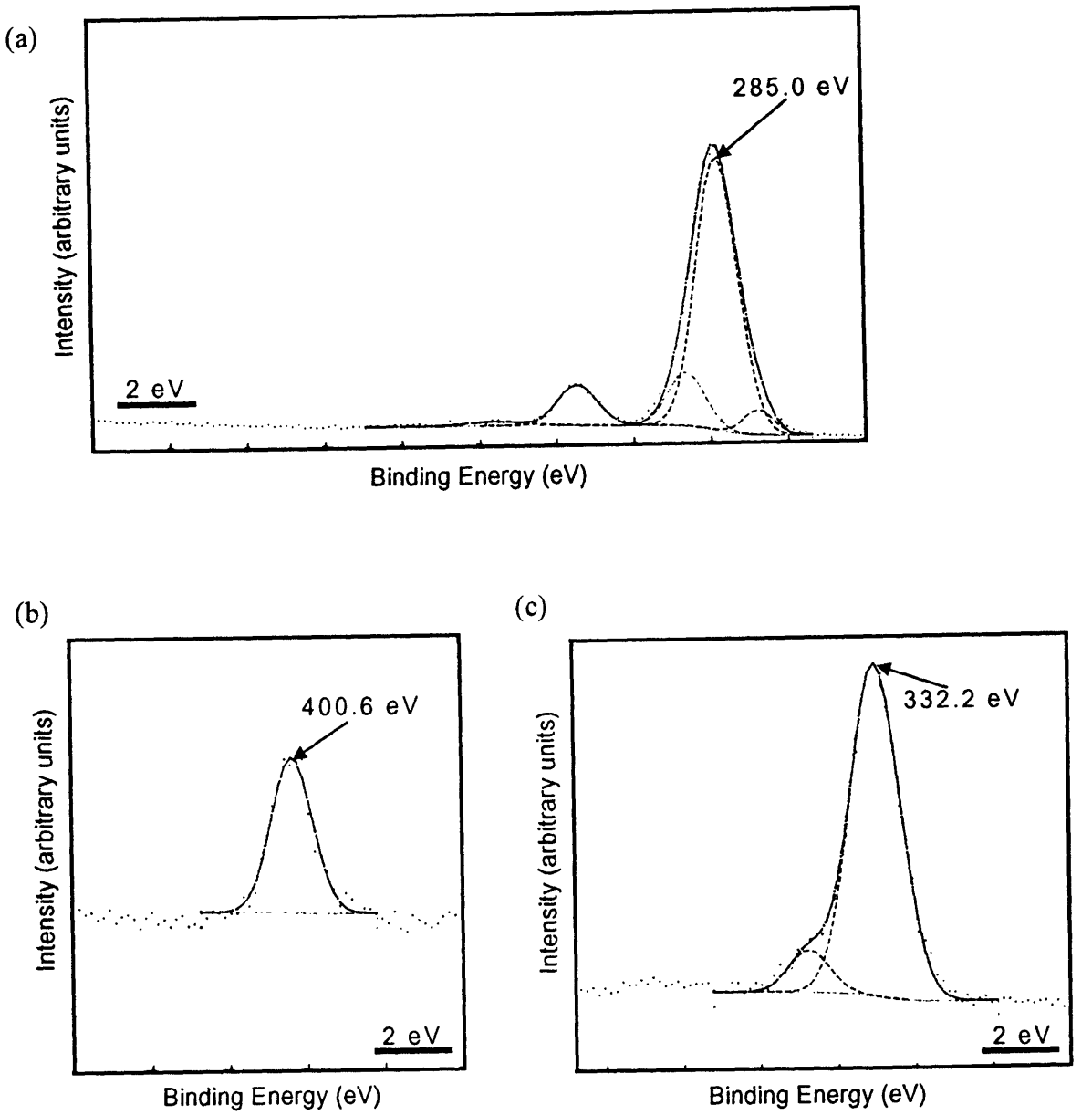

Figure 5.4.1: BPDA-PDA reference spectra: (a) carbon 1s, (b) nitrogen 1s, (c) oxygen 1s.

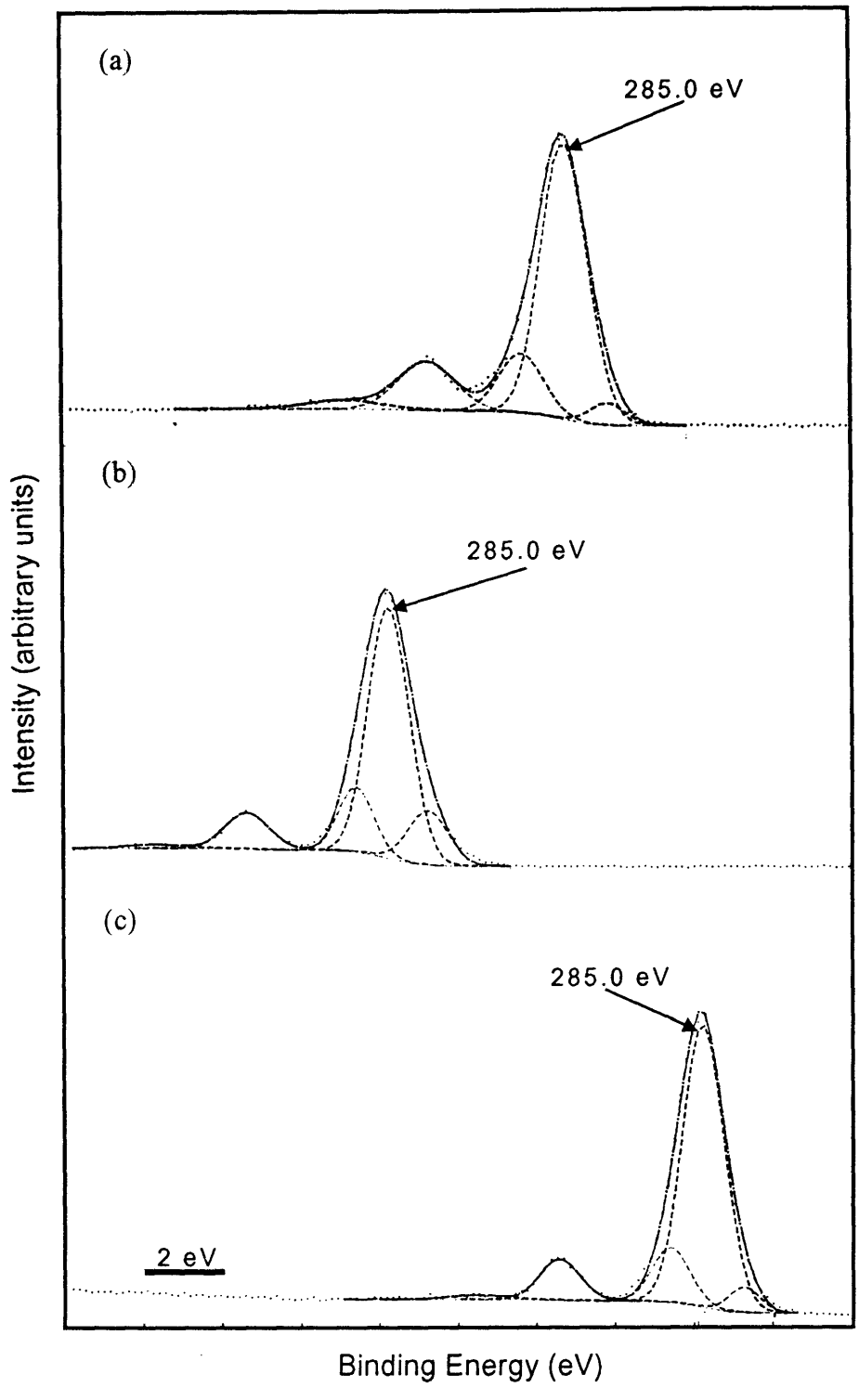

Figure 5.4.2: Carbon (1s) spectra of BPDA-PDA on Cr: (a) island side of IBT fracture, (b) substrate side of peel fracture, (c) reference spectrum.

No significant differences among these spectra are found indicating that the residual polyimide left behind on the adherend is not degraded or modified for either test. A small amount of oxidized Cr (~2 atomic % Cr) is found on the adherend side of the fracture in both cases. The failure appears to be almost entirely cohesive in an unmodified region of the polyimide. Nagarkar [119] and Lu *et al.* [143, 144] have found the appearance of a new peak positioned at ~286.7 eV when thin films of PI2611 are cured on Cr coated substrates. They attribute this peak to the reaction of the polyimide with the Cr. This new peak is not seen on the fracture surfaces studied in this work. This may be an indication that the residual polyimide left on the substrate is too thick to allow for probing of the interfacial reaction products. In the work of [143], a strong Cr signal was detected at a take-off-angle of 90° indicating that the interface was very close.

Table 5.4.3: Peak assignments and energy levels for BPDA-PDA on Cr. Peak positions are listed with relative intensities in parenthesis. Cr reference data shown in brackets is taken from [121].

Atom	Association	IBT (film)	IBT (island)	Peel (film)	Peel (substrate)	Reference
C	?	-1.2 (15)	-1.1 (3)	-0.8 (12)	-1.0 (13)	-
	C-H$^{BPDA-PDA}$	285.0 (57)	285.0 (65)	285.0 (58)	285.0 (63)	285.0 (71)
	C-N	+1.0 (12)	+1.1 (14)	+1.0 (5)	+1.0 (14)	+0.9 (13)
	C=O	+3.5 (13)	+3.5 (14)	+3.4 (12)	+3.6 (10)	+3.6 (10)
	π-π^*	+5.6 (3)	+5.7 (3)	+5.5 (3)	+6.0 (1)	+5.9 (1)
N	isoimide?	-1.3 (21)	-	-	-1.4 (10)	-
	C-N	400.3 (79)	400.3	400.3	400.5 (90)	400.6
O	Cr_2O_3	-	530.3 (17)	-	530.7 (16)	[530.3-530.6]
	C=O	531.8 (97)	531.9 (67)	531.8 (90)	532.1 (78)	532.2 (91)
	C-O	534.0 (3)	533.7 (16)	-	533.8 (6)	533.9 (13)
	π-π^* (?)	-	-	537.5 (10)	-	-
Cr	Cr_2O_3 ($2p_{3/2}$)	-	576.3 (56)	-	576.9 (63)	[576.6 (67)]
	Cr_2O_3 ($2p_{1/2}$)	-	+9.1 (44)	-	+9.8 (37)	[+9.7 (33)]

Comparison of Figures 5.4.2 (a) and (b) illustrates the similarity between the IBT and the peel fracture surfaces. Both occur almost entirely within the polyimide but exhibit 2 atomic percent of oxidized Cr. It is interesting to note that this is the same amount of metal discovered on the adherend side of PMDA-ODA on Cr fractures.

5.4.3 BPDA-PDA on AlCr

The following spectra were derived from IBT samples fabricated by spin casting two coats of BPDA-PDA on Si wafers metallized with 50 nm Cr followed by 50 nm Al. Figure 5.4.3 illustrates the degraded nature of the carbon (1s) spectra of (a) the film and (b) the island sides of the fracture surface relative to (c) the reference spectra. The island side has Al predominantly in the oxidized form as demonstrated by the peak at 74.7 eV in the Al (2p) spectrum and the peak at 531.3 eV in the O (1s) spectrum. The stoichiometry on the film side is close to theoretical while that on the island side is skewed by the strong aluminum oxide presence (Table 5.4.2).

The island side of the fracture surface was examined using SEM and AES. The results closely match those from the PMDA-ODA on AlCr samples presented in Section 5.3. The feature size and density is similar. Sputter profiling indicates that the residual polyimide in the matrix areas is somewhat thicker than in the PMDA-ODA case. The conclusion then is that the failure is again mixed mode, a combination of cohesive failure in the polyimide and adhesive failure between the polyimide and the oxidized metal features.

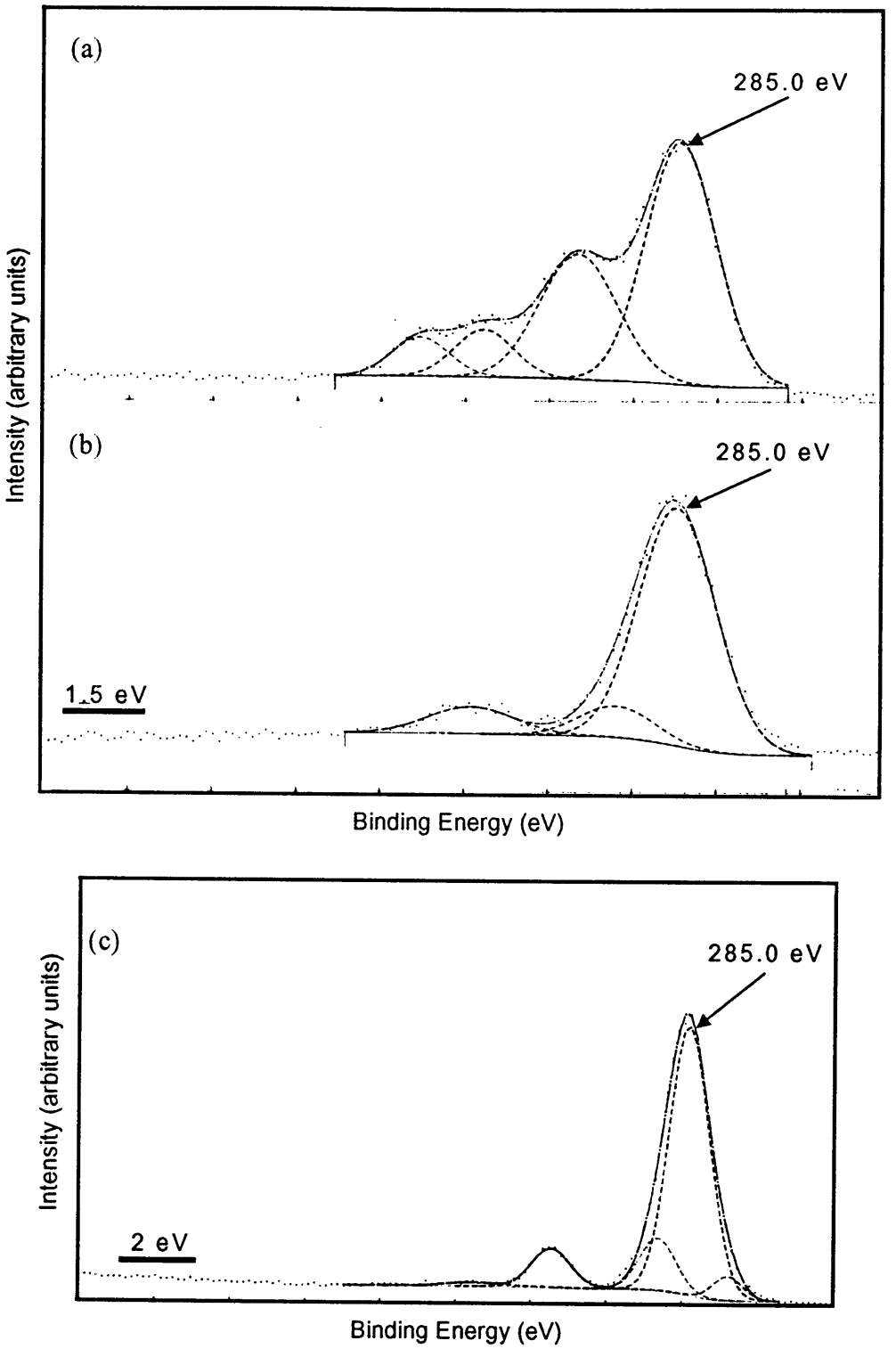

Figure 5.4.3: Carbon (1s) spectra of BPDA-PDA on AlCr: (a) film side of IBT fracture, (b) island side of IBT fracture, (c) reference spectrum.

Table 5.4.4: Peak assignments and energy levels for BPDA-PDA on AlCr. Peak positions are listed with relative intensities in parenthesis. Al reference data shown in brackets is taken from [119].

Atom	Association	IBT (film)	IBT (island)	Peel (film)	Peel (substrate)	Reference
C	?	-	-	-1.1 (8)	-1.0 (10)	-
	C-H$^{BPDA-PDA}$	285.0 (54)	285.0 (80)	285.0 (68)	285.0 (64)	285.0 (71)
	C-N	+1.8 (31)	+1.1 (10)	+1.0 (7)	+0.9 (16)	+0.9 (13)
	C=O	+3.5 (9)	+3.7 (10)	+3.5 (12)	+3.6 (9)	+3.6 (10)
	π-π^*	+4.6 (7)	-	+5.8 (5)	+5.7 (1)	+5.9 (1)
N	isoimide (?)	-	-	-	-	-
	C-N	400.1	400.6	400.2	400.6	400.6
O	Al_2O_3	-	531.3 (77)	-	-	[531.6]
	C=O	531.7 (64)	532.5 (23)	531.8 (87)	532.2 (94)	532.2 (91)
	C-O	532.1 (36)	-	533.5 (9)	534.0 (6)	533.9 (13)
	π-π^* (?)	-	-	536.5 (4)		-
Al	Al	-	71.9 (10)	-	-	[72.0-72.7]
	Al_2O_3	-	74.7 (90)	-	75.0 (68)	[74.0-74.7]
		-	-	-	76.4 (32)	

Peel samples were fabricated by evaporating 50 nm Cr followed by 1 μm Al. The fracture surface of these samples looks very different than the IBT. The surface of the substrate is marked by a series of linear features that run in a direction perpendicular to the peel direction (Figure 5.4.4), indicative of stick-slip peeling behavior. XPS analysis indicates that the adherend fracture surface contains unmodified polyimide (Figure 5.4.5) with a significant amount of Al present. The lower energy Al (2p) peak roughly corresponds to an oxide although it is still high in energy for such an assignment. The higher energy peak is beyond any conventional assignment for an aluminum compound. The oxygen (1s) spectrum shows no signs of a metal oxide peak. There is a trace amount of Si found on the substrate side, although this is not unusual and was found on the

(a)

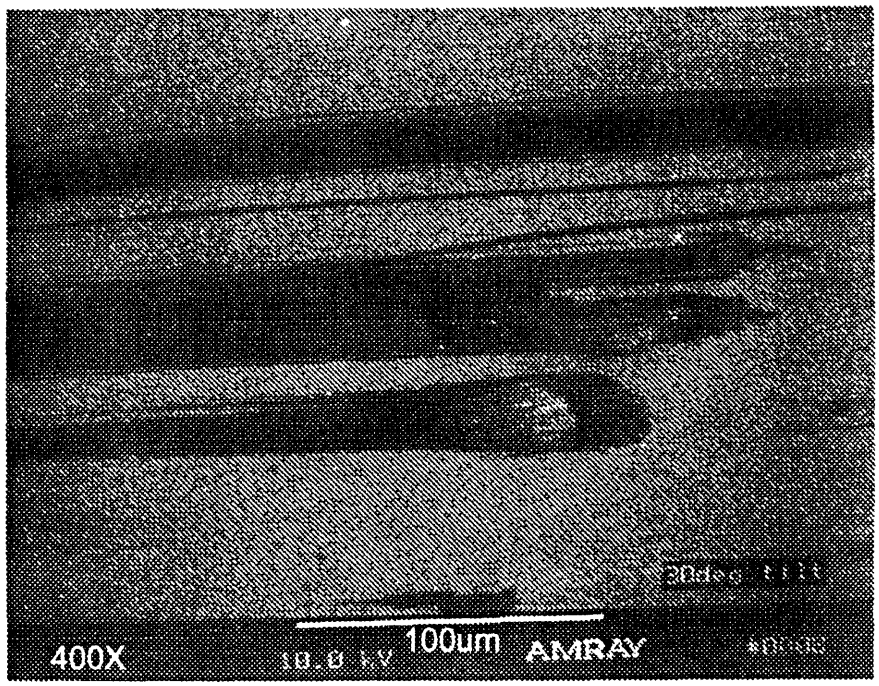

(b)

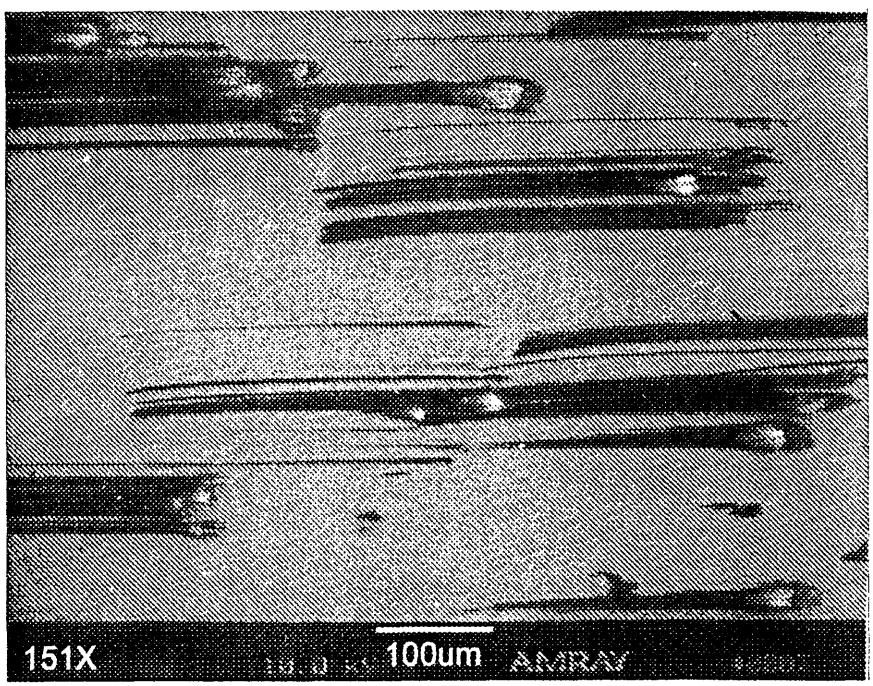

Figure 5.4.4: SEM micrographs of substrate side of BPDA-PDA on AlCr peel fracture: (a) 400X magnification, (b) 150X magnification.

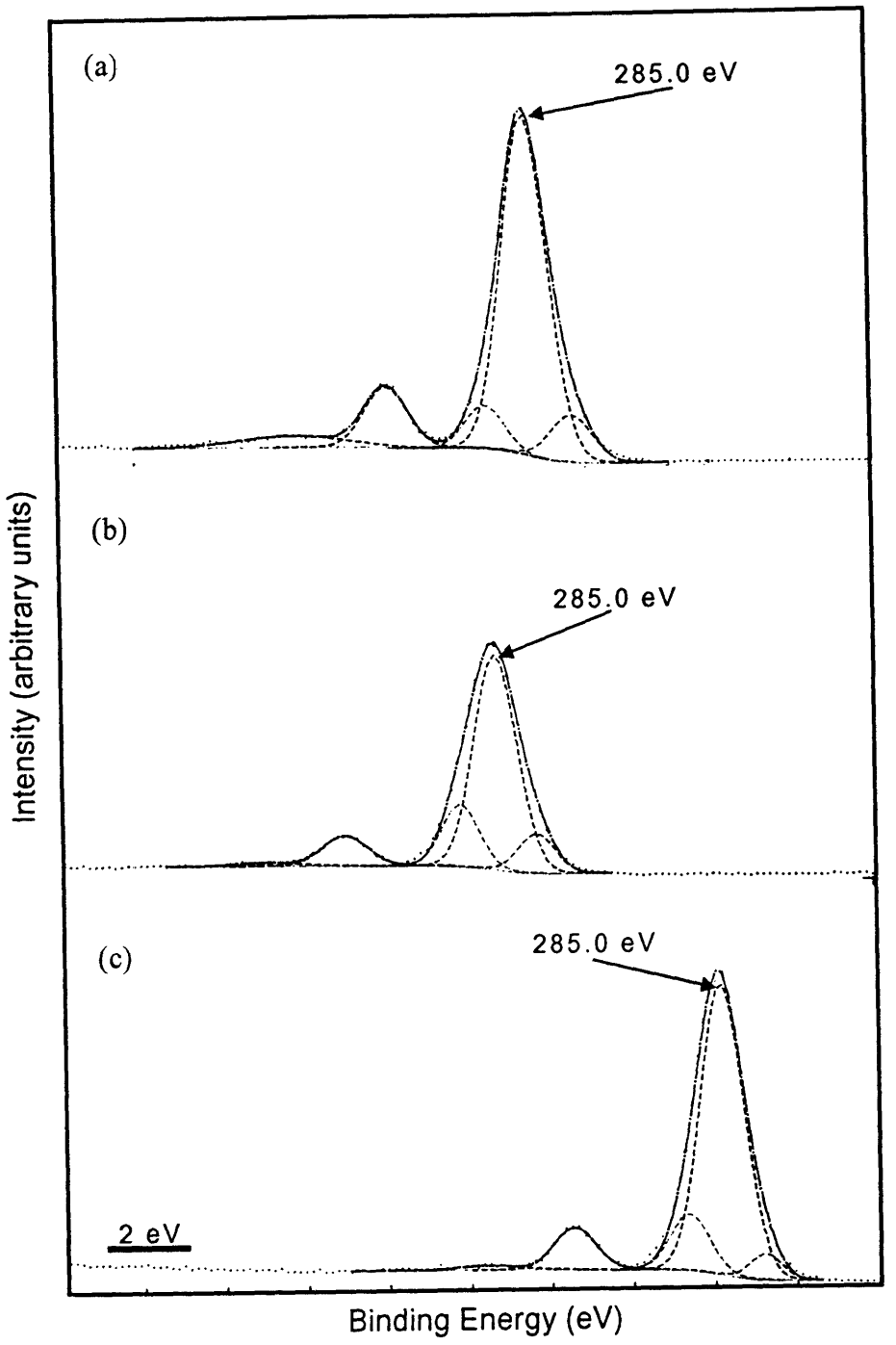

Figure 5.4.5: Carbon (1s) spectra of BPDA-PDA on AlCr: (a) film side of peel fracture, (b) substrate side of peel fracture, (c) reference spectrum.

substrate side of almost all of the peel samples. The energy of the Si peak is also quite high, beyond the energy of pure Si or of the oxide. No Cr is seen on either the film or the substrate sides indicating the Cr is not delaminating from the Si and the Al is not delaminating from the Cr. No explanation for this phenomenon is evident.

The stoichiometry of the fractures surfaces created by peel and island blister testing agrees very well. Approximately 23-24 atomic % Al is detected on the adherend side of both and both are rich in oxygen. The topography of the fracture surfaces are markedly different, however, as explained above.

Summary

BPDA-PDA on Cr samples fail cohesively in the polyimide for both the IBT and the peel test. No differences in locus of failure are found between the two tests. For BPDA-PDA on AlCr, the situation is more complex. A combination of XPS, AES, and SEM suggests that the IBT failure is similar to that of PMDA-ODA on AlCr. A series of features identified as oxidized aluminum create pockets of adhesive failure on a background of cohesive fracture in the polymer. Presumably in these areas the metal is able to form a solid bond with the polymer and the failure is pushed up into the bulk of the polymer itself. The topography left behind by peeling BPDA-PDA off AlCr is very different than either the IBT case for the same system of for PMDA-ODA on AlCr (peel or IBT). A series of brush strokes are left running perpendicular to the direction of crack propagation. It would be interesting to use AES to compare the chemical composition of these features to the background matrix.

5.5 Summary

The results of the surface analysis work presented in this chapter are summarized in Table 5.5.1. The major conclusions are stated below:

- The locus of failure created by the IBT and the peel test is similar for the debonding of Ultradel 4212, PI2545, and PI2611 from Cr and AlCr adherends.

- All three polyimides exhibit almost exclusively cohesive failure in the polyimide when debonded from Cr.

- The decrease in measured γ_{Ic} on samples with non-optimal process histories is explained through the XPS analysis as originating from a degraded carbon (1s) spectrum and an increased fraction of adhesive component in the fracture.

- All three polyimides exhibit a mix of cohesive failure in the polyimide and adhesive failure at the interface between the polyimide and oxidized features in the Al film. The adhesive component of the failure is the cause of the reduction in γ_{Ic} relative to the polymer-on-Cr case.

- For a given polyimide, high values of γ_{Ic} are associated with cohesive fracture in the pristine polyimide. There should only be polyimide-related peaks on both sides of the fracture, and they should be sharp and positioned correctly.

- The three techniques (XPS, SEM, AES) applied in this section are well suited to the analysis of fracture surfaces.

At the beginning of this section, the goal of this section was stated as being (a) determination of the locus of failure for the systems studied and (b) correlation of these results with the adhesion data presented in Chapter 4 in an attempt to provide a basis for

understanding variations in γ_{Ic}. The findings listed above suggest that these goals have largely been met.

Table 5.5.1: Summary of locus of failure studies. Fracture energies are expressed in J/m^2.

System	Test	γ_{Ic}, γ_a	Film Side	Adherend Side	Locus of Failure
UD4212-Cr$^{High\ Qual}$	IBT	105	Pristine PI	Pristine PI 0.2% Cr (oxide)	cohesive in PI
UD4212-Cr$^{Low\ Qual}$	IBT	60	Degraded PI	Degraded PI 6% Cr (oxide)	mostly cohesive in PI; some adhesive
UD4212-Cr	Peel	425	Pristine PI	PI; no F-related C(1s) 7% Cr (oxide)	mostly cohesive in PI; some adhesive
UD4212-AlCr	IBT	27	Pristine PI	PI; no F-related C(1s) 40% Al (oxide, fluoride)	~equally cohesive in PI, adhesive
UD4212-AlCr	Peel	105	Pristine PI	PI; no F-related C(1s) 40% Al (oxide, fluoride)	~equally cohesive in PI, adhesive
PI2545-Cr	IBT	175	PI	PI; 1% Cr (oxide)	cohesive in PI
PI2545-Cr	Peel	180	Pristine PI	PI; no ester C(1s); 2% Cr (oxide)	cohesive in PI
PI2545-Al	IBT	30	Pristine PI	Degraded PI; 6% F 28% Al (oxide)	~equally cohesive in PI, adhesive
PI2545-AlCr	IBT	19	Pristine PI	Degraded PI; 4% F 28% Al (oxide)	~equally cohesive in PI, adhesive
PI2545-AlCr	Peel	90	Pristine PI	Degraded PI 29% Al (oxide, fluoride)	~equally cohesive in PI, adhesive
PI2611-Cr	IBT	90?	Pristine PI	Pristine PI 2% Cr (oxide)	cohesive in PI
PI2611-Cr	Peel	530	Pristine PI	Pristine PI 2% Cr (oxide)	cohesive in PI
PI2611-AlCr	IBT	26	Degraded PI	PI; 1% F 23% Al (oxide)	~equally cohesive in PI, adhesive
PI2611-AlCr	Peel	380	Pristine PI	Pristine PI 24% Al (oxide?, other?)	~equally cohesive in PI, adhesive

Chapter 6: Conclusions and Summary

The goals of this work as stated in Chapter 1 were, (i) to refine the IBT into a technique capable of accurately providing the specific fracture energy broken down into its constituent loading modes, and (ii) to apply the refined test to define a fracture criterion relevant to these systems, to rank interfacial fracture strength for polyimide on metal systems, and to evaluate the utility of the widely used peel test.

Refinements in the IBT

Refinements of the IBT occurred in the areas of sample fabrication, testing protocol, and data analysis. The currently recommended polymer on metal sample fabrication procedure involves back side patterning with photosensitive polyimide, using a bilayer of Cr deposited on silicon nitride as an etch stop, and etching through the silicon with an HF-based solution. Sample yield is higher and fabrication time is reduced relative to the previously described method. The testing methodology is now rigorously defined including institution of a standard criterion to define the onset of crack propagation. Implementation of automated pressure control greatly reduces operator dependencies on the outcome of the test. Usage of a retain pin to secure the island during initial debond further improves testing yield.

Application of the finite element model developed by Margaritis enabled separation of the mode I and mode II components of the specific fracture energy. Testing of several polyimide on metal systems immediately lead to the conclusion that the initiation of the fracture process was governed by satisfaction of:

$$\gamma_I = \gamma_{Ic}$$

This result is independent of film thickness and does not appear to dependent on the degree of mode II loading as predicted by other researchers for interfacial fracture. The reproducibility of the IBT was demonstrated for the UD4212 on Cr system where γ_{Ic} was found to be 54 J/m^2 with a standard deviation of 7 J/m^2 across 12 samples.

UD4212 on Cr was used as a baseline case for an error analysis of the test. The important experimental parameters were systematically perturbed and the effect on the calculated γ_{Ic} was observed using an elasticity-based version of the FEM. This allowed creation of a series of relationships that described γ_{Ic} as a function of one experimental parameter each. These functions were combined to form a multivariable expression of γ_{Ic} as a function of all the experimental parameters. The error in γ_{Ic} was then calculated by estimating the error in each parameter and applying a standard propagation of error analysis to determine its ultimate effect on γ_{Ic}. The error is estimated at being ~13%. The error in γ_{Ic} contributed from the modeling of the plastic behavior of the film was explored by inputting different representation of the plasticity and comparing calculated values of γ_{Ic} with the baseline case. For the particular case explored, the change in plasticity models resulted in only ~2% change in γ_{Ic} for a total estimated error of ~15%, in good agreement with the reproducibility study mentioned above. The numerically derived function accurately predicts the values of γ_{Ic} based on the critical pressure, the site geometry, and film's modulus and residual stress level for all systems studied except PI2545 on Cr, where the plasticity is most extreme. This analysis coupled with a similar one of the stress level in the film provides a design tool for the prediction of whether a certain combination of geometry and mechanical properties will result in film debonding or film rupture.

One anomaly is that γ_{Ic} increases as the test proceeds. This effect is hypothesized to be caused by plastic history effects resulting from the cyclic nature of the loading and unloading of the test. The material model of the film was modified to provide a variable yield point depending on the location of the element relative to the island. The one run done with this modified materials model eliminated the effect substantiating the hypothesis. However, it is possible that viscoelastic effects such as stress recovery are also operative. To avoid complications, the first data point from each test is the only one used.

Ranking Based on γ_{Ic}

All three polyimides studied, PI2545, PI2611, and UD4212, had higher measured values of γ_{Ic} on Cr than on Al. Locus of failure analysis indicates that high values of γ_{Ic} are invariably associated with cohesive failure in the polyimide but close to the interface. The Al samples all showed a mixed locus of failure involving both cohesive fracture in the polymer and adhesive failure at the interface. Auger electron spectroscopy data suggest that the interfacial component may result from areas of excessive oxidation in the Al film. Fluorine contamination from the fabrication process was also detected and its influence on γ_{Ic} is unknown. Increasing the thickness of the silicon nitride etch stop layer is expected to eliminate such processing artifacts. The adhesion of each of the polyimides on Al ranged from 17 to 32 J/m^2. In all cases adhesion to Cr was more tenacious ranging from 54 - 175 J/m^2 with PI2545 being at the high end, UD4212 at the low end and PI2611 in the middle of this range.

The effects of processing were also seen in the case of UD4212 on Cr. Samples with the adherend metal evaporated at room temperature or allowed to sit in ambient for extended periods prior to application of the polymer adhered less well than those deposited at 175°C and coated

immediately after metallization. X-ray photoelectron spectroscopy of the locus of failure shows degraded looking polyimide on the island side of the fracture of the former samples, differing from the more pristine looking polymer found on the later. This result was also reproducible. There is evidence that in fluorinated polymers [123], optimal adhesion strength to metals is contingent upon formation of a metal fluoride at the interface. Nagarkar *et al.* [122] has shown that UD4212 can react with Cr and Al to form a fluoride. It is hypothesized here that the decrease in γ_{Ic} for the "poor quality" Cr samples is caused by excessive oxidation of the Cr adherend prior to polyimide apply hindering the reaction with the polyimide which would otherwise result in metal fluoride formation. The present work provides no direct evidence of the formation of a fluoride, but it does indicate that the higher fracture energy possible in UD4212 on Cr is interruptable. This has immediate implications for the processing of these polymers in a manufacturing scenario. The recommendation is to limit the amount of time allowed to expire between the high temperature metallization and application of the polyimide.

The surface analysis of the locus of failure presented earlier in this work amply demonstrated that in cases of strong adhesion, the failure surface moves into the polyimide. Creating a good interfacial bond between the metal and the polymer is only the first step; the polymer itself cannot be degraded leading to weak, cohesive failure in it.

The Mises criterion is applied to gauge the extend of far-field plasticity in the film. For the case of the Cr adherend, the membrane portion of the film is plastically deformed a distance of over 100 film-thicknesses away from the crack tip. In these cases, the stresses in the film near the crack tip approach the ultimate tensile strength of these polymer films. Overall, the plastic dissipation in the film was seen to be very significant relative to the specific fracture energies,

often being several times larger in magnitude. These high stress levels in the film emphasize the need to account for dissipative mechanisms.

Comparison of the IBT and the Peel Test

The technique of Kim *et al.* [15] for subtracting out the plastic component of work dissipated in the peel test was used to evaluate peel data from the same systems as tested with the IBT. A complete analysis requires knowledge of the peel angle local to the crack tip. Since this information was not collected, the best that could be done was to determine what that angle had to be to provide specific fracture energy values similar to those from the IBT. These angles were in the range of 10-30° a seemingly sensible range and comparable to the 8-18° found for the IBT. The system demonstrating poor agreement was again PI2545-Cr which showed a particularly low peel values. This system is the least likely to satisfy the assumptions which form the basis of the modified peel analysis, however. XPS offered no explanation of the low peel energies measured for this system.

A comparison with the IBT of the rankings based on the specific fracture energy for the peel test is not possible since the peel angle required for that calculation was not measured during the test. Based on the measured peel energy from the peel test, the two tests produce quite different rankings (Table 6.1.1). The differences in rankings for the cases on the Cr adherend are attributed to unaccounted for plasticity effects in the peel test. For the cases of the AlCr adherend, The IBT gives approximately the same γ_{Ic} value (~27 J/m^2) for all the polyimides tested. The peel test shows similar values for UD4212 and PI2545 on AlCr but a much higher value for PI2611 on AlCr. Processing related artifacts in the IBT samples may be

playing a role in this difference. Fluorine was detected at the locus of failure of the IBT samples by XPS analysis, the effect of which on the integrity of the interface is unknown.

Table 6.1.1: Comparison of relative rankings of adhesion in the material systems studied based on mode I specific fracture energy (γ_{Ic}) from the IBT with the peel energy (P) measured from the peel test.

Ranking	IBT	Peel Energy (P)
Highest	PI2545-Cr	UD4212-Cr
	PI2611-Cr	PI2611-Cr
	UD4212-Cr	PI2611-AlCr
	UD4212-AlCr	PI2545-Cr
	PI2611-AlCr	UD4212-AlCr
Lowest	PI2545-AlCr	PI2545-AlCr

Other than the detection of processing-related fluorine in the IBT polyimide on AlCr samples, both tests resulted in the same locus of failure. This is an important result that indicates that either (i) the mixity of loading mode at the crack tip is similar for the two tests, or (ii) the mode mixity is not important in determining the locus of failure in these heavily plastically deformed systems. The former conclusion is consistent with the relative values of the peel angles required to give numerically comparable result for the total specific fracture energies for the two tests.

Overall, the peel test is found to be insufficient to satisfy the development need for an adhesion test the requirements of which were stated in Chapter 1. The IBT is decidedly superior in its ability to account for plastic dissipation and to separate the mode I and mode II components. This last ability is particularly relevant to the case of modeling structures since the

fracture criterion stated earlier for these systems was based on the mode I contribution and not the total fracture energy.

One apparently fruitful area of future work is application of the modified crack closure methodology used here for the IBT to the peel test. Successful accomplishment of this would (i) eliminate the need for actual measurement of the peel angle, (ii) decouple the mode I and mode II contributions, and (iii) account for the plastic dissipation. Such work would be especially useful if a simple relationship such as Equation 3.3.1 could be derived, ultimately eliminating the need for the computationally intensive analysis that will surely be required. Such a tool would be extremely useful to practitioners of thin film adhesion tests.

Finally, a cursory study of the metal on polymer case indicates the need for further development work. The high stresses experienced at the crack tip during debonding cause the adhered metal film to crack, absorbing energy and confounding the results of the test. Using a polyimide backing layer and analyzing only the first p_c, r_i data set offer ways of minimizing the effects of film cracking on the measurement of the specific fracture energy. A more accurate analysis of the metal on polymer structure requires incorporating the metal adherend into the FEA. However, it appears that the film cracking effect will still result in a larger scatter in the data than reported for the polymer on metal case.

Appendix A: IBT Sample Fabrication Process Details

1. Wafer preparation:

a Pirahna Clean: immerse wafers in 3:1 by volume solution of sulfuric acid and hydrogen peroxide for 10 minutes. Dump rinse. Spin rinse/dry (160/240 sec).

b Dehydration Bake: bake at 200°C for 30 minutes.

2. Back Side Patterning:

a Cr Evaporation: e-beam evaporate 50 nm Cr at 5 A/s, room temperature, vacuum of better than 3 x 10^{-6} torr.

b PD2721 Apply: spin apply 4 ml PD2721 at 2200 rpm for 60 sec. Softbake for 120 minutes at 55°C, 2 minutes at 60°C, and 2 minutes at 120°C.

c PD2721 Expose/Develop: Expose at 11.2 mW/cm^2 for 80 seconds through appropriately patterned glass mask. While spinning at 1000 rpm, spray developer (D1209) for 50 sec, developer and rinser (R3210) together for 7 sec, and rinser alone for 20 sec. Let spin dry for at least 20 sec.

d PD2721 Cure: cure according to schedule shown in Appendix 4.2.

3. Front Side Processing:

a Plasma Clean: expose the front of each wafer to a 200 W O_2 plasma (25 sccm flow) at 200 mtorr for 5 min.

b Oxide Removal: immerse wafers in BOE solution for 1 min or until dewetting occurs. Dump rinse. Spin rinse/dry (160/240 sec).

c Metal Evaporation: e-beam evaporate 50 nm Cr at 175°C, 5 A/s, vacuum better than 3 x 10^{-6} torr; without breaking vacuum, e-beam evaporate adherend metal. For Al, rate of 7 A/s, vacuum better than 3 x 10^{-6} torr. Dome rotation ON to ensure good uniformity of deposit thickness. For metal-on-polymer samples, Cr can be deposited at room temperature.

d Polymer Apply: spin apply polymer of interest at appropriate speed. Softbake Ultradel for 30 min at 100°C. Softbake PI2545 or PI2611 for 30 min at 80-90°C.

e Polymer Cure: cure according to schedules shown in Appendix 4.2.

f Metal Evaporation *(for metal-on-polymer samples only)*: e-beam evaporate 50 nm Cr at 175°C, 5 A/s, vacuum better than 3 x 10^{-6} torr; without breaking vacuum, e-beam evaporate adherend metal. For Al, rate of 7 A/s, vacuum better than 3 x 10^{-6} torr. Dome rotation ON to ensure good uniformity of deposit thickness.

g Polymer Apply *(for metal-on-polymer samples only)*: spin apply polymer of interest at appropriate speed. Softbake Ultradel for 30 min at 100°C. Softbake PI2545 or PI2611 for 30 min at 80-90°C.

h Polymer Cure *(for metal-on-polymer samples only)*: cure according to schedules shown in Appendix 4.2.

4. Back Side Etching:

a Cr Etch: mount wafer in etching fixture. Etch Cr with perchloric acid ceric ammonium nitrate solution for 5-10 min. Rinse with DI H_2O.

b Si Etch: fill fixture half full with 6:1:1 parts by volume of hydrofluoric acid, nitric acid, and acetic acid. Siphon solution off after 3 min and refill. Siphon solution off after 3 min and refill. Etch should be complete within another ~1 min. Watch carefully to avoid overetching. When etching is complete, douse with DI H_2O to arrest etching. Rinse under tap water for at least 10 min. Remove from fixture, rinse with DI H_2O and blow dry.

c Polymer Etch *(metal-on-polymer samples only):* etch polymer in an O_2 plasma, 200 W, 25 sccm, 200 mtorr. Etch rate is approximately 0.5 μm/min.

d Metal Etch *(metal-on-polymer samples only):* wet etch metal layer. If Cr use hydrochloric acid diluted ~5:1 with DI H_2O. If Al, use standard etchant warmed to 50°C.

5. Final Preparations:

a Dicing: using diamond scribe, dice wafers into quarters. If desired, each quarter can be further diced into a square.

b Mount Island: smear a drop of cyano acrylate adhesive onto a 2" x 2" piece of PMMA that has a 3/32" hold drilled in its center. Press the island of the diced sample into the smear of adhesive. Rest the wafer and PMMA on a flat surface. place a piece of lent-free cloth over the island and place a wieght on the cloth to continue to apply pressure to the island/PMMA joint. Let sit like this at least 3 hours.

c Edge Seal: seal the edge of the sample with Duco 540 two-part epoxy. Let sit at least 3 hours. Alternatively, cyano acrylate adhesive can be applied to the entire back side of the wafer in step 5.b. This works well if there is relatively little etching damage such as pits on the back of the wafer, otherwise the seal may be compromised.

Appendix B: Polyimide Cure Schedules

Material	Soft Bake (in air)	Ramp Rate (°C/min)	Dwell Temp. (°C)	Dwell Time (min)	Ambient
PD2721	55°C - 120 min	4.5	150	30	air
	60°C - 2 min	2.0	300	30	air
	110°C - 2 min	2.0	400	45	N_2
UD4212	100°C - 30 min	4.0	100	10	N_2
		4.0	160	20	N_2
		4.0	200	30	N_2
		15.0	350	60	N_2
PI2545	85°C - 30 min	4.0	150	30	N_2
PI2611		4.0	230	30	N_2
		4.7	300	30	N_2
		1.7	380	60	N_2

Appendix C: IBT Testing Procedure

I. Power-Up

a. Make sure that the testing apparatus is not under pressure. Pressure controls are located on the wall to the right of the testing station. The system is under no pressure if the black knob to the left of the Main N_2 valve is turned all the way clockwise.

b. Turn ON the two power strips located on the shelf under the testing apparatus.

c. Turn ON the light source by rotating the knob on the face of the power transformer located to the left of the scope clockwise until the green bar lights up to around 5V. This can be adjusted later to provide the appropriate amount of illumination.

d. Turn on the video monitor (Panasonic model TD 930B) by pressing the power button.

e. Turn ON the VCR located on the shelf unit to the left of the scope.

f. Turn ON the Digimatic Multiplexer MUX-10.

g. Turn ON the HP power supply and multimeter located on the bottom shelf under the scope.

h. Turn ON the IBM XT computer (the circle indicates the OFF position).

i. Load the automated pressure controller software on the computer as follows:

   1. Move to the servo directory by typing `cd servo`
   2. Run the software by typing `servo30p`
   3. Select *indirect* control and a reaction parameter of 5.
   4. Make sure the valve is in the fully OPENED position. If it is not, open the valve by typing `P` and then 18000.
   5. Select the start and end ramp pressures appropriate to the system under test.
   6. Select a ramp time that results in a ramp rate of 1.0 psi/min.

   At this point, pressure readings should appear on the computer screen.

NOTE: If the system was correctly powered-down by the previous user, turning on the two power strips will activate all required equipment *except* for the computer.

II. Mounting

a. Place the IBT vehicle on the Nikon microscope stage, being sure that the hole in the baseplate of the IBT vehicle is contained within the o-ring on the stage.

b. Place the retaining plate over the IBT sample with the cut-out centered over the membrane. Secure the plate to the stage by hand-tightening the four screws.

III. Development of Circular Crack Front

a. Position the retaining pin such that the center of the pin coincides with the center of the island.
b. Slowly lower the scope objective until it contacts the top of the retaining pin. Lower the objective ~5μm more to secure the retaining pin between the island and the objective.
c. Turning the knob to the left of the Main N_2 valve all the way counter-clockwise, and slowly moving the green toggle valve from the 6 o'clock CLOSED position towards the 9 o'clock FULLY OPEN position. The pressure should be in the range of 0.75-1.5 psi.
d. Start the pressurizing of the blister by typing "G" for GO.
e. Once the debonding proceeds to the point where it has initiated from the entire periphery of the island and has formed a circle, discontinue ramping the pressure up load by pressing ENTER. Reduce the load by typing in a new valve position, one closer to the open position.
f. When the pressure is well below the critical pressure, raise the microscope objective and remove the retaining pin apparatus.

IV. Procurement of Data

a. Bring the pressure to approximately 0.75 p_c.
b. Focus on the crack front at 400X (using 40X objective). Position the crack front, which should now appear white, just in front of one of the dashed lines appearing on the screen (two vertical, two horizontal).
c. Input a ramp rate of 0.1 psi/min.
d. Observe the crack front on the monitor until the white area representing crack front overlaps the dashed line. Note the pressure at this point. This is the *critical pressure*. Allow the crack front to move in approximately 0.1 mm.
e. Decrease pressure by 1 psi. Move the dashed line just in front of the crack again.
f. Measure the diameter of the bonded area, 2 r_c, at 50X.
h. Start over again at step IV a. Repeat this cycle as many times as desired. Each pair of (r_c, p_c) provides one measure of interfacial fracture toughness, G_c.

V. Sample Removal

a. Remove pressure load by returning the green toggle valve to the vertical 6 o'clock position. Turn the knob to the left of the Main N_2 valve all the way clockwise. Open servo valve by typing "P" and then 18000.
b. Bring the scope objective all the way up.
c. Loosen the mounting screws on the retaining plate and remove the sample. The system is now ready to load the next sample (see III).

VI. Power-Down

a. To power down the servo vale, type "Q" for QUIT to get out of the program. Shut off the power supply using the red button on the front of its casing. Follow the instruction posted at the scope for powering-down the test station. Cover the scope with the plastic cover when done for the day.

b. Use the orange power switch on the computer to turn it OFF.

Appendix D: C Program for Creating ABAQUS Input Decks.

```
#include <stdio.h>
#include <math.h>
main()
{
  int n1, n2, n3, n4, n5, n6, n7, n8, n9;
  int m1, m2;
  int k1, k2;

  int k;
  float t, r1, r2, p, sr;

  scanf("%d", &k);
  scanf("%f", &t);
  scanf("%f", &r1);
  scanf("%f", &r2);
  scanf("%f", &p);
  scanf("%f", &sr);

  k1 = (int)((r1*k)/r2);
  k2 = k - k1;
  m1 = 2 * k1;
  m2 = 2 * k2;

  n1 = 1;
  n2 = n1 + m1;
  n7 = n2 + m2;
  n3 = n7 + 1;
  n4 = n3 + m1;
  n8 = n4 + m2;
  n5 = n8 + 1;
  n6 = n5 + m1;
  n9 = n6 + m2;

  printf("*HEADING\n");
  printf("IBT - ELASTIC/PLASTIC ANALYSIS\n");
  printf("*PREPRINT, HISTORY=NO, MODEL=NO, ECHO=NO\n");
  printf("*NODE\n");
  printf("%d, 0, 0\n", n1);
  printf("%d, %5.3f, 0\n", n2, r1);
  printf("%d, 0, %6.4f\n", n3, (t/2.0));
  printf("%d, %5.3f, %6.4f\n", n4, r1, (t/2.0));
  printf("%d, 0, %6.4f\n", n5, t);
  printf("%d, %5.3f, %6.4f\n", n6, r1, t);
  printf("%d, %5.3f, 0\n", n7, r2);
  printf("%d, %5.3f, %6.4f\n", n8, r2, (t/2.0));
  printf("%d, %5.3f, %6.4f\n", n9, r2, t);
  printf("*NGEN, NSET=ALL\n");
```

```
printf("%d, %d\n", n1, n2);
printf("%d, %d\n", n2, n7);
printf("%d, %d, 2\n", n3, n4);
printf("%d, %d, 2\n", n4, n8);
printf("%d, %d\n", n5, n6);
printf("%d, %d\n", n6, n9);
printf("*NSET, NSET=LSUP, GEN\n");
printf("%d, %d\n", n1, n2);
printf("*NSET, NSET=LSUP1, GEN\n");
printf("%d, %d\n", n1, n2-2);
printf("*NSET, NSET=LEFT\n");
printf("%d, %d, %d, LSUP\n", n1, n3, n5);
printf("*NSET, NSET=RIGHT\n");
printf("%d, %d, %d\n", n7, n8, n9);
printf("*NSET, NSET=LEFT1\n");
printf("%d, %d, %d, LSUP1\n", n1, n3, n5);
printf("*ELEMENT, TYPE=CAX8\n");
printf("%d, %d, %d, %d, %d, %d, %d, %d, %d\n", 1, n1,
   n1+2, n5+2, n5, n1+1, n3+2, n5+1, n3);
printf("%d, %d, %d, %d, %d, %d, %d, %d, %d\n", k1+1, n2,
   n2+2, n6+2, n6, n2+1, n4+2, n6+1, n4);
printf("*ELGEN, ELSET=SUP\n");
printf("1, %d, 2\n", k1);
printf("*ELGEN, ELSET=MEMBRANE\n");
printf("%d, %d, 2\n", k1+1, k2);
printf("*ELSET, ELSET=ALL\n");
printf("SUP, MEMBRANE\n");
printf("*ELSET, ELSET=NONE\n");
printf("11\n");
printf("*ELSET, ELSET=SCOTT1, GEN\n");
printf("1, 100, 1\n");
printf("*ELSET, ELSET=SCOTT2, GEN\n");
printf("100, 1000, 25\n");
printf("*ELSET, ELSET=SCOTT\n");
printf("SCOTT1, SCOTT2\n");
printf("*NSET, NSET=ONE\n");
printf("%d, %d\n", n2, n2-1);
printf("*SOLID SECTION, ELSET=ALL, MATERIAL=POLYMER\n");
printf("*MATERIAL, NAME=POLYMER\n");
printf("*ELASTIC, TYPE=ISO\n");
printf("2300, 0.40\n");
printf("*PLASTIC\n");
printf("48.2, 0.0\n");
printf("66.8, 0.012\n");
printf("87.0, 0.030\n");
printf("100.0, 0.046\n");
printf("137.3, 0.063\n");
printf("145.3, 0.079\n");
printf("160.3, 0.142\n");
printf("164.7, 0.181\n");
printf("174.8, 0.238\n");
```

```
printf("*AMPLITUDE, NAME=LOAD, TIME=A, VALUE=R\n");
printf("1.0, 0, 1.5, 0.75, 7.5, 1\n");
printf("*BOUNDARY\n");
printf("LEFT, 1, 2\n");
printf("RIGHT, 1, 2\n");
printf("*INITIAL CONDITIONS, TYPE=STRESS\n");
printf("ALL, %3.1f, 0, %3.1f, 0\n", sr, sr);
printf("*STEP, INC=1, CYCLE=5\n");
printf("*STATIC, PTOL=0.03\n");
printf("1., 1.\n");
printf("*EL PRINT, POSITION=CENTROIDAL, ELSET=NONE\n");
printf("S\n");
printf("*NODE PRINT, NSET=ONE\n");
printf("U\n");
printf("*ENERGY PRINT\n");
printf("ALLSE\n");
printf("*END STEP\n");
printf("*STEP, NLGEOM, INC=100, CYCLE=15, ROTTOL=0.78,
   SUBMAX\n");
printf("*STATIC, PTOL=0.03, DIRECT=NO STOP\n");
printf("0.05, 0.5\n");
printf("*DLOAD, AMPLITUDE=LOAD\n");
printf("MEMBRANE, P1, %6.4f\n", (p/145.0));
printf("*EL PRINT, POSITION=CENTROIDAL, ELSET=NONE,
   FREQ=100\n");
printf("S\n");
printf("*NODE PRINT, FREQ=100, NSET=ONE\n");
printf("U\n");
printf("RF\n");
printf("*NODE PRINT, FREQ=100, NSET=LSUP1\n");
printf("U\n");
printf("*ENERGY PRINT\n");
printf("ALLSE\n");
printf("*END STEP\n");
printf("*STEP, NLGEOM, INC=100, CYCLE=15, ROTTOL=0.78,
   SUBMAX\n");
printf("*STATIC, PTOL=0.03, DIRECT=NO STOP\n");
printf("1.0, 6.0\n");
printf("*DLOAD, AMPLITUDE=LOAD\n");
printf("MEMBRANE, P1, %6.4f\n", (p/145.0));
printf("*EL PRINT, POSITION=CENTROIDAL, ELSET=NONE,
   FREQ=100\n");
printf("S\n");
printf("*NODE PRINT, FREQ=100, NSET=ONE\n");
printf("U\n");
printf("RF\n");
printf("*NODE PRINT, FREQ=100, NSET=LSUP1\n");
printf("U\n");
printf("*ENERGY PRINT\n");
printf("ALLSE\n");
printf("*END STEP\n");
```

```
  printf("*STEP, NLGEOM, INC=100, CYCLE=15, ROTTOL=0.78,
     SUBMAX\n");
  printf("*RESTART, WRITE, FREQUENCY=100\n");
  printf("*STATIC, PTOL=0.03, DIRECT=NO STOP\n");
  printf("0.10, 1.\n");
  printf("*BOUNDARY, OP=NEW\n");
  printf("LEFT1, 1, 2\n");
  printf("RIGHT, 1, 2\n");
  printf("*EL PRINT, POSITION=CENTROIDAL, ELSET=SCOTT,
     FREQ=100\n");
  printf("MISES\n");
  printf("S11\n");
  printf("S22\n");
  printf("S33\n");
  printf("E11\n");
  printf("E22\n");
  printf("E33\n");
  printf("*NODE PRINT, NSET=ONE, FREQ=1\n");
  printf("U\n");
  printf("RF\n");
  printf("*ENERGY PRINT\n");
  printf("ALLSE\n");
  printf("*END STEP\n");
}
```

Appendix E: Sample Xess Spreadsheet for Calculation of Specific Fracture Energies.

IBT Calculation - Sample 45AIP12_2 (20.5 um PI2545-Al, Ri = 0.638 mm, Pc = 2.51 psi, stress=19.8
(K = 1000, PTOL = 0.03, CAX8)

Node 98

Increment	RF1	RF2	U1	U2	Delta U1	Delta U2	ENERGY 1	ENERGY 2
0	0.4739	-0.2582	0	0	4.4532e-05	6.1293e-05	2.0049e-05	-1.5035e-05
1	0.4265	-0.2324	4.4532e-05	6.1293e-05	4.6242e-05	6.3357e-05	1.8627e-05	-1.3905e-05
2	0.3791	-0.2066	9.0774e-05	1.2465e-04	4.6976e-05	6.6020e-05	1.6696e-05	-1.2785e-05
3	0.3317	-0.1807	1.3775e-04	1.9067e-04	5.0020e-05	7.6670e-05	1.5408e-05	-1.2868e-05
4	0.2843	-0.1549	1.8777e-04	2.6734e-04	5.5980e-05	8.7590e-05	1.4591e-05	-1.2439e-05
5	0.2369	-0.1291	2.4375e-04	3.5493e-04	5.9240e-05	9.8600e-05	1.2633e-05	-1.1456e-05
6	0.1896	-0.1033	3.0299e-04	4.5353e-04	6.0730e-05	1.0012e-04	1.0073e-05	-9.0478e-06
7	0.1422	-0.0775	3.6372e-04	5.5365e-04	6.1880e-05	1.0322e-04	7.3312e-06	-6.6629e-06
8	0.0948	-0.0516	4.2560e-04	6.5687e-04	6.3220e-05	1.1036e-04	4.4940e-06	-4.2742e-06
9	0.0474	-0.0258	4.8882e-04	7.6723e-04	6.8120e-05	1.2929e-04	1.6141e-06	-1.6691e-06
10	0.0000	-0.0000	5.5694e-04	8.9652e-04				
					TOTAL ENERGY:		0.00012	-0.00010

ri =	*0.638*	ro=	*12.83*	Increment =	*10*
		size =	0.0130		

Node 99

Increment	RF1	RF2	U1	U2	Delta U1	Delta U2	ENERGY 1	ENERGY 2
0	-3.8280	-1.749	0	0	9.7641e-05	1.3609e-04	-3.5508e-04	-2.2612e-04
1	-3.4452	-1.5741	9.7641e-05	1.3609e-04	9.9789e-05	1.3588e-04	-3.2469e-04	-2.0201e-04
2	-3.0624	-1.3992	1.9743e-04	2.7197e-04	1.0338e-04	1.4109e-04	-2.9680e-04	-1.8507e-04
3	-2.6796	-1.2243	3.0081e-04	4.1306e-04	1.1763e-04	1.6675e-04	-2.9269e-04	-1.8957e-04
4	-2.2968	-1.0494	4.1844e-04	5.7981e-04	1.2666e-04	1.7625e-04	-2.6667e-04	-1.6954e-04
5	-1.9140	-0.8745	5.4510e-04	7.5606e-04	1.3535e-04	1.8991e-04	-2.3315e-04	-1.4947e-04
6	-1.5312	-0.6996	6.8045e-04	9.4597e-04	1.3810e-04	1.9083e-04	-1.8503e-04	-1.1682e-04
7	-1.1484	-0.5247	8.1855e-04	1.1368e-03	1.4098e-04	1.9430e-04	-1.3492e-04	-8.4958e-05
8	-0.7656	-0.3498	9.5953e-04	1.3311e-03	1.4937e-04	2.1150e-04	-8.5768e-05	-5.5487e-05
9	-0.3828	-0.1749	1.1089e-03	1.5426e-03	1.6560e-04	2.3870e-04	-3.1696e-05	-2.0874e-05
10	-0.0000	-0.0000	1.2745e-03	1.7813e-03				
					TOTAL ENERGY:		-0.00221	-0.00140

Area = 0.0517 mm^2

ENERGY TOTALS:

Node	Direction	Total Energy (N mm)	Energy/Area (N/mm)	Energy/Area (J/m^2)
98	1	0.00012	0.00235	2.4
	2	-0.00010	-0.00194	-1.9
99	1	-0.00221	-0.04271	-42.7
	2	-0.00140	-0.02710	-27.1
	TOTAL:			-69.4

Absolute value of total in 1 (radial = MODE II):	-40.4 J/m^2	58.2%
Absolute value of total in 2 (axial = MODE I):	-29.0 J/m^2	41.8%

Plastic Work		N mm			
	P (step 2)	*0.02651*	Plastic Work	63.1 J/m^2	47.6%
	P (step 3)	*0.02977*	Debond Energy	69.4 J/m^2	52.4%
	delta P	0.00326			

Bibliography

1. Handbook of Microelectronic Packaging, eds. R.R. Tummala and E.J. Rymaszewski, van Nostrand Reinhold, New York (1989).
2. A.J. Blodgett, "Microelectronics Packaging," *Scientific American*, 86-96, July 1963.
3. C.W. Ho, D.A. Chance, C.H. Bajorek, and R.E. Acosta, "The Thin-Film Module as a High-Performance Semiconductor Package", *IBM J. Res. Devel.* **26**, 3, 286 (1982).
4. J.H. Lupinski and R.S. Moore, "Polymeric Materials for Electronics Packaging and Interconnection," American Chemical Society Symposium, Los Angeles, CA (September 1988).
5. R.R. Tummala and S. Ahmed, "Advanced Multichip Packaging Technology for IBM System 390/ES 9000 Family of Mainframe Computers", in Proc. of 1991 Japan International Electronics Manufacturing Technology Symp., 17 (1991).
6. D.M. Mattox, "Electronic Thin Films", *ECS J.*, **10**, 1 (1983).
7. R.H. Lacombe, L.P. Buchwalter, and K. Holloway, "Comparison of Finite Element Stress Analysis Results with Peel Strength at the Copper-Polyimide Interface," *J. Adhesion Sci. Tech.*, **7**, 12, 1293-1307 (1993).
8. K. Mittal, "Adhesion Measurement of Thin Films", *Electrocomponent Sci. Tech.*, **3**, 21 (1976).
9. B. Chapman, "Thin-Film Adhesion", *J. Vac. Sci. Tech.*, **11**, 1, 106 (1974).
10. J. Vali, "A Review of Adhesion Test Methods for Thin Hard Coatings", *J. Vac. Sci. Tech.*, **4**, 6, 3007 (1986).
11. J. Pawel and C. McHargue, "Testing of Adhesion of Thin Films to Substrates", *J. Adhesion Sci. Tech.*, **2**, 5, 369 (1988).
12. K-S Kim and J. Kim, "Elasto-Plastic Analysis of the Peel Test for Thin Film Adhesion", Trans. of the ASME, *J. Eng. Mater. Tech.*, **110**, 266 (1988).
13. K.S. Kim and J. Kim, "Elasto-Plastic Analysis of the Peel Test for Thin Film Adhesion," Am. Soc. Mech. Eng. Winter Annual Meeting, Anaheim, CA, December 1986.
14. J. Kim, K.S. Kim, Y.H. Kim, "Mechanical Effects in Peel Adhesion Test", *J. Adhesion Sci. Tech.*, **3**, 3, 175 (1989).
15. K.S. Kim and N. Aravas, "Elastoplastic Analysis of the Peel Test," *Int. J. Solids Structures*, **24**, 417-435 (1988).
16. N. Aravas, K.S. Kim, and M.J. Loukis, "On the Mechanics of Adhesion Testing of Flexible Films," *Mat. Sci. Eng.*, **107**, 159-168 (1989).
17. R. Jacobsson, "Measurement of the Adhesion of Thin Films," *Thin Solid Films*, **34**, 191 (1976).

18. R. Jacobsson and B. Kruse, "Measurement of Adhesion of Thin Evaporated Films on Glass Substrates by Means of the Direct Pull Method," *Thin Solid Films*, **15**, 71 (1973).

19. K. Kendall, "The Adhesion and Surface Energy of Elastic Solids," *J. Phys. D: Appl. Phys.*, **4**, 4, 1186-1195 (1971).

20. J.E. Pawel and C.J. McHargue, "Testing of Adhesion of Thin Films to Substrates," *J. Adhesion Sci. Tech.*, **2**, 5, 369 (1988).

21. J.E. Pawel, W.E. Lever, D.J. Downing, C.J. McHargue, L.J. Romana, and J.J. Wert, "Using Weibull Statistics to Analyze Ion Beam Enhanced Adhesion as Measured by the Pull Test," Mat. Res. Soc. Symp. Proc., **239**, 541 (1992).

22. J.E. Pawel and C.J. McHargue, "Analysis of Pull Tests for Determining the Effects of Ion Implantation on the Adhesion of Iron Films to Sapphire Substrates," *J. Adhesion Sci. Tech.*, **7**, 8, 845-852 (1993).

23. M.T. Laugier, "The Development of the Scratch Test Technique for the Determination of the Adhesion of Coatings," *Thin Solid Films*, **76**, 295-306 (1981).

24. M.T. Laugier, "An Energy Approach to the Adhesion of Coatings Using the Scratch Test," *Thin Solid Films*, **117**, 243-249 (1984).

25. S.J. Bull, "Failure Modes in Scratch Adhesion Testing," *Surface Coatings Tech.*, **50**, 25-32 (1991).

26. D.W. Butler, C.T.H. Stoddart, and P.R. Stuart, "Some Factors Affecting the Adhesion of Thin Metal Films", *Aspects of Adhesion*, **6**, CRC Press, Cleveland, OH (1971).

27. S. Krongelb, "Electromagnetic Tensile Adhesion Test Method," *Adhesion Measurement of Thin Films, Thick Films, and Bulk Coatings, ASTM STP 640*, K.L. Mittal, ed., Am. Soc. for Testing and Mat., 107-121 (1978).

28. B.P. Baranski and J.H. Nevin, "Adhesion of Aluminum Films on Polyimide by the Electromagnetic Tensile Test", *J. Elect. Mat.*, **16**, 1, 39 (1987).

29. H. Dannenberg, "Measurement of Adhesion by a Blister Method", *J. Appl. Polym. Sci.*, **5**, 125 (1961).

30. G.P. Anderson, S.J. Bennett, and K.L. DeVries, *Analysis and Testing of Adhesive Bonds*, Academic Press, Inc., Ch. 6, (1977).

31. M.L. Williams, "The Continuum Interpretation for Fracture and Adhesion," *J. Appl. Polym. Sci.*, **13**, 29-40 (1969).

32. S.J. Bennett, K.L. Devries, and M.L. Williams, "Adhesive Fracture Mechanics," *Int. J. Fracture*, **10**, 1, 33-43 (1974).

33. J.A. Hinkley, "A Blister Test for Adhesion of Polymer Films to SiO_2," *J. Adhesion*, **16**, 115-126 (1983).

34. A.N. Gent and L.H. Lewandowski, "Blow-Off Pressures for Adhering Layers," *J. Appl. Polym. Sci.*, **33**, 1567 (1987).

35. H. Hencky, *Zr. Math. Phys.*, **63**, 311-317 (1915).

36. H.S. Jeong, Y.Z. Chu, M.B. Freiler, C. Durning, and R.C. White, "Thin Film Adhesion Study of Microelectronics Packaging," *Mat. Res. Soc. Symp. Proc.*, **239**, 547 (1992).

37. Y.Z. Chu and C.J. Durning, "Application of the Blister Test to the Study of Polymer-Polymer Adhesion," *J. Appl. Polym. Sci.*, **45**, 1151 (1992).

38. H.S. Jeong, Y.Z. Chu, C.J. Durning, and R.C. White, "Adhesion Study of Polyimide to Silicon Surfaces," *Surf. Interface Analysis*, **18**, 289 (1992).

39. H.M. Jensen, "The Blister Test for Interface Toughness Measurement," *Engineering Fracture Machanics*, 40,3, 475 (1991).

40. H.M. Jensen and M.D. Thouless, "Effects of Residual Stresses in the Blister Test," The Danish Center for Applied Mathematics and Mechanics, Report #439 (1992).

41. Z. Sou and J.W. Hutchinson, "Interface Crack Between Two Elastic Layers," *Int. J. Fracture*, **43**, 1-18 (1990).

42. F. Maseeh-Tehrani, Ph.D. Thesis, Massachusetts Institute of Technology Department of Civil Engineering, May 1990.

43. F. Maseeh and S.D. Senturia, "Viscoelasticity and Creep Recovery of Polyimide Thin Films," Proc. of IEEE Solid-State Sensors and Actuators Workshop, Hilton-Head Island, SC, June 1990.

44. M.J. Napolitano, A. Chudnovsky, and A. Moet, "The Constrained Blister Test for the Energy of Interfacial Adhesion," *J. Adhesion Sci. Tech.*, **2**, 2, 311 (1988).

45. Y-S. Chang, Y-H. Lai, and D.A. Dillard, "The Constraing Blister - A Nearly Constant Strain Energy Release Rate Test for Adhesives," *J. Adhesion*, **27**, 197 (1989).

46. Y.H. Lai and D.A. Dillard, "Numerical Analysis of the Constrained Blister Test," *J. Adhesion*, **33**, 63-74 (1990).

47. D.A. Dillard and Y.S. Chang, "The Constrained Blister - A Novel Constant Energy Release Rate Test for Adhesives," Virginia Polytechnic Institute Report #VPI-E-87-24, Blacksburg, VA (1987).

48. Y.H. Lai and D.A. Dillard, "An Elementary Plate Theory Prediction for Strain Energy Release Rate of the Constrained Blister Test", *J. Adhesion*, **31**, 177-189 (1990).

49. M.G. Allen, "Measurement of Adhesion and Mechanical Properties of Thin Films Using Microfabricated Structures," PhD Thesis, Massachusetts Institute of Technology, Department of Electrical Engineering and Computer Science (1989).

50. M.G. Allen and S.D. Senturia, "Analysis of Critical Debonding Pressures of Stressed Thin Films in the Blister Test," *J. Adhesion*, **25**, 303 (1988).

51. M.G. Allen and S.D. Senturia, "Microfabricated Structires for the Measurement of Adhesion and Mechanical Properties of Polymer Films," *Adhesives, Sealants, and Coatings for Space and Harsh Environments*, 501 (1988).

52. M.G. Allen and S.D. Senturia, "Application of the Island Blister Test for Thin Film Adhesion", *J. Adhesion*, **29**, 219-231 (1989).

53. M.G. Allen, P. Nagarkar, and S.D. Senturia, "Aspects of Adhesion Measurement of Thin Polyimide Films," Third Annual Conference on Polyimides, Ellenville, NY (1988).

54. Y. Bao, D.A. Dillard, H.F. Webster, and J.P. Wrightman, "Application of the Peninsula Blister Test to Measure Adhesion of Thin Polymer Films," Proc. of the 15th Annual Meeting of the Adhesion Society, Hilton Head, SC, 63 (1992).

55. D.A. Dillard and Y. Bao, "The Peninsula Blister Test: A High and Constant Strain Energy Release Rate Fracture Specimen for Adhesives," *J. Adhesion*, **33**, 253 (1991).

56. Y-H. Lai, Y. Bao, and D. Dillard, "Further Development of Peninsula Blister Test and a Study of Test Efficiency for the Blister Tests," 1993 Proc. of the Adhesion Soc., (1993).

57. D.A. Dillard, Y. Bao, T. Corson, and Y-H. Lai, "The Peninsula Blister Test: A Constant Strain Energy Release Rate Test for Adhesives," 1990 Proc. of the Adhesion Soc., Savannah, GA (1990).

58. K.M. Liechti and A. Shirani, "Nonlinear Plate Analysis of Thin Film Blistering," 1993 Proc. of the Adhesion Soc., (1993).

59. G. Margaritis, E. Stafanis, S. Sikorski, E. Shaffer II, unpublished results.

60. G. Margaritis and F.J. McGarry, "Viscoelastic Analysis of Thin Polymer Films in Electronic Packages," SAMPE Quarterly, **24**, 2 (1993).

61. G. Margaritis, "Thermomechanical Effects in Electronic Packages," PhD Thesis, Massachusetts Institute of Technology, Department of Materials Science and Engineering, Ch. 2-3 (1994).

62. G. Margaritis, S.A. Sikorski, and F.J. McGarry, "Elastic-Plastic Finite Element Method Analysis and Application of the Island Blister Test," *J. Adhesion Soc. Tech.*, **8**, 3, 1-15 (1994).

63. J.Y. Pan, "A Study of Suspended-Membrane and Acoustic Techniques for the Determination of the Mechanical Properties of Thin Polymer Films," PhD Thesis, Massachusetts Institute of Technology, Department of Electrical Engineering and Computer Science, Ch. 2 (1991).

64. F. Maseeh and S.D. Senturia, "Elastic Properties of Thin Polyimide Films," in Polyimides: Materials, Chemistry and Characterization, eds. C. Feger, M.M. Khojasteh, and J.E. McGrath, Elsevier Science Publishers, 575-584 (1989).

65. F. Maseeh, M.A. Schmidt, M.G. Allen, and S.D. Senturia, "Calibrated Measurements of Elastic Limit, Modulus, and the Residual Stress of Thin Films Using Micromachined Suspended Structures," IEEE Workshop on Solid-State Sensors, Hilton Head, SC (1988).

66. J.Y. Pan, P. Lin, F. Maseeh, and S.D. Senturia, "Verification of FEM Analysis of Load-Deflection Methods for Measuring Mechanical Properties of Thin Films," Technical Digest IEEE 1990 Solid State Sensor and Actuator Workshop, Hilton Head, SC, 70-73 (1990).

67. J.W. Beams, "Mechanical Properties of Thin Films of Gold and Silver," in Structure and Properties of Thin Films, ed. C.A. Neugebauer, 183-192 (1959).

68. S.C. Noe, "A Prism Coupling Study of Optical Anisotropy in polyimide Including Moisture, Stress, and Thickness Effects," PhD Thesis, Massachusetts Institute of Technology, Department of Materials Science and Engineering, Ch. 4 (1992).

69. W.M. Prest and D.J. Luca, "The Alignment of Polymers During the Solvent-coating Process," *J. Appl. Phys.*, **51**, 10, 5170-5174 (1980).

70. J.S. Machell, J. Greener, and B.A. Contestable, "Optical Proeprties of Solvent-Cast Polymer Films," *Macromolecules*, **23**, 1, 186-194 (1990).

71. D. Volfson and F. Trusell, personal communication (1992).

72. H. Robbins and B. Schwartz, "Chemical Etching of Silicon II: The System HF, NHO_3, and $HC_2H_3O_2$," *J. Electrochem. Soc.*, **107**, 2, 108-111 (!959).

73. A.J. Kinloch, "Review: The Science of Adhesion," *J. Mat. Sci.*, **17**, 617-651 (1982).

74. H. Tada, P.C. Paris, and G.R. Irwin, The Stress Analysis of Cracks Handbook, Del Research Corp. (1973).

75. H.W. Westergaard, *J. Appl. Mech.*, **6**, 46 (1939).

76. C.F. Shih, R.J. Asaro, and N.P. O'Dowd, *Scripta Metall.* (1991).

77. A.G. Evans and J.W. Hutchinson, "Effects of Non-Planarity on the Mixed Mode Fracture Resistance of Bimaterial Interfaces," *Acta Metall.*, **37**, 3, 909-916 (1989).

78. Z. Suo and J.W. Hutchinson, "Sandwich Test Specimens for Measuring Interface Crack Toughness," *Mat. Sci. Eng.*, **107**, 135-143 (1989).

79. Z. Suo and J.W. Hutchinson, "Steady-State Cracking in Brittle Substrates Beneath Adherent Films," *Int. J. Solids Structures*, **25**, 1, 1, 1337-1353 (1989).

80. J-S Wang and Z. Suo, "Experimental Determination of Interfacial Toughness Curves Using Brazil-Nut Sandwiches," *Acta Metall.*, **38**, 7, 1279-1290 (1990).

81. M.D. Thouless, "Fracture of a Model Interface Under Mixed Mode Loading," *Acta Metall.*, **38**, 6, 1135-1140 (1990).

82. S. Suresh and C.F. Shih, "Combine Mode I -Mode II and Mode I -Mode III Fracture of Brittle Materials," *Scripta Metall. Mater.*, **25**, 991-996 (1991).

83. D.K. Shetty and A.R. Rosenfield, "Slow Crack Growth in Glass in Combined Mode I and Mode II Loading," *Scripta Metall. Mater.*, **25**, 997-1002 (1991).

84. M.D. Thouless, "Fracture Resistance of an Adhesive Interface," *Scripta Metall. Mater.*, **26**, 949-951 (1992).

85. A.A. Griffith, "The Phenomenon of Rupture and Flow in Solids," *Phil. Trans. Roy. Soc. of London*, **221**, 163-197 (1921).

86. C.E. Inglis, "Stresses in a Plate Due to the Presence of Cracks and Sharp Corners," *Trans. Inst. Naval Arch.*, **55**, 219-241 (1913).

87. G.R. Irwin, "Fracture Dynamics," in Fracture of Metals, ASM, Cleveland, OH, 147-166 (1948).

88. B. Orowon, "Fracture and the Strength of Solids," Reports on Progress in Physics, XII, 185 (1948).

89. G. Irwin, "Fracture," *Handbuch der Physik*, **6**, 551 (1958).

90. H.M. Westergaard, "Bearing Pressures and Cracks," *Trans. Am. Soc. Mech. Eng.*, **61**, 49-53 (1939).

91. E.F. Rybicki and M.F. Kanninen, "A Finite Element Calculation of Stress Intensity Factors by a Modified Crack Closure Integral," *Eng. Fract. Mech.*, **9**, 931-938 (1977).

92. R.D. Cook, Concepts and Applications of Finite Element Alanysis, John Wiley, New York, NY (1981).

93. ABAQUS User's Manual, Hibitt, Karlsson, & Sorenson, Inc., Providence, RI (1989).

94. J.R. Taylor, An Introduction to Error Analysis, University Science Books, Oxford University Press, Mill Valley, CA (1982).

95. R.N. Haward and G. Thackray, "The Use of a Mathematical Model to Describe Isothermal Stress-Strain Curves in Glassy Thermoplastics," Proc. Royal Soc., **302**, 453 (1968).

96. A.S. Argon, "A Theory for the Low-Temperature Plastic Deformation of Glassy Polymers," Phil. Mag., **30**, 67 (1973).

97. M.C. Boyce, D.M. Parks, and A.S. Argon, "Large Inelastic Deformation of Glassy Polymers. Part 1: Rate Dependent Constitutive Model," *Mechanics of Materials*, **7**, 15-33 (1988).

98. W.T. Chen and T.F. Flavin, "Mechanics of Film Adhesion: Elastic and Elastic-Plastic Behavior," *Film Adhesion*, 203-213 (1972).

99. A.N. Gent and G.R. Hamed, "Peel Mechanics for an Elastic-Plastic Adherend," *J. Applied Polymer Sci.*, **21**, 2817-2831 (1977).

100. G.R Irwin, *J. Appl. Mech.*, Trans. ASME, **24**, 361 (1957).

101. F. Erdogan and G.C. Sih, "On the Crack Extension in Plates Under Plane Loading and Transverse Shear", *J. Basic Eng.*, 519-527 (December 1963).

102. M.D. Chang, K.L. DeVries, and M.L. Williams, "The Effects of Plasticity in Adhesive Fracture," *J. Adhesion*, **4**, 221-231 (1972).

103. G.C. Trantina, "Combined Mode Crack Extension in Adhesive Joints," *J. Composite Mat.*, **6**, 371-385 (1972).

104. M.D. Chang, PhD Thesis, University of Utah, Department of Mechanical Engineering (1972).

105. W.D. Bascom, C.O. Timmons, and R.L. Jones, "Apparent Interfacial Failure in Mixed Mode Adhesive Fracture", *J. Mat. Sci.*, **10**, 1037-1048 (1975).

106. J.W. Hutchinson and Z. Suo, "Mixed Mode Cracking in Layered Materials," in Advances in Applied Mechanics, **29**, 64-187 (1992).

107. H.M. Jensen, J.W. Hutchinson, and K-Y. Kim, "Decohesion of a Cut Compressed Film on a Substrate," *J. Solids Struct.*, **26**, 1099-1114 (1990).

108. H.C. Cao and A.G. Evans, "An Experimental Study of the Fracture Resistance of Bimaterial Interfaces," *Mech. Mat.*, **7**, 295-304 (1989).

109. M.D. Thouless and H.M. Jensen, "Elastic Fracture Mechanics of the Peel-Test Geometry," IBM Research Report 17640, #77870 (1992).

110. G.P. Anderson, K.L. DeVries, and M.L. Williams, "The Influence of Loading Direction upon the Character of Adhesive Debonding," *J. Colloid Interface Sci.*, **47**, 600-609 (1974).

111. M.L. Williams, and G.P. Anderson, "Adhesive Fracture Mechanics," *Fracture*, **1** (1977).

112. D. Briggs and J.C. Riviere, "Spectral Interpretation," in Practical Surface Analysis by Auger and X-ray Photoelectron Spectroscopy, eds. B. Briggs and M.P. Seah, John Wiley & Sons, (1988).

113. P.V. Nagarkar, J-P. Lu, D. Volfson, K.F. Jensen, and S.D. Senturia, "Characterization of Fluorinated Polyimide Films," in P.S. Ho, K.A. Jackson, C.-Y. Li, and G.F. Lipscomb, eds., Electronics Packaging Materials Science VI, Materials Research Society Spring Symp. Proc., **264**, 263-268, Materials Research Society, Pittsburgh, PA (1992).

114. L.P. Buchwalter, B.D. Silverman, L. Witt, and A.R. Rossi, "X-ray Photoelectron Spectroscopy Analysis of Hexafluorodianhydride-oxydianiline Polyimide: Substantiation for Substituent Effects on Aromatic Carbon 1s Binding Energies," *J. Vac. Sci. Tech.*, **5**, 2, 226-230 (1987).

115. P. Cadman and G.M. Gossedge, "The Chemical Interaction of Metals with Polytetrafluoroethylene," *J. Mater. Sci.*, **14**, 2672-1678 (1979).

116. L.P. Buchwalter, "Adhesion of Polyimides to Metal and Ceramic Surfaces: An Overview," IBM, Interdivisional Technical Liason, Thornwood, NY, 1-13 (1989).

117. J.C. Bolger, in Adhesion Aspects of Polymeric Coatings, ed.: K.L. Mittal, Plenum Press, New York, NY, 3-18 (1983).

118. F. Faupel, C.H. Yang, S.T.Chen, and P.S. Ho, *J. Appl. Phys.*, **65**, 5, 1911 (1989).

119. G.E. Muilenberg (Ed.), Handbook of X-Ray Photoelectron Spectroscopy. Perkin-Elmer Corp., Eden Prarie, MN (1979).

120. B.D. Silverman, J.W. Bartha, J.G. Clabes, and P.S. Ho, "Molecular Orbital Analysis of the XPS Spectra of PMDA-ODA Polyimide and Its Polyamic Acid Precursor," *J. Polym. Sci.*, **24**, 3325-3333 (1986).

121. E. Desimoni, C. Malittesta, P.G. Zambonin, and J.C. Riviere, "An X-Ray Photoelectron Spectroscopic Study of Some Chromium-Oygen Systems," *Surf. Interface Anal.*, **13**, 173-179 (1988).

122. P.V. Nagarkar, in The EPP Databook: A Compendium of Research Results of the MIT Electronics Packaging Program (EPP) for the Years 1991-1993, eds. E.O. Shaffer II and S.D. Senturia, MIT, Cambridge, MA, 65-94 (!993).

123. J. M. Park, L.J. Matienzo, and D.F. Spencer, "Adhesion and XPS Studies on a Fluoropolymer-Metal Interface," *J. Adhesion Sci. Tech.*, **5**, 2, 153-163 (1991).

124. H.J. Leary, Jr. and D.S. Campbell, *Surf. Interface Anal.*, **1**, 75 (1979).

125. H.J. Leary, Jr. and D.S. Campbell, "ESCA Studies of Polyimide and Modified Polyimide Surfaces," ACS Sym. Ser. 162, 419-433 (1981).

126. N.J. Chou, D.W. Dong, J. Kim, and A.C. Liu, "An XPS and TEM Study of Intrinsic Adhesion Between Polyimide and Cr Films," *J. Electrochem. Soc.*, **131**, 10, 2335-2340 (1984).

127. N.J. Chou and C.H. Tang, "Interfacial Reaction During Metallization of Cured Polyimide: An XPS Study," *J. Vac. Soc. Tech.*, **2**, 2, 751-755 (1984).

128. P.I. Buchwalter and A.I. Baise, in Polyimides: Synthesis, Characterization and Applications, K.L. Mittal, ed., **1**, 537-545, Plenum, New York, NY (1984).

129. J.W. Bartha, P.O. Hahn, F. LeGoues, and P.S. Ho, "Photoemission Spectroscopy Study of Aluminum-Polyimide Interface," *J. Vac. Sci. Tech.*, **3**, 3, 1390-1393 (1985).

130. P.S. Ho, P.O. Hahn, J.W. Bartha, G.W. Rubloff, F.K. LeGoues, and B.D. Silverman, "Chemical Bonding and Reaction at Metal/Polymer Interfaces," *J. Vac. Sci. Tech.*, **3**, 3, 739-745 (1985).

131. M.J. Goldberg, J.G. Clobes, and C.A. Kovac, "Metal-Polymer Chemistry II: Chromium-Polyimide Interface Reactions and Related Organometallic Chemistry," *J. Vac. Sci. Tech.*, **6**, 3, 991-996 (1988).

132. P.S. Ho, R. Haight, R.C. White, and B.D. Silverman, "Chemistry and Microstructure at Metal-Polymer Interfaces," IBM Technical Report: RC 13141 (#58798) (1987).

133. N.J. Dinado, "Surface Spectroscopic Techniques Applied to Metallized Plastics," in Metallized Plastics I: Fundamental and Applied Aspects, eds. K.L. Mittal and J.R. Susko, New York, 137-170 (1989).

134. R. Haight, R.C. White, B.D. Silverman, and P.S. Ho, "Complex Formation and Growth at the Cr and Cu Polyimide Interface," *J. Vac. Sci. Tech.*, **6**, 4, 2188-2199 (1988).

135. H.M. Clearfield, private communication (1994).

136. D.T. Clark and A. Dilks, "ESCA Studies of Polymers, VII. Shake-up Phenomenoa in Some Alkane-Styrene Copolymers," *J. Polym. Sci. Polym. Chem.*, **14**, 533-542 (1976).

137. M.G. Allen, P.V. Nagarkar, and S.D. Senturia, "Adhesion of Polyimide Films to Various Substrates: An XPS Study," in Proc. of The Adhesion Society Meeting, Savannah, GA (1990).

138. A. Chenite, A. Selmani, B. Lamontange, and A. Yelon, "Interfacial Reactions Between Aluminum and BPDA-PDA," *J. Vac. Sci. Tech.*, **11**, 5, 2411-2418 (1993).

139. L.P. Buchwalter and R. Saraf, "Tanatalum and Chromium Adhesion to Polyimide. Part 1. BPDA-PDA Surface Imidization and Modification," *J. Adhesion Sci. Tech.*, **7**, 9, 925-940 (1993).

140. W.C. Stewart, J. Leu, K.F. Jensen, "FTIR and XPS Studies of Polyimdie/Metal Interface Formation," Mat. Res. Soc. Symp. Proc., **154**, 329-334 (1989).

141. J. Russat, "Characterization of Polyamic Acid/Polyimide Films in the Nanometric Thickness Range from Spin-deposited Polyamic Acid," *Surf. Interface Anal.*, **11**, 414-429 (1988).

142. S.G. Anderson, J. Leu, B.D. Silverman, and P.S. Ho, "The Chemistry and Morphology of Cr/BPDA-PDA Interface Formation," IBM Research Report RC 17416 (1991).

143. J-P. Lu, P.V. Nagarkar, D. Volfson, F. Trusell, K.F. Jensen, and S.D. Senturia, "Interfacial Chemistry and Adhesion Studies for Polyimide-Metal Systems," in Int. Symp. on the Interphase, The Adhesion Society Meeting, Williamsburg, VA, (1993).

144. J-P. Lu, P.V. Nagarkar, D. Volfson, K.F. Jensen, and S.D. Senturia, "Characterization of Polyimide Thin Films on Metals," in P.S. Ho, K.A. Jackson, C.-Y. Li, and G.F. Lipscomb, eds., Electronics Packaging Materials Science VI, MRS Symposium Proceedings, **264**, 199-204, Materials Research Society, Pittsburgh, PA (1992).

145. K.H. Tsai, K.S. Kim, "Stick-Slip in the Thin Film Peel Test - 1. The 90° Peel Test," *Int. J. Solids Structures*, **30**, 1789-1806 (1993).

146. E.O. Shaffer, S. Sikorski, and F.J. McGarry, "The Edge Delmaination Test: Measuring the Critical Adhesion Energy of Thin Film Coatings, Part II: Mode Mixity and Application," invited paper at Spring Mat. Res. Soc., San Francisco, CA (1994).

147. E.O. Shaffer, F.J. McGarry, and F. Trusell, "Edge Delamination Testing: A Method of Measuring the Adhesion Strength of Thin Coatings in Microelectronic Applications, Part I: Numerical Modeling," Proc. Mat. Res. Soc., Vol. 309, 535 (1993).

148. E.O. Shaffer, "Development and Application of the Edge Delamination Test for Measuring the Adhesive Strength of Polymer Coatings," PhD Thesis, Massachusetts Institute of Technology, Department of Materials Science and Engineering, in progress.